

Imperial College London
Department of Mechanical Engineering
Exhibition Road
London, SW7 2AZ

Modelling of Gas-Solid Flows with Non-spherical Particles

Fan Zhao

MSc

September 2014

Supervised by Dr Berend van Wachem

Submitted in part fulfilment of the requirements for the degree of
Doctor of Philosophy in Mechanical Engineering of Imperial College London
and the Diploma of Imperial College London

Abstract

Dispersed multiphase flows are common in nature and industry and are governed by complex physical phenomena. The complex features of the turbulence continuity carrier phase and the dispersed phase make the problem of a dispersed multiphase flow much more complex than a single phase flow. This research work focuses on modelling and analysing one type of dispersed multiphase flows: solid particles suspended in a turbulent channel flow. The aim of this thesis is to numerically investigate the effects of Stokes number, particle shape and particle volume fraction on the behaviour of gas-solid turbulent channel flows with non-spherical particles.

This study not only considers spherical particles but also studies non-spherical fibre-like ellipsoids suspended in the channel flow. To fully describe the complex dynamics of non-spherical particles, the rotational motion and orientation is efficiently and accurately resolved by applying unit Quaternions. To address inevitable numerical errors caused by the Quaternion integration algorithms in previous studies, a novel Quaternion integration method is derived, validated and applied for more accurately updating the unit Quaternions. This work also derives a new Quaternion equation to relate second order tensor variables between different frameworks.

This research work applies four-way coupling to accurately model the complex gas-solid turbulent channel flows, and the fluid-particle, particle-particle and particle-wall interactions are all taken into account. Important conclusions from this work are summarized as follows. In four-way coupled simulations, the average viscosity of the fluid flow is not affected by the particles, whereas the turbulence intensity is reduced by adding small heavy particles. The average direct dissipation by the particles is negligible, and the primary mechanism by which the particles affect the flow is by altering the turbulence structure near and around the turbulence kinetic energy peak. For non-spherical particles, the distributions of the orientation angles clearly demonstrate that ellipsoids tend to align within the plane that lies perpendicular to the span-wise direction in the very near wall region, follow the stream-wise direction in the buffer layer, and almost randomly distribute in the central region of the channel.

Declaration of Originality

I hereby declare that I am the author of this thesis with my own words expected where I declare otherwise. Any ideas, techniques, or any other work in any form by any other authors in my thesis are fully acknowledged where used. A list of all the references used has been included. I declare that this thesis has not been submitted for a high degree to any other University or Institution.

Fan Zhao
September 2014

Copyright Declaration

The copyright of this thesis rests with the author and is made available under a Creative Commons Attribution Non-Commercial No Derivatives licence. Researchers are free to copy, distribute or transmit the thesis on the condition that they attribute it, that they do not use it for commercial purposes and that they do not alter, transform or build upon it. For any reuse of redistribution, researchers must make clear to others the licence terms of this work.

Fan Zhao
September 2014

Publications

Journal papers

M. Zastawny, G. Mallouppas, F. Zhao and B. G. M. van Wachem, “Derivation of drag and lift force and torque coefficients for non-spherical particles in flows”, International Journal of Multiphase Flow, 39, 227-239 (2012)

F. Zhao and B. G. M. van Wachem, “A novel Quaternion integration approach for describing the behaviour of non-spherical particles”, Acta Mech 224(12), 3091-3109 (2013).

F. Zhao and B. G. M. van Wachem, “Direct numerical simulations of ellipsoidal particles in turbulent channel flow”, Acta Mech 224(10), 2331-2358 (2013)

B. G. M. van Wachem, M. Zastawny, F. Zhao and G. Mallouppas, “Modelling of gassolid turbulent channel flow with non-spherical particles with large Stokes numbers”, International Journal of Multiphase Flow, 68, 80-92. (2014)

F. Zhao, W. K. George and B. G. M. van Wachem, “Four-way coupled simulations of small particles in turbulent channel flows: the effects of particle shape and Stokes number”, submitted to Physics of Fluids (2014).

Conference papers

B. G. M. van Wachem, M. Zastawny, G. Mallouppas and F. Zhao, “Modelling of gas-solid turbulent flows with non-spherical particles”, 8th International Conference on Multiphase Flow (ICMF 2013), 1-6, (2013)

B. G. M. van Wachem, M. Zastawny, F. Zhao and G. Mallouppas, “Modelling of gas-solid turbulent flows with non-spherical particles”, 13th Workshop on Two-Phase Flow Predictions, Halle, Germany, 17 - 20 September (Vol. 39) (2012).

Acknowledgements

I would like to express my sincere gratitude to my supervisor Dr. Berend van Wachem for the support of my MSc and PhD study and research, for his patience and immense knowledge. His guidance has helped me in the research and writing of this thesis and other papers.

I would like to thank Mr. John M Hughes for his encouragement and comments to help me improve my English and academic writing. Furthermore, I would like to thank Prof. William K George for his help and discussions about my work.

I thank my colleagues and friends in the office: Dr. George Mallouppas, Dr. Fabian Denner and John. I am also grateful to all my friends for your friendship and support.

Last but not the least. I would like to thank my family: parents and my fiance Jindi for their unconditional support me all the time.

To my parents.
For their endless love and support

Contents

List of Figures	17
List of Tables	25
Abbreviations	26
Nomenclature	26
1. Background	28
1.1. Introduction	28
1.2. Outline of thesis	30
1.3. Single phase fully developed turbulent channel flow and turbulence	32
1.3.1. Kolmogorov scales and wall units	32
1.3.2. Fluid velocity fluctuations and Reynolds stresses	33
1.3.3. Turbulence kinetic energy (TKE) equation for a single phase fully developed channel flow	34
1.3.4. Fluid flow dissipation rate and local isotropic and axisymmetric assumptions for turbulent channel flows	35
1.3.5. Fluid flow mean square vorticity	36
1.4. Parameters in gas-solid turbulent channel flow	36
1.4.1. Particle size and particle shape	37
1.4.2. Particle volume fraction and mass loading	37
1.4.3. Particle Reynolds number	38
1.4.4. Wall roughness	38
1.4.5. Stokes number	38
1.5. Computational fluid dynamics (CFD) of gas-solid multiphase flow	39
1.5.1. Numerical approaches for dispersed multiphase flows	39
1.5.2. Fluid phase modelling and governing equations	41
1.5.2.1. Governing equations	41
1.5.3. Particle phase modelling	42
1.5.3.1. Hydrodynamic forces on solid particles in a fluid flow . . .	42
1.5.3.2. Particle-particle and particle-wall collisions	43
1.5.4. Coupling between discrete particles and the fluid phase	43
1.6. Non-spherical particles	44

2. Modelling the rotational motion of Non-spherical particles: a novel Quaternion method	46
2.1. Introduction	48
2.2. Rotation and Quaternions	50
2.2.1. Rotation dynamic equations	50
2.2.2. Rotation operators	51
2.2.2.1. Euler angles	51
2.2.2.2. Rotation matrix	51
2.2.2.3. Unit Quaternions	52
2.2.3. Quaternion and Quaternion operators	52
2.2.3.1. Multiplication of Quaternions	53
2.2.4. Rotation by unit Quaternion	54
2.3. Numerical integration of unit Quaternions	57
2.3.1. Previously proposed methods based on Taylor polynomial expansion	57
2.3.1.1. Euler method	57
2.3.1.2. Leap frog method	58
2.3.1.3. Scalar factor method	59
2.3.2. Direct multiplication method	60
2.3.3. Newly proposed predictor-corrector direct multiplication method .	62
2.4. Comparison of methods and discussion	63
2.4.1. Energy conservation	64
2.4.2. Comparison with three test-cases: energy conservation	64
2.4.2.1. First test-case: single falling fibre	65
2.4.2.2. Second test-case: nine falling fibres	66
2.4.2.3. Third test-case: prescribed one-dimensional torque on a particle	67
2.4.3. Rate of convergence	68
2.4.3.1. Fourth test-case: prescribed three-dimensional torque on a fibre	69
2.4.4. Discussion	70
2.5. Conclusion	71
3. Methodology: four-way coupling gas-solid multiphase channel flow simulations	73
3.1. Introduction	75
3.2. Dynamics of gas-solid turbulent channel flow	78
3.2.1. Fluid flow	78
3.2.2. Turbulence kinetic energy (TKE) equation for a fully developed gas-solid turbulent channel flow	78
3.2.3. Numerical settings of the fluid phase	79
3.2.4. The dynamics of non-spherical particles	80
3.2.4.1. Particle translational dynamics	80
3.2.4.2. The rotation of ellipsoidal particles	81

3.2.5. Particle mesh	83
3.3. Lagrangian point-particle four-way coupling method	84
3.3.1. Fluid effects on particles: hydrodynamic drag forces and torques . .	84
3.3.2. Particle coupling with the fluid flow	86
3.3.3. Inter-particle and particle-wall collisions	86
3.3.4. Limitations	88
3.4. Validation of the single phase flow simulation	89
3.5. Summary	90
4. Four-way coupled simulations of small non-spherical particles in turbulent channel flows: the effects of particle shape and Stokes number	92
4.1. Introduction	94
4.2. Simulation set-up	95
4.2.1. Particle properties	95
4.2.2. Numerical setting	96
4.3. Fluid Statistics	96
4.3.1. Fluid velocity statistics	97
4.3.2. The modulation of turbulence	100
4.3.2.1. Turbulence transport terms	100
4.3.2.2. The production of turbulence	101
4.3.2.3. Dissipation terms	102
4.3.2.4. Components of the fluid flow turbulence dissipation . . .	104
4.3.3. Vorticity	106
4.4. Contour plots of instantaneous fluid velocities	107
4.5. Particle statistics	109
4.5.1. Particle distribution	109
4.5.2. Particle velocity	111
4.5.3. Velocity correlation coefficients between fluid and particle phases .	112
4.5.4. Mean slip velocities between the fluid flow and dispersed particles .	113
4.5.5. The angular velocity of particles	115
4.5.6. The orientation of ellipsoidal particles	115
4.6. Conclusion	120
5. Four-way coupled simulations of small particles in turbulent channel flows: the effects of particle volume fraction and a wide range of Stokes number	124
5.1. Introduction	126
5.2. Simulation set-up	127
5.3. Contour plots of instantaneous fluid velocities and particle distribution .	128
5.3.1. Particle deposition	135
5.4. Fluid flow statistics	136
5.4.1. Fluid velocity	136

5.4.2. The turbulence modulation	141
5.4.2.1. Turbulence transport terms	141
5.4.2.2. The production of turbulence	142
5.4.2.3. The fluid flow dissipation rate	143
5.4.2.4. Dissipation rate caused by the coupling force of the particles	143
5.4.2.5. Components in the fluid dissipation rate	144
5.5. Particle statistics	146
5.5.1. Particle velocity statistics	146
5.5.2. Particle-fluid interactions	148
5.5.2.1. Slip velocity between particle and fluid mean velocities . .	148
5.5.2.2. The correlation coefficient between fluid and particle ve-	
locities	150
5.6. Conclusions	151
6. Summary and recommendation for future plans	153
6.1. Summary	153
6.2. Future plans	156
Bibliography	158
A. Turbulent Kinetic energy (TKE) equation	166
A.1. TKE equation in fully developed channel flow	169
A.2. The fluid flow dissipation rate	171
B. Some characteristics of turbulence in gas-solid channel flows	172
B.1. The components of dissipation rate	172
B.2. Taylor microscales	175
B.3. Kolmogorov scales	176
B.4. Summary	177
C. The distribution of particle angular velocity	178
D. The orientation of ellipsoidal particles	180
D.1. The comparison of the mean absolute cosine values $ \cos(\theta_i) $ and the mean	
orientation angles θ_i	180
D.2. The distribution of orientation angle (ψ_i)	180

List of Figures

1.1.	The solid line represents a fluid turbulence eddy and the dash line represents particle motion. (a) Stokes number is less than 1, (b) Stokes number is around 1, and (c) Stokes number is much larger than 1.	39
1.2.	The construction of an ellipsoidal particle by spheres	44
2.1.	The relation between body space (a) and world space (b). The fixed axes of body space, x^b , y^b and z^b are indicated in both figures. The position of a fixed point in body space, p^b is transformed to world space, $p(t)$	49
2.2.	A quaternion Q Changes the orientation and length of vector \mathbf{A} to vector \mathbf{B} , and this quaternion is vertical to the vector A and B	54
2.3.	The scalar method: Δq represent Quaternion increment in other algorithm, $f\Delta q$ represent the increment in the scalar method, and Δqr represents the real increment.	60
2.4.	The error in energy resulting from the four different rotational integration algorithms for test-case 1: a single falling fibre.	65
2.5.	The error in total energy resulting from the four different rotational integration algorithms in the case of 9 falling fibres.	66
2.6.	The error in total energy resulting from the scalar factor method and the novel PCDM method in the case of 9 falling fibres.	67
2.7.	Different particle trajectories as predicted by: (a) the novel PCDM method, and (b) the scalar factor method for the case of 9 falling fibres.	68
2.8.	The error in the prediction of the unit vector as a function of time for the scalar factor method and the PCDM method.	69
2.9.	The angle error of the unit vector as a function of the inverse of time step $\frac{1}{\Delta t}$ (log-log plot)	70
3.1.	The computational channel domain	80
3.2.	(a) Body space and (b) World space co-ordinates. The x^b axis of the body-space co-ordinate system always aligns with the major-axis of the ellipsoidal particle, whereas the world-space co-ordinates remain fixed in space and time.	81
3.3.	Particle mesh and fluid mesh	83
3.4.	Fluid stream-wise direction mean velocities as a function of the distance to the wall for: clear fluid ($-x$), Marchioli <i>et. al.</i> [70] data ($-o$)	89
3.5.	Fluid stream-wise direction RMS velocities as a function of the distance to the wall for: clear fluid ($-x$), Marchioli <i>et. al.</i> [70] data ($-o$)	89

3.6. Fluid wall-normal direction RMS velocities as a function of the distance to the wall for: clear fluid ($-x$), Marchioli <i>et. al.</i> [70] data ($-o$)	90
3.7. Fluid wall-normal direction RMS velocities as a function of the distance to the wall for: clear fluid ($-x$), Marchioli <i>et. al.</i> [70] data ($-o$)	90
3.8. Turbulence structures in TKE equation	91
4.1. Fluid mean velocity in the flow direction as a function of distance to the wall	97
4.2. Fluid mean velocity in the flow direction as a function of distance to the wall in the near wall region	98
4.3. Fluid mean velocity in the flow direction in the central region of the channel	98
4.4. Fluid RMS velocity in the wall-normal direction as a function of distance to the wall	98
4.5. Fluid RMS velocity in the span-wise direction as a function of distance to the wall	98
4.6. Fluid RMS velocity in the stream-wise direction as a function of distance to the wall	99
4.7. Fluid RMS velocity in the stream-wise direction as a function of distance to the wall	99
4.8. Reynolds stress as a function of distance to the walls	100
4.9. TKE turbulence itself transport term as a function of distance to the wall .	101
4.10. TKE pressure fluctuation transport term as a function of distance to the wall	101
4.11. TKE viscous transport term as a function of distance to the wall	101
4.12. The production of turbulence as a function of distance to the wall	102
4.13. The minus fluid flow dissipation rate as a function of distance to the wall .	102
4.14. The dissipation rate caused by the coupling force from particles as a function of distance to the wall	103
4.15. Mean-square derivative $\langle u_{1,2}^{\prime f+2} \rangle$ as a function of distance to the wall . .	104
4.16. Mean-square derivative $\langle u_{1,3}^{\prime f+2} \rangle$ as a function of distance to the wall . .	105
4.17. Mean-square derivative $\langle u_{3,2}^{\prime f+2} \rangle$ as a function of distance to the wall . .	105
4.18. The ratio of homogeneous dissipation rate ($\tilde{\varepsilon}_{hom}$) to the fluid dissipation rate ($\tilde{\varepsilon}$) as a function of distance to the wall	105
4.19. The ratio of isotropic dissipation rate ($\tilde{\varepsilon}_{iso}$) to the fluid dissipation rate ($\tilde{\varepsilon}$) as a function of distance to the wall	105
4.20. The ratio of the axisymmetric dissipation rate 1 ($\tilde{\varepsilon}_{axis_1}$) to the fluid dissipation rate ($\tilde{\varepsilon}$) as a function of distance to the wall	106
4.21. The ratio of axisymmetric dissipation rate 2 ($\tilde{\varepsilon}_{axis_2}$) to the fluid dissipation rate ($\tilde{\varepsilon}$) as a function of distance to the wall	106
4.22. The mean square vorticity in the stream-wise direction as a function of distance to the wall	106
4.23. The mean square vorticity in the wall-normal direction as a function of distance to the wall	107
4.24. The mean square vorticity in the span-wise direction as a function of distance to the wall	107

4.25. The instantaneous fluid velocity (indicated by colour) in the wall-normal direction and the distribution of spherical particles with $St = 5$ near the cross-sectional y-z plane at $x^+ = 942$	107
4.26. The instantaneous fluid velocity (indicated by colour) in the wall-normal direction and the distribution of ellipsoids with $St = 30$ and $\lambda = 5$ near the cross-sectional y-z plane at $x^+ = 942$	108
4.27. The instantaneous fluid velocity (indicated by colour) in the stream-wise direction and the distribution of spherical particles with $St = 5$ near the cross-sectional x-z plane at $y^+ = 8$	108
4.28. The instantaneous fluid velocity (indicated by colour) in the stream-wise direction and the distribution of ellipsoids with $St = 30$ and $\lambda = 5$ near the cross-sectional x-z plane at $y^+ = 8$	109
4.29. The ratio of the particle volume fraction $\langle \alpha_y^p \rangle$ in the wall-normal direction to averaged particle volume fraction $\langle \alpha_n^p \rangle$ of the whole channel as a function of distance to the wall	110
4.30. The ratio of the particle volume fraction $\langle \alpha_y^p \rangle$ in the wall-normal direction to averaged particle volume fraction $\langle \alpha_n^p \rangle$ of the whole channel in the near wall region	110
4.31. Particle mean velocity in the flow direction as a function of distance to the wall	111
4.32. Particle mean velocity in the flow direction in the near wall region	111
4.33. Particle RMS velocity in the stream-wise direction as a function of distance to the wall	111
4.34. Particle RMS velocity in the wall-normal direction as a function of distance to the wall	112
4.35. Particle RMS velocity in the span-wise direction as a function of distance to the wall	112
4.36. The stream-wise correlation coefficient of particle and fluid velocities as a function of distance to the wall	113
4.37. The span-wise correlation coefficient of particle and fluid velocities as a function of distance to the wall	113
4.38. Mean stream-wise slip velocity between dispersed particles and the fluid flow as a function of distance to the wall	114
4.39. Mean wall-normal slip velocity between dispersed particles and the fluid flow as a function of distance to the wall	114
4.40. Mean span-wise slip velocity between dispersed particles and the fluid flow as a function of distance to the wall	114
4.41. The mean particle angular velocity in the span-wise direction as a function of distance to the wall	115
4.42. Three orientation angle θ_i between three axes of world space and the vector of the ellipsoid major axis \mathbf{X}^p , which aligns with the x axis of body space, in world space.	116

4.43. Mean orientation angle θ_3 between particle Major axis vector x^p and z axis of world space as a function of distance to the wall	116
4.44. Mean orientation angle θ_1 between particle major axis x^p and x axis of world space as a function of distance to the wall	117
4.45. Mean orientation angle θ_2 between particle major axis x^p and y axis of world space as a function of distance to the wall	117
4.46. The distribution of θ_1 in the near wall region ($y^+ < 10$)	117
4.47. The distribution of θ_2 in the near wall region ($y^+ < 10$)	117
4.48. The distribution of θ_3 in the near wall region ($y^+ < 10$)	118
4.49. The distribution of θ_1 at channel center.	118
4.50. The distribution of θ_2 at channel center.	118
4.51. The distribution of θ_3 at channel center	118
4.52. The particle major axis x^p projects on the y - z , x - z and x - y planes, leading to three 2-D vectors x_{yz}^p , x_{xz}^p and x_{xy}^p . The angles ψ_i represent the angles between the 2-D vectors x_{yz}^p , x_{xz}^p and x_{xy}^p and the z , x and x axes of world space.	119
4.53. The distribution of ψ_1 in the near wall region ($y^+ < 10$)	120
4.54. The distribution of ψ_2 in the near wall region ($y^+ < 10$)	120
4.55. The distribution of ψ_3 in the near wall region ($y^+ < 10$)	120
4.56. The distribution of ψ_1 at channel center.	120
4.57. The distribution of ψ_2 at channel center.	121
4.58. The distribution of ψ_3 at channel center	121
4.59. An ellipsoidal particle with ψ_3 less than 90° next to the wall	121
4.60. An ellipsoidal particle with ψ_3 more than 90° next to the wall	121
 5.1. The instantaneous fluid velocity (indicated by colour) in the wall-normal direction and the distribution of spherical particles with $St = 1$ near the cross-sectional y - z plane at $x^+ = 942$ for the case with 0.2 million particles	129
5.2. The instantaneous fluid velocity (indicated by colour) in the wall-normal direction and the distribution of spherical particles with $St = 5$ near the cross-sectional y - z plane at $x^+ = 942$ for the case with 0.2 million particles	129
5.3. The instantaneous fluid velocity (indicated by colour) in the wall-normal direction and the distribution of spherical particles with $St = 30$ near the cross-sectional y - z plane at $x^+ = 942$ for the case with 0.2 million particles	129
5.4. The instantaneous fluid velocity (indicated by colour) in the wall-normal direction and the distribution of spherical particles with $St = 50$ near the cross-sectional y - z plane at $x^+ = 942$ for the case with 0.2 million particles	130
5.5. The instantaneous fluid velocity (indicated by colour) in the wall-normal direction and the distribution of spherical particles with $St = 5$ near the cross-sectional y - z plane at $x^+ = 942$ for the cases with 1 million particles .	130
5.6. The instantaneous fluid velocity (indicated by colour) in the wall-normal direction and the distribution of spherical particles with $St = 30$ near the cross-sectional y - z plane at $x^+ = 942$ for the cases with 1 million particles .	130

5.7. The instantaneous fluid velocity (indicated by colour) in the stream-wise direction and the distribution of spherical particles with $St = 1$ near the cross-sectional x-z plane at $y^+ = 8.0$ for the case with 0.2 million particles	132
5.8. The instantaneous fluid velocity (indicated by colour) in the stream-wise direction and the distribution of spherical particles with $St = 5$ near the cross-sectional x-z plane at $y^+ = 8.0$ for the case with 0.2 million particles	132
5.9. The instantaneous fluid velocity (indicated by colour) in the stream-wise direction and the distribution of spherical particles with $St = 30$ near the cross-sectional x-z plane at $y^+ = 8.0$ for the case with 0.2 million particles	132
5.10. The instantaneous fluid velocity (indicated by colour) in the stream-wise direction and the distribution of spherical particles with $St = 50$ near the cross-sectional x-z plane at $y^+ = 8.0$ for the case with 0.2 million particles	133
5.11. The instantaneous fluid velocity (indicated by colour) in the stream-wise direction and the distribution of spherical particles with $St = 5$ near the cross-sectional x-z plane at $y^+ = 8.0$ for the cases with 1 million particles	133
5.12. The instantaneous fluid velocity (indicated by colour) in the stream-wise direction and the distribution of spherical particles with $St = 30$ near the cross-sectional x-z plane at $y^+ = 8.0$ for the cases with 1 million particles	133
5.13. The instantaneous fluid velocity (indicated by colour) in the wall-normal direction and the distribution of spherical particles with $St = 50$ near a x-y plane across a low-speed streak for the case with 0.2 million particles	134
5.14. The instantaneous fluid velocity (indicated by colour) in the stream-wise direction and the distribution of spherical particles with $St = 50$ near a x-y plane across a high-speed area for the cases with 0.2 million particles	134
5.15. The instantaneous fluid velocity (indicated by colour) in the wall-normal direction and the distribution of spherical particles with $St = 30$ near a x-y plane across a low-speed streak for the case with 1 million particles	134
5.16. The instantaneous fluid velocity (indicated by colour) in the stream-wise direction and the distribution of spherical particles with $St = 30$ near a x-y plane across a high-speed area for the cases with 1 million particles	134
5.17. The local particle volume fraction $\langle \alpha_y^p \rangle$ in the wall normal direction as a function of distance to the wall	136
5.18. The ratio of the local particle volume fraction $\langle \alpha_y^p \rangle$ and the average particle volume fraction $\langle \alpha_n^p \rangle$	136
5.19. The local particle volume fraction $\langle \alpha_y^p \rangle$ in the wall normal direction as a function of distance to the wall in the cases with low total particle volume fraction ($\alpha^p = 0.0073\%$)	137
5.20. The peak and minimum values of local particle volume fraction $\langle \alpha_y^p \rangle$ in the wall normal direction as a function of Stokes number in the cases with low total particle volume fraction ($\alpha^p = 0.0073\%$)	137
5.21. Fluid stream-wise mean velocity as a function of distance to the wall	137

5.22. Fluid velocity RMS in the stream-wise direction as a function of distance to the wall	138
5.23. Fluid velocity RMS in the wall-normal direction as a function of distance to the wall	138
5.24. Fluid velocity RMS in the span-wise direction as a function of distance to the wall	138
5.25. Reynolds stress $\langle u_1'^f u_2'^f \rangle$ as a function of distance to the wall	138
5.26. Fluid stream-wise mean velocity as a function of distance to the wall	139
5.27. Fluid velocity RMS in the stream-wise direction as a function of distance to the wall	139
5.28. Fluid velocity RMS in the wall-normal direction as a function of distance to the wall	139
5.29. Fluid velocity RMS in the span-wise direction as a function of distance to the wall	140
5.30. Reynolds stress $\langle u_1'^f u_2'^f \rangle$ as a function of distance to the wall	140
5.31. TKE turbulence itself transport term as a function of distance to the wall	141
5.32. TKE pressure fluctuation transport term as a function of distance to the wall	141
5.33. TKE viscous transport term as a function of distance to the wall	141
5.34. TKE turbulence itself transport term as a function of distance to the wall	141
5.35. TKE pressure fluctuation transport term as a function of distance to the wall	142
5.36. TKE viscous transport term as a function of distance to the wall	142
5.37. Turbulence kinetic energy production as a function of distance to the wall	142
5.38. Turbulence kinetic energy production as a function of distance to the wall	142
5.39. Turbulence kinetic energy dissipation rate as a function of distance to the wall	143
5.40. Turbulence kinetic energy dissipation rate as a function of distance to the wall	143
5.41. The dissipation rate caused by the coupling force from particles as a function of distance to the wall	144
5.42. The dissipation rate caused by the coupling force from particles as a function of distance to the wall	144
5.43. Mean-square derivative $\langle u_{1,2}^{\prime+f^2} \rangle$ as a function of distance to the wall	145
5.44. Mean-square derivative $\langle u_{1,3}^{\prime+f^2} \rangle$ as a function of distance to the wall	145
5.45. Mean-square derivative $\langle u_{3,2}^{\prime+f^2} \rangle$ as a function of distance to the wall	145
5.46. Mean-square derivative $\langle u_{1,2}^{\prime+f^2} \rangle$ as a function of distance to the wall	145
5.47. Mean-square derivative $\langle u_{1,3}^{\prime+f^2} \rangle$ as a function of distance to the wall	146
5.48. Mean-square derivative $\langle u_{3,2}^{\prime+f^2} \rangle$ as a function of distance to the wall	146
5.49. Particle mean velocity in the steam-wise direction as a function of distance to the wall	146
5.50. Particle RMS velocity in the stream-wise direction as a function of distance to the wall	146

5.51. Particle RMS velocity in the wall-normal direction as a function of distance to the wall	147
5.52. Particle RMS velocity in the span-wise direction as a function of distance to the wall	147
5.53. Particle mean velocity in the steam-wise direction as a function of distance to the wall	147
5.54. Particle RMS velocity in the stream-wise direction as a function of distance to the wall	147
5.55. Particle RMS velocity in the wall-normal direction as a function of distance to the wall	148
5.56. Particle RMS velocity in the span-wise direction as a function of distance to the wall	148
5.57. Mean stream-wise slip velocity between particles and the fluid flow as a function of distance to the wall	148
5.58. Mean wall-normal slip velocity between particles and the fluid flow as a function of distance to the wall	148
5.59. Mean span-wise slip velocity between particles and the fluid flow as a function of distance to the wall	149
5.60. Mean stream-wise slip velocity between particles and the fluid flow as a function of distance to the wall	149
5.61. Mean wall-normal slip velocity between particles and the fluid flow as a function of distance to the wall	149
5.62. Mean span-wise slip velocity between particles and the fluid flow as a function of distance to the wall	149
5.63. The stream-wise correlation coefficient of particle and fluid velocities as a function of distance to the wall	150
5.64. The wall-normal correlation coefficient of particle and fluid velocities as a function of distance to the wall	150
5.65. The stream-wise correlation coefficient of particle and fluid velocities as a function of distance to the wall	150
5.66. The wall-normal correlation coefficient of particle and fluid velocities as a function of distance to the wall	150
B.1. Mean-square derivative $\langle u_{1,2}^{\prime f+2} \rangle$ as a function of distance to the wall	172
B.2. Mean-square derivative $\langle u_{1,3}^{\prime f+2} \rangle$ as a function of distance to the wall	172
B.3. Mean-square derivative $\langle u_{3,2}^{\prime f+2} \rangle$ as a function of distance to the wall	173
B.4. Mean-square derivative $\langle u_{2,3}^{\prime f+2} \rangle$ as a function of distance to the wall	173
B.5. Mean-square derivative $\langle u_{3,3}^{\prime f+2} \rangle$ as a function of distance to the wall	173
B.6. Mean-square derivative $\langle u_{2,2}^{\prime f+2} \rangle$ as a function of distance to the wall	173
B.7. Mean-square derivative $\langle u_{1,1}^{\prime f+2} \rangle$ as a function of distance to the wall	174
B.8. Mean-square derivative $\langle u_{3,1}^{\prime f+2} \rangle$ as a function of distance to the wall	174
B.9. Mean-square derivative $\langle u_{2,1}^{\prime f+2} \rangle$ as a function of distance to the wall	174

B.10. Cross derivative $\langle u_{1,2}^{\prime f+} u_{1,2}^{\prime f+} \rangle$ as a function of distance to the wall	174
B.11. Cross derivative $\langle u_{1,3}^{\prime f+} u_{3,1}^{\prime f+} \rangle$ as a function of distance to the wall	175
B.12. Cross derivative $\langle u_{2,3}^{\prime f+} u_{3,2}^{\prime f+} \rangle$ as a function of distance to the wall	175
B.13. The longitudinal Taylor scale in the stream-wise direction	175
B.14. The wall-normal transverse Taylor scale in the stream-wise direction	175
B.15. The span-wise transverse Taylor scale in the stream-wise direction	176
B.16. The longitudinal Taylor scale in the span-wise direction	176
B.17. The stream-wise transverse Taylor scale in the span-wise direction	176
B.18. The wall-normal transverse Taylor scale in the span-wise direction	176
B.19. The Kolmogrov length scale (η) as a function of distance to the wall	177
C.1. The frequency of stream-wise angular velocity in the near wall region of $0 < y^+ < 10$	178
C.2. The frequency of wall-normal angular velocity in the near wall region of $0 < y^+ < 10$	178
C.3. The frequency of span-wise angular velocity in the near wall region of $0 <$ $y^+ < 10$	179
C.4. The frequency of stream-wise angular velocity in the central region of the channel	179
C.5. The frequency of wall-normal angular velocity in the central region of the channel	179
C.6. The frequency of span-wise angular velocity in the central region of the channel	179
D.1. The mean orientation angles in the stream-wise direction: \diamond and \square indicate the results of mean angles, while \blacklozenge and \blacksquare represent the angle computed from the results of mean cosine	180
D.2. The mean orientation angles in the wall-normal direction: \diamond and \square indicate the results of mean angles, while \blacklozenge and \blacksquare represent the angle computed from the results of mean cosine	180
D.3. The mean orientation angles in the span-wise direction: \diamond and \square indicate the results of mean angles, while \blacklozenge and \blacksquare represent the angle computed from the results of mean cosine	181
D.4. The frequency of ψ_1 in the buffer-layer region ($15 < y^+ < 20$).	181
D.5. The frequency of ψ_2 in the buffer-layer region ($15 < y^+ < 20$).	181
D.6. The frequency of ψ_3 in the buffer-layer region ($15 < y^+ < 20$).	182

List of Tables

1.1.	Numerical methods for modelling solid-fluid multiphase flows in “Multi-Flow” [100]	40
1.2.	The phase couplings	44
2.1.	The properties of cylindrical fibres and the boundary wall of the box. The diameter (D), Youngs’ modulus (E), Poisson’s ratio (ν), coefficient of friction, (μ), and coefficient of restitution (e).	65
2.2.	The orientation of a unit vector $x = (1.0, 0.0, 0.0)$ after a second simulation with a non-linear torque by Scalar factor method and the novel PCDM method	67
3.1.	The properties of the fluid and the flow	79
3.2.	The properties of the computational domain and grid in all three directions	79
4.1.	Particle properties in different simulations	96
4.2.	The portion of particles in the low-speed streaks around $y^+ = 8.0$	109
5.1.	Particle properties in different simulations	128
5.2.	The portion of particles in the low-speed streaks around $y^+ = 8.0$	135

Nomenclature

Vectors and tensors are either denoted in **bold** or in tensor notation by subscripts i (vector) or ij (tensor), dependent on the context. All units are SI units.

Roman Letters

α^f	Fluid volume fraction
α^p	Particle volume fraction
ϵ_{ijk}	Premutation tensor
η	Kolmogorov length scale (m)
λ	The aspect ratio of an ellipsoidal particle
\mathcal{P}	The production of turbulence kinetic energy ($m^2 s^{-3}$)
μ^f	Fluid viscosity ($kg m^{-1} s^{-1}$)
ν^f	Fluid dynamic viscosity ($m^2 s^{-1}$)
ω_i^f	Mean square vorticity ($m^2 s^{-3}$)
ω_i^p	Particle angular velocity ($rads^{-1}$)
Φ	Mass loading
ρ^f	Fluid density ($kg m^{-3}$)
ρ^p	Particle density ($kg m^{-3}$)
τ_f	Fluid response time (s)
τ_p	Particle response time (s)
τ_η	Kolmogorov time scale (s)
τ_{ij}	Shear stress tensor ($kg m^{-1} s^{-2}$)
$\tilde{\varepsilon}$	Fluid flow dissipation rate ($m^2 s^{-3}$)
$\tilde{\varepsilon}_{Axis_1}$	Modelled dissipation rate 1 based on axisymmetric assumption ($m^2 s^{-3}$)
$\tilde{\varepsilon}_{Axis_2}$	Modelled dissipation rate 2 based on axisymmetric assumption ($m^2 s^{-3}$)
$\tilde{\varepsilon}_{Hom}$	Homogeneous turbulence dissipation rate ($m^2 s^{-3}$)
$\tilde{\varepsilon}_{Iso}$	Isotropic turbulence dissipation rate ($m^2 s^{-3}$)
ε_p	Dissipation rate caused by coupling particles($m^2 s^{-3}$)
a	The length of semi-minor axis of an ellipsoidal particle (m)
C_D	Drag coefficient
D^p	Spherical particle diameter (m)
F	Force (N)
g	Gravity (ms^{-2})
h	Half channel height (m)
I_{ij}	Inertia tensor
k	Turbulence Kinetic Energy (J)
K_{ij}	Particle resist tensor
l_τ^f	Friction length scale (m)

p	Pressure ($kgms^{-2}$)
q	Quaternion
Re_τ	Friction Reynolds number
Re_{bulk}	Bulk Reynolds number
Re_p	Particle Reynolds number
St	Stokes number
T	Torque (Nm)
u_i^f	Fluid velocity (ms^{-1})
u_τ^f	Friction velocity (ms^{-1})
u_i^p	Particle velocity (ms^{-1})
u_η	Kolmogorov velocity scale (ms^{-1})
x_i	Lagrangian particle position (m)
δ_{ij}	Kronecker delta

1. Background

1.1. Introduction

Dispersed multiphase flows are commonly found in industrial applications such as fuel combustion processes, cyclones, fluidized beds, and pollution control systems, and in environmental phenomena such as sand storms, flows of mud, and the spread of soot particles, to name a few. These flows cover a wide range of flow fields, such as solid particles suspended in liquid or gas flows, dispersed droplets in gases and bubbles in liquid flows. These flow fields can be also distinguished by geometrical boundary and boundary conditions, such as wall-bounded flows and free-surface flows. Due to diversified flow conditions and complex inter-phase exchanges of mass, momentum and energy, the problem of multiphase flows is much more difficult to solve than a single phase fluid flow. Although dispersed multiphase flows have been widely experimentally and numerically studied in the past decades, there are still many challenges and problems left, due to the limited experimental technology and computing capacity. This thesis only focuses on one such challenging area, modelling a large number of small solid non-spherical particles suspended in a turbulent channel flow.

For precisely modelling a dispersed multiphase flow, a proper numerical method must be applied according to flow conditions and accuracy requirements. Recently, Balachandar and Eaton [8] review the modelling of dispersed multiphase flows, introducing various methods to simulate multiphase flows in the literature, recommending appropriate choices for different numerical methods, and reporting several important phenomena in different multiphase flows. Among the numerical methods introduced in [8], the Lagrangian point-particle approach seems to be the most widely used method, and there is only one limitation of this method: the particle size is smaller than the Kolmogorov scale. Moreover, different momentum coupling between the fluid flow and particles should be properly chosen according to the flow condition, including one-way coupling, two-way coupling and four-way coupling. The one-way coupling only models the effect of the fluid flow on particles, and two-way coupling considers both the effect of the fluid flow on particles and the reverse effect of particles on the flow. Including these two effects, the four-way coupling also take the inter-particle collision into account. This study applies the four-way coupled Direct Numerical Simulation (DNS) combined with the Lagrangian point-particle approach to model the gas-solid channel flow with non-spherical particles.

In the literature, gas-solid multiphase channel flows are extensively studied, experimentally *e.g.* [11, 36, 60–62, 91] and numerically *e.g.* [33, 70, 83, 90, 97, 111]. Most of the research studies consider spheres as solid particles. Unfortunately, particle shape in realistic applications can be arbitrary. Therefore, the understanding of gas-solid multiphase

flows with non-spherical particles is of growing interest. However, there are only a few papers concerned with gas-solid channel flow containing non-spherical particles. Over the past decade, several studies investigate non-spherical ellipsoids suspended in channel flows, applying one-way or two-way coupling, *see* [3, 71, 76, 77, 108]. In these papers, one-way coupled simulations are incapable of resolving the effect of particles on the fluid flow, inter-particle and particle-wall collisions, and thus these research studies only reported the statistics of ellipsoids with different particle inertia and aspect ratio. Moreover, in many of these studies, it is unclear if the fluid and particle statistics have become truly steady. The ellipsoidal particle is also chosen as the non-spherical particle in this research work.

When modelling a dynamic system with a large number of non-spherical particles, one crucial issue is how to accurately and efficiently describe the complex dynamics of the non-spherical particles. The motion of non-spherical particles is much more complex than that of spheres. For spherical particles, modelling their translational motion can describe their dynamics but this does not suffice for non-spherical particles. The orientations of non-spherical particles in a fluid flow can influence the interactions between the particles and the fluid flow. Therefore, the orientation and rotation of non-spherical particles must be accurately resolved. In the literature, many papers, *e.g.* [1, 9, 56, 71, 76, 103], apply unit Quaternions to partially represent the rotation and orientation of non-spherical particles, and use the Quaternion integration algorithms based on the Taylor expansion with the necessity of the corresponding rotation matrices. However, all these methods lead to an inevitable numerical error: Quaternions exceeding the unit length. To fix this severe error, Quaternions are re-normalized to preserve their unit length after each time step. As a result, relationships between the elements of a unit Quaternion are changed, and the rotation information in the Quaternion is then varied. Therefore, these Quaternion integration methods only loosely approximate the rotational motion of particles.

The collisions of inter-particle and particle-wall play an important role in particle dynamics, but they are very difficult to be accurately resolved. Many research papers preform simulations with one-way or two-way coupling to describe gas-solid channel flows, neglecting the problem of the particle collision. However, particle collisions may influence the fluid flow and the particles, especially for flows with non-spherical particles. At which level of particle volume fraction or mass loading, the effect of particle collisions on both phases becomes significant is still unclear for the channel flow with non-spherical particles. This study attempts to deal with the above two problems. In order to precisely describe the orientation and rotational motion of non-spherical particles, an novel Quaternion integration method for updating unit Quaternions is developed. It implicitly preserves the unit length of the Quaternions. Furthermore, a new Quaternion expression is derived to transform second order tensors between different reference frameworks. In this study, only unit Quaternions are employed without the necessity of the rotation matrices. Without rotation matrices, a large amount of computational time and memory is saved. On the other hand, all potential particle collisions can be directly detected and determined applying an deterministic collision model: the soft-sphere model, and the effect of particles on the fluid

flow is also considered in the simulations. Therefore, this study applies four-way coupling to fully resolve particle-fluid interactions, inter-particle and particle-wall collisions. For gas-solid channel flows, there are several important physical features, such as low-speed streaks, particle deposition in the near wall region and the flow turbulence modulation by the presence of heavy particles in the flow. In the literature, *e.g.* [70, 71, 76, 108], one-way coupled simulations can only predict particle behaviour, and two-way coupled frameworks [3, 111] can partially analyse the fluid flow. However, these papers are not able to provide accurate models of gas-solid flows due to neglecting the effects of particles and particle collisions on both phases. In this study, the applied four-way coupling guarantees to obtain more precise results of the fluid flow and the discrete particles than the previous works. The modulation of the flow turbulence is rigorously explored by analysing complex turbulence terms, such as the fluid flow turbulence dissipation rate, the production of turbulence and the mean-square vorticity in the gas-solid turbulent channel flows. Although applying four-way coupled DNS can provide an accurate way of modelling gas-solid turbulent channel flows, the extremely high cost DNS simulations and tracking a large amount of individually particles limit the size of system that can be considered. In this study, the friction Reynolds number of the channel flow is restricted at a quite low value, 150, with only a few hundred thousand particles, but the computational time of a simulation is still over 4 month. The Lagrangian point-particle approach requires the particle size smaller than the length of the mesh cell and, more importantly, to the Kolmogorov micro-scale. Furthermore, the particle shape is limited. At current stage, hydrodynamic drags on spheres and ellipsoids have been well studied, and their empirical models have been extensively applied. However, fluid effects on solid particles with other complex non-spherical shapes have not been well predicted yet due to the significantly complex interactions between non-spherical particles and the fluid flow, and only very a few research papers works on this. Recently, Zastawny *et. al.* [106] proposes drag models for four types of non-spherical particle (two ellipsoids, one disc and one fibre) and tests these models. In the current thesis, only spherical and ellipsoidal particles are used in the simulations. The aim of this thesis is to numerically investigate the effects of Stokes number, elongated particle shape and particle volume fraction on the behaviour of the gas-solid turbulent channel flow. The future work should further explore gas-solid multiphase flows with other complex shape particles.

1.2. Outline of thesis

This thesis is organised as follows. Chapter 1 introduces the research area, identifying the research gaps between previous studies and this work and mentioning the limitations in this work. Several key features of a fully developed single phase channel flow are introduced, and some important turbulence terms in the channel flow are formulated. Moreover, important parameters are described, which describes the dispersed multiphase flow. This chapter then briefly introduces the Computational fluid dynamics (CFD), including numerical methods for dispersed multiphase flows, governing equations for the fluid flow

and particles and momentum coupling methods. Finally, the mathematical treatment of non-spherical particles in this study is interpreted.

In Chapter 2, a novel Quaternion integration method is derived for accurately updating unit Quaternions to represent the rotational motion and orientation of non-spherical particles. Three commonly used rotation operators (Euler angle, rotation matrix and unit Quaternion) are first introduced and compared with each other. Among these three rotation operators, the unit Quaternion is applied in many studies as well as this work. After introducing the basic Quaternion properties and operators, a new Quaternion expression is derived to transform second order tensors between different reference frameworks. Applying this novel equation, the rotation matrices, which are required by all other methods, are completely replaced by unit Quaternions in this work. A novel Quaternion integration algorithm, called predictor-corrector direct multiplication (PCDM) method is developed [109], only using Quaternion multiplication between unit Quaternions. This method guarantees to implicitly preserve the unit length of Quaternions. To validate this method, it is compared with three other Quaternion integration methods via four comparison tests. Chapter 3 describes the applied DNS four-way coupling combined with the Lagrangian point-particle approach. The governing equations for the dynamics of both phases are put forward, and flow conditions and computational settings are then provided. After that, this chapter fully describes the four-way coupling, which consists of the effect of particles on the fluid flow, the effect of the fluid flow on dispersed particles, particle-particle collisions and particle-wall collisions. In addition, there are several limitations confining the current research, which are discussed. Finally, the numerical settings for the fluid flow are validated by comparing the velocity statistics of the clear flow simulation with the one-way coupling flow data in [70].

Chapter 4 investigates the effects of Stokes number and particle shape on behaviour of the gas-solid channel flow with ellipsoidal particles. Firstly, some previous studies are reviewed, and particle properties in different particle-laden simulations are then listed. The statistical results of cases considering ellipsoids with various particle inertia and aspect ratio are shown and analysed. The particle effects on the flow turbulence are deeply investigated by analysing turbulence terms in the turbulence kinetic energy (TKE) equations, the components of the fluid flow dissipation rate and mean square vorticity. The velocity relationship between the fluid flow and particles is also explored. Furthermore, this chapter shows and analyse the particle accumulation and orientation of ellipsoidal particles in the channel flow.

Chapter 5 expands the research to investigate the effects of a wide range of Stokes number and particle volume fraction on both fluid and particle phases. The results of the fluid flow shows the modulation of the flow turbulence among the cases with various particle volume fraction and Stokes number. The effect of a wide range of Stokes number on the particle distribution is carefully analysed.

Chapter 6 summarises the research work and highlights the contributions and important results in Chapter 2, 4 and 5. Finally, some possible future work is put forward.

1.3. Single phase fully developed turbulent channel flow and turbulence

A fully developed fluid channel flow has several important features, which are quite different from other turbulence flows. The flow field is confined by the boundaries of the channel. “Fully developed” means that the channel flow reaches steady state and is in a statistical sense independent of the flow initial conditions and time. The mean fluid velocity is predominantly in the stream-wise direction, whereas the mean velocities in the wall normal and span-wise directions are zero. If the stream-wise and span-wise lengths of the channel are sufficiently large compared to the channel height, the stream-wise and span-wise directions can be treated as homogeneous directions. In these two homogeneous directions, all time averaged variables are in essential identical, and time averaged partial differential variables equals zero. The properties of the fully developed channel flow are statistically stationary, *i.e.* the statistics are independent of time, and statistically one-dimensional, with fluid statistics only depending on wall-normal direction. Another important feature is that the mean axial pressure gradient is uniform across the whole channel and equal to the mean wall shear stress at the wall. In order to overcome this wall stress and maintain the channel flow, two approaches in simulating channel flows are generally used: fixed mass flow rate and constant pressure gradient in the stream-wise direction.

The turbulent channel flow can be characterized by the bulk Reynolds number, given as:

$$Re_{bulk} = \frac{h\mathbf{U}^f}{\nu^f} \quad (1.1)$$

where \mathbf{U}^f represents the bulk fluid velocity, *i.e.* mean fluid flow velocity in the stream-wise direction, ν^f is the fluid kinematic viscosity, and h is the half length of the channel height. The superscript f on the variables indicates these variables for the fluid phase. Turbulence flow properties can be represented by their mean values and statistical fluctuations. This is referred as the Reynolds decomposition:

$$u(t) = U + u' \quad (1.2)$$

where the mean value of variable $u(t)$ is represented by the capital letter U , while the superscript, prime, denotes that the variable u' is the fluctuating term. The symbol prime is used to represents fluctuating variables through the whole thesis.

1.3.1. Kolmogorov scales and wall units

The smallest scale in a turbulence flow can be characterised by Kolmogorov scales: Kolmogorov length scale (η), Kolmogorov velocity scale (u_η), and Kolmogorov time scale (τ_η), expressed as: [40, 82]

$$\eta = (\nu^{f^2}/\tilde{\varepsilon})^{1/4} \quad (1.3)$$

$$u_\eta = (\tilde{\varepsilon} \nu^f)^{1/4} \quad (1.4)$$

$$\tau_\eta = (\nu^f / \tilde{\varepsilon})^{1/2} \quad (1.5)$$

where $\tilde{\varepsilon}$ represents the fluid flow dissipation rate. Only DNS simulations can fully resolve the smallest scale turbulence eddies, requiring the length of the mesh cell to be smaller than Kolmogorov scale.

When modelling a turbulent channel flow, wall units are widely used for analysing the statistical results, including the friction length scale (l_τ^f), the friction velocity (u_τ^f) and the fluid response time (τ_f). These wall units are defined by

$$l_\tau^f = \frac{\nu^f}{u_\tau^f} \quad (1.6)$$

$$u_\tau^f = \sqrt{\frac{\tau_0}{\rho^f}} \quad (1.7)$$

$$\tau_f = \frac{\nu^f}{u_\tau^f} \quad (1.8)$$

where τ_0 is the averaged wall shear stress, and ρ^f represents the density of the fluid flow. In this study, the simulation results of both fluid and particle phases are scaled by the wall units, obtaining their non-dimensional forms. In addition, the friction Reynolds number is defined by

$$Re_\tau = \frac{h u_\tau^f}{\nu^f} \quad (1.9)$$

1.3.2. Fluid velocity fluctuations and Reynolds stresses

The turbulence is generated and maintained by the shear due to boundary walls, and is strongly anisotropic near the walls. The basic single point turbulence structures are the fluid Root Mean Square (RMS) velocity and Reynolds stresses, which are defined by

$$\tau_{ij}^{Re} = -\rho^f \langle u_i'^f u_j'^f \rangle \quad (1.10)$$

where the symbol $\langle \rangle$ represents averaged operator, and the subscript i represents the i^{th} ($i = 1, 2$ or 3) component, where the Einstein convention is assumed, and $1, 2$ and 3 represent the stream-wise (x), wall normal (y) and span-wise (z) directions, respectively. For a fully developed channel flow, the matrix Reynolds stress is simplified into one component:

$$\tau^{Re} = -\rho^f \langle u_1'^f u_2'^f \rangle \quad (1.11)$$

In the averaged Navier-Stokes equation the Reynolds stress is expressed as a divergence term $-\rho^f \frac{\partial}{\partial x_j} \langle u_i'^f u_j'^f \rangle$. In the wall normal and span-wise directions, the divergence terms $-\rho^f \frac{\partial}{\partial x_j} \langle u_i'^f u_j'^f \rangle$ ($i = 2$ or $i = 3$) equal zero due to all the other terms in the averaged Navier-Stokes equation are all zero in these two directions. Since averaged partial derivatives are equal to zero in the homogeneous directions, $-\rho^f \frac{\partial}{\partial x_1} \langle u_1'^f u_1'^f \rangle$ and

$-\rho^f \frac{\partial}{\partial x_3} < u_1'^f u_3'^f >$ are exactly zero. Therefore, only the component $-\rho^f \frac{\partial}{\partial x_2} < u_1'^f u_2'^f >$ in the averaged Navier-Stokes equation has a value for a fully developed channel flow. At solid walls, the Reynolds stresses and the RMS velocities are exactly zero due to the no-slip boundary condition. As the distance from the wall increases in the wall-normal direction, τ^{Re} increases to the peak value in the buffer layer and then reduces to zero again at the center of the channel.

1.3.3. Turbulence kinetic energy (TKE) equation for a single phase fully developed channel flow

The turbulence terms in the turbulence kinetic energy (TKE) equation describe key features of the flow turbulence, and include the fluid flow turbulence dissipation rate, the production of turbulence and the transport of turbulence. The TKE equation of a single fluid phase flow is directly derived from the Reynolds stress equation with the assumptions of Newtonian fluid and constant fluid density, is given as [40]:

$$\begin{aligned} \frac{\partial}{\partial t} k + U_j^f \frac{\partial k}{\partial x_j} = & \frac{\partial}{\partial x_j} \left(-\frac{1}{2} < u_i'^f u_i'^f u_j'^f > - \frac{< u_j'^f p' >}{\rho^f} + 2\nu^f < s_{ij}'^f u_i'^f > \right) \\ & - < u_i'^f u_j'^f > \frac{\partial U_i^f}{\partial x_j} - 2\nu^f < s_{ij}'^f s_{ij}'^f > \end{aligned} \quad (1.12)$$

where $k = \frac{1}{2} < u_i'^f u_i'^f >$ is the turbulence kinetic energy, $s_{ij}'^f$ represents the strain rate tensor, the first three terms in the parentheses on the right hand side represent turbulence transport terms: by the turbulence itself, by the pressure fluctuations and by the viscous stresses, the term $- < u_i'^f u_j'^f > \frac{\partial U_i^f}{\partial x_j}$ is the turbulence production \mathcal{P} , and the last term represents the fluid flow dissipation rate $\tilde{\varepsilon}$. The strain rate tensor $s_{ij}'^f$ is expressed as:

$$s_{ij}'^f = \frac{1}{2} \left[\frac{\partial u_i'^f}{\partial x_j} + \frac{\partial u_j'^f}{\partial x_i} \right] \quad (1.13)$$

The mean velocity gradient in the turbulence production indicates that the turbulence kinetic energy k is generated from the mean flow, whereas k dissipates at the small scale eddies.

For a fully developed channel flow, averaged partial differential terms in homogeneous stream-wise and span-wise directions are equal to zero, and thus the TKE equation can be simplified into [82]:

$$\frac{d}{dx_2} \left(\frac{1}{2} < u_2'^f u_i'^f u_i'^f > + \frac{< u_2'^f p' >}{\rho^f} - \nu^f \frac{d}{dx_2} (k + u_2'^f)^2 \right) = \mathcal{P} - \tilde{\varepsilon} \quad (1.14)$$

The production of turbulence \mathcal{P} is expressed as:

$$\mathcal{P} = - < u_1'^f u_2'^f > \frac{dU_1^f}{dx_2} \quad (1.15)$$

and the fluid flow dissipation rate $\tilde{\varepsilon}$ is given as:

$$\tilde{\varepsilon} = 2\nu^f \langle s_{ij}'^f s_{ij}'^f \rangle \quad (1.16)$$

Both the mean flow gradient and shear stresses vanish at the channel center, where \mathcal{P} reaches the minimum value, zero. The peak of \mathcal{P} is at the position, where the Reynolds stress equals the viscous stress. As the largest shear occurs at the boundaries, the fluid dissipation rate $\tilde{\varepsilon}$ peaks at the walls and reaches the minimum magnitude at the center of the channel. All three turbulence transport terms do not generate or dissipate any turbulence energy in the flow field, but transport the TKE from one location to another location.

The detail about the derivation of the TKE equation 1.12 and TKE equation 1.14 in a fully developed channel flow is further interpreted in Appendix A.

1.3.4. Fluid flow dissipation rate and local isotropic and axisymmetric assumptions for turbulent channel flows

The TKE equation, mean square fluid flow vorticity and components in the fluid flow dissipation rate have been widely investigated for single phase channel flows, *e.g.* [4, 5, 39, 54, 55]. In these papers, the assumptions of local isotropy and local axisymmetric turbulence in the channel center were discussed. This study explore these assumptions for the gas-solid turbulent flow.

The fluid flow dissipation rate, $\tilde{\varepsilon}$, contains a total of twelve components (nine mean square derivative terms and three cross terms), given as:

$$\begin{aligned} \tilde{\varepsilon} = & \nu [2(\langle u_{1,1}'^f \rangle + \langle u_{2,2}'^f \rangle + \langle u_{3,3}'^f \rangle) \\ & + (\langle u_{1,2}'^f \rangle + \langle u_{2,1}'^f \rangle + \langle u_{1,3}'^f \rangle + \langle u_{3,1}'^f \rangle + \langle u_{3,2}'^f \rangle + \langle u_{2,3}'^f \rangle) \\ & + 2(\langle u_{1,2}'^f u_{2,1}'^f \rangle + \langle u_{1,3}'^f u_{3,1}'^f \rangle + \langle u_{2,3}'^f u_{3,2}'^f \rangle)] \end{aligned} \quad (1.17)$$

Among all 12 components, only three components ($\langle u_{1,2}'^2 \rangle$, $\langle u_{3,2}'^2 \rangle$ and $\langle u_{1,3}'^2 \rangle$) significantly contribute to $\tilde{\varepsilon}$, whereas the other components are much smaller than those three in the near wall region.

The isotropic dissipation rate of the fluid, $\tilde{\varepsilon}_{iso}$, is defined by a square derivative term [5, 94],

$$\tilde{\varepsilon}_{iso} = 15\nu^f \langle u_{1,1}'^f \rangle \quad (1.18)$$

or

$$\tilde{\varepsilon}_{iso} = \frac{15}{2}\nu^f \langle u_{1,2}'^f \rangle \quad (1.19)$$

and the fluid homogeneous dissipation rate, $\tilde{\varepsilon}_{hom}$, can be expressed as [38]

$$\tilde{\varepsilon}_{hom} = \nu^f \langle u_{i,j}'^f u_{i,j}'^f \rangle \quad (1.20)$$

$\tilde{\varepsilon}_{hom}$ does not contain all three cross-terms, which are cancelled out by $\langle u_{1,1}^{\prime f} \rangle + \langle u_{2,2}^{\prime f} \rangle + \langle u_{3,3}^{\prime f} \rangle$.

The local axisymmetric turbulence for single phase flow is reported and discussed in earlier studies [39, 55], and two modelled axisymmetric dissipation rates are given as:

$$\tilde{\varepsilon}_{axis_1} = \nu^f \left[\frac{5}{3} \langle u_{1,1}^{\prime f} \rangle + 2 \langle u_{1,3}^{\prime f} \rangle + 2 \langle u_{2,1}^{\prime f} \rangle + \langle u_{2,3}^{\prime f} \rangle \right] \quad (1.21)$$

$$\tilde{\varepsilon}_{axis_2} = \nu^f \left[-\langle u_{1,1}^{\prime f} \rangle + 2 \langle u_{1,2}^{\prime f} \rangle + 2 \langle u_{2,1}^{\prime f} \rangle + 8 \langle u_{2,2}^{\prime f} \rangle \right] \quad (1.22)$$

1.3.5. Fluid flow mean square vorticity

The flow mean square vorticity vector, ω^f , is defined as the curl of the velocity fluctuation:

$$\omega_i^{f2} = \epsilon_{ijk} u_{k,j}^{\prime f} \quad (1.23)$$

where the permutation tensor is defined by

$$\epsilon_{ijk} = \begin{cases} 1, & \text{if } ijk \text{ is an even permutation} \\ -1, & \text{if } ijk \text{ is an odd permutation} \\ 0 & \text{otherwise} \end{cases} \quad (1.24)$$

The mean square vorticity is determined as:

$$\begin{aligned} \langle \omega^f \rangle^2 &= (\langle u_{1,2}^{\prime f} \rangle + \langle u_{2,1}^{\prime f} \rangle + \langle u_{1,3}^{\prime f} \rangle + \langle u_{3,1}^{\prime f} \rangle + \langle u_{3,2}^{\prime f} \rangle + \langle u_{2,3}^{\prime f} \rangle) \\ &\quad - 2(\langle u_{1,2}^{\prime f} u_{2,1}^{\prime f} \rangle + \langle u_{1,3}^{\prime f} u_{3,1}^{\prime f} \rangle + \langle u_{2,3}^{\prime f} u_{3,2}^{\prime f} \rangle) \end{aligned} \quad (1.25)$$

Three components are separately expressed as:

$$\langle \omega_1^f \rangle^2 = \langle u_{3,2}^{\prime f} \rangle + \langle u_{2,3}^{\prime f} \rangle - 2 \langle u_{2,3}^{\prime f} u_{3,2}^{\prime f} \rangle \quad (1.26)$$

$$\langle \omega_2^f \rangle^2 = \langle u_{1,3}^{\prime f} \rangle + \langle u_{3,1}^{\prime f} \rangle - 2 \langle u_{1,3}^{\prime f} u_{3,1}^{\prime f} \rangle \quad (1.27)$$

$$\langle \omega_3^f \rangle^2 = \langle u_{1,2}^{\prime f} \rangle + \langle u_{2,1}^{\prime f} \rangle - 2 \langle u_{1,2}^{\prime f} u_{2,1}^{\prime f} \rangle \quad (1.28)$$

Like in the dissipation rate $\tilde{\varepsilon}$, components $\langle u_{1,2}^{\prime 2} \rangle$, $\langle u_{3,2}^{\prime 2} \rangle$ and $\langle u_{1,3}^{\prime 2} \rangle$ are also dominant in mean square vorticity. It should be also noted that the three cross terms give the opposite effects for $\langle \omega^f \rangle^2$ and $\tilde{\varepsilon}$, and $\langle \omega^f \rangle^2$ does not contain the principle terms $\langle u_{i,i}^{\prime f} \rangle$.

1.4. Parameters in gas-solid turbulent channel flow

There are some important parameters in gas-solid multiphase flows such as particle size, particle shape, particle volume fraction, particle mass loading, Reynolds number, wall roughness and Stokes number. Each parameter can considerably influence the fluid flow and dispersed particles, and the combination of these variables makes the problem of mul-

tiphase flows complex and difficult to predict.

1.4.1. Particle size and particle shape

The particle size plays an important role in gas-solid flows. It can be measured by the diameter of spherical particles or the equivalent diameter of non-spherical particles. The mechanism of fluid-particle interactions strongly depends on the particle size. When the particle diameter is much larger than Kolmogrov length scale, the particle boundary effect becomes important. The fluid flowing over large particles may separate from the particle surface and form a wake area after the particle due to the non-slip condition on the particle surface and large fluid flow inertia. On the other hand, particles with small diameter, *i.e.* smaller than Kolmogrov length scale, can extract momentum from the fluid flow so as to reduce turbulence intensity. The effect of particle boundary can be neglected, and particles can be considered as points in the flow [22].

The hydrodynamic drag forces and torques are strongly influenced by the particle shape. Therefore, particles with different shapes may have quite different behaviours in the turbulent flow [106], and need different empirical drag models to predict the flow effect on them. The particle size and shape can considerably influence the fluid-particle interactions.

1.4.2. Particle volume fraction and mass loading

The particle volume fraction (α^p) and mass loading (Φ) determine the level of interactions between particle and fluid phases. The mass loading is expressed as:

$$\Phi = \frac{\alpha^p \rho^p U_1^p}{\alpha^f \rho^f U_1^f} \quad (1.29)$$

where the superscript p represents the variables for the particle phase.

In a gas-solid channel flow, particles with large Stokes numbers tend to accumulate in the near wall region, and hence the local particle volume fraction near the wall can be several times more than the averaged particle volume fraction of the whole channel. Sommerfeld *et. al.* [92] proposes that the one-way coupling for modelling the gas-solid flows is only valid when α^p is less than 10^{-6} , the two-way coupling can be used for $10^{-6} < \alpha^p < 10^{-3}$, and the full four-way coupling should be applied for dense flows ($\alpha^p > 10^{-3}$). These criterion are well accepted for modelling dispersed spherical particles in fluid flows. However, at which level of particle volume fraction or mass loading, the inter-particle and particle-wall collisions becoming significant is still uncertain for multiphase flows with non-spherical particles.

1.4.3. Particle Reynolds number

The particle Reynolds number is defined as:

$$Re_p = \frac{D^p |\mathbf{U}^p - \mathbf{U}^f|}{\nu_f} \quad (1.30)$$

where D^p is the particle diameter. The drag coefficient of the hydrodynamic drag forces varies with the change of the particle Reynolds number. Large Re_p generally leads to a large mean slip velocity between the fluid and particle phases. This indicates a high level of fluid-particle interactions.

1.4.4. Wall roughness

For gas-solid turbulent channel flows, the roughness of boundaries is an important parameter, especially if the gravity is perpendicular to the wall. Rough wall can considerably influence the behaviour of the particles and the fluid flow, *e.g.* [11, 33, 61]. Sommerfeld *et. al.* [91] and Benson *et. al.* [11] experimentally exploring the effect of wall roughness demonstrates that rough walls can enlarge the fluid velocity gradient in the very near wall region and strengthen the turbulence intensity, compared to the cases with smooth walls. The effect of rough walls is even stronger on dispersed particles. The rough wall increases particle-wall collision frequency and also leads to irregular particle motion after particle collisions. The mean particle velocity can be considerably reduced by the rough wall, but the particle velocity fluctuations are enhanced. Moreover, the profile of the particle velocity tends to become uniform in the wall normal direction. In addition, collisions between particles and the rough wall lead to more particles moving back into the flow than collisions between particles and the smooth wall, thus weakening the phenomenon of particle accumulation in the near wall region. The rough wall not only enhances the fluid-particle interactions but also the particle-particle interactions. In general, large particles have more chance colliding with rough walls than relatively small particles; therefore, the wall roughness effect can be enhanced by increasing the particle size. Recently, Mallouppas and van Wachem [67] propose a rough wall model for modelling multiphase channel flows.

1.4.5. Stokes number

The Stokes number is one of the most important parameters in the gas-solid multiphase flows and defined as the ratio of the particle response time to the fluid response time:

$$St = \frac{\tau^p}{\tau^f} \quad (1.31)$$

As can be seen from Figure 1.1(a), when Stokes number is extremely small ($St \ll 1$), solid particles follow the fluid flow, moving as fluid particles. The velocities of both phases are almost equal. The effect of particles on the fluid flow can be neglected. On the other hand, particles with extremely large Stokes number ($St \gg 1$) shown in Fig. 1.1(c) can strongly resist flow effects on them so that their motion is hardly influenced by the fluid

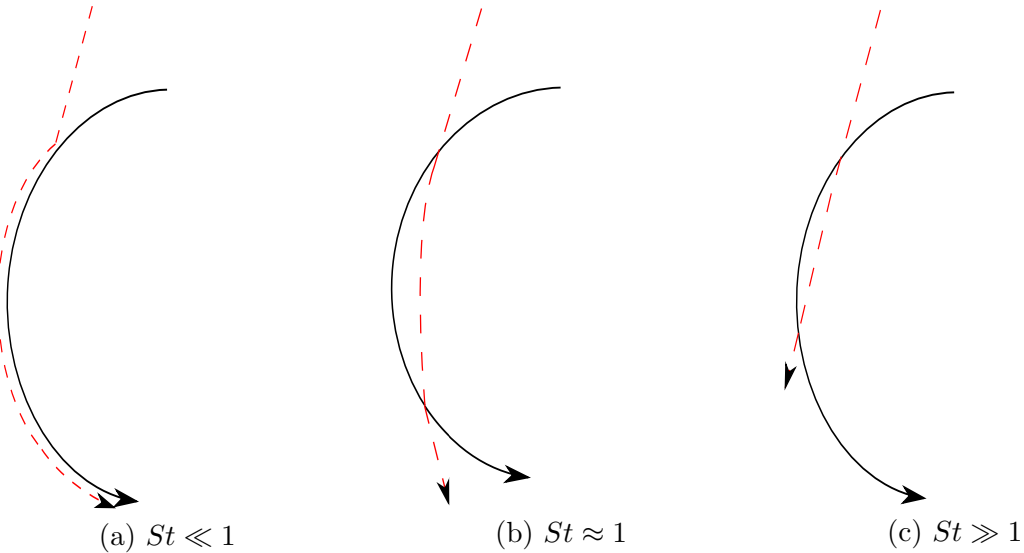


Figure 1.1.: The solid line represents a fluid turbulence eddy and the dash line represents particle motion. (a) Stokes number is less than 1, (b) Stokes number is around 1, and (c) Stokes number is much larger than 1.

flow.

1.5. Computational fluid dynamics (CFD) of gas-solid multiphase flow

Computational Fluid Dynamics (CFD) is the analysis of dynamic systems involving fluid flow, heat transfer and other related phenomena through numerical models. With the development of computational technology and computer capacity, CFD has become a vital technique for solving flow problems in recent decades, and it provides a way of exploring and studying the complex physics of flow fields. In the literature, various CFD approaches have been derived and applied for modelling dispersed multiphase flows [8]. Choosing a proper numerical method should be based on flow conditions and the accuracy requirement. All simulations in this study are carried out in the in-house multiphase flow solver “MultiFlow” [17, 100], which provides several numerical approaches to model different multiphase flows. For accurately and efficiently modelling gas-solid channel flows, this research work applies the four-way coupled DNS with the Lagrangian point-particle approach.

1.5.1. Numerical approaches for dispersed multiphase flows

In the flow solver “MultiFlow”, there are three computational approaches for modelling dispersed multiphase flows: the Eulerian-Eulerian approach, the Lagrangian point-particle approach and the immersed boundary (fully resolved) approach, *see* Table 1.1. The latter method is the most accurate approach to perform fully resolved DNS simulations. When the particle diameter is larger than Kolmogorov length scale (η), the boundary effect of

Approach	Definition	Limitation
Eulerian-Eulerian	The Eulerian-Eulerian approach treats both the carrier fluid and dispersed phases as continuous fluid media. closure models are required to describe all interactions.	1. $D^p < \eta$
Lagrangian point-particle	The point-particle approach solves the fluid phase in an Eulerian framework, and retains the Lagrangian description of the particles.	1. $D^p < \eta$
Immersed boundary	The immersed boundary approach fully resolves the whole flow field, using boundary conditions on moving particles to resolve the fluid around them.	1. $D^p > \eta$ 2. A few particles (up to thousands)

Table 1.1.: Numerical methods for modelling solid-fluid multiphase flows in “Multi-Flow” [100]

particles can strongly influence the flow, and the fluid flow around the particle must be fully resolved. To achieve this, the immersed boundary method is applied, resolving the effects of individual moving particle surface. Due to the extremely high computational cost, this fully resolved approach is currently only feasible for modelling a few dispersed particles, up to thousands. This limitation implies that this method is clearly impractical for the current work, which focuses on channel flows with a relatively large number of particles, up to a few million. To efficiently model a great number of particles with small diameters, Eulerian-Eulerian and Lagrangian point-particle approaches can be applied. The Eulerian-Eulerian method, or two-fluid approach, considers both Eulerian fluid and dispersed particles as interpenetrating continuity media, and solves both particle and fluid phases in an Eulerian framework. The interactions of fluid-particle and particle-particle require closure models, which require a large number of assumptions and are often complex and (semi) empirical. The two-fluid method is quite fast but incapable of tracking individual particle, only statistically computing and representing particle properties in the framework of the probability density function (PDF). Therefore, particle-fluid interactions cannot always be accurately determined. On the other hand, the Lagrangian point-particle approach individually tracks all particles in the flow field, and particle properties, such as position, mass momentum and energy, are also precisely solved. Furthermore, the fluid-particle and particle-particle interactions can be well approximated by applying proper empirical models. The restriction is that the particle size must be smaller than Kolmogorov length scale. In the literature, the point-particle approach has been extensively applied for modelling dispersed multiphase flows, *e.g.* [29, 70, 83, 93, 99], as well as chosen for the current work.

1.5.2. Fluid phase modelling and governing equations

The behaviour of turbulent fluid flows is naturally random and chaotic, and turbulence motion can be well recognised by a wide range of turbulence eddies. There are three commonly used numerical approaches for describing the turbulence fluid flow: Reynolds-Averaged Navier-Stokes equations (RANS), Large Eddy Simulation (LES) and Direct Numerical Simulation (DNS). Applying turbulence models, RANS focuses on the mean flow and turbulence effect on mean flow properties. The LES methodology can resolve the behaviour of large turbulent eddies through spatial filtering operations to separate large and small eddies. In LES simulations, the effect of the small, unresolved eddies is captured by sub-grid-scale (SGS) turbulence models. Neither the RANS or the LES can resolve eddies at the smallest scales, whereas only DNS can fully and accurately compute both the mean flow and all scale turbulent eddies. In order to resolve the smallest scale turbulence, DNS simulations must be performed on extremely fine meshes, of which the cell length is smaller than the Kolmogorov length scale, and the time step is also sufficiently small to be consistent with the fine mesh. Therefore, the computational cost of DNS is extremely high, rapidly rising with the Reynolds number. The number of computational grid points increase with $Re^{9/4}$.

This study applies the DNS approach without using any empirical turbulence models to fully and accurately describe the fluid channel flow. However, the considerably high cost restricts the flow bulk Reynolds number to a small value, 2300.

1.5.2.1. Governing equations

For the Eulerian fluid phase, the governing equations are continuity and Navier-Stokes (momentum) equations. In multiphase flows, continuity equation is defined by

$$\frac{\partial \alpha^f \rho^f}{\partial t} + \frac{\partial}{\partial x_i} (\alpha^f \rho^f u_i^f) = 0 \quad (1.32)$$

where α^f is the fluid volume fraction, ρ^f is the fluid density, and \mathbf{u}^f represents the fluid velocity. Navier-Stokes equation is expressed as:

$$\frac{\partial \alpha^f \rho^f u_i^f}{\partial t} + \frac{\partial}{\partial x_j} (\alpha^f \rho^f u_i^f u_j^f) = -\alpha^f \frac{\partial p^f}{\partial x_i} + \frac{\partial}{\partial x_j} \alpha^f \tau_{ij}^f + S_i^f u_i^f + Q_i^f + \Pi_i \quad (1.33)$$

where $\boldsymbol{\tau}^f$ represents the stress tensor of the fluid, p^f represents the fluid pressure, S^f is the source term linear with the velocity field, \mathbf{Q}^f represents the other source terms, and the last term $\mathbf{\Pi}$ represents the inter-phase momentum transfer from the dispersed particles to the fluid flow. The stress tensor is given by:

$$\tau_{ij}^f = \mu^f \left(\frac{\partial u_i^f}{\partial x_j} + \frac{\partial u_j^f}{\partial x_i} \right) + \delta_{ij} \left(\lambda^f - \frac{2}{3} \mu^f \right) \left(\frac{\partial u_k^f}{\partial x_k} \right) \quad (1.34)$$

where λ^f is the second viscosity relating to the volumetric deformation, μ^f represents the dynamic viscosity of the fluid, and δ_{ij} is the Kronecker delta, given as.

$$\delta_{ij} = \begin{cases} 0, & \text{if } i \neq j \\ 1, & \text{if } i = j \end{cases} \quad (1.35)$$

1.5.3. Particle phase modelling

In this study, dispersed solid particles are individually tracked by solving Newton's second law in Lagrangian frameworks. This approach is well-known as discrete element method (DEM) proposed by Cundall [24]. The external forces acting on a dispersed particle are generated by fluid effects on the particle, inter-particle and particle-wall collisions.

1.5.3.1. Hydrodynamic forces on solid particles in a fluid flow

Solid particles moving in a fluid flow encounter several hydrodynamic forces. These forces have been widely studied and formulated as the Basset-Boussinesq-Oseen (BBO) equation [23, 72], given as:

$$F_i = F_{i,Drag} + F_{i,Press} + F_{i,Add} + F_{i,History} + F_{i,Buoyancy} + F_{i,Faxen} \quad (1.36)$$

where $F_{i,Drag}$ is the hydrodynamic drag force, $F_{i,Press}$ is the pressure and shear stress forces, $F_{i,Add}$ represents the virtual or added mass force, $F_{i,History}$ is the history or Basset force, $F_{i,Buoyancy}$ is the buoyancy force, and the last term $F_{i,Faxen}$ represents the Faxen correction force.

On the right hand side of Equation 1.36, the drag force $F_{i,Drag}$ is determined by the projected area and the slip velocity between the particle and fluid phases, and $F_{i,Press}$ is the fluid pressure acting on the particle. Due to the acceleration or deceleration of the fluid surrounding a particle, the added mass force, $F_{i,Add}$, works like a rise in the mass of the particle. $F_{i,History}$ arises from the time required to develop the boundary layer around an accelerated particle. The density difference between the particle and fluid flow is the cause of the buoyancy force, $F_{i,Buoyancy}$. The last term, Faxen correction force, $F_{i,Faxen}$, is corresponding to all other forces in BBO equation 1.36.

In the BBO equation 1.36, several forces, such as added mass, history and Faxen forces, are proportional to the density ratio, $\frac{\rho^f}{\rho^p}$. If the particle density, ρ^p , is sufficiently larger than the fluid density ρ^f , these three forces can be neglected.

The hydrodynamic forces on the particles also reversely work on the fluid flow. In equation 1.33, the last term on the right hand side Π_i represents the hydrodynamic effect on the fluid. More details about the relation between Π_i and hydrodynamic force, F_i , is described in Sec. 3.3.2.

1.5.3.2. Particle-particle and particle-wall collisions

When the particle volume fraction rises to a high level ($\alpha^p > 0.1\%$) in a dispersed multiphase flow, the frequency of particle collisions is considerably high and the effects of the collisions become important. The dynamics of the particles can be considerably influenced by the particle collisions.

In general, the particle contact collision can be ignored (particles do not “see” each other) or modelled using a stochastic method or a deterministic method. In “MultiFlow”, two deterministic methods are provided for accurately resolving particle collisions: the hard-sphere and soft-sphere collision models. The hard-sphere model estimates contact forces using the conservation of momentum (impulse) and kinetic energy. The collisions are considered as instantaneous, binary and no deformation of the particles takes place. On the other hand, the soft-sphere method approximates the local deformation resulting from the particle contact interaction, and the collision forces arising from the deformation are determined by the strain-stress relation. These two models treat the solid contact collision in different way. In a dilute particle-laden flow, the results of the two models are almost the same, but the hard sphere model is not applicable in dense flows. In addition, the particle kinetic energy loss are taken account in both of the models. Mallouppas *et. al.* [67] gives more detail about these two collision models.

1.5.4. Coupling between discrete particles and the fluid phase

In multiphase flows, couplings occur through interactions between phases and can be divided into three categories: the mass coupling, the momentum coupling and the energy coupling. This study only focuses on modelling the dynamics of the gas-solid channel flows. Therefore, the heat transfer between the two phases is assumed to be negligible, and there is also no mass exchange between solid particles and fluid flows. Only the momentum coupling is considered in the current work, including fluid effects on dispersed particles, particle effects on the continuous fluid flow, particle-particle and particle-wall collisions. Table 1.2 lists three momentum coupling methods: one-way, two-way and four-way couplings.

The choice of the coupling methods in Table 1.2 strongly depends on the flow conditions. In very dilute flows with extremely low Stokes numbers ($St < 1$), the particle effects on both fluid phase and particles can be safely ignored. The one-way coupling is suitable for modelling such flows, only estimating the effects of the fluid flow on the particles. If the dispersed multiphase flow is sufficiently dilute with large Stokes number ($St \gg 1$), the particle effect on the fluid flow turbulence may be of importance. Due to the fact that the average distance between particles are significantly large in the dilute flow, the particles can be treated as isolated elements, ignoring their possible collisions. Therefore, the two-way coupling should be applied for such cases. For modelling particle-laden flows with a large particle volume fraction, larger than 0.1%, the four-way coupling method must be employed to fully resolve both fluid-particle and particle-particle interactions.

Momentum coupling methods	Definition
One-way coupling	One-way coupling only resolves the continuous fluid effects on dispersed particles, neglecting other interactions between the two phases.
Two-way coupling	Two-way coupling employs both particle and fluid effects working on each other in the simulation.
Four-way coupling	Four-way coupling fully consists of fluid effects on particles, particle effects on the fluid flow, particle-particle and particle-wall collisions.

Table 1.2.: The phase couplings

1.6. Non-spherical particles

In the literature, most research papers explore gas-solid multiphase flows, just using or modelling spheres as solid particles. However, the shape of solid particles can be arbitrary in realistic applications. For describing a non-spherical particle with a random shape, a mathematical description of the particle surface should be applied. Using a finite element method, the surface can be described by meshes, or a non-spherical particle is constructed by a large number of small, fictitious spheres. The surface of all spheres in the particle provides an accurate representation of the particle surface, *e.g.* [63, 103]. “MultiFlow” uses the latter method to represent non-spherical particles. The more spheres used in a non-spherical particle, the more precisely the surface is represented. As illustrated in Fig. 1.2, an ellipsoid is built by 11 different diameter spheres. Solid particles built in the

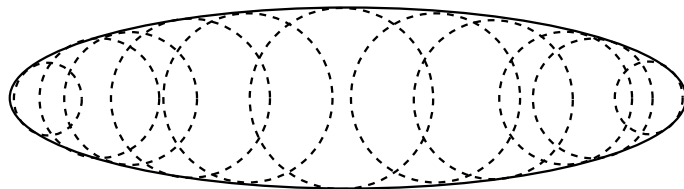


Figure 1.2.: The construction of an ellipsoidal particle by spheres

simulations of this study are assumed to be rigid and homogeneous. This indicates that there is no plastic deformation on particles after collisions, and particle density, ρ^p , is constant. The particle mass, m^p , can be determined by:

$$m^p = \rho^p V^p \quad (1.37)$$

where V^p is the particle volume.

Comparing with spherical particles, the mass and mass center of non-spherical particles are more difficult to determine. To achieve this, the particle volume is first computed as follows. An imaginary box enclosing an non-spherical particle is generated, and a large number of fictitious points are generated to span the volume of the box. When the number

of points becomes infinite, the ratio between the points inside the particle, N^p , and the total points in the box, N , equals the ratio of the particle volume to the box volume, expressed as:

$$\lim_{N \rightarrow \infty} \frac{N^p}{N} = \frac{V^p}{V_{box}} \quad (1.38)$$

The particle volume can be properly approximated by this equation when the total number of the points becomes sufficiently large. The mass center of the particle, \mathbf{x}^p , can be determined by summing the positions of all points in the particle, \mathbf{r}^p :

$$\mathbf{x}^p = \lim_{N^p \rightarrow \infty} \frac{1}{N^p} \sum_{n=1}^{N^p} \mathbf{r}^{np} \quad (1.39)$$

A similar method is also used for determining another important particle parameter, the inertia tensor \mathbf{I}^p . The diagonal terms in \mathbf{I}^p are determined by:

$$I_{ii} = \lim_{N^p \rightarrow \infty} \frac{1}{N^p} \frac{m^p}{N^p} \sum_{n=1}^{N^p} ((\mathbf{r}_j^{np} - x_j^p)^2 + (\mathbf{r}_k^{np} - x_k^p)^2) \quad (1.40)$$

and the off-diagonal terms are expressed as:

$$I_{ij} = \lim_{N^p \rightarrow \infty} \frac{1}{N^p} \frac{m^p}{N^p} \sum_{n=1}^{N^p} (\mathbf{r}_i^{np} - x_i^p)(\mathbf{r}_j^{np} - x_j^p) \quad (i \neq j) \quad (1.41)$$

In “MultiFlow”, the moment of inertia of a non-spherical particle is determined in particle body-framework, on which the particle is fixed, and \mathbf{I}^p of the particle is then constant in time.

2. Modelling the rotational motion of Non-spherical particles: a novel Quaternion method

This chapter is based on the published paper:

F. Zhao and B. G. M. van Wachem, “A novel Quaternion integration approach for describing the behaviour of non-spherical particles”, Acta Mech 224(12), 3091-3109 (2013).

Abstract

The purpose of this chapter is to derive a new Quaternion integration method for accurately representing the rotation of non-spherical particles. In the literature, there are three main frameworks to describe the orientation and rotation of non-spherical particles: Euler angles, rotation matrices and unit Quaternions. Of these operators, the latter seems the most attractive for describing the behaviour of non-spherical particles. However, there are several limitations when using unit Quaternions: the necessity of applying rotation matrices in conjunction to facilitate the transformation from body-space to world-space, and the algorithm integrating unit Quaternions cannot inherently conserve the length of the Quaternion, requiring a normalisation procedure. Both of the drawbacks are addressed in this chapter. The present chapter derives a new framework to transform vectors and tensors by unit Quaternions, and thus the requirement of explicitly using rotation matrices is avoided. This means that the algorithm derived here can describe the rotation of a non-spherical particle with four parameters (a unit Quaternion) only. Furthermore, this chapter develops a novel corrector-predictor method to integrate unit Quaternions, which can inherently conserves the length of the Quaternion.

The novel framework and integration method are compared to a number of other methods put forward in the literature. All the integration methods are discussed, scrutinized, and compared to each other by comparing the results of four test-cases, involving a single falling particle, nine falling and interacting particles, a 2-D prescribed torque on a sphere and a 3-D prescribed torque on a non-spherical particle. Moreover, a convergence study is presented, comparing the rate of convergence of the various methods. All the test-cases show a significant improvement of the new framework put forward in this chapter over existing algorithms. Moreover, the new method requires less computational memory and fewer operations, due to the complete omission of the rotation matrix in the algorithm.

2.1. Introduction

Understanding the behaviour of rigid particles is important for many industrial processes and phenomena occurring in nature, as well as in gas-solid multiphase flows modelled in this thesis. It is estimated that over 70% of chemical processes involve small particles at some point. Moreover, particles play an important role in natural phenomena, such as avalanches, sediment transport, and erosion, to name just a few. Because of this importance, the field of modelling the behaviour of large number particles is well established. In 1979, Cundall *et al* [24] proposed the distinct element method (DEM), which models the behaviour of individual particles by solving the Newton's second law in a Lagrangian framework. This method has proved to be highly useful, and has been applied in hundreds of research papers as well as in this work. Moreover, numerical simulations of multi-body dynamics, especially those involving free-body rotations, require accurate integration of the rigid-body orientation equations.

In the literature, most of the simulations with DEM consider purely spherical particles. Although this may be an acceptable approximation for a number of applications, sometimes this is not the case. As described in Section 1.6, modelling the behaviour of non-spherical particles can be done by: using a mathematical description of the surface (*e.g.* [26]), a finite element approach, describing a mesh of the surface (*e.g.* [64]), or by building a non-spherical particle from spheres (*e.g.* [63, 103]). In these methods, the dynamic equations of the particles, and the subsequent integration of these equations are significantly more complex than for spherical particles. The present chapter focuses on developing a novel fast, efficient and accurate method to formulate and integrate the equations of rotation for non-spherical particles.

The translational and rotational motion of a solid particle can be determined in two Cartesian co-ordinate frameworks: body space and world space. In body space, the origin of the Cartesian co-ordinates are fixed on the particle mass centre and the axis of the co-ordinates rotate along with the particle. This is often referred to as the Lagrangian framework. In world-space, the co-ordinates are fixed in the origin of the initial Cartesian reference framework. This is often referred to as the Eulerian framework. These frameworks with a non-spherical particle are depicted in Fig. 2.1. Although the translational motion of the particle can be easily converted between the two types of spaces, the rotational motion needs to be determined by a more complex rotational operator. There are various ways to formulate this operator. Among the numerous methods describing the rotation operator, the most commonly used frameworks are: Euler angles, rotation matrices and unit Quaternions. All of these methods have some kind of limitation, which will be discussed in this chapter.

In the literature, there are a number of research studies describing the rotation of a rigid body in the framework of Hamilton dynamic systems (*e.g.* [18, 19, 46, 58, 73]). Kosenko [58] reported a complex algorithm to represent the rotation of a free rigid body in the framework of Quaternions. Moreover, the Euler dynamic governing equations are also determined by Quaternion groups in the Hamiltonian framework. However, this algorithm is limited to the Euler case (*i.e.* free body dynamics), referring to a framework without the

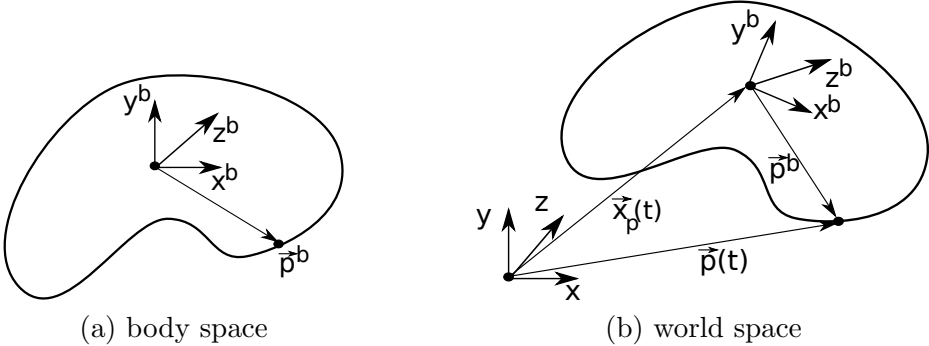


Figure 2.1.: The relation between body space (a) and world space (b). The fixed axes of body space, x^b , y^b and z^b are indicated in both figures. The position of a fixed point in body space, p^b is transformed to world space, $p(t)$.

application of an external torque. For modelling free body dynamics in Hamiltonian systems, the discrete Moser-Veselov (DMV) algorithm [78] is an accurate numerical integrator to update the rotation matrix, \mathbf{R} , exactly conserving the kinetic energy and angular momentum. After that, Hairer and Vilmart [46] and MacLaurgh and Zanna [73] have further improved the DMV algorithm by modifying the momentum of inertia at each integration and time transformation, respectively. Both of these improved DMV methods can avoid singularity problems and increase the accuracy of the algorithms, guaranteeing to be suitable for long time modelling. Moreover, Hairer and Vilmart [46] used unit Quaternions to represent the rotation matrix, and transform the DMV method into the framework of Quaternions to simplify the implementation. However, these improved DMV algorithms are limited to free body dynamics. To modelling the full dynamic rigid body problem (including the application of a torque working on the body), Celledoni *et al.* [18] proposed a Stormer/Verlet splitting method to divide the rotation motion into two parts: the free rigid body kinetic part and the torque part, both of them in the Hamilton system. The free rigid body problem consists of Euler dynamic equations and a differential equation for updating the rotation matrix. The Euler equations can be determined by an exact method using the Jacobi elliptic function, and the approximate update of the rotation matrix or corresponding unit Quaternion is described for free body dynamics in [19]. The torque part can be determined by a differential function involving the rotation matrix. This method is very expensive, and thus it is not feasible for modelling a dynamic system with a large number of rigid particles.

Due to the limitation and extremely high computational cost, the above algorithms are not suitable for modelling the rotational motion of particles in a fully dynamic system with a large number of rigid particles. On the other hand, other lower order algorithms fast integrating the rotation matrix are inaccurate, always leading to inevitable singularity problems for long time simulations. Moreover, Euler angles suffer from the “Gimbal-lock” problem when representing 3D rotation (e.g. [34]). To avoid these numerical difficulties, the unit Quaternion is more and more popular used to describe, at least part of, the rotation of particles. Unit Quaternions, sometimes referred to as Euler parameters, are well known to represent rotation without singularity problems in molecular dynamics modelling

and rigid particle modelling (*e.g.* [1, 34, 53, 103]). The singular problem of the rotation matrix occurs during the time integration of the rotation matrix. To prevent this, at least the time integration of the rotation operator is done by the unit Quaternion. After the time integration, most approaches found in the literature convert the Quaternion to the corresponding rotation matrix (*e.g.* [1, 13, 53, 76]). This rotation matrix is then used to transform the vector and tensor variables between different frameworks, such as the vector $\mathbf{p}(t)$ in Fig. 2.1.

In the current work, unit Quaternions are not only applied to represent the time integration of the rotation operator, but also to replace rotation matrices completely and transform vector and tensor variables between different co-ordinate systems directly. Hence, there is no requirement for a rotation matrix in this new method. This saves both computational memory and effort. This chapter derives a novel equation to describe the transformation of the second order tensors between frameworks based solely on Quaternions.

The outline of the chapter is as follows: section two briefly reviews rotation operators in general, properties of Quaternions, and a novel model is then derived to transform tensors between different co-ordinate frameworks. In addition, the equations relating the rotation matrix to the unit Quaternion are introduced. In section three, several algorithms which have been put forward in the literature to integrate unit Quaternions are scrutinized and discussed and a novel integration method is put forward. In section four, the algorithms are compared to each other by applying them to four different test-cases, and the outcomes of this are discussed. Conclusions are drawn in the final section.

2.2. Rotation and Quaternions

2.2.1. Rotation dynamic equations

The equations of motion describing non-spherical rigid particles consist of translational and rotational components. The position of a particle can be represented equally simple in world space and in body space, but for the orientation of a particle the rotational equations are significantly more complex in world space than body space. Therefore, the most common and convenient way is to compute rotational properties of particles in body space and, if required, transform them into world space. The governing equations of rotational motion are angular momentum equations and the differential equation of rotation operators. Firstly, the angular momentum \mathbf{L}^b is defined by:

$$\mathbf{L}^b = \mathbf{I}^b \boldsymbol{\omega}^b \quad (2.1)$$

where the second order tensor \mathbf{I}^b is the constant moment of inertia in body space, and the $\boldsymbol{\omega}^b$ represents the angular velocity of a particle. The superscript b means the variables are in the body space framework. For a particle undergoing the effect of an external torque, the torque, \mathbf{T}^b , is determined by:

$$\dot{\mathbf{T}}^b = \dot{\mathbf{L}}^b + \boldsymbol{\omega}^b \times \mathbf{L}^b \quad (2.2)$$

where the time derivative of angular momentum is given as

$$\dot{\mathbf{L}}^b = \dot{\mathbf{I}}^b \boldsymbol{\omega}^b + \mathbf{I}^b \dot{\boldsymbol{\omega}}^b \quad (2.3)$$

Due to the fact that the moment of inertia tensor \mathbf{I}^b does not change in body space for a rigid particle, the first term on the right hand side of the above equation is equal to zero. The angular acceleration can then be expressed as:

$$\dot{\boldsymbol{\omega}}^b = \mathbf{I}^{b^{-1}} (\mathbf{T}^b - \boldsymbol{\omega}^b \times \mathbf{I}^b \boldsymbol{\omega}^b) \quad (2.4)$$

On the other hand, the differential equation of a rotation operator Q can be simply expressed as:

$$\dot{Q} = f(Q)Q \quad (2.5)$$

where $f(Q)$ is a function involving the operator Q .

2.2.2. Rotation operators

In the literature, there are three commonly used operators to describe rotation: Euler angles, rotation matrices and unit Quaternions. All of them have advantages and drawbacks, (*e.g.* [31, 44]). In addition, they can be translated from one form to another. The details about the performance and issues of these rotation frameworks are reported and discussed in [28, 31].

2.2.2.1. Euler angles

With the orientation of a solid particle fixed in body space, Euler angles (ϕ, θ, ψ) represent three composed axis-rotations mapping the particle in body space to the world space. These three angles involve in a sequence combination of sine and cosine functions, which are non-linear. According to different combination sequences, there are total twelve ways to represent three Euler angles [28]. Although only three independent quantities denote this operator, there are several drawbacks of Euler angles, such as the **Gimbal lock problem, which gives rise to the loss of one degree of freedom, when two of three axes are rotating into parallel configuration.** This operator can only work well in applications involving one or two dimensional rotation only. **For a general 3D rotation framework the Gimbal lock problem will occur and the method is mostly not suitable.**

2.2.2.2. Rotation matrix

In dynamics, the rotation matrix may be the most widely used rotation operator, and it is a 3×3 orthogonal matrix performing a rotational motion in three dimensions with determinant of 1. A vector \mathbf{v} transforms from one co-ordinate system to another by

application of the rotation matrix \mathbf{R} as:

$$\mathbf{v}' = \mathbf{R}\mathbf{v} \quad (2.6)$$

where the vector \mathbf{v}' represents the rotated counterpart of vector \mathbf{v} . A second order tensor \mathbf{M} is transformed by the rotation matrix as

$$\mathbf{M}' = \mathbf{R} \mathbf{M} \mathbf{R}^T \quad (2.7)$$

A rotation matrix is by definition an orthogonal matrix, the columns of which are of unit length. During the integration or differentiation of the rotation matrix, six constraints are required, as the three degrees of freedom associated with the rotation are described by nine components. Three constraints require a rotation matrix maintains the unit length of each rotation matrix column and the other three enable the columns to keep orthogonal to each other. When these six constraints are not met implicitly by the numerical integration or differentiation, singularity problems may arise, making the required inversion difficult or impossible. In order to avoid these problems, unit Quaternions can be applied instead.

2.2.2.3. Unit Quaternions

Due to the absence of singularity and Gimbal lock problems, unit Quaternions are increasingly applied to represent rotational motion of particles. Unlike 6 limitations of the rotation matrix, the unit Quaternion only have one constraint: the length of Quaternions must be always and exactly unity. Otherwise, the rotated variables by a general Quaternion may be scaled. Rotation without scaling is performed by unit Quaternions, see e.g. [30, 49].

2.2.3. Quaternion and Quaternion operators

Quaternions were first introduced in Hamilton [45, 47] in the nineteenth century and have been widely used to represent rotation for modelling dynamic systems in the past decades. They are expressed in a complex number system, consisting of a scalar part and a vector part. Hence, there are a total of 4 unknowns. A Quaternion is defined by:

$$q = q_0 + q_1\mathbf{i} + q_2\mathbf{j} + q_3\mathbf{k} \quad (2.8)$$

where q_0, q_1, q_2 and q_3 are real numbers, and \mathbf{i}, \mathbf{j} and \mathbf{k} are unit vectors directed to x, y and z axis, respectively. Quaternions can also be written as a real number and a vector:

$$q = [q_0, \mathbf{q}] \quad (2.9)$$

Three useful operations of a Quaternion itself can be defined: conjugate, norm and inverse. The conjugate of a Quaternion is defined as,

$$q^* = q_0 - q_1 \mathbf{i} - q_2 \mathbf{j} - q_3 \mathbf{k} \quad (2.10)$$

the norm of a Quaternion is determined by,

$$|q| = \sqrt{|q|^2} = \sqrt{qq^*} = \sqrt{q_0^2 + q_1^2 + q_2^2 + q_3^2} \quad (2.11)$$

and the inverse of a Quaternion is given as

$$q^{-1} = \frac{q^*}{|q|} \quad (2.12)$$

A unit Quaternion is a Quaternion of norm 1, then the inverse Quaternion is equal to the conjugate Quaternion:

$$|q| = \sqrt{|q|^2} = 1 \rightarrow q^* = q^{-1} \quad (2.13)$$

2.2.3.1. Multiplication of Quaternions

The multiplication between two Quaternions represents the subsequent application of each Quaternion. This product is often referred to as the Grassman product [6, 53]. In vector representation, the product of Quaternions p and q is given as Quaternion t :

$$t = pq = [p_0 q_0 - \mathbf{p}\mathbf{q}, p_0 \mathbf{q} + q_0 \mathbf{p} + \mathbf{p} \times \mathbf{q}] \quad (2.14)$$

The equation consists of vector dot and cross products. Due to anti-commutative property of the cross product, the multiplication of Quaternions is not commutative. Quaternion multiplication can also be represented by matrices multiplication:

$$t = \mathbf{Q}(p)q = \begin{pmatrix} p_0 & -p_1 & -p_2 & -p_3 \\ p_1 & p_0 & p_3 & -p_2 \\ p_2 & -p_3 & p_0 & p_1 \\ p_3 & p_2 & -p_1 & p_0 \end{pmatrix} \begin{pmatrix} q_0 \\ q_1 \\ q_2 \\ q_3 \end{pmatrix} \quad (2.15)$$

More detail about Quaternion algebra is introduced in [2, 51, 59].

In dynamics, the physical meaning of a Quaternion over a vector is to scale the vector and change its orientation [51]. This means that Quaternions, in general, do not only represent the orientation of a vector, but also alter the vector length, *see* Fig. 2.2. Therefore, the rotation cannot be simply represented by Quaternion multiplication. The following section describes the detail about rotation by unit Quaternions.

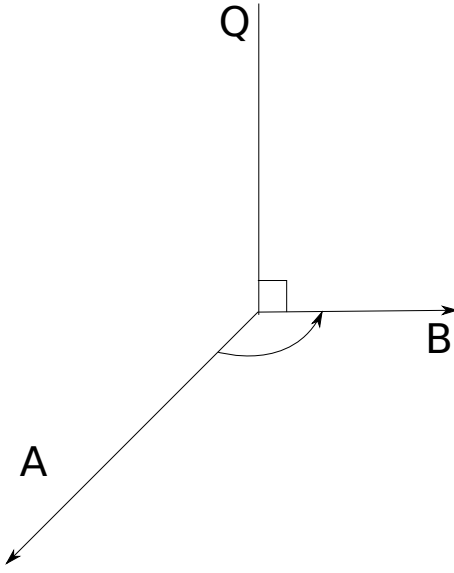


Figure 2.2.: A quaternion Q Changes the orientation and length of vector A to vector B , and this quaternion is vertical to the vector A and B

2.2.4. Rotation by unit Quaternion

A vector s rotated without scaling its length is determined by multiplying a pair of unit Quaternions, given as:

$$s' = qsq^{-1} \quad (2.16)$$

where q is a unit Quaternion, q^{-1} represents the conjugate of q , and the vector s is interpreted as a Quaternion, $s = [0, s]$, of which the scalar part is equal to zero. The unit Quaternion q can be directly expressed in a form containing the vector around which the rotation takes place and the angle of the rotation [12, 53]:

$$q = \cos \frac{\alpha}{2} + \sin \frac{\alpha}{2} \hat{q} \quad (2.17)$$

where \hat{q} is the normalised vector around which the rotation takes place and the angle α indicates the rotational angle. In the unit Quaternion q , the coefficients q_0, q_1, q_2 and q_3 are sometimes referred to as Euler parameters (e.g. [12]), which are not independent of each other, and they must always satisfy

$$|q| = \sqrt{q_0^2 + q_1^2 + q_2^2 + q_3^2} = 1 \quad (2.18)$$

Many integration algorithms do not inherently respect this constraint and explicitly renormalise the Quaternion after the algorithms are applied, by defining the corrected Quaternion as

$$\hat{q} = \frac{q}{\sqrt{q_0^2 + q_1^2 + q_2^2 + q_3^2}} \quad (2.19)$$

This is, however, not the same as inherently embedding the unit length of the Quaternion, as expressed by equation 2.18, into the algorithm itself. Applying equation 2.19 modifies

the relation between the four parameters of the Quaternion, thus modifying the rotation it represents.

In most research papers dealing with the rotational motion of solid particles, the numerical time integration of the rotation operator is addressed by employing unit Quaternions. After the time-integration itself, the corresponding rotation matrices are obtained from the updated Quaternions, and are applied to determine the orientation of the particles and transform vector and tensor properties between body space and world space by equations 2.6 and 2.7. This requires an inverse relationship between rotation matrices and unit Quaternions. The rotation matrix corresponding to the unit Quaternion is given by the Quaternion components as:

$$\mathbf{R} = \begin{pmatrix} 1 - 2(q_2^2 + q_3^2) & 2q_1q_2 - 2q_0q_3 & 2q_0q_2 + 2q_1q_3 \\ 2q_1q_2 + 2q_0q_3 & 1 - 2(q_1^2 + q_3^2) & 2q_2q_3 - 2q_0q_1 \\ 2q_1q_3 - 2q_0q_2 & 2q_0q_1 + 2q_2q_3 & 1 - 2(q_1^2 + q_2^2) \end{pmatrix} \quad (2.20)$$

The additional conversion procedure using equation 2.20 takes extra computation and memory, and also easily gives rise to numerical errors. To avoid these drawbacks, this study derive a new framework to represent rotation solely by unit Quaternions.

Equation 2.6, expressing the transformation of a vector by a rotation matrix, is equivalent to equation 2.16,

$$\mathbf{v}' = q\mathbf{v}q^{-1} = \mathbf{R}\mathbf{v} \quad (2.21)$$

Some second order tensor variables are also required to transform between the two different co-ordinates systems, such as inertia tensor and resistance tensors [76]. These tensors can be transformed by applying equation 2.7. However, there seems to be no equivalent equation using unit Quaternions to perform the same transformation in the literature. All methods presented so-far determine the rotation matrix from the Quaternion and apply the rotation matrix subsequently, as expressed in equation 2.7 to compute the tensors in the rotated framework.

In this chapter, a novel equation is derived for determining a tensor in the rotated framework directly by unit Quaternions without the necessity of determining the corresponding rotation matrix, as follows. Firstly, equation 2.7 applying rotation matrix determines a second order tensor in a rotated framework, given as:

$$\mathbf{M}' = \mathbf{R} \mathbf{M} \mathbf{R}^T$$

where the tensors \mathbf{M}' and \mathbf{M} can be considered as three sequential column vectors \mathbf{M}_1 , \mathbf{M}_2 and \mathbf{M}_3 as:

$$\mathbf{M} = \begin{pmatrix} \begin{pmatrix} M_{11} \\ M_{21} \\ M_{31} \end{pmatrix} & \begin{pmatrix} M_{12} \\ M_{22} \\ M_{32} \end{pmatrix} & \begin{pmatrix} M_{13} \\ M_{23} \\ M_{33} \end{pmatrix} \end{pmatrix} = (\mathbf{M}_1 \quad \mathbf{M}_2 \quad \mathbf{M}_3)$$

A temporary tensor \mathbf{M}'' can be expressed as:

$$\mathbf{M}'' = \mathbf{R} \mathbf{M} \quad (2.22)$$

where \mathbf{M}'' can be considered as transforming the three sequential column vectors ($\mathbf{M}_1 \mathbf{M}_2 \mathbf{M}_3$) by the rotation matrix \mathbf{R} , thus a corresponding unit Quaternion can replace the rotation matrix, given as:

$$\begin{aligned}\mathbf{M}_1'' &= q\mathbf{M}_1q^{-1} \\ \mathbf{M}_2'' &= q\mathbf{M}_2q^{-1} \\ \mathbf{M}_3'' &= q\mathbf{M}_3q^{-1}\end{aligned}\quad (2.23)$$

A new expression combining the above three equations is defined as:

$$\mathbf{M}'' = q\mathbf{M}q^{-1} \quad (2.24)$$

which is equivalent to equation 2.22. Equation 2.7 can be represented by the tensor \mathbf{M}'' , given as:

$$\mathbf{M}' = \mathbf{R} \mathbf{M} \mathbf{R}^T = \mathbf{M}'' \mathbf{R}^T \quad (2.25)$$

The transpose of the tensor \mathbf{M}' is determined by

$$\mathbf{M}'^T = \mathbf{R} \mathbf{M}''^T \quad (2.26)$$

in which a unit Quaternion q can replace the rotation matrix by applying equation 2.24,

$$\mathbf{M}'^T = q\mathbf{M}''^T q^{-1} \quad (2.27)$$

where $\mathbf{M}''^T = (q\mathbf{M}q^{-1})^T$, given,

$$\mathbf{M}'^T = q(q\mathbf{M}q^{-1})^T q^{-1} \quad (2.28)$$

Finally, the transformation of second order tensors by unit Quaternions is expressed as

$$\mathbf{M}' = (q(q\mathbf{M}q^{-1})^T q^{-1})^T \quad (2.29)$$

Following the above analysis, unit Quaternions can be adopted to directly transform both vector and tensor properties during rotation. Accordingly, corresponding rotation matrices can be completely replaced by unit Quaternions, and are no longer required in this research work. This will save a significant amount of computer memory (4 instead of 9 floating point numbers per particle), and increase the accuracy introduced by round-off errors, as fewer operations are required.

2.3. Numerical integration of unit Quaternions

In the literature, several algorithms have been put forward to integrate unit Quaternions for modelling rotational motion. Most of algorithms are based on Taylor expansion of the unit Quaternion (*e.g.* [1, 34]). In these algorithms, addition and subtraction operators are required to add or subtract the derivatives of the Quaternion. The time derivative of a unit Quaternion q has a very simple form, determined by the angular velocity vector ω and the Quaternion itself, see for instance [9, 20, 87]:

$$\dot{q} = \frac{1}{2}\omega q = \begin{pmatrix} 0 & -\frac{\omega_x}{2} & -\frac{\omega_y}{2} & -\frac{\omega_z}{2} \\ \frac{\omega_x}{2} & 0 & \frac{\omega_z}{2} & -\frac{\omega_y}{2} \\ \frac{\omega_y}{2} & -\frac{\omega_z}{2} & 0 & \frac{\omega_x}{2} \\ \frac{\omega_z}{2} & \frac{\omega_y}{2} & -\frac{\omega_x}{2} & 0 \end{pmatrix} \begin{pmatrix} q_0 \\ q_1 \\ q_2 \\ q_3 \end{pmatrix} \quad (2.30)$$

where the angular velocity ω is considered as a Quaternion, $[0, \omega]$. However, if the sum of additions and subtractions is not exactly of zero length, an increase in the length of the integrated Quaternion is obtained. To preserve the constraint of a unit Quaternion when applying such a method, the updated Quaternion needs to be re-normalised back to a unit Quaternion after each integration time-step. However, this re-normalisation procedure does not only enforce the constraint concerning unit length, but it also affects the relationship between the four Euler parameters, resulting in numerical errors. In order to integrate a unit Quaternion without the application of addition or subtraction operators between Quaternion derivatives, a patent was filed by [104], and similar methods are also derived by *e.g.* [12, 53, 87].

2.3.1. Previously proposed methods based on Taylor polynomial expansion

In many other research papers, such as [1, 9, 34, 56, 71, 76, 85, 103], the integration of unit Quaternions is solved based on Taylor series expansion, and equation 2.30, or an equivalent form, is employed. All algorithms require Quaternions are re-normalised after each integration, leading to inevitable numerical errors. Although higher order methods may be more accurate than lower order algorithms, the re-normalisation could cause even larger numerical errors. Therefore, the high order algorithms cannot ensure precise Quaternion integration. Three Quaternion integration methods are put forward and discussed below.

2.3.1.1. Euler method

The first order Euler method is the most simple method for integrating unit Quaternions. The unit Quaternion at the new time-step, q_{n+1} , is approximated by:

$$q_{n+1} = q_n + \frac{1}{2}\omega_n q_n \delta t + O(\delta t^2) \quad (2.31)$$

where q_{n+1} is determined by a first order Taylor expansion. Due to the small increment $\frac{1}{2}\omega_n q_n \delta t$ added to the unit Quaternion q_n , the length of q_{n+1} are clearly different from unity. In order to preserve the unity constraint, the Quaternion q_{n+1} requires re-normalisation at each time step:

$$\hat{q}_{n+1} = \frac{q_{n+1}}{|q_{n+1}|} \quad (2.32)$$

However, the re-normalisation procedure gives rise to numerical errors, adding to the relatively large truncation errors of the first order Euler method. To decrease the truncation errors in the Euler method, several higher order algorithms, which are also based on Taylor series expansion, are applied in the literature, such as the leap frog method [1, 103], the second order Taylor series expansion, the second-order Adams-Bashforth method [76], the Runge-Kutta method [84] and the scalar factor method introduced in [56].

2.3.1.2. Leap frog method

The leap frog, or mid-point, method for the time integration of unit Quaternions is derived by Walton and Braun [103], whereas unit Quaternions and angular velocities at the mid-point between two adjacent time steps are evaluated in this algorithm. It is expressed as

$$q_{n+1} = q_n + \frac{1}{2}\omega_{n+\frac{1}{2}} q_{n+\frac{1}{2}} \delta t \quad (2.33)$$

where the angular velocity ω , expressed above as Quaternion ω , at time-level $n + \frac{1}{2}$ is explicitly determined by leap frog method. On the other hand, $q_{n+\frac{1}{2}}$ is simply determined by:

$$q_{n+\frac{1}{2}} = \frac{q_n + q_{n+1}}{2} \quad (2.34)$$

Due to q_{n+1} appearance on both side in equation 2.33, this leap-frog algorithm is significantly more complex and requires more variables and operations than the Euler method. However, because the application of Quaternion addition operators, the algorithm still causes the length of the integrated Quaternion, q_{n+1} , to exceed unity. Therefore, the Quaternions need to be re-normalised at each time step.

In this study, this algorithm for Quaternion integration is reformulated and written in terms of Quaternion multiplication only. This novel formulation prevents the application of addition or subtraction to the Quaternion. To illustrate the algorithm, two new Quaternions (β and \tilde{q}) are defined as

$$\tilde{q} = f\beta\beta \quad \beta = [1, \beta_x, \beta_y, \beta_z] \quad (2.35)$$

where the components of β are given as

$$\begin{aligned}\beta_x &= \frac{\delta t}{4} \omega_x^{n+\frac{1}{2}} \\ \beta_y &= \frac{\delta t}{4} \omega_y^{n+\frac{1}{2}} \\ \beta_z &= \frac{\delta t}{4} \omega_z^{n+\frac{1}{2}}\end{aligned}\quad (2.36)$$

The scale factor f is defined as

$$f = \frac{|\beta|^2}{A} \quad (2.37)$$

where A is determined by the components of β ,

$$A = 1 + 2\beta_x^2 + 2\beta_y^2 + 2\beta_z^2 \quad (2.38)$$

The unit Quaternion at next time-level is determined by

$$q_{n+1} = \tilde{q}q_n \quad (2.39)$$

The unit q_{n+1} at new time level also requires re-normalisation at each time step. The above algorithm is the Quaternion counterpart of equation 2.33 and the results are essentially identical. Furthermore, the relation between the unit Quaternions q_n and q_{n+1} is not linear. Therefore, equation 2.34, approximating $q_{n+\frac{1}{2}}$ in a linear fashion, is not appropriate and inaccurate. Some higher order methods based on the same idea are proposed by other researchers, where multiple evaluations of the Quaternion between time-levels n and $n+1$ are required, such as Runge-Kutta or Adams-Basforth methods [76]. However, there is in principle no direct physical meaning for the addition or subtraction of Quaternions. Moreover, the higher order methods based on this principle cannot prevent the length of the Quaternion deviating from unity, the more addition or subtraction operators in higher order methods can even influence the relationship between q_n and q_{n+1} . Hence, all these algorithms require re-normalisation at each time step, giving rise to numerical errors.

2.3.1.3. Scalar factor method

Kleppmann [56] concludes that the Euler method and other higher order methods as outlined above do not properly integrate unit Quaternions and that the required re-normalisation procedure introduces significant errors. In [56], a scalar factor is introduced in the derivative equation directly:

$$\dot{q}_n = f\omega_n q_n \quad (2.40)$$

where f is defined as

$$f(\delta t, |\omega|) = \frac{1}{|\omega|\delta t} \tan\left(\frac{|\omega|\delta t}{2}\right) \quad (2.41)$$

The unit Quaternion q_{n+1} at next time step is then determined by the Euler method as

$$q_{n+1} = q_n + \dot{q}_n \delta t \quad (2.42)$$

where δt represents the size of the time step. Writing out $\dot{q}_n \delta t$ in the above equation gives

$$\dot{q}_n \delta t = f\omega q \delta t = \tan(|\delta q|) \frac{\delta q}{|\delta q|} \quad (2.43)$$

where δq is

$$\delta q = \frac{\delta t}{2} \omega q \quad (2.44)$$

Finally, after the re-normalisation procedure, q_{n+1} is expressed as

$$q_{n+1} = \left[q_n + \tan(|\delta q|) \frac{\delta q}{|\delta q|} \right] \cos(|\delta q|) \quad (2.45)$$

As illustrated in Fig. 2.3, the magnitude of the quaternion must be always on the unit sphere surface, and this algorithm is strikingly more accurate than the Eulerian method. It should be also noted that there is a possibility that numerical instabilities occur when $|\delta q|$ is equal to $\frac{\pi}{2}$ during a single time step, due to the discontinuities in the tan function.

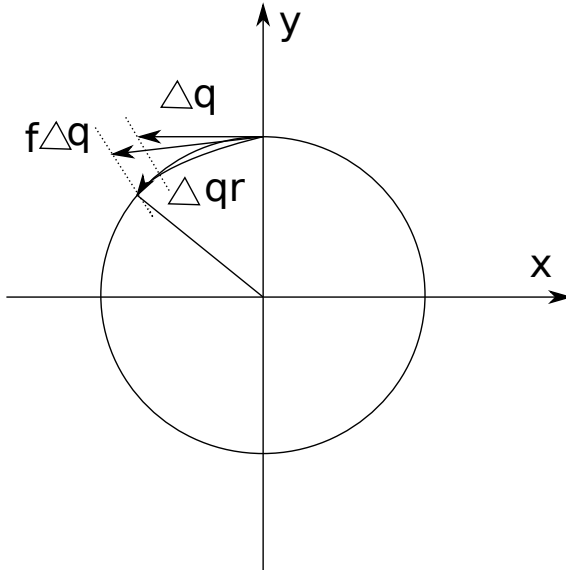


Figure 2.3.: The scalar method: Δq represent Quaternion increment in other algorithm, $f\Delta q$ represent the increment in the scalar method, and Δqr represents the real increment.

2.3.2. Direct multiplication method

In order to derive a better integration method of unit Quaternions for representing rotation, a patent was developed by Whitemore [104], and an analogous derivation is also reported in [12, 53, 87]. In these papers, the Quaternion multiplication replaces the addition operator in the integral equation altogether. The derivative of unit Quaternion q

evaluated by equation 2.30 is replaced by an exponential map, which is given by:

$$T(\omega, \delta t) = \exp(\Omega \delta t) \quad (2.46)$$

where:

$$\Omega = \begin{pmatrix} 0 & -\frac{\omega_x}{2} & -\frac{\omega_y}{2} & -\frac{\omega_z}{2} \\ \frac{\omega_x}{2} & 0 & \frac{\omega_z}{2} & -\frac{\omega_y}{2} \\ \frac{\omega_y}{2} & -\frac{\omega_z}{2} & 0 & \frac{\omega_x}{2} \\ \frac{\omega_z}{2} & \frac{\omega_y}{2} & -\frac{\omega_x}{2} & 0 \end{pmatrix}$$

The Quaternion at next time level, q_{n+1} , is determined by:

$$q_{n+1} = T(\Omega, \delta t) q_n \quad (2.47)$$

The exponential term in the above equation is expanded in Maclaurin series and a simplified form is obtained,

$$T(\omega, \delta t) = (\cos \frac{|\omega|}{2} \mathbf{I} + \frac{2}{|\omega|} \sin \frac{|\omega|}{2} \Omega) \delta t \quad (2.48)$$

where \mathbf{I} is the fourth order identity matrix and the vector ω is the angular velocity. The matrix T in the above equation can be also represented as a unit Quaternion,

$$\tilde{q} = \left[\cos \frac{|\omega| \delta t}{2}, \sin \frac{|\omega| \delta t}{2} \frac{\omega}{|\omega|} \right] \quad (2.49)$$

Finally, the unit Quaternion at time level $n + 1$ is expressed as

$$q_{n+1} = \tilde{q}_n q_n \quad (2.50)$$

In this method, there is no necessity for an addition or subtraction operator. An exponential map is employed to approximate the increment of a unit Quaternion. Theoretically, the multiplication between unit Quaternions can preserve the result with unit length. A similar method as outlined above can also be put forward, by starting from the sequential rotation as given by equation 2.16,

$$\begin{aligned} s_1 &= \tilde{q}_0 s_0 \tilde{q}_0^{-1} \\ s_2 &= \tilde{q}_1 s_1 \tilde{q}_1^{-1} \\ s_3 &= \tilde{q}_2 s_2 \tilde{q}_2^{-1} \\ &\dots \\ s_{n+1} &= \tilde{q}_n s_n \tilde{q}_n^{-1} \end{aligned}$$

where the unit Quaternion \tilde{q}_i ($i = 1, 2, 3\dots n$) represents rotation within a time step and is defined analogously to equation 2.49,

$$\tilde{q}_n = \left[\cos \frac{|\omega_n| \delta t}{2}, \sin \frac{|\omega_n| \delta t}{2} \frac{\omega_n}{|\omega_n|} \right]$$

where the rotation angle α in a time step is determined by the length of angular velocity at that time step and the time step as $|\boldsymbol{\omega}_n|\delta t$, and the direction of rotation is the same as the direction of the angular velocity $\boldsymbol{\omega}_n$. The unit Quaternion q_n , which represents a vector rotated from original position at $t = 0$ to time level n , is defined by:

$$q_n = \prod_{i=1}^n \tilde{q}_{n-i} \quad (2.51)$$

Finally, the unit Quaternion for the next time level q_{n+1} is described by

$$q_{n+1} = \tilde{q}_n q_n \quad (2.52)$$

which is same as defined in equation 2.50.

2.3.3. Newly proposed predictor-corrector direct multiplication method

The novel method put forward in this thesis approximates the angular velocity with a basic Lie-Euler method, or predictor-corrector method, which is described in Allen and Tildesley [1]. However, the Quaternion integration method in [1] is directly based on Taylor series, so that

$$q_{n+\frac{1}{2}} = q_n + \frac{1}{2}\dot{q}_n\delta t \quad (2.53)$$

$$q_{n+1} = q_n + \dot{q}_{n+\frac{1}{2}}\delta t \quad (2.54)$$

As mentioned early in this section, the addition and subtraction operators appear in Quaternion integration equations is physically meaningless and can give rise to numerical errors. This chapter proposes a new algorithm, **predictor-corrector direct multiplication (PCDM) method**, which is not based on Taylor series, but applies the direct multiplication algorithm. Firstly, the variables describing the rational motion of a particle are transformed into body space from world space at current time level n :

$$\boldsymbol{\omega}^b_n = q_n^{-1} \boldsymbol{\omega}_n q_n \quad (2.55)$$

$$\boldsymbol{\tau}^b_n = q_n^{-1} \boldsymbol{\tau}_n q_n \quad (2.56)$$

The angular velocity expressed in body space at the mid-point of the next time level, $\boldsymbol{\omega}^b_{n+\frac{1}{2}}$, and at a quarter of next time level, $\boldsymbol{\omega}^b_{n+\frac{1}{4}}$, are determined by

$$\begin{aligned} \boldsymbol{\omega}^b_{n+\frac{1}{2}} &= \boldsymbol{\omega}^b_n + \frac{1}{2}\dot{\boldsymbol{\omega}}^b_n\delta t \\ \boldsymbol{\omega}^b_{n+\frac{1}{4}} &= \boldsymbol{\omega}^b_n + \frac{1}{4}\dot{\boldsymbol{\omega}}^b_n\delta t \end{aligned} \quad (2.57)$$

where the angular acceleration $\dot{\boldsymbol{\omega}}^b_n$ is determined by equation 2.4. In equation 2.49, the application of $\boldsymbol{\omega}$ represents the spatial angular velocity of a particle within a time step in world space. In most algorithms, the angular velocity is defined at the mid-point in

world-space, $\omega_{n+\frac{1}{2}}$, which is transformed to world space by application of the unit Quaternion q_n , as the value of $q_{n+\frac{1}{2}}$ is unknown at that time level. Hence, the time-level of the Quaternion is not respected in these algorithms. To decrease the error caused by the mixing of time-levels, the predictor-corrector method is applied to approximate the angular velocity at the mid-point. Firstly, the predicted angular velocity at a quarter at next time level in world space, $\omega_{n+\frac{1}{4}}$, is approximated based on the unit Quaternion q_n :

$$\omega_{n+\frac{1}{4}} = q_n \omega^b_{n+\frac{1}{4}} q_n^{-1} \quad (2.58)$$

Then, a prediction of the unit Quaternion at the half time interval, $q'_{n+\frac{1}{2}}$, is determined by the velocity $\omega_{n+\frac{1}{4}}$. The prime on the variable emphasises that it concerns an initial prediction of the variable, not its final value.

$$q'_{n+\frac{1}{2}} = \left[\cos \frac{|\omega_{n+\frac{1}{4}}| \delta t}{4}, \sin \frac{|\omega_{n+\frac{1}{4}}| \delta t}{4} \frac{\omega_{n+\frac{1}{4}}}{|\omega_{n+\frac{1}{4}}|} \right] q_n \quad (2.59)$$

Using this predicted unit Quaternion $q'_{n+\frac{1}{2}}$, the angular acceleration $\dot{\omega}_{n+\frac{1}{2}}$ is determined by application of equation 2.4, and the angular velocity $\omega_{n+\frac{1}{2}}$ at mid-point of next time level in world space is determined by:

$$\omega_{n+\frac{1}{2}} = q'_{n+\frac{1}{2}} \omega^b_{n+\frac{1}{2}} q'^{-1}_{n+\frac{1}{2}} \quad (2.60)$$

and the corrected unit Quaternion q_{n+1} at the new time level is then expressed as:

$$q_{n+1} = \left[\cos \frac{|\omega_{n+\frac{1}{2}}| \delta t}{2}, \sin \frac{|\omega_{n+\frac{1}{2}}| \delta t}{2} \frac{\omega_{n+\frac{1}{2}}}{|\omega_{n+\frac{1}{2}}|} \right] q_n \quad (2.61)$$

Finally, the angular velocity in body space at the new time level can be determined and transformed to the angular velocity in world space,

$$\omega^b_{n+1} = \omega^b_n + \dot{\omega}_{n+\frac{1}{2}} \delta t \quad (2.62)$$

$$\omega_{n+1} = q_{n+1} \omega^b_{n+1} q_{n+1}^{-1} \quad (2.63)$$

As described above, this predictor-corrector direct multiplication (PCDM) method can consistently and accurately update the unit Quaternion to represent the orientation of a non-spherical particle and its angular velocity. Moreover, this method does not use a rotation matrix and does not mix time-levels inconsistently in its final correction. In the next section, the different methods as discussed and derived above will be compared to each other in a number of realistic conditions.

2.4. Comparison of methods and discussion

The various methods which have been discussed in this chapter in Section 2.3.1 are compared with the novel PCDM method as outlined in Section 2.3.3, equations 2.55 to 2.62.

The comparison is done considering two criteria: energy conservation and the rate of convergence. Each of these criteria is used to analyze four different test-cases, each representing a realistic problem involving the behaviour of non-spherical particles.

In the modelling of non-spherical particles, both translation and rotation need to be considered. The translation of the particles is determined by a velocity Verlet scheme [1] for all methods and test-cases.

2.4.1. Energy conservation

For solving the equations governing the behaviour of particles, one of the most important features of a particle dynamic system is that the system conserves its total energy. If the behaviour of non-spherical particles is determined in a gravity field without any source of dissipation, the total mechanical energy (E_{tot}) of the particles in this framework is represented by:

$$E_{tot} = \sum_{i=1}^N (m_i g \delta h_i + \frac{1}{2} m_i \mathbf{v}_i^2 + \frac{1}{2} \boldsymbol{\omega} \cdot \mathbf{I}_i \boldsymbol{\omega}_i) = \text{Constant} \quad (2.64)$$

where N is the total number of particles, δh_i represents the height of the mass centre of the i^{th} particle.

All particle-particle and particle-boundary collisions are determined by the soft-sphere collision model. To ensure no kinetic energy loss due to all collisions, the friction and restitution coefficient of both particles and boundary walls are set to zero and 1 for all cases. The error in energy conservation can then be expressed as:

$$E_{\text{error}} = \left| \frac{E_{tot}^n - E_{tot}^0}{E_{tot}^0} \right| \times 100\% \quad (2.65)$$

where E_{tot}^n represents the total energy of the particles after the n^{th} integration time step. E_{tot}^0 represents the initial total energy of the particles.

2.4.2. Comparison with three test-cases: energy conservation

The first two test-cases used to compare the integration methods consider a cylindrical fibre with an aspect ratio, given as $r = \frac{b}{D}$, of 3, and a density and a volume of $1.1 \times 10^3 \text{ kg/m}^3$ and $1.961 \times 10^{-6} \text{ m}^3$, respectively. The simulations of the first two test-cases are carried out in a computational domain of a unit cube ($1 \times 1 \times 1$). The boundaries of this box are considered as frictionless, rigid walls. The properties of the fibre and the computational domain are presented in Table 2.1.

In the domain, forces and torques acting on each particle are caused by gravity (body force) and by collisions between particles themselves or by the particle and boundary walls. As described earlier, there is no energy loss due to particle collisions.

	Dimension [m]	E [Pa]	ν [-]	μ [-]	e [-]
Fibre	$0.01 \times 0.01 \times 0.05$	5.0×10^7	0.35	0.0	1.0
Walls	$1 \times 1 \times 1$	5.0×10^7	0.23	0.0	1.0

Table 2.1.: The properties of cylindrical fibres and the boundary wall of the box. The diameter (D), Youngs' modulus (E), Poisson's ratio (ν), coefficient of friction, (μ), and coefficient of restitution (e).

2.4.2.1. First test-case: single falling fibre

In the first test a single elongated fibre, initially placed exactly in the middle of the box with a 30 degree angle between the principle axis of the fibre and the plane of the bottom wall, falls down under the effect of gravity. Due to its initial angle, a torque acts on the particle during the first collision with the bottom wall and the particle starts to rotate. The results of the simulations, with four different numerical methods as previously discussed, are compared to each other in Fig. 2.4, showing the total energy error as a function of time for the various integration methods. These methods are: the Euler method, the leap-frog method, the scalar factor method, and the newly proposed PCDM method.

In Fig. 2.4, the errors of the different methods are shown for this test-case over two seconds of simulation with a fixed time step of $\Delta t = 1.0^{-7}s$. The Euler method predicts

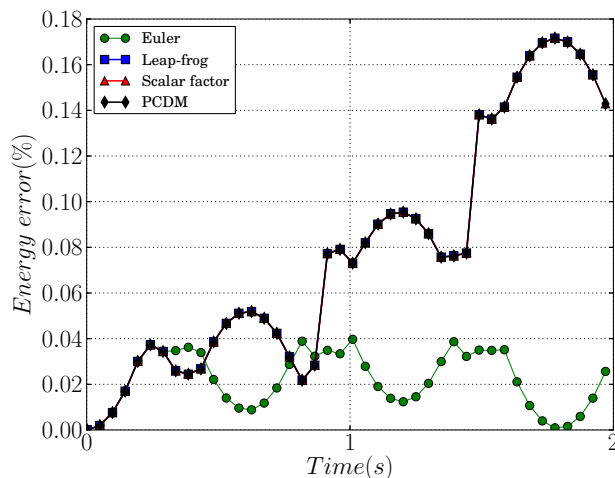


Figure 2.4.: The error in energy resulting from the four different rotational integration algorithms for test-case 1: a single falling fibre.

the minimum error in kinetic energy, very close to zero and non-increasing, whereas the errors in energy produced by all the other integration algorithms are small, typically less than 0.2%, but are larger and increasing. Also, the error produced by the other 3 integration algorithms almost overlap each other. Although the errors from other algorithms are somewhat bigger than that from Euler method, all the algorithms can be considered acceptable for this case.

2.4.2.2. Second test-case: nine falling fibres

A second test-case comprises of 9 fibres in the same box, falling under gravity. In order to increase the number of collisions within the total period of two seconds, all the nine particles are given an initial velocity of $(1.0, -1.0, 0.0)$. Their initial positions are distributed evenly on a vertical plane halfway through the box. The angle between the principle axis of the fibre and the plane of the bottom wall is 75 degrees. Compared to the previous test-case, which only involves particle-wall collisions, also numerous particle-particle collisions occur.

Fig. 2.5 shows the errors of energy conservation for this case, comparing the four integration algorithms as outlined previously. The errors for only the scalar factor method and the newly proposed PCDM method are shown in Fig. 2.6. For this second test-case, the

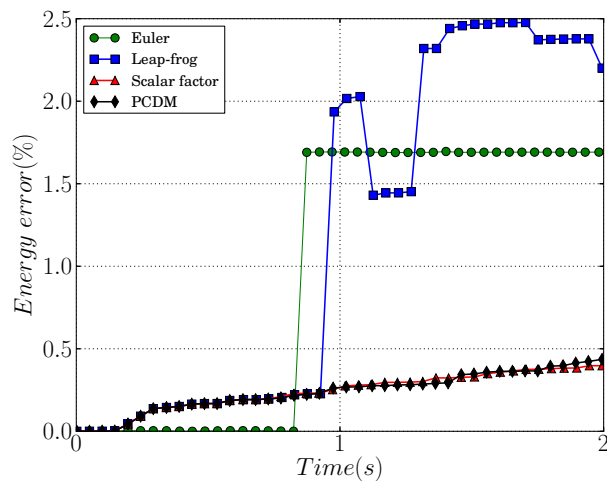


Figure 2.5.: The error in total energy resulting from the four different rotational integration algorithms in the case of 9 falling fibres.

Euler and leap-frog methods become unstable and the absolute errors rapidly exceed 1.5% and 2%, respectively. On the other hand, the errors produced by the scalar factor algorithm and novel PCDM method are steady and very close to each other. The difference in the plot between the two algorithms indicates that the particles have different trajectories and orientations. Fig. 2.7 shows the snapshot of one particle trajectory and the locations of the fibres for: (a) the novel PCDM method, and (b) the scalar factor method. This figure shows the trajectories predicted by both methods as well as the dynamics of the trajectories are significantly different. As very small errors produced in each time-step will dramatically change the trajectory and orientation of each particle, so different algorithms cannot produce exactly the same trajectories over time. This phenomenon is referred to as the Lyapunov instability [50]. From this second test case, it is not possible to distinguish between the scalar factor method and the PCDM method. Although the trajectories and final positions differ significantly, the energy conservation error is comparable for both methods, and the case is too complex to compare with an analytical solution.

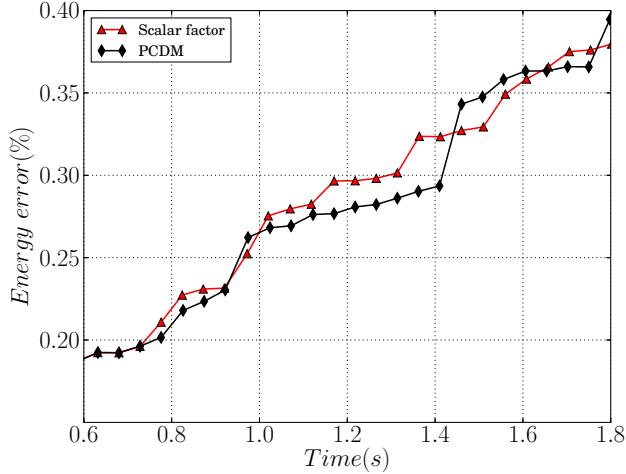


Figure 2.6.: The error in total energy resulting from the scalar factor method and the novel PCDM method in the case of 9 falling fibres.

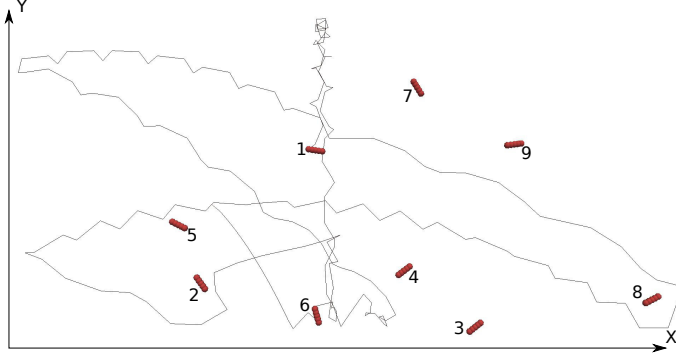
2.4.2.3. Third test-case: prescribed one-dimensional torque on a particle

The third test case considers the rotation of a particle by prescribing its torque. The particle considered is a sphere with a diameter and density of $2m$ and 1100 kg/m^3 respectively. To precisely follow the rotation of this particle, a unit vector, initially $x = (1.0, 0.0, 0.0)$, is projected onto the sphere. The function prescribing the torque is given by $\tau = (0.0, A \exp(Ct), 0.0)$, in which A and C are 1×10^5 and 1, respectively, and t represents time. This test-case has only been performed with the scalar factor method and the PCDM method, as all other methods do not achieve convergence. This test-case can be evaluated analytically, by integrating the torque function with respect to time. A direct comparison between the different algorithms can thus be made. The results of these two methods are presented in Table 2.2, which shows the orientation of the unit vector after one second of physical time with a constant time step $\Delta t = 1 \times 10^{-4}\text{s}$, whereas the error in angle with time is shown in Fig. 2.8. The results from the newly proposed PCDM

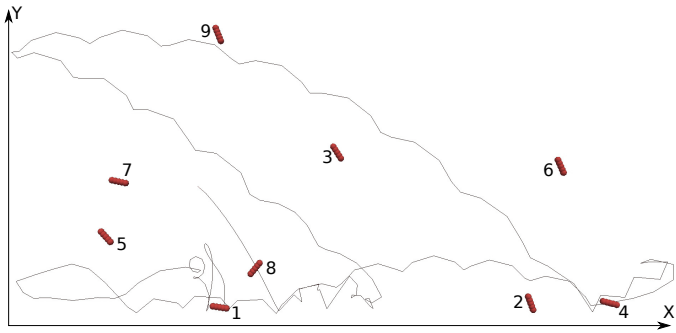
	position at time $t = 1.0$	Position error
Theoretical result	$(2.934253 \times 10^{-1}, 0.0, -9.55982 \times 10^{-1})$	0.0
Scalar factor method	$(2.871152 \times 10^{-1}, 0.0, -9.578961 \times 10^{-1})$	2.15%
PCDM method	$(2.915775 \times 10^{-1}, 0.0, -9.565472 \times 10^{-1})$	0.63%

Table 2.2.: The orientation of a unit vector $x = (1.0, 0.0, 0.0)$ after a second simulation with a non-linear torque by Scalar factor method and the novel PCDM method

method are significantly closer to the analytical result than the results obtained from the scalar factor method. Fig. 2.8 shows the error in the angle of the unit vector as a function



(a) one particle trajectory and nine particle positions at the end of 2 second simulation by the novel PCDM method.



(b) one particle trajectory and nine particle positions at the end of 2 second simulation by scalar factor method.

Figure 2.7.: Different particle trajectories as predicted by: (a) the novel PCDM method, and (b) the scalar factor method for the case of 9 falling fibres.

of time, comparing the analytical result with the PCDM method and the scalar factor method. This figure clearly shows the effect of the re-normalisation which is required by the scalar factor method; when re-normalisation is applied the error in angle increases rapidly.

2.4.3. Rate of convergence

A very important aspect of a numerical integration method is the rate of convergence. For many types of engineering problems, millions of particles will be studied and a favourable integration algorithm should quickly converge as the time-step decreases. In this section, the rate of convergence of the most common methods is analyzed.

A numerical integration algorithm for unit Quaternions will never diverge, as unit Quaternions are by definition of unit length. In other words, the error of the rotational angles cannot diverge, and the range of angle errors is from 0 to π rad. Hence, this makes the analysis somewhat more complicated.

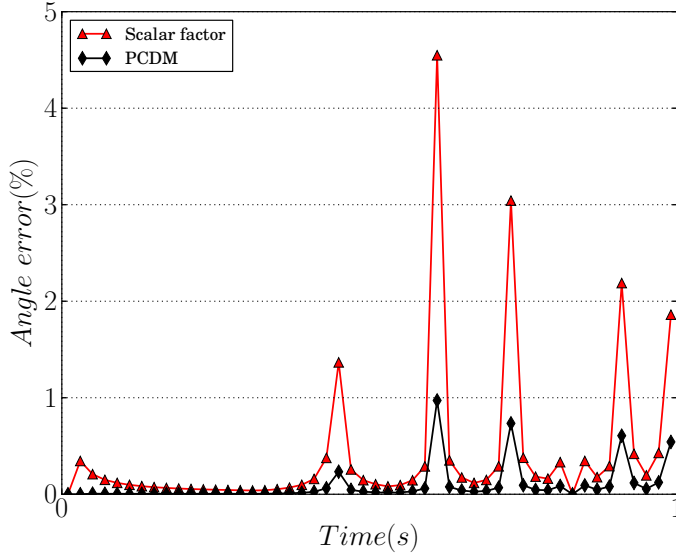


Figure 2.8.: The error in the prediction of the unit vector as a function of time for the scalar factor method and the PCDM method.

2.4.3.1. Fourth test-case: prescribed three-dimensional torque on a fibre

To compare the rate of convergence, the test case of a fibre, with an initial orientation of $\mathbf{B} = (1.0, 0.0, 0.0)$, is placed in a torque field. A small non-linear torque, $\boldsymbol{\tau} = (A \sin(200\pi t), C \exp(3.0 + 24t), C 5^{52t})$, in which A and C are 5.0×10^{-4} and 1.0×10^{-5} respectively, is applied on the fibre to force it to rotate.

The various Quaternion integration methods are used to evaluate the evolution of the rotation of the fibre around its axis up to $T = 0.1\text{ s}$. The error of the orientation at time-step n of the fibre is determined by evaluating:

$$\alpha_n^{error} = \| \arccos(\mathbf{b}_n \cdot \mathbf{B}) - \arccos(\mathbf{B}_n \cdot \mathbf{B}) \| \quad (2.66)$$

where \mathbf{b}_n in world space is the unit vector projection of \mathbf{B}_n as determined by the numerical methods described in Section 3, and \mathbf{B}_n considered as the analytical result of the unit vector in world space at time step n . The total rotational angle error is then summed as

$$\alpha = \frac{\Delta t}{T} \sum_{n=1}^{n_{final}} \alpha_n^{error} \quad (2.67)$$

where n_{final} represents the total number of time-steps required to achieve time T . The time step, Δt , is varied between 1.0×10^{-5} to 1.0×10^{-7} , as the Euler method does not converge for a larger time-step. The effect of the time-step on the total error is shown on a log-log scale in Fig. 2.9. In this figure, also the slopes of first and second order of convergence are indicated. The error in the prediction of the orientation of the PCDM

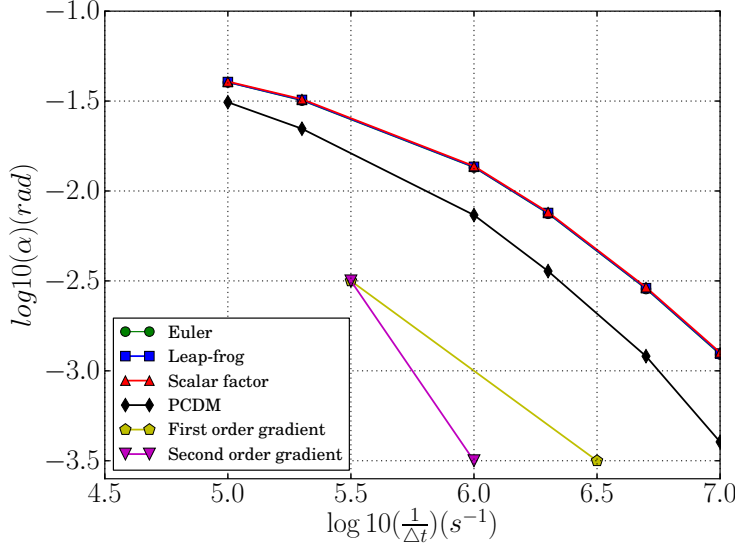


Figure 2.9.: The angle error of the unit vector as a function of the inverse of time step $\frac{1}{\Delta t}$ (log-log plot)

method is always significantly less compared to the other methods. Because the Euler, leap-frog and scalar function methods are derived from the Taylor expansion, they have a very similar rates of convergence, which is first order for small time-steps. This is because they all inhibit the error of the renormalisation of the Quaternion, irrespective of the order of the Taylor series considered. With a time-step larger than $\Delta t = 1.0 \times 10^{-6}$, the rate of convergence is less than 1.

The rate of convergence of the PCDM method is significantly larger than of the other methods, even for large time-steps and approaching second order rate of convergence as the time-step decreases.

2.4.4. Discussion

For the simplest test-case considered, a single falling fibre, all four methods show acceptable results in terms of energy conservation and convergence rate. For all other test-cases, the Euler method and leap frog method show a rapid increase in energy conservation error in time. Although the scalar factor method always shows a stable solution, the error in prediction for the two test-cases involving a prescribed torque on a particle are larger than with the newly proposed predictor-corrector method. Moreover, the study of the rate of convergence in the fourth test-case shows that the scalar factor method shows a significantly slower rate of convergence than the predictor-corrector method. Moreover, there are no significant differences in computational cost for these methods. The novel PCDM method is more accurate and stable than the other methods for any time-step considered in the four test-cases.

2.5. Conclusion

The modelling of the dynamics of non-spherical particles is significantly more complex than the modelling of spherical particles. The difference arises from the requirement of determining the orientation and rotation of non-spherical particles. For spherical particles, this is done by the application of a vector only. For non-spherical particles, several frameworks are available to describe the orientation: Euler angles, rotation matrices and unit Quaternions. The application of Euler angles and rotation matrices both suffer from serious drawbacks, concerning lack of stability and uniqueness and the occurrence of singularities. Therefore, unit Quaternions seem as the most attractive framework and are used widely within the modelling of the dynamics of non-spherical particles.

However, there are a number of potential drawbacks when using unit Quaternions to represent the orientation and rotation of non-spherical particles. The first drawback is that almost all research papers so-far employ both unit Quaternions as well as rotation matrices to determine the rotational behaviour of a non-spherical particle. This results in an increased requirement of computer memory and possible inaccuracies which are introduced by the frequent conversion from the unit Quaternion to rotation matrix and back.

The second drawback concerns the conservation of length of a unit Quaternion. As a Quaternion describes both orientation and scaling, a unit Quaternion describing solely rotation must remain of constant, unit, length throughout all of the operations. Most methods put forward in the literature are based on a Taylor series expansion of the unit Quaternion and require addition, subtraction or scaling. This inherently leads to a change of length of the Quaternion during integration and, consequently, re-normalisation is required. Although the re-normalisation restores the correct length of the Quaternion, it changes the relationship between the four parameters of which the Quaternion exists, thereby introducing a significant error. Applying higher order methods, such as based on Runge-Kutta, do not prevent these errors from arising, and worsen rather than improve the overall accuracy of the method.

Both of the drawbacks are addressed in this chapter. The present chapter derives a new framework to transform vectors and tensors by unit Quaternions directly and the necessity of rotation matrices is removed altogether. This means that the algorithm derived in this chapter can describe the rotation of non-spherical particles using four parameters only, making it favourable for large-scale computations involving many particles.

To address the second drawback, a novel framework to integrate unit Quaternions is put forward in Section 2.3.3, the predictor-corrector direct multiplication (PCDM) method. This novel algorithm avoids the use of subtraction or addition of Quaternions and uses multiplication of Quaternions only, so that re-normalisation is not required. The algorithm is based on a predictor-corrector method, so that the various time-levels are not mixed.

In this chapter, various numerical integration methods for Quaternions put forward in the literature are scrutinized and compared by applying each of them to four test cases: a single falling fibre, nine falling fibres, the 2-D rotation of a vector projected on a sphere with a prescribed torque function and a 3-D prescribed torque on a non-spherical fibre. In the first two test-cases, the error in total energy is compared between the different

methods and in the third test-case the predicted orientation of the vector as a function of time is compared to the analytical solution. The last test case, in which the rate of convergence is studied, it is shown that the novel predictor-corrector direct multiplication method has a higher order rate of convergence than other methods from the literature. The other methods never exceed a rate of convergence of 1, caused by the addition or subtraction of Quaternions and the subsequent necessity of renormalisation. The novel predictor-corrector direct multiplication method put forward in this chapter approaches a rate of convergence of 2. All the test-cases presented in this chapter show a significant improvement in accuracy of the algorithm put forward in this study compared to other algorithms found in the literature.

3. Methodology: four-way coupling gas-solid multiphase channel flow simulations

This chapter is based on the published paper:

F. Zhao, W. K. George and B. G. M. van Wachem, “Four-way coupled simulations of small particles in turbulent channel flows: the effects of particle shape and Stokes number”, submitted to Physics of Fluids (2014).

Abstract

This research thesis numerically studies gas-solid turbulent channel flows. The computation employs a unique DNS four-way coupling with the Lagrangian point-particle approach. The aim of this chapter is to introduce the governing equations and numerical settings of both particle and fluid phases and interpret the applied four-way couplings. The Eulerian fluid phase is modelled by direct numerical simulation (DNS), while dispersed particles are tracked individually. The linear motion of discrete particles is affected by the hydrodynamic drag forces and collision forces, and the rotation of the particles is influenced by the hydrodynamic torques and torques due to the collision. The drag models for ellipsoidal particles depend on the particle orientation and are much more complex than those for spheres. The effects of discrete particles on the fluid flow are modelled as an source term added into the Navier-Stokes (momentum) equation, applying the cubic spline interpolation scheme. Based on this particle source term, an additional term, *i.e.* a dissipation rate caused by the coupling force of the particles, is added in the TKE equation. To precisely represent the dynamics of particles after particle collisions, all potential inter-particle and particle-wall collisions are detected and approximated by the deterministic soft-sphere collision model. In addition, the limited computation capacity confines the fluid channel flow at a low Reynolds number, $Re_\tau = 150$, with a limited number of particles. The comparisons of fluid velocity statistics show a reasonably good agreement between the single phase flow simulation and the fluid data from the UUD research group in Marchioli *et. al.* [70]. This indicates that the numerical setting of the fluid flow and the applied flow assumptions in this work are well accepted.

3.1. Introduction

Small solid particles suspended in a turbulent channel flow are commonly found in a number of industrial and environmental applications. Although this classic problem has been widely numerically studied, *e.g.* [29, 33, 70, 83, 90, 97, 108], some elements of the interactions between the fluid and particle phases are still not well-understood, leaving many unsolved questions, especially for flows with non-spherical particles. The gas-solid flows are influenced by some flow parameters such as the particle volume fraction, the mass loading, the Reynolds number, the wall roughness, the particle size, the particle shape and the Stokes number. Even in very dilute flows (extremely low particle volume fractions), dispersed solid particles may still somewhat influence the fluid flow turbulence. Thus the way of describing those key parameters and fluid-particle interactions in simulations is extremely important for accurately and efficiently modelling dispersed multiphase flows. Recently, Balachandar and Eaton [8] review basic numerical approaches and their applications in the literature for modelling dispersed multiphase flows. These methods include the dusty gas approach, the equilibrium Eulerian approach, the Eulerian-Eulerian approach, the Lagrangian point-particle approach and the fully resolved approach. The above sequence is according to the accuracy from least to most accurate method, and more accurate approaches, of course, need more computational resources and time. As introduced in Section 1.5, the flow solver “MultiFlow” provides the Eulerian-Eulerian, Lagrangian point-particle and immersed boundary (fully resolved) approaches. It is believed that extremely small and heavy particles, *i.e.* smaller than Kolmogorov scale, may extract the momentum from the fluid flow, thus leading to a turbulence reduction. By contrast, large particles (much larger than Kolomogrov scale) can strengthen the flow turbulence intensity. This is mainly because the fluid flow can form a wake area after a large particle due to the particle boundary effect, and this wake area is a significant source of turbulence. For large particles, the fully resolved approach should be applied to completely resolve the whole flow field, *e.g.* [79]. However, this method is only feasible for simulations with a few particles, up to thousands, due to the extremely high computational cost. Therefore, it is not suitable for this study, which models a great number of small solid particles. The Eulerian-Eulerian approach treats both fluid and particle phases as continuous fluid media, *e.g.* [10, 33, 75, 98]. Although this two-fluid method can be used to efficiently describe gas-solid flows with a large number of small particles, modelling discrete particles as a continuous phase is incapable of accurately describing the particle orientation and particle effects on the fluid flow. Due to the limitations and drawbacks of the full resolved and Eulerian-Eulerian approaches, this study applies the Lagrangian point-particle approach to properly model the gas-solid channel flow with a great number of particles and a wide range of Stokes number.

The Lagrangian point-particle approach developed by Crowe *et. al.* [22] has been extensively adopted for modelling dispersed multiphase flows, *e.g.* [29, 70, 83, 93, 99]. With this approach, solid particles are tracked individually, and their properties such as position, mass, momentum and energy of individual particle, are determined by Newton’s second law. The particle size has to be smaller than Kolmogorov length scale for the point-source

approximation to be valid. To incorporate particle effects on the fluid, two-way or four-way couplings should be applied, and the effects can be summed and added into the fluid momentum equation as a source term.

Most papers, *e.g.* [29, 70, 93, 111], model gas-solid multiphase flows, just using spheres as solid particles. However, particles in realistic applications can be any arbitrary shape. In recent decades, fibre-like ellipsoids suspended in a turbulent channel flow have been numerically studied, *see* [3, 35, 65, 71, 76, 77, 101, 108]. Ellipsoidal particles in these papers is referred to as spheroids with two equal minor axes, and this type of ellipsoid is also used in the present work. Zhang *et. al.* [108] is the first to apply Direct Numerical Simulation (DNS) to solve fluid channel flows with ellipsoids. After that, Mortensen *et. al.* [76, 77] and Marchioli *et. al.* [71] focus on statistical results of ellipsoids with different aspect ratio and different inertia. Similar to spherical particles, elongated ellipsoids also tend to accumulate in the near wall region and preferentially concentrate in the regions of low-speed and high strain.

Most of these previous papers only applied one-way coupling to model the gas-solid channel flow, and the effects of discrete particles on the fluid flow, particle-particle and particle-wall collisions were ignored. Thus only particle statistics were discussed in their works. However, these fluid-particle and particle-particle interactions may play an important role in gas-solid channel flows with non-spherical particles, even in dilute flows. To perform more realistic simulations of gas-solid channel flows, this study employs the four-way coupling to fully resolve particle-fluid and particle-particle interactions. This means that the effects of particles on the fluid flow and inter-particle and particle-wall collisions are all resolved in the simulations of this study. Therefore, more accurate statistics of both fluid and particle phases can be obtained.

The effect of the fluid flow on discrete particles is described in the BBO equation 1.36. This work only employs hydrodynamic drags acting on particles, neglecting the other forces in the BBO equation. The drag force on a particle depends on the particle shape and Reynolds number. For spherical particles, the drag coefficient derived by Schiller and Naumann [88] is applied in the simulations with spheres. For non-spherical ellipsoids in a viscous fluid flow, the drag interactions are derived by Jeffery [52] and Brenner [14–16], which approximates drag forces and torques under the creeping flow condition. Further theoretical work of drag forces on ellipsoidal particles was reported in Gallily *et. al.* [37]. Drag models based on these studies provide good approximations for the hydrodynamic force and torque on ellipsoids in a turbulence flow with very small particle Reynolds number, and they have been applied in many numerical studies *e.g.* [3, 71, 76, 108, 110], as well as the current work. These effects also reversely influence the fluid flow. Andersson and Zhao *et. al.* [3, 111] propose an torque-coupling method to describe the torque effect on the fluid flow in their simulations. As the particle size is extremely small in the simulations of this study, the particle torque effect on the flow is ignored. The drag force is only taken into account. Through applying the cubic spline interpolation scheme, the effects of particles on the fluid flow is added into the governing Naiver-Stokes equation as a source term.

In the literature, an alternative approach for solving interactions between the ellipsoidal particles and the fluid flow is commonly applied in two-fluid (Eulerian-Eulerian) frameworks, and the interactions are determined according to the statistics of the ellipsoids, *e.g.* [41, 42, 80, 81].

By applying the one-way coupling, the previous studies [71, 76, 108] ignore the effects of non-spherical ellipsoids on fluid flows and the effects of particle collisions on both fluid flows and particles. However, at which level of particle volume fraction or mass loading the collision effect on both phases becomes significant is still uncertain for non-spherical particles, and inter-particle and particle-wall collisions can strongly influence the dynamics of non-spherical particles; therefore, ignoring these collision effects are not appropriate. To precisely resolve particle collisions, this research work applies a soft-sphere collision model. Moreover, the presence of discrete particles may influence the flow turbulence, even in very dilute flows. Therefore, this study applies the four-way coupling with the Lagrangian point-particle approach to model the gas-solid channel flows, fully describing the fluid-particle interactions, particle-particle and particle-wall collisions.

One difficulty when modelling non-spherical particles is to accurately represent the orientation and rotation of non-spherical particles. In most previous studies, *e.g.* [71, 76, 108], the rotation and orientation of ellipsoids are described by unit Quaternions in conjunction with the corresponding rotation matrices which can explicitly transform variables to the various co-ordinate frameworks. In this study, only unit Quaternions are used without the necessity of the corresponding rotation matrices. To achieve this, the Quaternion equation 2.29 relating tensor variables in different frameworks is applied. Furthermore, The novel Quaternion integration method, *i.e.* PCDM method, described in Chapter 2 is applied to accurately update unit Quaternions. Using only Quaternion multiplications, this algorithm avoids the numerical errors caused by the addition or subtraction of Quaternions presenting in the other integration algorithms, and precisely predicts the rotational motion and orientation of non-spherical particles.

The current study adopts the same computational domain and fluid properties as those in Marchioli *et. al.* [70, 71], following and extending these research works. For the sake of simplicity, several assumptions are made. First, no gravity. Second, effects of Brownian motion are negligible. And third, the particle sizes are assumed smaller than the Kolmogorov microscale so they can be treated as point particles [22, 32].

The aim of this chapter is to fully describe the applied four-way coupling method. The chapter is organized as follows. In section 3.2, the dynamics of both fluid and particle phases are formulated, and numerical setting of the fluid phase is then put forward. Section 3.3 describes the applied four-way couplings combined with the point-particle method. After that, difficulties and limitations in this work are introduced. To validate the numerical setting for the fluid phase, fluid velocity statistics of the single phase flow simulation are compared with the data of the UUD research group in Marchioli *et. al* [70] in Section 3.4.

3.2. Dynamics of gas-solid turbulent channel flow

In this study, all simulations are carried out in the in-house code “MultiFlow” [17, 100], which has been used to model many different multiphase flows, *e.g.* [27, 66, 68, 101, 106, 107, 110].

3.2.1. Fluid flow

The fluid governing continuity and momentum equations are expressed by equations 1.32 and 1.33, respectively, in Sec. 1.5.2.1. These two fluid governing equations are discretized through second order numerical schemes. In the continuity and momentum equations, the advective terms are approximated by a second order accuracy central differencing scheme, while the temporal terms are computed with the second order 3 point backward Euler scheme. The time step (Δt^f) for the fluid phase equals $1 \times 10^{-4}(s)$, corresponding to non-dimensional form $\Delta t^{f+} = 0.08826$. The domain consists of body fitted multi-blocks, and the “MultiFlow” solver can cut up a block even further into multiple pieces, based on the amount of processors available for the simulation. Moreover, the discretized continuity and momentum equations are solved by a fully-coupled solution method [27].

In this study, the channel flow in all simulations are driven by a pressure gradient ∇P_1 in the stream-wise direction. ∇P_1 is expressed by:

$$\nabla P_1 = \frac{\rho^f \nu^f 2 Re_\tau^2}{h^3} \quad (3.1)$$

where h is the half channel height, and the friction Reynolds number $Re_\tau = u_\tau h / \nu^f$ is fixed at 150 for all the simulations in this study. The value of Re_τ is identical to that in Marchioli *et. al.* [70, 71].

3.2.2. Turbulence kinetic energy (TKE) equation for a fully developed gas-solid turbulent channel flow

In Section 1.3.3, equation 1.14 represents the TKE equation for a fully developed single phase channel flow. For fully developed gas-solid turbulent channel flow, the TKE equation adds an additional term, expressed as:

$$\frac{d}{dx_2} \left(\frac{1}{2} \langle u_2'^f u_i'^f u_i'^f \rangle + \frac{\langle u_2'^f p' \rangle}{\rho^f} - \nu^f \frac{d}{dx_2} (k + u_2'^f)^2 \right) = \mathcal{P} - \tilde{\varepsilon} - \varepsilon_p \quad (3.2)$$

where ε_p represents the dissipation rate caused by the coupling force with particles. This additional term is directly derived from the source term $\boldsymbol{\Pi}$ in equation 1.33, given as:

$$\varepsilon_p = - \langle \Pi_i' u_i'^f \rangle \quad (3.3)$$

3.2.3. Numerical settings of the fluid phase

Table 3.1 lists properties of the fluid channel flow. The friction Reynolds number Re_τ is

Parameter	Definition	Value(Units)
ρ^f		1.3 (kg/m^3)
ν^f		1.57×10^{-5} (m^2/s)
u_τ	$u_\tau = \sqrt{\tau_0/\rho^f}$	0.11775 (m/s)
l_τ	$l_\tau = \nu^f/u_\tau$	1.333×10^{-4} (m)
τ_f	$\tau_f = \nu^f/u_\tau^2$	0.001132 (s)
Re_τ	$Re_\tau = u_\tau h/\nu^f$	150 (-)
Re_{bulk}	$Re_{bulk} = U^f h/\nu^f$	2300 (-)
δP_1	$\delta P_1 = \frac{\rho^f \nu^f h^2 Re_\tau^2}{h^3}$	0.90123 (Pa/m)

Table 3.1.: The properties of the fluid and the flow

fixed at a small number, 150, in all simulations, and three wall units are evaluated based on this Re_τ . In this study, the results of both phases are scaled with the wall units, presenting in non-dimensional forms, for which the superscript + is used.

As shown in Table 3.2, the computational channel domain with two smooth walls is $4\pi h \times 2h \times 2\pi h$ long in stream-wise (x), wall-normal (y) and span-wise (z) directions respectively, corresponding to $1885 \times 300 \times 942$ in wall units. The half channel height, h , is equal to 0.02 (m). The channel domain is depicted in Fig. 3.1. In the wall-normal

Directions	Stream-wise (x)	Wall-normal (y)	Span-wise (y)
Length (m)	0.2511 ($2\pi h$)	0.039963 ($2h$)	0.125549(πh)
number of grid points	159	169	159
Spatial resolution(Δx^+)	11.7	$0.57 \sim 2.18$	5.897

Table 3.2.: The properties of the computational domain and grid in all three directions

direction, non-slip boundary conditions are applied at both walls, while a periodic boundary is set in the other two directions. The computation is executed on $159 \times 169 \times 159$ grid points. The grid spacing is uniform in the stream-wise and span-wise directions but refined towards the two walls in the wall-normal direction using a tanh distribution with a growth factor of 1.6 on both sides, given for the grid point number n :

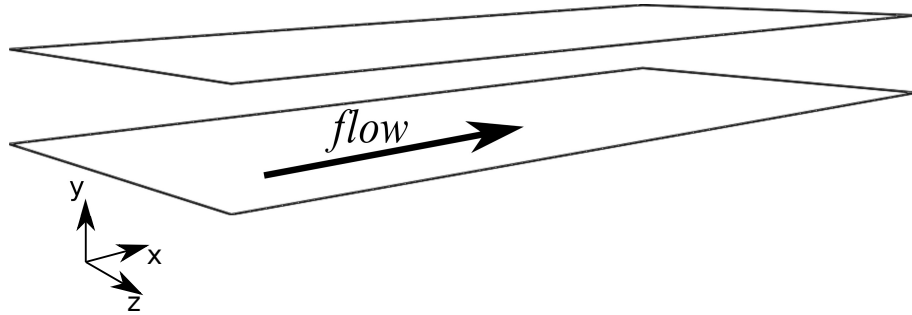


Figure 3.1.: The computational channel domain

$$y_n = y_{max} \left[\frac{1}{2} \left(\frac{1 + \tanh(1.6 * (\frac{n * \Delta y}{y_{max}} - \frac{1}{2}))}{\tanh(\frac{1}{2} * 1.6)} \right) \right] \quad (3.4)$$

This refinement ensures at least 4 grid points within $y^+ <= 5$ layer near the wall. These are comparable to the studies by Kim *et. al.* [55] and Marchioli *et. al.* [70].

3.2.4. The dynamics of non-spherical particles

The motion of a non-spherical particle can be divided into translational and rotational motion. To precisely and conveniently determine the dynamics of non-spherical particles, body-space and world-space are employed, *see* Fig. 2.1 in Chapter 2. Here, Fig. 3.2 displays an ellipsoidal particle in these two frameworks. In world space, the axes are fixed in the origin of the initial Cartesian framework which corresponds to the Eulerian fluid framework. On the other hand, the axes of body-space are aligned with the principle axes of an ellipsoidal particle, and the framework origin is fixed on the particle center of mass. The particle position in body space shown in Fig. 3.2(a) is applied for all ellipsoids in the simulations. For variables in body space, the superscript b will be used, whereas variables without this superscript mean they are in world space.

For non-spherical particles, particle properties, such as mass, mass center, volume and inertia tensor, are estimated by using the method explained in Section 1.6. In this study, two types of ellipsoids with aspect ratio $\lambda = 3$ and $\lambda = 5$ are modelled by 5 and 7 spheres, respectively. The centers of spheres in each type ellipsoid are fixed on the major axis of the ellipsoidal particle. One sphere is located at the center of an ellipsoid, and the other spheres in this ellipsoid are equally positioned from the center to the two sides of the ellipsoid. The diameter of the spheres in an ellipsoid decreases from the particle center to the two ends, as illustrated in Fig. 1.2.

3.2.4.1. Particle translational dynamics

The translational motion of particles is governed by the Newton's second law in world space:

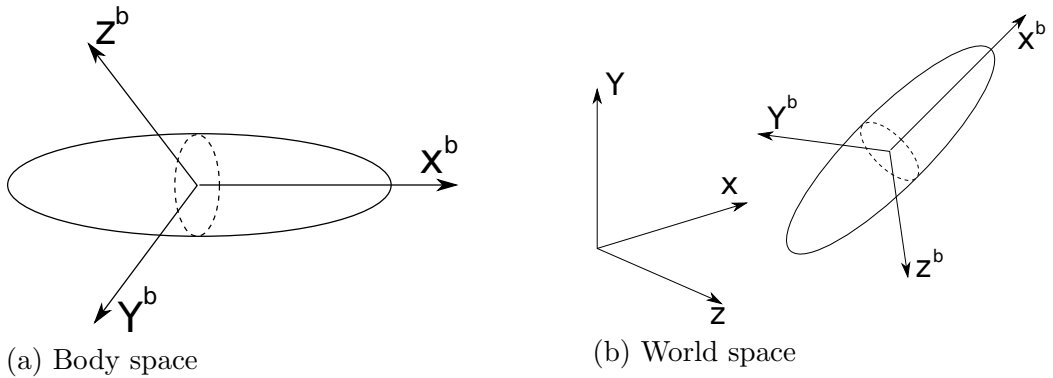


Figure 3.2.: (a) Body space and (b) World space co-ordinates. The x^b axis of the body-space co-ordinate system always aligns with the major-axis of the ellipsoidal particle, whereas the world-space co-ordinates remain fixed in space and time.

$$\sum \mathbf{F} = m \frac{d\mathbf{u}^p}{dt} \quad (3.5)$$

where $\sum \mathbf{F}$ is the resultant external force on a solid particle, m is the particle mass, and \mathbf{u}^p represents the particle translational velocity. $\sum \mathbf{F}$ consists of collision forces and forces in the BBO equation 1.36. As the particle density, ρ^p , is sufficiently larger than the fluid density, ρ^f , in the simulations, added mass, history and Faxen forces, which are linear with the density ratio, $\frac{\rho^f}{\rho^p}$, can be neglected. The buoyancy force is negligible because of the assumption of no gravity. Only hydrodynamic drag and collision forces work on particles. The particle linear velocity, \mathbf{u}_{n+1}^p , and the position, \mathbf{x}_{n+1}^p , at the time-level $n + 1$ are determined, using a second order Verlet scheme [1], given as:

$$\mathbf{x}_{n+1}^p = 2\mathbf{x}_n^p - \mathbf{x}_{n-1}^p + \mathbf{a}^p \Delta t^{2,p} + O(\Delta t^{4,p}) \quad (3.6)$$

$$\mathbf{u}_{n+1}^p = \frac{\mathbf{x}_{n+1}^p - \mathbf{x}_{n-1}^p}{2\Delta t} + O(\Delta t^{2,p}) \quad (3.7)$$

Although the order of equation 3.7 is lower than Equation 3.6, it is not influenced the accuracy of particle positions. The particle linear velocity is not essential in this method, and it is clear that equation 3.6 is not directly link to the particle velocity. For spherical particles, only modelling translational motion can appropriately represent their dynamics. On the other hand, the orientation of a non-spherical particle plays an important role in determining the effects of the fluid flow, *i.e.* the hydrodynamic drag force and torque, on the particles so that the rotational motion of non-spherical ellipsoids is required to be resolved.

3.2.4.2. The rotation of ellipsoidal particles

The governing equations of the particle rotation are considerably complex in world space, and the most common way is to solve them in body space. Equation 2.4 expresses the particle angular velocity acceleration, given as:

$$\dot{\boldsymbol{\omega}}^b = \mathbf{I}^{b-1} (\mathbf{T}^b - \boldsymbol{\omega}^b \times \mathbf{L}^b)$$

where all the variables are in body-space. The torque, \mathbf{T}^b , on an ellipsoidal particles include collision and drag torques. The inertia tensor \mathbf{I}^b is constant and only depends on the position and orientation of the ellipsoid in body space. As shown in Fig. 3.2(a), the arrangement of particle position leads a simple form of \mathbf{I}^b , given as:

$$\mathbf{I}^b = \begin{pmatrix} \frac{2ma^2}{5} & 0 & 0 \\ 0 & \frac{(1+\lambda^2)ma^2}{5} & 0 \\ 0 & 0 & \frac{(1+\lambda^2)ma^2}{5} \end{pmatrix} \quad (3.8)$$

where a and λ are the semi-minor axis and aspect ratio of the ellipsoid, respectively.

As interpreted in Chapter 2, only unit Quaternions are applied as rotation operators to determine the rotation of non-spherical particles. Relevant previous studies *e.g.* [71, 76, 108] also apply unit Quaternions to represent rotation, but they use corresponding rotation matrices to determining the vector and second order tensor variables among different co-ordinate frameworks, not Unit Quaternions. This may give rise to inaccuracies or instability, and it also requires more computational time and memory. To avoid these drawbacks, this study uses unit Quaternions to determine the variable transformation directly, instead of rotation matrices. The transformations of vector and second order tensor variables between body-space and world-space are determined by equations 2.16 and 2.29 respectively [109],

$$\begin{aligned} \mathbf{s} &= q\mathbf{s}^bq^{-1} \\ \mathbf{M} &= (q(q\mathbf{M}^bq^{-1})^Tq^{-1})^T \end{aligned}$$

Applying these two equations, the necessity of rotation matrix is avoided in this work. In the previous studies [25, 71, 76], integration methods for updating unit Quaternions are performed based on Taylor expansions. Unfortunately, all these algorithms cannot exactly preserve the unit length of Quaternions. As a result, the Quaternions must be re-normalized after each particle time step. Although the re-normalization procedure ensures that Quaternions keep the unit lengths, the inherent relationship among the four components in a Quaternion is affected and leads to unavoidable numerical errors. To avoid the errors from these integration methods, the current work applies the novel PCDM method [109] described in Chapter 2 for precisely integrating unit Quaternions. This new algorithm is briefly outlined as follows. A unit Quaternion at the next time-level $n + 1$ is determined as equation 2.63:

$$q_{n+1} = \tilde{q}_{n+1}q_n$$

where the multiplication product between the two unit Quaternions \tilde{q}_{n+1} and q_n can guarantee the result q_{n+1} to keep the unit length. Quaternion \tilde{q}_{n+1} represents the rotation from time-level n to $n + 1$, expressed as:

$$\tilde{q}_{n+1} = \left[\cos\left(\frac{|\boldsymbol{\omega}_{n+\frac{1}{2}}|\delta t^p}{2}\right), \sin\left(\frac{|\boldsymbol{\omega}_{n+\frac{1}{2}}|\delta t^p}{2}\right)\frac{\boldsymbol{\omega}_{n+\frac{1}{2}}}{|\boldsymbol{\omega}_{n+\frac{1}{2}}|} \right]$$

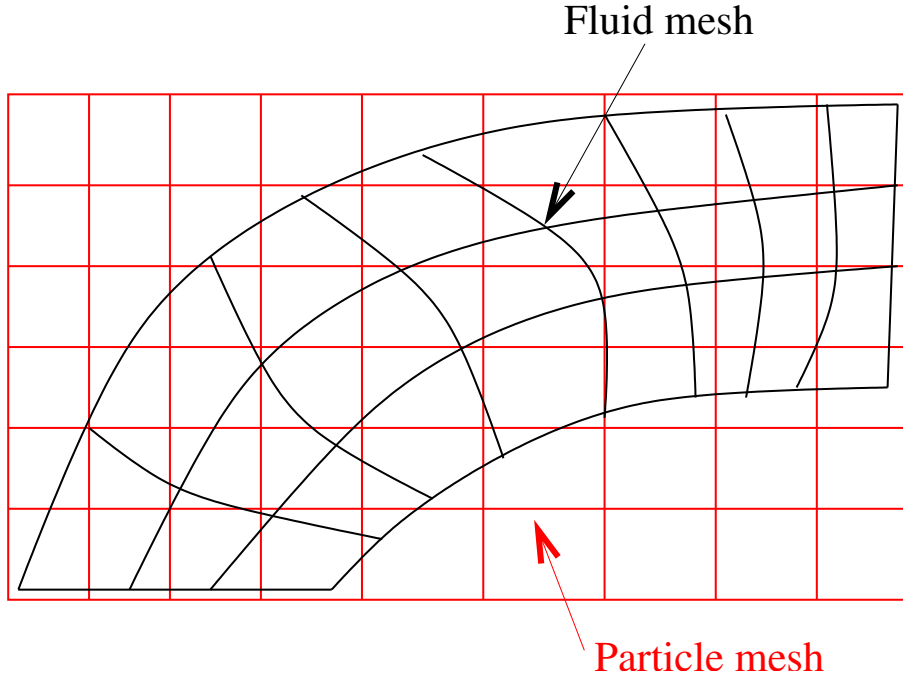


Figure 3.3.: Particle mesh and fluid mesh

where δt^p represents the particle time step, and $|\omega_{n+\frac{1}{2}}|$ is the length of angular velocity $\omega_{n+\frac{1}{2}}$.

The angular velocity of particles and unit Quaternions are approximated by a predictor-corrector method. Firstly, the external torque, \mathbf{T}_n , and angular velocity, ω_n , of a particle are transformed from world space to body space using equation 2.16 based on Quaternion q_n , and temporal $\omega_{n+\frac{1}{4}}^b$ and $\omega_{n+\frac{1}{2}}^b$ in body space are then computed by a first order Euler algorithm. After that, a predictor Quaternion $q''_{n+\frac{1}{2}}$ can be determined by

$$q''_{n+\frac{1}{2}} = \left[\cos \frac{|\omega_{n+\frac{1}{4}}| \delta t^p}{4}, \sin \frac{|\omega_{n+\frac{1}{4}}| \delta t^p}{4} \frac{\omega_{n+\frac{1}{4}}}{|\omega_{n+\frac{1}{4}}|} \right] q_n \quad (3.9)$$

Using $q''_{n+\frac{1}{2}}$, $\omega_{n+\frac{1}{2}}^b$ is transformed to world space to determine \tilde{q}_{n+1} . Finally, unit Quaternion q_{n+1} and ω_{n+1}^b is updated.

3.2.5. Particle mesh

To efficiently track a great number of discrete particles, rapidly detect all potential collisions, and precisely interpolate properties between the Eulerian fluid flow and discrete particles, a new grid mesh is created, called particle mesh. Fig. 3.3 shows an example of particle mesh with fluid mesh. This new mesh is Cartesian and uniform, and completely overlaps the mesh for the fluid flow. The length of an particle cell must be larger than the largest length of the biggest particle in the computational domain to ensure that a particle only belongs to one particle mesh cell. Particle collisions are rapidly searched and located through the particle mesh, and the interpolation between particles and Eulerian fluid flow

are also achieved based on this mesh. The fluid properties are first interpolated on the particle cells, and these information are then transformed on the particle position. On the other hand, the particle variables are interpolated into the fluid cell center by applying the cubic spline scheme.

3.3. Lagrangian point-particle four-way coupling method

In Marchioli *et. al* [70, 71], one-way coupling simulations are performed, and thus only fluid drag on particles is computed, neglecting the effect of particles on the fluid flow and particle collisions. However, fluid-particle and particle-particle interactions are complex for non-spherical ellipsoids. One-way coupling cannot properly describe the gas-solid multiphase flow. When an ellipsoidal particle collides with other particles or channel walls, the motion of the particle is very difficult to predict and its orientation may be randomly changed. The complex dynamics of ellipsoidal particles strengthen the fluid-particle interactions. Furthermore, it is still unclear that, at which level of particle volume fraction or mass loading, the collision effect on both phases becomes significant. To address the above complex and uncertain problems, this study performs the simulations of the gas-solid channel flow, using the DNS four-way coupling method with the point-particle approach. The full four-way couplings are the effects of the fluid flow on particles, the effects of dispersed particles on the fluid flow, particle-particle and particle-wall collisions.

3.3.1. Fluid effects on particles: hydrodynamic drag forces and torques

In this work, the effect of the fluid flow on particles is approximated by the hydrodynamic drag force and torque models. In general, the drag coefficient strongly depends on particle parameters such as the particle shape and the particle orientation with respect to the flow direction, as well as flow conditions such as turbulence level and Reynolds number. Hence, different empirical drag models are used for spheres and ellipsoids.

For spherical particles, the drag force is determined by [23]

$$\mathbf{F}_{drag} = 0.75 * V^p * \rho^f * \frac{C_D}{D_p} * |\mathbf{u}^p - \mathbf{u}^{f@p}| * (\mathbf{u}^p - \mathbf{u}^{f@p}) \quad (3.10)$$

where $\mathbf{u}^{f@p}$ represents the undisturbed fluid velocity at the center of the particle, and C_D is the drag coefficient, given as: [86, 88]

$$C_D = \begin{cases} \frac{24}{Re_p} (1 + 0.15 * Re_p^{0.687}) & ((1 - \alpha^p)Re_p < 1000) \\ 0.44 & ((1 - \alpha^p)Re_p > 1000) \end{cases} \quad (3.11)$$

where Re_p represents the particle Reynolds number:

$$Re_p = \frac{|\mathbf{u}^p - \mathbf{u}^{f@p}| D_p}{\nu^f} \quad (3.12)$$

On the other hand, the drag force expression for ellipsoidal particles is derived by Brenner [16], given as:

$$\mathbf{F}_{drag} = \mu^f \pi a \mathbf{K} (\mathbf{u}^{f@p} - \mathbf{u}^p) \quad (3.13)$$

where \mathbf{K} is the resistance tensor, which strongly depends on the orientation of the particle in world space. Using equation 2.29, \mathbf{K} can be simply transformed from body space to world space:

$$\mathbf{K} = (q(q\mathbf{K}^b q^{-1})^T q^{-1})^T \quad (3.14)$$

Here, \mathbf{K}^b is a constant resistant tensor in body space. The off-diagonal components of it are 0, whereas three diagonal components are determined by the ellipsoid aspect ratio λ ,

$$K_{xx}^b = \frac{8(\lambda^2 - 1)^{3/2}}{[(2\lambda^2 - 1)\ln(\lambda + \sqrt{\lambda^2 - 1}) - \lambda(\sqrt{\lambda^2 - 1})]} \quad (3.15)$$

$$K_{yy}^b = K_{zz}^b = \frac{16(\lambda^2 - 1)^{3/2}}{[(2\lambda^2 - 3)\ln(\lambda + \sqrt{\lambda^2 - 1}) + \lambda(\sqrt{\lambda^2 - 1})]} \quad (3.16)$$

For approximating the hydrodynamic torque on an ellipsoid, Jeffery's equation [52] is employed, given as:

$$T_x^{b,h} = \frac{32\pi\mu^f a^3 \lambda}{3(\alpha_2 + \alpha_3)} (\Omega_{zy}^{bf} - \omega_x^{bf}) \quad (3.17)$$

$$T_y^{b,h} = \frac{16\pi\mu^f a^3 \lambda}{3(\alpha_3 + \lambda^2 \alpha_1)} [(1 - \lambda^2) S_{xz}^{fb} + (1 + \lambda^2)(\Omega_{xz}^{fb} - \omega_y^{pb})] \quad (3.18)$$

$$T_z^{b,h} = \frac{16\pi\mu^f a^3 \lambda}{3(\alpha_2 + \lambda^2 \alpha_1)} [(\lambda^2 - 1) S_{yx}^{fb} + (1 + \lambda^2)(\Omega_{yx}^{fb} - \omega_z^{pb})] \quad (3.19)$$

where three constants α_1 , α_2 and α_3 are given by [37]:

$$\alpha_1 = -\frac{2}{\lambda^2 - 1} - \frac{\lambda}{(\lambda^2 - 1)^{3/2}} \ln \left[\frac{\lambda - (\lambda^2 - 1)^{1/2}}{\lambda + (\lambda^2 - 1)^{1/2}} \right] \quad (3.20)$$

$$\alpha_2 = \alpha_3 = \frac{2}{\lambda^2 - 1} + \frac{\lambda}{2(\lambda^2 - 1)^{3/2}} \ln \left[\frac{\lambda - (\lambda^2 - 1)^{1/2}}{\lambda + (\lambda^2 - 1)^{1/2}} \right] \quad (3.21)$$

and the fluid strain rate tensor, \mathbf{S}^{fb} , and the rotation tensor, $\mathbf{\Omega}^{fb}$, in body space are expressed as:

$$S_{ij}^{fb} = \frac{1}{2} \left(\frac{\partial u_i^{fb}}{\partial x_j} + \frac{\partial u_j^{fb}}{\partial x_i} \right) \quad (3.22)$$

$$\Omega_{ij}^{fb} = \frac{1}{2} \left(\frac{\partial u_i^{fb}}{\partial x_j} - \frac{\partial u_j^{fb}}{\partial x_i} \right) \quad (3.23)$$

It should be noted that all the fluid velocity derivatives, $\partial u_i^{fb} / \partial x_j$, are interpolated from Eulerian fluid framework into the particle framework (body space).

3.3.2. Particle coupling with the fluid flow

The hydrodynamic drags can reversely influence the channel fluid flow. The rotational Stokes numbers of interest are assumed to be small, so that the effect of hydrodynamic torques can be neglected, an assumption consistent with the fact our particles are assumed to be much smaller than a mesh cell. Therefore, only the effect of the particle drag force is summed as the source term $\boldsymbol{\Pi}$ in equation 1.33:

$$\boldsymbol{\Pi}_i = -\frac{1}{V_{cell}^f} \sum_{l=1}^{N_p} \mathbf{F}_i^{drag,l} \quad (3.24)$$

where N_p is the number of particles in a fluid computational cell, V_{cell}^f is the volume of the fluid cell, and drag forces F_{drag} are summed and then volume averaged in the cell. This approach is referred to as the particle-source-in-cell method, and requires a proper interpolation scheme to transform the Lagrangian properties to the Eulerian cell. Having the least effect on the fluid energy spectrum, the cubic spline scheme proposed by Yeung and Pope [105] is used in this work.

3.3.3. Inter-particle and particle-wall collisions

In many numerical studies, *e.g.* [71, 77, 108], both particle-particle and particle-wall collisions are not computed in their gas-solid simulations with ellipsoidal particles. However, it is not clear, at which particle volume fractions and mass loadings, particle collisions become important for non-spherical particles. When particle collisions occur, the dynamics of ellipsoids are much more complex than spheres. Therefore, all particle collisions in the simulations should be directly detected and estimated. To achieve this, “MultiFlow” provides two deterministic approaches: hard-sphere and soft-sphere collision models. Currently, the hard-sphere model is only available for resolving collisions of spherical particles in “MultiFlow”, but not for non-spherical particles. The soft-sphere model can be applied for both spherical and non-spherical particles, thus chosen for this study. The soft sphere collision model is outlined as follows.

A collision is detected when two fictitious spheres from different non-spherical particles overlap. When a particle collision occurs, the soft-sphere collision model determines a slightly overlapping at the contact point, and this overlapping is then used to approximate the local deformation of the colliding particle, leading to normal $\mathbf{F}_n(t)$ and tangential $\mathbf{F}_t(t)$ forces. These two contact forces are determined using the Hertzian-Mindlin force

model derived by Mindlin and Deresiewicz [74]

$$\begin{aligned}\mathbf{F}_n(t) &= K_n(t) \delta_n^{\frac{3}{2}}(t) \mathbf{n}(t) \\ \mathbf{F}_t(t) &= \min(\mu \mathbf{F}_n(t), K_t(t) \boldsymbol{\delta}_t(t))\end{aligned}\quad (3.25)$$

where μ is the coefficient of friction, $\mathbf{n}(t)$ is the collision normal, $\delta_n(t)$ is the normal displacement scalar, and $\boldsymbol{\delta}_t(t)$ represents the total tangential displacement vector, which is derived by integrating the successive tangential displacements and mapping this into the current reference framework of the collision. In equation 3.25, K_n and K_t are the spring constants for the normal and tangential forces respectively, and are predicted by Hertzian contact theory:

$$\begin{aligned}K_{n,l}(t) &= \frac{4}{3} E^* \sqrt{r(t)} \\ K_{t,l}(t) &= 8G^* \sqrt{r(t)\delta(t)}\end{aligned}$$

where $r(t)$ represents the local radius of the particle-particle contact area, E^* is the normal spring constant, and G^* is the tangential constants. The subscript, l , represents loading, *i.e.* the particles moving towards each other. The local radius $r(t)$ of the particle-particle collision is expressed as:

$$r(t) = \frac{0.5 * D_1^p * D_2^p}{D_1^p + D_2^p} \quad (3.26)$$

where D^p is the particle diameter, and the subscript 1 and 2 represent the two contact particles. If the collision is between a particle and a boundary wall, $r(t)$ is determined by:

$$r(t) = 0.5 * D_1^p \quad (3.27)$$

The normal spring and tangential constants are defined by:

$$\frac{1}{E^*} = \frac{1 - \sigma_1^2}{E_1} + \frac{1 - \sigma_2^2}{E_2} \quad (3.28)$$

$$\frac{1}{G^*} = \frac{2 * (2 - \sigma_1)(1 + \sigma_1)}{E_1} + \frac{2 * (2 - \sigma_2)(1 + \sigma_2)}{E_2} \quad (3.29)$$

where E represents particle Young's modulus, and σ is the particle Poisson's ratio. To account for the dissipative nature of particle collisions, a coefficient of restitution is introduced to determine the spring constant value for unloading, represented by the subscript u , following Walton *et. al.* [102]:

$$e = \sqrt{\frac{K_{n,u}}{K_{n,l}}} \quad (3.30)$$

The coefficient of restitution e is set to be a constant ($0 < e \leq 1$) and does not depend on the impact velocity. The subsequent forces and torques arising from particle-particle

and particle-wall collisions are then added both of the particles in contact. The collisional torque for each collision is determined as:

$$\mathbf{T}^c = (\mathbf{F}_n + \mathbf{F}_t) \times \mathbf{X}_{mp-cp} \quad (3.31)$$

where \mathbf{X}_{mp-cp} represents the vector from the center of the particle to the contact point of the collision. To accurately compute the particle dynamics and collisions, the time step for particles (Δt^p) are required to be extremely small, thousand times less than fluid time step (Δt^f).

3.3.4. Limitations

Although applying the DNS four-way coupling can accurately describe gas-solid channel flows, there are still several limitations and difficulties confining the current research work. Firstly, the point particle assumption is only feasible for particles smaller than Kolmogorov length scale (η), otherwise the boundary effects of relatively large particles become important and need to be properly resolved by the fully resolved approach. The length of a particle mesh cell is confined by the particle size and must be larger than the largest length of the biggest particle in the domain. The size of particle mesh should be properly chosen for efficiently tracking particles, rapidly searching collisions and precisely interpolating properties between the two phases. In turbulent flows, the ratio of the smallest scale (η) to the largest scales (l_0) can be approximated by Reynolds number as $\eta/l_0 = Re^{-3/4}$. Since η is rapidly and dramatically reduced with the increase of Reynolds number, the Reynolds number is restricted at a quite low level to ensure a reasonable size of the fluid and particle meshes.

Although “MultiFlow” provides a way to model particles with any random shape, the shape of particles in this study only includes spheres and ellipsoids, due to the lack of empirical drag models for complex particle shape. In the literature, only a few research studies explored non-spherical particles suspended in a fluid flow, and thus there are very a few empirical equations modelling hydrodynamic drag on particles with few shapes. Following the research works [35, 65, 71, 76, 77, 108, 111], only spherical and ellipsoidal particles are used in the current study.

The biggest restriction is the limited capacity of computational power. DNS simulations cost extremely high computing source and time. Determining complex particle dynamics and collisions takes over 80% of the computing time. Therefore, only a limited number of particles are modelled in the channel flow, up to 1 million for simulations with spheres and 0.2 million for simulations with ellipsoids. Even if modelling such a few ellipsoids, the simulations still run several months to reach the steady state. The limited computing power is the biggest limitation for numerical solving the problems of dispersed multiphase flows.

3.4. Validation of the single phase flow simulation

In Marchioli *et. al.* [70], several research groups establish a benchmark test for modelling spherical particles in a turbulent channel flow based on the exactly same flow conditions, just using the one-way coupling method. This study applies the same flow assumptions and the computation domain as in [70, 71], and performs simulations using the four-way coupling method. To validate the numerical settings for the fluid phase, the fluid velocity statistics of the clear fluid flow simulation are compared to the data obtained from the research group UUD in Marchioli *et. al.* [70].

As shown in Figs. 3.4 to 3.7, the statistics of the fluid velocity, *i.e.* mean fluid velocity (U_1^f) in the flow direction and fluid velocity fluctuations ($u_i''^f$) in all three directions, are plotted as functions of distance to the wall within half channel height between $0 \leq y^+ \leq 150$. As can be seen from Fig. 3.4, U_1^f in the clear flow case is only slightly over the UUD data in the central region of the channel, and the bulk velocity is 1.805 m/s in the clear channel flow slightly larger than 1.77 m/s in UUD. The two profiles of U_1^f throughout the channel are in a reasonably good agreement. Figs. 3.5 to 3.7 show the fluid root mean

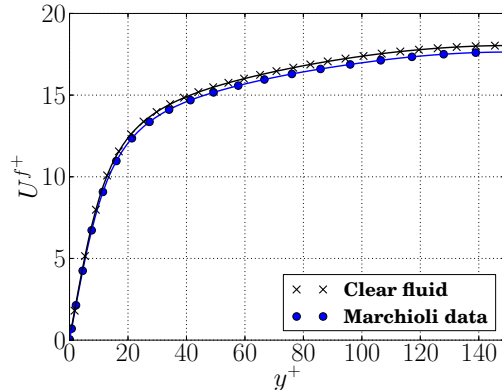


Figure 3.4.: Fluid stream-wise direction mean velocities as a function of the distance to the wall for: clear fluid ($-x$), Marchioli *et. al.* [70] data ($-o$)

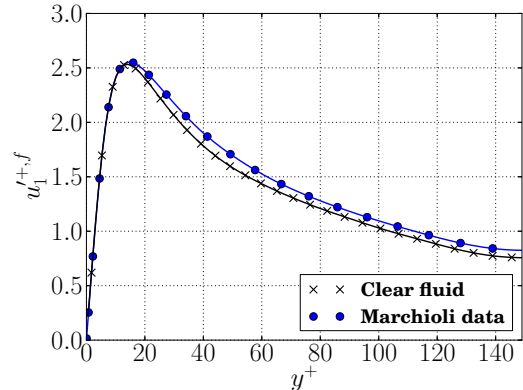


Figure 3.5.: Fluid stream-wise direction RMS velocities as a function of the distance to the wall for: clear fluid ($-x$), Marchioli *et. al.* [70] data ($-o$)

square (RMS) velocities in all three directions. In the near wall region ($0 < y^+ < 20$), the curves of velocity fluctuations in the clear flow and UUD data nearly coincide. In the outer region ($20 < y^+ < 150$), three fluid RMS velocities in the clear flow simulation are a bit lower than the data from UUD. In Marchioli *et. al.* [70], it is evident that the velocity fluctuations obtained from different research groups are clearly different in the central region. The deviations of the results in Figs. 3.4 to 3.7 are considerably small and well accepted. These comparison results prove that the numerical settings of the fluid flow in the current work are accurate.

This study not only discusses these simple fluid velocity statistics, but also analyses more complex turbulence terms such as turbulence terms in the TKE equation and the mean-square vorticity. Turbulence terms in the TKE equation are very important for analysing the flow turbulence and have special features for a fully developed channel flow.

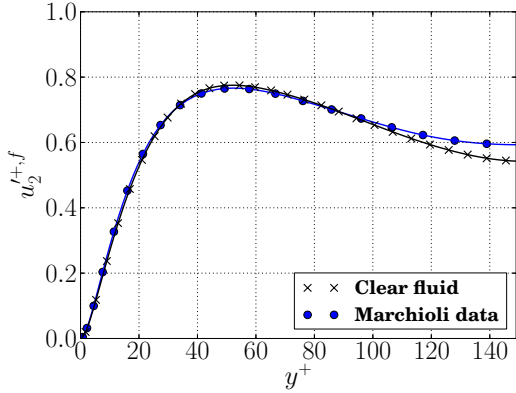


Figure 3.6.: Fluid wall-normal direction RMS velocities as a function of the distance to the wall for: clear fluid ($-x$), Marchioli *et. al.* [70] data ($-o$)

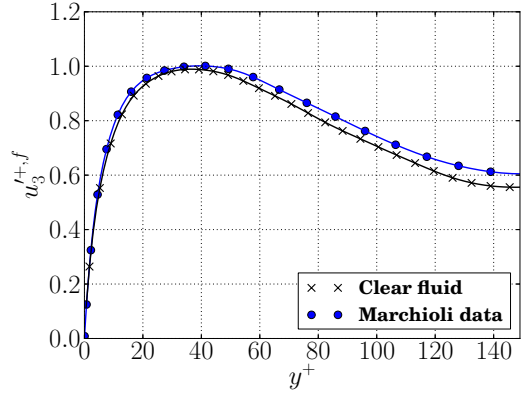


Figure 3.7.: Fluid wall-normal direction RMS velocities as a function of the distance to the wall for: clear fluid ($-x$), Marchioli *et. al.* [70] data ($-o$)

Fig. 3.8 displays all five dimensionless turbulence terms in the TKE equation of the clear fluid flow simulation. Although fluid velocities and velocity fluctuations are zero at the wall, the fluctuation strain rate s_{ij}^{tf} are very large in the near wall region. Therefore, the fluid flow dissipation rate $\tilde{\varepsilon}$ has value near the wall and peaks at the wall, where the turbulence kinetic energy k is zero. In the buffer sublayer, the magnitude of $\tilde{\varepsilon}$ has a local peak and a local minimum points and gradually decrease towards the channel center.

The production of turbulence \mathcal{P} rises from zero at the wall to the peak value in the buffer layer, around $y \approx 11.5$, where the viscous stress and Reynolds stress are equal, and then decreases to minimum value 0 again at the center of the channel.

The other three terms represent turbulence transports, which do not destroy or produce any turbulence energy, and only transport k from a location to another location. At the wall, the viscous term transports all the turbulence energy to the wall, to be consistent with the peak absolute value of the fluid flow dissipation rate. It should be noted that all the turbulence terms in the TKE equation reaches the largest magnitudes in the near wall region of $0 < y^+ < 20$, where the magnitude of turbulence kinetic energy k are large.

3.5. Summary

Unlike the previous papers [70, 71, 76, 108] only perform one-way coupling simulations, this study applies the four-way coupled DNS combined with the point-particle approach. This chapter expresses the dynamic equations of both phases, introduces numerical setting for the fluid flow and interprets the four-way couplings.

An additional source term, Π_i , is added into the fluid momentum equation to include the effects of particles on the fluid flow, and a dissipation rate caused by the coupling force of the particles ϵ_p is added into the TKE equation. Using the novel PCDM method for integrating unit Quaternions ensures that the rotation accuracy of non-spherical ellipsoids. This study applies the same flow condition assumptions, fluid properties and computa-

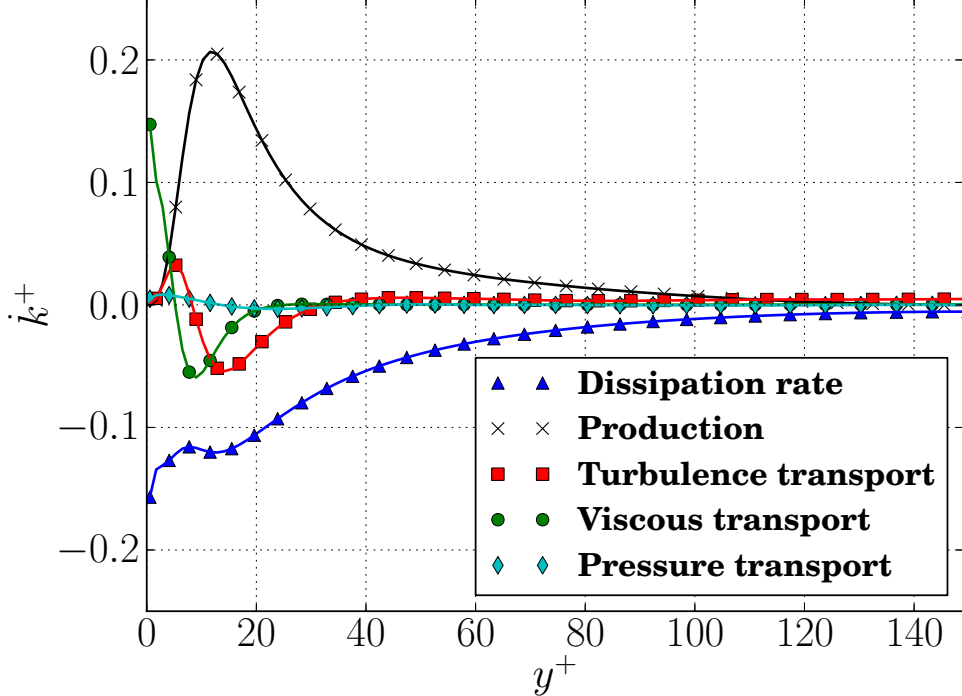


Figure 3.8.: Turbulence structures in TKE equation

tional domain as those in [70, 71]. The simulations of gas-solid channel flows are carried out in flow solver ‘‘MultiFlow’’.

The drag models for ellipsoidal particle are much more complex than for spheres, and they depend on the orientation of the ellipsoids. The particle forces in a fluid mesh cell are summed and added into Eulerian fluid phase by applying the cubic spline interpolation scheme. In order to accurately predict the motion of non-spherical particles when particle-particle and particle-wall collisions occur, all potential particle collisions are directly detected and resolved applying the soft-sphere collision model. In ‘‘MultiFlow’’, the created particle mesh overlapping the fluid cells ensures rapidly detecting collisions and properly interpolating properties between particles and Eulerian fluid flow. Because of the limited computing capacity, the gas-solid channel flows are modelled at quite low Reynolds number, 150, and only spherical and ellipsoidal particles are used in this study. The statistics of the fluid velocity in the clearly fluid case are well compared with the fluid data from the UUD research group in [70], to validate the applied assumptions and numerical settings for the fluid phase.

The simulations of gas-solid flows are performed by varying the particle inertia, particle aspect ratio and particle volume fraction. In the following two chapters, the statistical results are displayed and discussed to investigate the effects of particle inertia, particle aspect ratio and particle volume fraction on both fluid flow and particles.

4. Four-way coupled simulations of small non-spherical particles in turbulent channel flows: the effects of particle shape and Stokes number

This chapter is based on the published paper:

F. Zhao, W. K. George and B. G. M. van Wachem, “Four-way coupled simulations of small particles in turbulent channel flows: the effects of particle shape and Stokes number”, submitted to Physics of Fluids (2014).

Abstract

This chapter numerically investigates the effects of elongated particle shape and Stokes number on the behaviour of gas-solid turbulent channel flows with non-spherical ellipsoids, applying four-way coupled DNS combined with the point-particle approach. The Eulerian fluid phase is modelled by direct numerical simulation (DNS), while dispersed particles are tracked individually and inter-particle and particle-wall interactions, *i.e.* contact collisions, are taken into account. To explore the effects of particles on the flow turbulence, the statistics of the fluid flow, such as the fluid velocity, the terms in turbulence kinetic energy (TKE) equation, the slip velocity between the two phases and velocity correlations, are analysed for cases considering ellipsoidal particles with different inertia and aspect ratio. The results of the simulations including particles with large Stokes numbers show that the turbulence is considerably attenuated, even in the very dilute regime. The reduction of the turbulence intensity is predominant in the near wall region, where dispersed particles preferentially accumulate. Moreover, the elongated shape of ellipsoids strengthens the turbulence attenuation compared to spherical particles. In the channel center, there is almost no effect of the particle shape on the flow. In simulations with ellipsoidal particles, the fluid-particle interactions strongly depend on the orientation of the ellipsoids. In the near wall region, the distribution of the orientation angle clearly demonstrates that ellipsoids tend to align predominantly within the x-y plane and perpendicular in the spanwise direction, whereas no preferential orientation in the central region of the channel is observed. Important conclusions from this chapter include: the average viscosity of the flow is not affected, the average direct dissipation by the particles is negligible, and the primary mechanism by which the particles affect the flow is by altering the turbulence structure near and around the turbulence kinetic energy peak.

4.1. Introduction

The behaviour of small particles suspended in a turbulent channel flow is of importance in industrial and environmental fluid mechanics. In the past decades, non-spherical fibre-like ellipsoids suspended in wall-bounded turbulence flows have been investigated and reported in [3, 35, 65, 69, 71, 76, 77, 101, 108]. Among those papers, Zhang *et. al.* [108] is the first to apply Direct Numerical Simulation (DNS) to solve fluid channel flows with spheroids. Following Zhang's work, Mortensen *et. al.* [76] and Marchioli *et. al.* [71] report the statistics of ellipsoids with different aspect ratio and inertia. As most of these research works apply one-way coupling method, the effect of particles on the fluid flow and the effect of particle collisions on the two phases are not taken into account, but these effects may considerably influence both the fluid flow and particles in the channel flow. These studies only reported and discussed the statistics of ellipsoidal particles. To perform more accurate simulations, this study applies four-way coupling method as described in Sec. 3.3, fully resolving the fluid-particle and particle-particle interactions. Therefore, more precisely results of both phases can be obtained and analysed.

In the gas-solid flows with non-spherical particles, the orientation of non-spherical particles are very important, which determines the hydrodynamic drag forces and torques on ellipsoids. To describe the rotation and orientation of ellipsoids, PCDM Quaternion integration method are applied to update unit Quaternions, and vector and tensor variables are transformed between different coordinate frameworks by Quaternions. The applied Quaternion methods are much more accurate than the Quaternion integration methods used in previous studies [71, 76, 108]. More detail about the applied Quaternion method is interpreted in chapter 2. In the papers [71, 76, 108], the orientation of particles were discussed by representing the mean absolute cosine values of the orientation angles. However, the non-linear cosine function may not accurately describe the orientation of the particles. Therefore, the orientation angles θ_i between the ellipsoid major axis vector x^p and the axes of world space are used to analyse the orientation of ellipsoidal particles. This chapter also provides an other orientation angle to analyse the orientation of particles. The ellipsoid major axis vector x^p projects on three planes (y-z, x-y and x-z planes) perpendicular to the x, z and y axes of world space. The angles ψ_i can represent the angle between 2-D projected vector x_{jk}^p and axis of world space. The distributions of the orientation angles ψ_i in the near wall and central regions are analysed to investigate the particle orientations in the channel flow.

As introduced in Sec. 1.4, several parameters influence the behaviour of the gas-solid channel flows such as particle size, particle volume fraction, Reynolds number, wall roughness, Stokes number and particle shape. Variable combination of these factors makes the dispersed multiphase flows extremely complex and difficult to predict. Following the studies [71, 76, 108], this chapter numerically explores the behaviours of ellipsoids suspended in the channel flow. The four-way coupled simulations are performed by varying the ellipsoid inertia (Stokes number) and the ellipsoid aspect ratio. Particles are considered as point-particles for the fluid phase, and all simulations analysed in this chapter contain particles with the same number, 200,000. The friction Reynolds number is fixed at 150.

Additionally, the smooth wall condition is applied. The differences of the particle size, friction Reynolds number and wall roughness are negligible in all simulations. The effects of Stokes number and particle shape are only considered.

It is believed that small particles tend to accumulate in the near wall region and preferentially concentrate in the regions of low-speed and high strain [43, 93]. Similar phenomena is also found for the ellipsoidal particles [71, 76]. The particle deposition and distribution in the channel flow are carefully discussed in this chapter. In the literature, the flow turbulence modulation due to the presence of solid particles is widely discussed by comparing the statistics of fluid velocities, *i.e* the mean flow velocity, the fluid root mean square (RMS) velocity and the Reynolds stress, among different simulations. However, more complex information on the flow turbulence, such as the fluid flow turbulence production, the fluid flow dissipation rate and the dissipation rate caused by particles, are rarely discussed for gas-solid channel flows, especially for flows with non-spherical particles. The current thesis will directly analyse these statistics of the fluid flow to explore the effects of the particle shape and Stokes numbers on the flow turbulence.

The aim of this chapter is to investigate not only the behaviours of ellipsoidal particles in a turbulent channel flow but also the effects of the particle shape and Stokes number on the flow turbulence. The ongoing chapter is organised as follows. In section 4.2, simulation settings are put forward. Section 4.3 shows and analyses the statistics of fluid flows, and the contour plots of fluid velocity and particle distribution in the near wall region are shown in Section 4.4. After that, Section 4.5 discusses the results of the particles. Finally, some conclusions are drawn in section 4.6.

4.2. Simulation set-up

4.2.1. Particle properties

As described in Sec. 1.6, a non-spherical particle is constructed by fictitious spherical particles. More spheres are required to model an ellipsoid with larger aspect ratio. The number of particles is 200,000 in all simulations. To achieve reasonable and feasible simulations, the aspect ratio of ellipsoids is limited as small as 5.

Particle properties in different particle-laden simulations are listed in Table 4.1. The simulations are separated by different Stokes numbers (particle inertia) and different ellipsoid aspect ratios. Ellipsoids with $\lambda = 3$ and $\lambda = 5$ are modelled by 5 and 7 spheres respectively. Sec. 1.6. The particle response time τ_p of elongated ellipsoids is different from that of spheres, determined by the aspect ratio [89]:

$$\tau_p = \frac{2a^2\rho^p}{9\nu^f\rho^f} \frac{\lambda \ln(\lambda + (\lambda^2 - 1)^{\frac{1}{2}})}{(\lambda^2 - 1)^{\frac{1}{2}}} \quad (4.1)$$

Table 4.1.: Particle properties in different simulations

St	λ	ρ [kg/m ³]	minor-axis (a) [μm]	Major-axis (b) [μm]	Volume fraction [%]
5.0	1.0	225.68	96.0	96.0	0.0073
30	1.0	1354.21	96.0	96.0	0.0073
5.0	3.0	120.77	96.0	287.93	0.022
30.0	3.0	724.23	96.0	287.93	0.022
5.0	5.0	93.7	96.0	480.0	0.036
30.0	5.0	578.77	96.0	480.0	0.036

4.2.2. Numerical setting

The linear motion of ellipsoids are resolved by the second order Velocity-Verlet numerical algorithm, while the rotation of ellipsoids are determined applying the PCDM method. The numerical settings for the fluid channel flow are presented in Section 3.2.3.

The simulations are initialized with the results from single phase flow simulations. After single phase fluid channel flows reach steady-state, particles are homogeneously positioned in the whole channel with a velocity of the bulk fluid velocity without rotation in each case. In order to ensure the accuracy of the soft-sphere collision model for the given particles and flow conditions, the particle time-step, Δt^p , is chosen to be extremely small, $1 \times 10^{-7}(s)$. This time-step is 1000 times smaller than the fluid time step. To avoid any energy loss during particle collisions, the restitution coefficient e equals unity.

4.3. Fluid Statistics

In this section, fluid statistics are displayed and analysed, including the fluid velocity, all terms in the turbulence kinetic energy (TKE) equation, the major components of the fluid flow dissipation rate and the mean square vorticity. As the stream-wise and spin-wise directions are homogeneous, the time averaging results on this two directions are identical. The averaged results only vary in the wall-normal direction and are computed as follows. On a plane perpendicular to the wall-normal direction, the values of a variable on all the mesh nodes in this plane are summed over sampling time steps, and the summation of the samples is then divided by the total sample number, which is equal to the number of the nodes in the plane multiplying the number of all the sampling time steps. To sample independent variables on the same mesh node, a variable on the same node is sampled on every 30 time steps, and the total number of sampling time steps are over 450. The total number of samples for one averaged result is over 12 million. These ensure the accuracy of the averaged results in this study.

4.3.1. Fluid velocity statistics

Figs. 4.1 to 4.8 compare the mean fluid velocity U_1^f in the flow direction, the fluid root mean square (RMS) velocity $u_i'^f$ and Reynolds stresses $\langle u_x'^f u_y'^f \rangle$ among all 6 particle-laden simulations and the single phase flow simulation. For the RMS (root mean square) values of variables, the superscript prime is used, while capital letters represent mean values of the variables. The symbols $\langle \rangle$ represent the averaging operator.

Fig. 4.1 displays the mean fluid flow velocities U_1^f from the wall, $y^+ = 0$, to the channel center, $y^+ = 150$. The curves of the mean fluid flow velocities in all particle-laden simu-

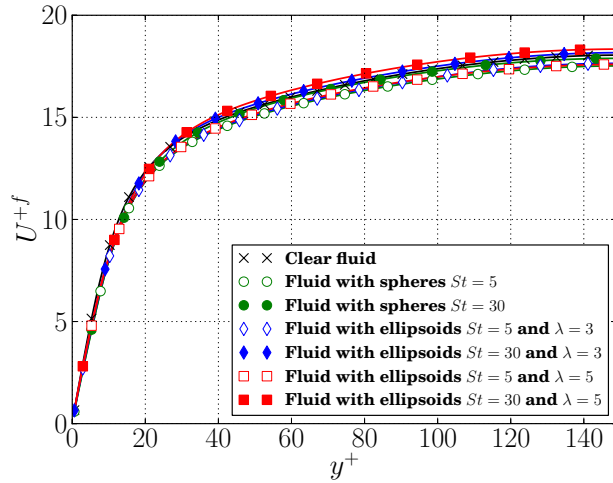


Figure 4.1.: Fluid mean velocity in the flow direction as a function of distance to the wall

lations nearly coincide in the very near wall region ($0 < y^+ < 10$) as shown in Fig. 4.2. This collapse in classic inner variables together with the constancy of the wall shear stress means that the viscosity of the flow with particles must be the same as for the flow without. As can be seen in Figs. 4.1 and 4.3, there is an increase in U_1^f between $40 < y^+ < 150$ for the cases with large Stokes number ($St = 30$). This will be seen to be because particles with high inertia attenuate the turbulence intensity and cause a drag reduction in the channel flow. The mean fluid velocity in the cases with high particle inertia ($St = 30$) is larger in the outer region ($40 < y^+ < 150$), compared to the cases with relatively low St ($St = 5$), even in such dilute flows. The bulk fluid velocity increases from 1.750 m/s in the case considering spheres with $St = 5$ to 1.832 m/s in ellipsoid-laden case with $\lambda = 5$ and $St = 30$. It is also clearly observed from Fig. 4.3 that U_1^f in the cases considering particles of $St = 30$ increases with increasing particle aspect ratio in the channel central region. The elongated shape of ellipsoids with considerably high inertia clearly strengthens the effect of particles on the fluid flow and enhances the drag reduction, thus increasing the mean flow velocity. Moreover, since the profile of U_1^f collapses perfectly near $y = 0$ and u_τ is constant and has the same value for all simulations, this means that the viscosity ν^f is equal in all cases. Therefore, the drag reduction has nothing to do with changes in the viscosity due to the particles. This also implies that the changes in the flow due to the

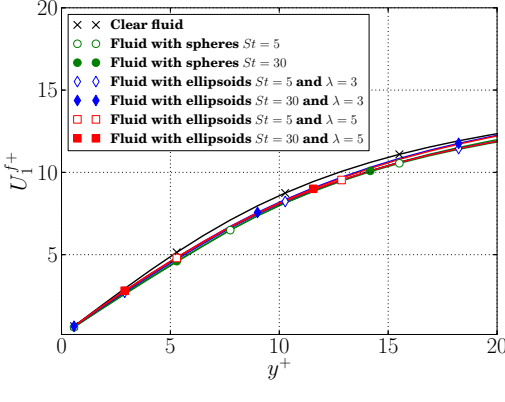


Figure 4.2.: Fluid mean velocity in the flow direction as a function of distance to the wall in the near wall region

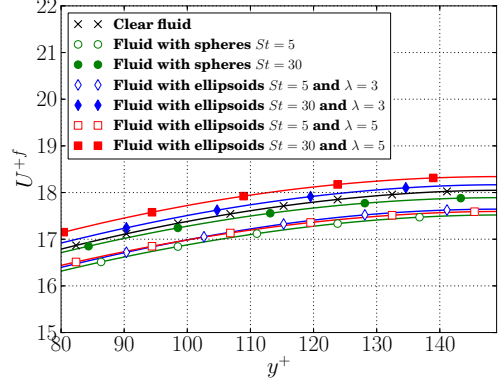


Figure 4.3.: Fluid mean velocity in the flow direction in the central region of the channel

presence of particles has everything to do with the turbulence.

It is generally believed that in gas-solid channel flows, dispersed small particles with high particle inertia increase the fluid stream-wise RMS velocity, but reduce velocity fluctuations in the other two cross-stream directions, e.g. [111]. These phenomena seem to be caused by two factors: the inertia of particles and the flow velocity gradients. In the wall-normal and span-wise directions, particles with high inertia cannot respond quickly to changes of the fluid flow and delay it, resulting in the decrease of the fluid RMS velocities in these two directions. As can be seen in Figs. 4.4 and 4.5, the velocity fluctuations in

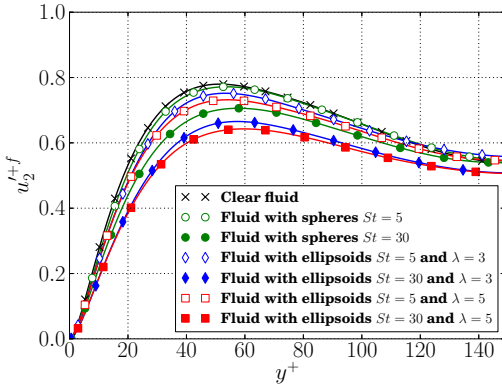


Figure 4.4.: Fluid RMS velocity in the wall-normal direction as a function of distance to the wall

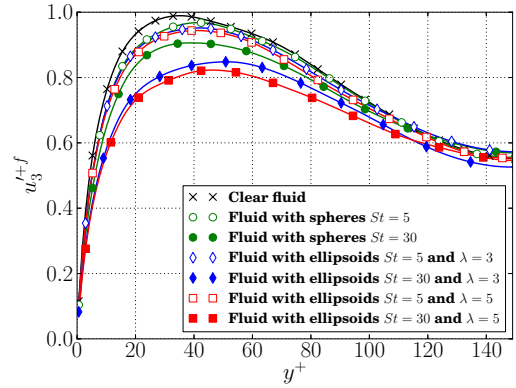


Figure 4.5.: Fluid RMS velocity in the span-wise direction as a function of distance to the wall

the wall-normal and span-wise directions in all particle-laden cases are smaller than for the clear fluid flow, especially within the region ($0 < y^+ < 80$). The higher the particle inertia, the lower the fluid RMS velocities in the wall-normal and span-wise directions. It is also clearly observed from Figs. 4.4 and 4.5 that the effect of the elongated shape further decreases the fluid velocity fluctuations in these two directions in the cases with the same Stokes number. This is because the interactions between ellipsoidal particles and the fluid

flow strongly depend on the particle orientation and are more complex and stronger than those between spheres and the fluid. Thus the effect of elongated shape further decreases the fluid velocity fluctuations in the wall-normal and span-wise directions in the cases with the same Stokes number. Because the mean fluid velocities in these two direction are zero throughout the channel, their gradients are also close to zero, and so there is, of course, no effect of the fluid velocity gradient on the fluid velocity fluctuations in the wall-normal and span-wise directions. In addition, the peaks of $u_2^{\prime f}$ and $u_3^{\prime f}$ shift towards the centre of the channel as particles get heavier.

The situation is more complex in the stream-wise direction. Like the other directions, the fluid velocity fluctuation in the stream-wise direction is somewhat reduced by particles with high inertia. Due to no-slip conditions applied at the walls for the fluid phase and the non-zero mean stream-wise velocity, the continuous fluid flow has a large velocity gradient in the near wall region. When the particles with high inertia move vertically in the wall-normal direction, the large momentum transfer between the two phases strengthens the velocity fluctuations of both the particles and the fluid flow. As the Stokes number rises, the velocity profiles of particles in the stream-wise direction becomes flatter. This considerably enlarges the slip velocity and strengthens momentum transfer between the fluid flow and particles. Fig. 4.6 shows the fluid RMS velocity $u_1^{\prime f}$ in the stream-wise direction. In the particle-laden cases with relatively low Stokes number ($St = 5$), the peaks of $u_1^{\prime f}$ are slightly higher than in clear fluid flow case, and the effect of increasing particle aspect ratio is not clearly observed. In the cases with large Stokes number ($St = 30$),

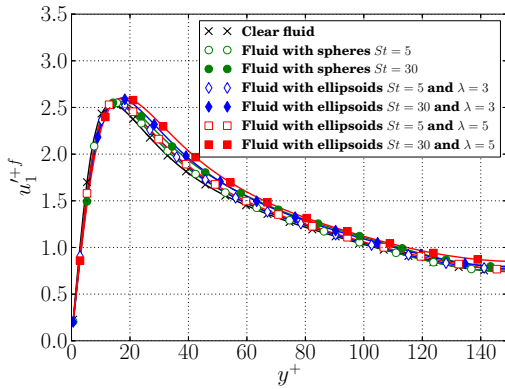


Figure 4.6.: Fluid RMS velocity in the stream-wise direction as a function of distance to the wall

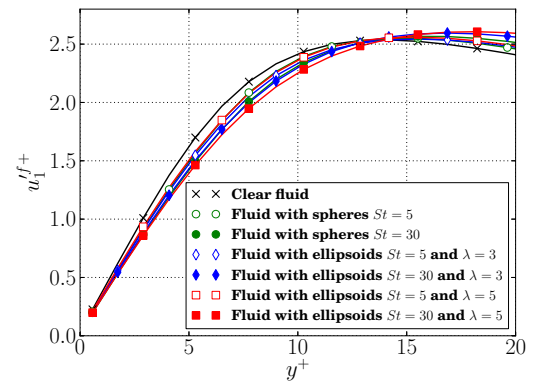


Figure 4.7.: Fluid RMS velocity in the stream-wise direction as a function of distance to the wall

the effect of the velocity gradient is dominant, and $u_1^{\prime f}$ therefore increases significantly between $15 < y^+ < 150$. Moreover, $u_1^{\prime f}$ further rises with increasing particle aspect ratio in these cases with $St = 30$. Thus the elongated shape of ellipsoids with high inertia can considerably strengthen the fluid-particle interactions and enhance the effect of the velocity gradient on the fluid RMS velocity in the stream-wise direction. As can be seen in Fig. 4.7, it is important to note that the large effects notwithstanding away from the wall, all profiles of $u_1^{\prime f}$ collapse in classic inner variables very close to the wall ($y^+ < 5$). This is consistent with the observation above that the particles have at most a very minimal effect

on the fluid viscosity, as might be expected in view of their very dilute concentrations. Obviously, the reasons for the changes at larger distances from the wall must lie elsewhere. Fig. 4.8 shows that the magnitude of the Reynolds stress decreases with increasing particle aspect ratio and Stokes number. The reduction of the Reynolds stress confirms that the

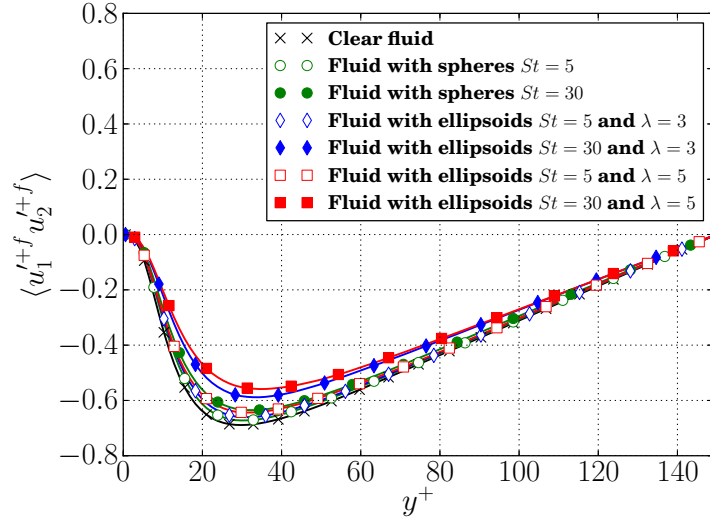


Figure 4.8.: Reynolds stress as a function of distance to the walls

flow turbulence is attenuated in the cases with large Stokes number, even in dilute flow conditions, and the elongated shape of non-spherical ellipsoids tends to further strengthen the turbulence modification. It should be also noted that the position of the minimum Reynolds stresses slightly shift towards the center of the channel as well as the peak points of fluid RMS velocities in the particle-laden cases.

4.3.2. The modulation of turbulence

To directly explore how dispersed particles influence the flow turbulence, all terms in the TKE equation are compared among different simulations. The TKE equation 1.12 is expressed in Sec. 1.3.3. For a fully developed solid-gas channel flow, equation 1.12 can be simplified and modified into equation 3.2.

4.3.2.1. Turbulence transport terms

On the left hand side of equation 3.2, the three transport terms (turbulence itself, the pressure fluctuations and viscous stresses) only transport the TKE from one location to another, but do not generate any TKE. Figs. 4.9 to 4.11 show these turbulence transport terms between $0 < y^+ < 60$. As shown in Fig. 4.11, the viscous transport term peaks at the wall and transports large amount of TKE to the wall. This is consistent with the largest value of the fluid dissipation rate at the wall, where the other three terms in equation 3.2 are all close to zero. The peak and minimum values of all three terms near

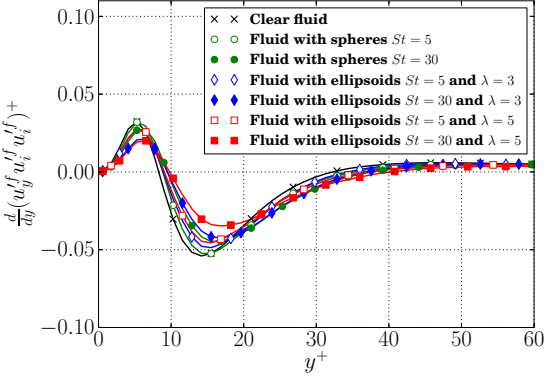


Figure 4.9.: TKE turbulence itself transport term as a function of distance to the wall

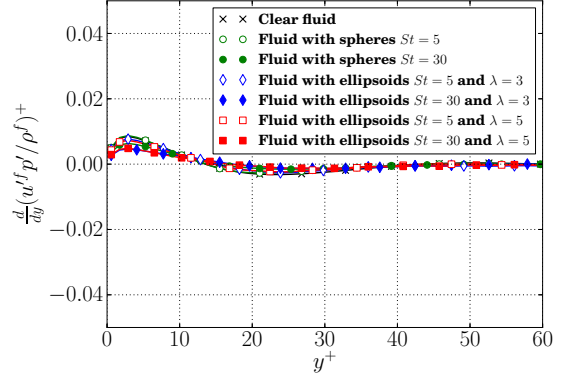


Figure 4.10.: TKE pressure fluctuation transport term as a function of distance to the wall

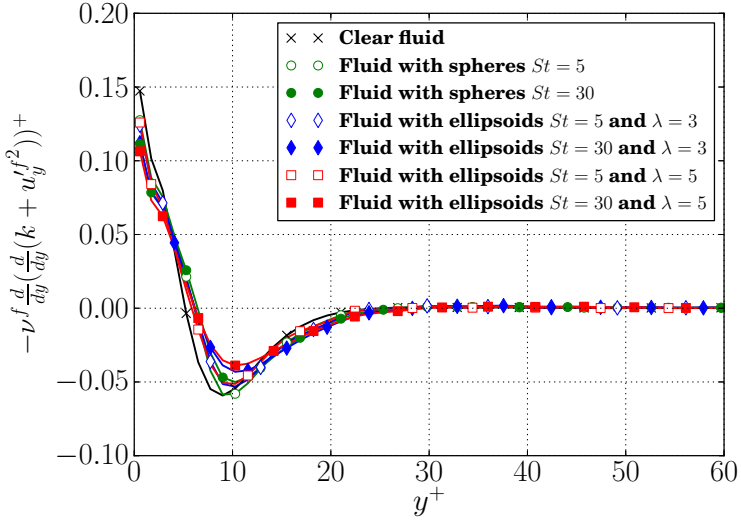


Figure 4.11.: TKE viscous transport term as a function of distance to the wall

the wall are slightly reduced, with the particles of increasing Stokes number and aspect ratio. In the region far away from the wall, $40 < y^+ < 150$, the pressure fluctuations and viscous transport terms in all simulations are almost zero, while the turbulence itself transport term is slightly larger than zero, around 0.005. These results indicate that the turbulence transport is weak in the central region of the channel. Finally, note that like all the preceding plots, the region closest to the wall collapses in classic wall variables using the fluid viscosity which are the same for all simulations. So clearly the effects on the turbulence cannot be related to a viscosity change.

4.3.2.2. The production of turbulence

Fig. 4.12 shows that the dimensionless turbulence production \mathcal{P}^+ rises steeply from zero at the wall to a peak value around $y^+ \approx 11$ to 15, and then smoothly drops to zero again towards the center of the channel. Like the preceding plots, the region very close to the

wall ($y^+ < 5$) collapses in inner variables, consistent with the observations above that the kinematic viscosity is unaffected by the particles. As the Stokes number rises, the peak

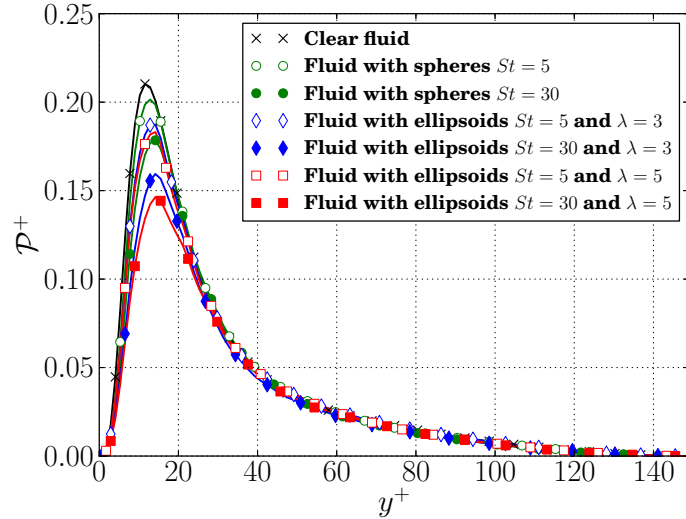


Figure 4.12.: The production of turbulence as a function of distance to the wall

value of \mathcal{P}^+ decreases from 0.2096 for the single phase case to 0.1455 for the ellipsoid-laden case with $\lambda = 5$ and $St = 30$. This shows that particles with high inertia reduce the turbulence production of the fluid flow. Similar to the velocity statistics, the peaks of the production slightly move towards the center of the channel. Furthermore, particles with large aspect ratio show lower values of \mathcal{P}^+ compared to particles with a smaller aspect ratio and the same Stokes number.

4.3.2.3. Dissipation terms

The minus fluid turbulence dissipation rate ($-\tilde{\varepsilon}^+$) is plotted in Fig. 4.13, in which $-\tilde{\varepsilon}^+$ has

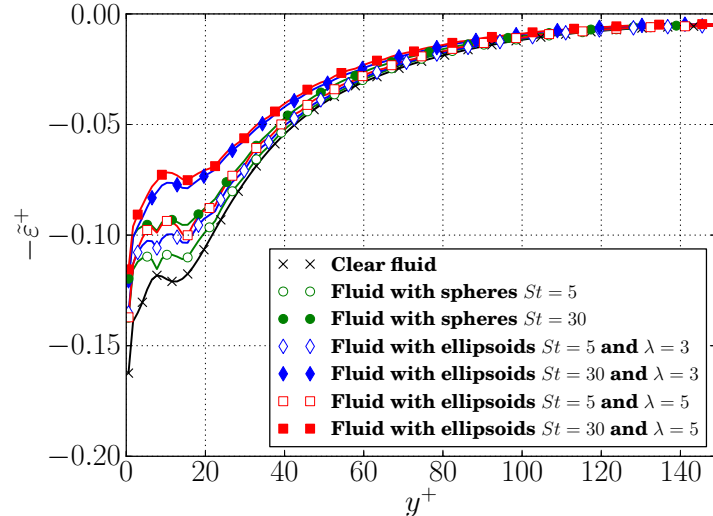


Figure 4.13.: The minus fluid flow dissipation rate as a function of distance to the wall

the largest magnitude at the wall and decreases towards the central region. In the near wall region, it is clearly observed that increasing Stokes number and particle aspect ratio contributes to an increase in the fluid dissipation rate. In addition, $-\tilde{\varepsilon}^+$ in all particle-laden cases tends to smoothly rise between $60 < y^+ < 150$ and reach almost the same small absolute value at the center of the channel. This behaviour very near the wall is quite remarkable, and nothing like the previous plots. It does not make sense that viscosity would be one thing for the dissipation, and something quite different for everything else. So clearly the effect of the particles is either to dissipate the energy directly (to make up the difference), or to change the turbulence structures doing the dissipation. It will be seen in the next paragraph that the particle dissipation is itself nearly insignificant. So the differences observed here must be directly related to changes in flow structures.

Fig. 4.14 shows the minus dissipation rate caused by the coupling force of the particles, $-\varepsilon_p$. In equation 3.3, $-\varepsilon_p$ is the value of the covariance of the particle-fluid interaction

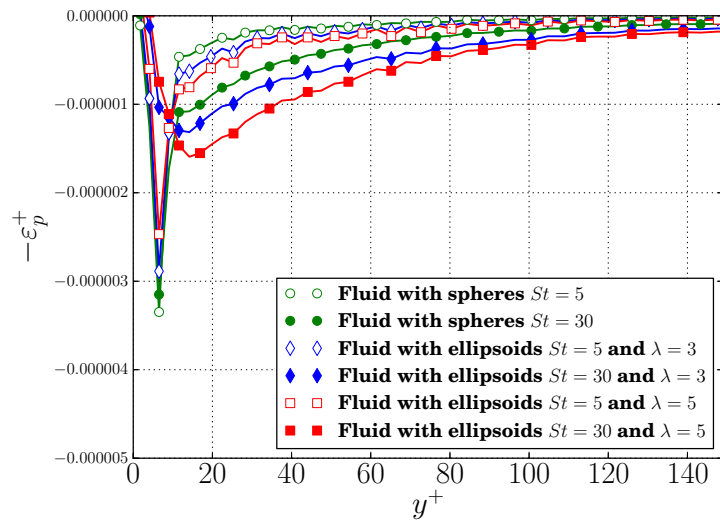


Figure 4.14.: The dissipation rate caused by the coupling force from particles as a function of distance to the wall

force fluctuations and fluid velocity fluctuations and is influenced by two factors: the local particle volume fraction and the slip velocity between the particles and the fluid. As the particles preferentially accumulate in the near wall region, $-\varepsilon_p$ peaks near the wall as shown in Fig. 4.14. The magnitude of ε_p is orders of magnitude smaller, compared to the fluid flow dissipation rate $\tilde{\varepsilon}$, and thus the contribution of ε_p to dissipate the flow turbulence is negligible. Therefore, the significant effect on the flow turbulence due to the two-way coupling between particles and the fluid flow is not directly attributable to the increased dissipation by the particles, *i.e.* ε_p . Nonetheless, the two-way coupling must be taken into account, since it has a dramatic effect on both the dissipative structures very near the wall, as well as those producing the turbulence kinetic energy near the peak in productions.

4.3.2.4. Components of the fluid flow turbulence dissipation

In view of the large effects on the near wall dissipation it is useful to examine whether and how the components of the dissipation and vorticity are affected by the particles. The expression for the fluid dissipation rate contains a total of twelve components (nine mean square derivative terms and three cross terms), and defined by equation 1.17:

$$\begin{aligned}\tilde{\varepsilon} = \nu [2(< u'_{1,1}^f > + < u'_{2,2}^f > + < u'_{3,3}^f >) \\ + (< u'_{1,2}^f > + < u'_{2,1}^f > + < u'_{1,3}^f > + < u'_{3,1}^f > + < u'_{3,2}^f > + < u'_{2,3}^f >) \\ + 2(< u'_{1,2}^f u'_{2,1}^f > + < u'_{1,3}^f u'_{3,1}^f > + < u'_{2,3}^f u'_{3,2}^f >)]\end{aligned}$$

Only three components, $< u'_{1,2}^f >$, $< u'_{3,2}^f >$ and $< u'_{1,3}^f >$, mainly contribute to $\tilde{\varepsilon}$, whereas the other nine components are significantly smaller than these three. Figs. 4.15 to 4.17 show the three main components in the fluid dissipation rate for the various cases. Strikingly different from all the plots above are the dramatic effects very close to the wall, especially for $< u'_{1,2}^f >$ and $< u'_{3,2}^f >$, which do not collapse in classical viscous variables. The effects over the rest of the flow mirror those of the dissipation as a whole and the production, with large effects near the kinetic energy peak near $y^+ = 11$. These can only be explained by a change in turbulence structure due to the presence of particles. In

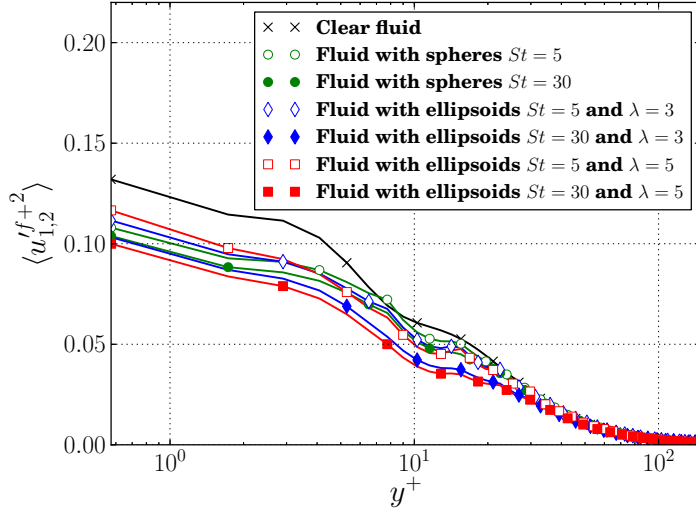


Figure 4.15.: Mean-square derivative $< u'_{1,2}^{f+2} >$ as a function of distance to the wall

Figs. 4.15 and 4.17, both $< u'_{1,2}^{f+2} >$ and $< u'_{3,2}^{f+2} >$ decrease within $y^+ < 5$ when particles are added to the flow. The combination of these reductions results in a decrease in the magnitude of $\tilde{\varepsilon}$ the linear sublayer, as can be seen from Fig. 4.13. The local peak and minimum values of $\tilde{\varepsilon}$ in buffer layer are obviously caused by the rise in $< u'_{1,3}^{f+2} >$ and $< u'_{3,2}^{f+2} >$ in the region of $5 < y^+ < 15$. Around $y^+ = 10$, the deflection of $< u'_{1,2}^{f+2} >$ and the peak of $< u'_{1,3}^{f+2} >$ are results of the “low-speed” streaks in the near wall region. For particle-laden cases, all the components of the fluid turbulence dissipation decrease as the particle inertia and aspect ratio increase in the near wall region, but these effects are not

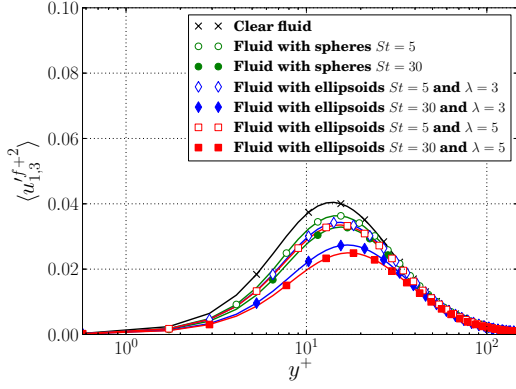


Figure 4.16.: Mean-square derivative $\langle u_{1,3}^{f+2} \rangle$ as a function of distance to the wall

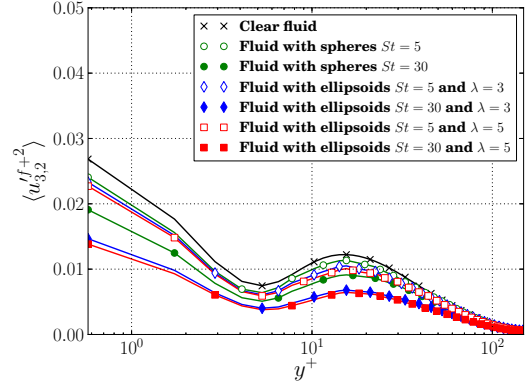


Figure 4.17.: Mean-square derivative $\langle u_{3,2}^{f+2} \rangle$ as a function of distance to the wall

important in the region between $80 < y^+ < 150$.

In the literature, the fluid flow dissipation rate, the mean square vorticity and their components are widely reported for a single phase fluid channel flow, *e.g.* [4, 5, 39, 54, 55], and the assumption of local isotropy and local axisymmetric turbulence in the channel center were also discussed. This study explores these assumption for the gas-solid turbulent flow. The isotropic dissipation rate of the fluid, $\tilde{\varepsilon}_{iso}$, is defined by equations 1.18 and 1.19, and the fluid homogeneous dissipation rate $\tilde{\varepsilon}_{hom}$ is determined by equation 1.20. $\tilde{\varepsilon}_{hom}$ does not contain the three cross-terms, which are cancelled out by less $\langle u_{1,1}^{f+2} \rangle + \langle u_{2,2}^{f+2} \rangle + \langle u_{3,3}^{f+2} \rangle$.

The local axisymmetric turbulence for single phase flow is reported and discussed in earlier studies [39, 55]. If it is assumed that the axis of local symmetry is the stream-wise direction, two of many axisymmetric dissipation rates are given by equations 1.21 and 1.22.

Figs. 4.18 to 4.21 show the ratios of $\tilde{\varepsilon}_{iso}$, $\tilde{\varepsilon}_{hom}$, $\tilde{\varepsilon}_{axis_1}$ and $\tilde{\varepsilon}_{axis_2}$ to $\tilde{\varepsilon}$ as a function of position in the flow channel. For all particle-laden cases, these ratios are in good agree-

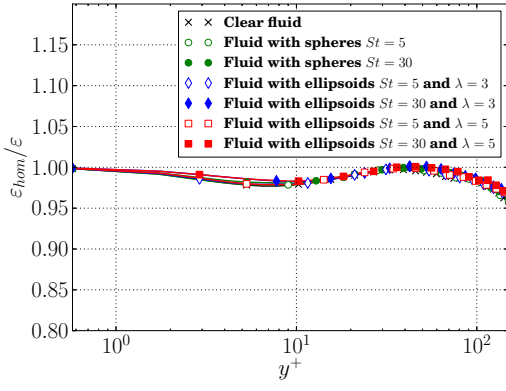


Figure 4.18.: The ratio of homogeneous dissipation rate ($\tilde{\varepsilon}_{hom}$) to the fluid dissipation rate ($\tilde{\varepsilon}$) as a function of distance to the wall

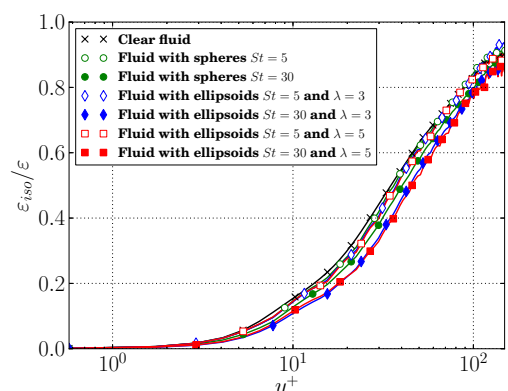


Figure 4.19.: The ratio of isotropic dissipation rate ($\tilde{\varepsilon}_{iso}$) to the fluid dissipation rate ($\tilde{\varepsilon}$) as a function of distance to the wall

ment with the curve of clear fluid case. It seems that dispersed particles do not change the relationship between these modelled dissipation rates and the original dissipation rate. This is probably due to the fact that the high particle inertia and elongated shape have

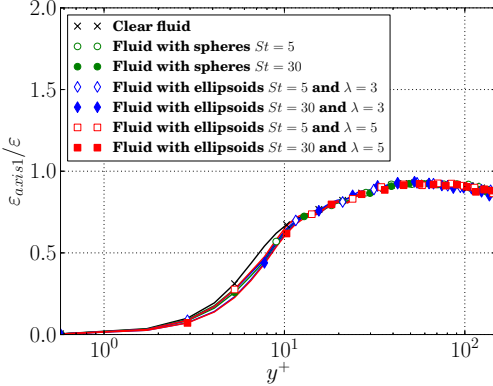


Figure 4.20.: The ratio of the axisymmetric dissipation rate 1 ($\tilde{\varepsilon}_{axis1}$) to the fluid dissipation rate ($\tilde{\varepsilon}$) as a function of distance to the wall

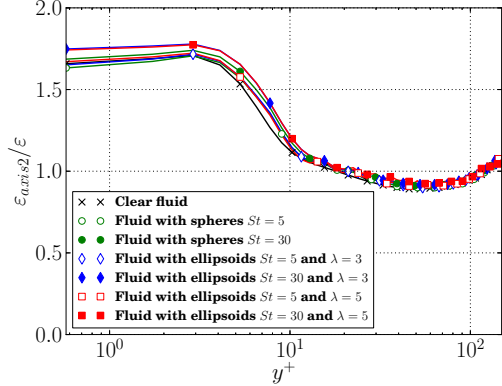


Figure 4.21.: The ratio of axisymmetric dissipation rate 2 ($\tilde{\varepsilon}_{axis2}$) to the fluid dissipation rate ($\tilde{\varepsilon}$) as a function of distance to the wall

almost the same effects on each component of $\tilde{\varepsilon}$ throughout the channel.

4.3.3. Vorticity

The flow mean square vorticity ω^f is defined as the curl of the fluid velocity fluctuation by equation 1.23. Similar to the fluid dissipation rate $\tilde{\varepsilon}$, only three components $\langle u_{1,2}^f \rangle^2$, $\langle u_{3,2}^f \rangle^2$ and $\langle u_{1,3}^f \rangle^2$ are dominant in the vorticity. As illustrated in Figs. 4.22 to

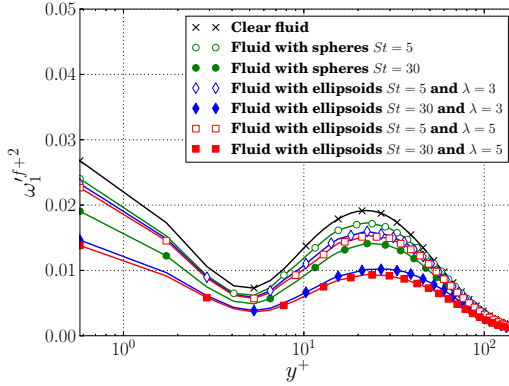


Figure 4.22.: The mean square vorticity in the stream-wise direction as a function of distance to the wall

4.24, the curves of each vorticity component ω_1^f , ω_2^f and ω_3^f are similar to $\langle u_{3,2}^f \rangle^2$, $\langle u_{1,3}^f \rangle^2$ and $\langle u_{1,2}^f \rangle^2$ respectively, but slightly larger than these mean-square velocity derivatives. This is due to the negative contribution of the cross-terms to ω_i^f . The effects of particle inertia and aspect ratio on the vorticity are also as the same as these effects

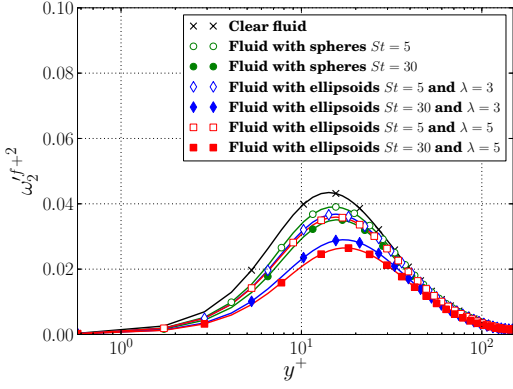


Figure 4.23.: The mean square vorticity in the wall-normal direction as a function of distance to the wall

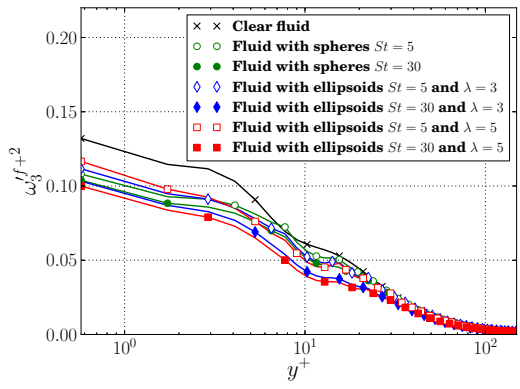


Figure 4.24.: The mean square vorticity in the span-wise direction as a function of distance to the wall

on the three main dissipation rate components. In the near wall region of $0 < y^+ < 30$, each vorticity component in the particle-laden cases decreases with the increasing particle inertia and aspect ratio.

4.4. Contour plots of instantaneous fluid velocities

Figs. 4.25 and 4.26 show the instantaneous fluid velocity with particles in the wall-normal direction (u_2^f) in the cross-sectional y-z plane at $x^+ = 942$ for the case considering spheres with $St = 5$ and the case considering ellipsoids with $St = 30$ and $\lambda = 5$, respectively. The

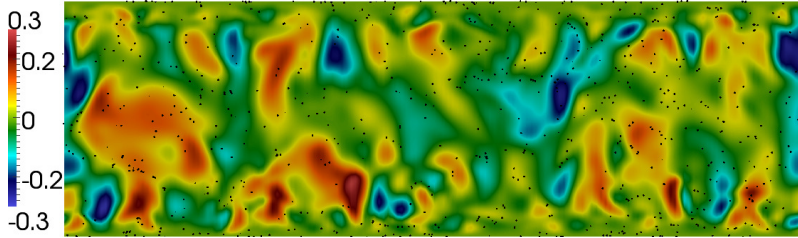


Figure 4.25.: The instantaneous fluid velocity (indicated by colour) in the wall-normal direction and the distribution of spherical particles with $St = 5$ near the cross-sectional y-z plane at $x^+ = 942$

black dots represent the small particles around the plane. Comparing these two figures, it is clearly observed that the size and number of the high speed areas (red circle zones) decrease with increasing particle inertia and aspect ratio, and particles spend less time in these high speed areas.

Figs. 4.27 and 4.28 show the contour plots of the fluid velocity with particles in the stream-wise direction (u_1^f) in the x-z plane at $y^+ = 8$. In these two figures, the blue regions, *i.e* low fluid velocity areas, represent the low-speed streaks in the channel flow. This feature is clearly seen in both cases with spheres and ellipsoids. As particle inertia and aspect

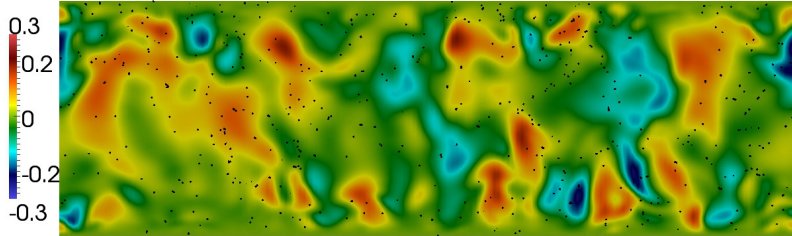


Figure 4.26.: The instantaneous fluid velocity (indicated by colour) in the wall-normal direction and the distribution of ellipsoids with $St = 30$ and $\lambda = 5$ near the cross-sectional y-z plane at $x^+ = 942$

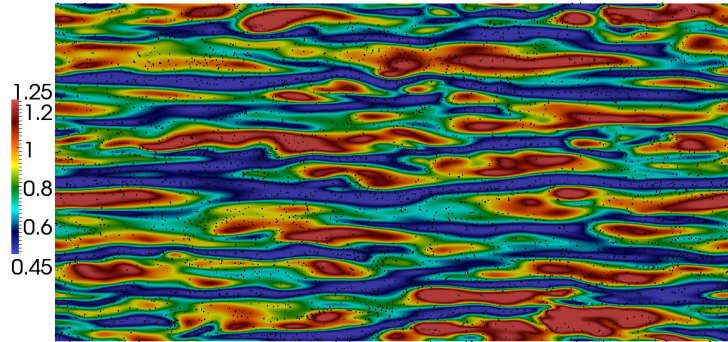


Figure 4.27.: The instantaneous fluid velocity (indicated by colour) in the stream-wise direction and the distribution of spherical particles with $St = 5$ near the cross-sectional x-z plane at $y^+ = 8$

ratio rises, the low-speed streaks become wider and more distinct. Between the low-speed streaks, the fluid moves relatively faster (dark red zones). In the near wall region of a turbulent channel flow, fluid flow in a low-speed streak slowly moves away from the wall with increasing downstream distance, but at some areas in the streak, the flow moves rapidly away from the wall. This process is referred as a lifting process [57], or known as bursting. On the other hand, the fluid flow in the large and long vortices in the high speed areas moves towards the wall, called sweeps [21]. Due to the small particle size and volume fraction, the particle distribution cannot be clearly seen in these contour plots.

Table 4.2 shows the portion of particles and fluid flow in the low-speed areas around $y^+ = 8.0$ in the cases with various Stokes number and particle aspect ratio. The low-speed fluid flow accounts for around 52% to 53% in the x-z plane at $y^+ = 8.0$ in all simulations, while over 60% of the particles near the x-z plane at $y^+ = 8.0$ are found in the low-speed streaks. This indicates that particles spend more time in the low-speed streaks than in the high speed eddy zones, and this phenomena is not affected significantly by Stokes number and particle aspect ratio. This is in good agreement with Goto and Vassilicos [43] in homogeneous turbulence.

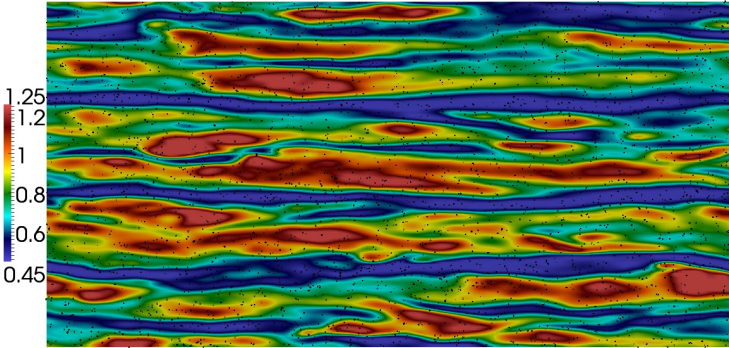


Figure 4.28.: The instantaneous fluid velocity (indicated by colour) in the stream-wise direction and the distribution of ellipsoids with $St = 30$ and $\lambda = 5$ near the cross-sectional x-z plane at $y^+ = 8$

Case with	The area of low-speed fluid flow ($u_1^f - U_1^f < 0$) at $y^+ = 8.0$	Particles in the low speed area around $y^+ = 8.0$
sphere ($St = 5 \lambda = 1$)	53.1%	65.60%
sphere ($St = 30 \lambda = 1$)	53.2%	65.8%
ellipsoid ($St = 5 \lambda = 3$)	52.1%	64.75%
ellipsoid ($St = 30 \lambda = 3$)	52.0%	64.4%
ellipsoid ($St = 5 \lambda = 5$)	53.4%	69.4%
ellipsoid ($St = 30 \lambda = 5$)	52.3%	59.8%

Table 4.2.: The portion of particles in the low-speed streaks around $y^+ = 8.0$

4.5. Particle statistics

In order to sample and analyse the statistics of the particles in the channel, the channel is divided into 100 equally spaced bins in the wall-normal direction. In which bin a particle is located is determined by the position of the center of mass.

4.5.1. Particle distribution

The ratio of the local particle volume fraction $\langle \alpha_y^p \rangle$ in the wall-normal direction to the averaged particle volume fraction $\langle \alpha_n^p \rangle$ of the whole channel is shown in Figs. 4.29 and 4.30 for the various cases as a function of distance to the wall. As expected, particles with high inertia accumulate in the near wall region ($0 < y^+ < 10$), and the ratio $\langle \alpha_y^p \rangle / \langle \alpha_n^p \rangle$ peaks around 2 – 7 close to the wall. This is because the large and long vortices sweep both the fluid and particles towards the wall, whereas the particles with relatively high inertia ($1 \ll St \ll \infty$) cannot follow the fluid burst which rapidly

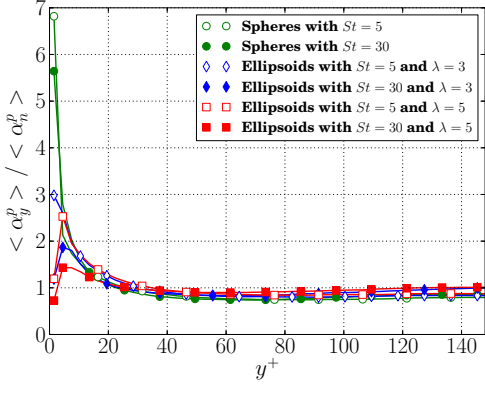


Figure 4.29.: The ratio of the particle volume fraction $\langle \alpha_y^p \rangle$ in the wall-normal direction to averaged particle volume fraction $\langle \alpha_n^p \rangle$ of the whole channel as a function of distance to the wall

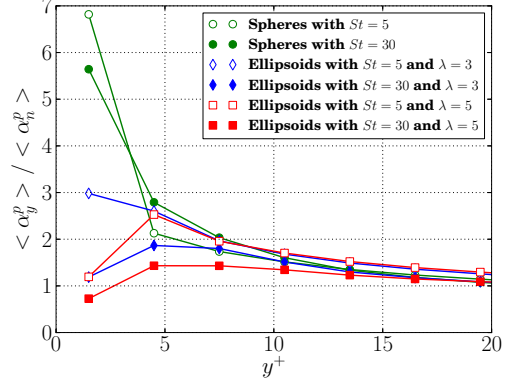


Figure 4.30.: The ratio of the particle volume fraction $\langle \alpha_y^p \rangle$ in the wall-normal direction to averaged particle volume fraction $\langle \alpha_n^p \rangle$ of the whole channel in the near wall region

move fluid away from the wall in the low-speed areas near the wall. The combination of these two effects is the main mechanism by which particles preferentially accumulate in the near wall region. In the gas-solid channel flow, not only the fluid bursts are slowed, but also the fluid sweeps are reduced since the inflow of fluid toward the wall must balance the outflow (to satisfy mass conservation). The solid particles have no such conservation law, so can accumulate. For spherical particles, the ratio reaches the largest value, 6.83 directly next to the wall for $St = 5$ spheres and moderately lower to 5.54 for $St = 30$. This, as noted above, is because particles with sufficiently high inertia ($St = 30$) attenuate turbulence intensity and weaken vortices. Furthermore, particles with considerably high inertia can strongly resist the effect of turbulence on them. Therefore, fewer particles with $St = 30$ accumulate near the wall, compared to the case with relatively low inertia spheres ($St = 5$). Next to the wall, particle-wall collisions force the mass center of ellipsoids to lie farther away from the wall than for spheres. This is because the non-sphericity of the ellipsoid hitting the wall can acquire angular momentum, whereas a sphere can only bounce. Therefore, as can be seen from Fig. 4.30, the position of peak $\langle \alpha_y^p \rangle$ is slightly farther from the wall for ellipsoidal particles. As the elongated shape of ellipsoids with high inertia strongly resists the effect of turbulence on the ellipsoids, the peak value of $\langle \alpha_y^p \rangle$ decreases with increasing ellipsoid aspect ratio. For cases with $St = 5$, the peak of the ratio decreases from 6.83 for spheres to 2.5 for ellipsoids of $\lambda = 5$, while it drops from 5.52 to 2.0 for the cases with particles of $St = 30$. Small particles accumulating near the wall strongly affect the fluid turbulence in the near wall region.

4.5.2. Particle velocity

Fig. 4.31 displays particle mean velocities (U_1^p) in the direction of the fluid flow for the various types of particles as a function of distance to the wall. Between $20 < y^+ < 150$,

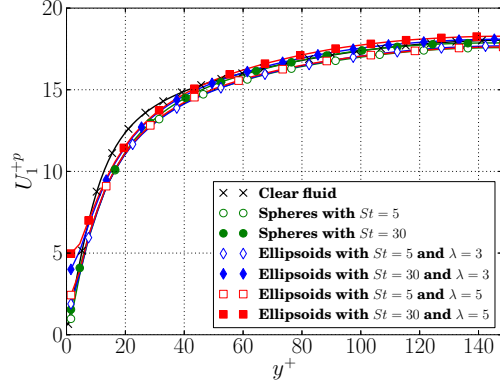


Figure 4.31.: Particle mean velocity in the flow direction as a function of distance to the wall

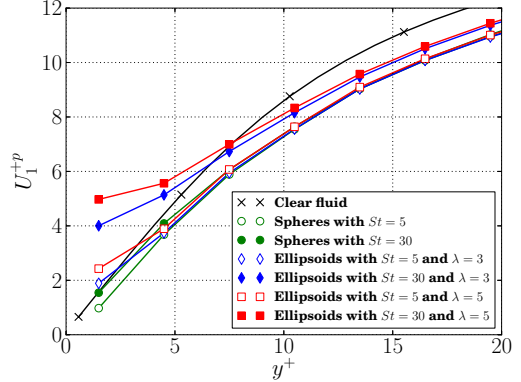


Figure 4.32.: Particle mean velocity in the flow direction in the near wall region

the curves of U_1^p in particle-laden cases are quite similar to their fluid mean velocities as shown in Fig. 4.1. However, in the near wall region ($0 < y^+ < 10$), particles with $St = 30$ are moving on average significantly faster than the relatively low inertia particles with $St = 5$, and the elongated shape also increases U_1^p in the cases with the same particle inertia, as illustrated in Fig. 4.32.

The particle RMS velocities are shown in Figs. 4.33 to 4.35. In the near wall region

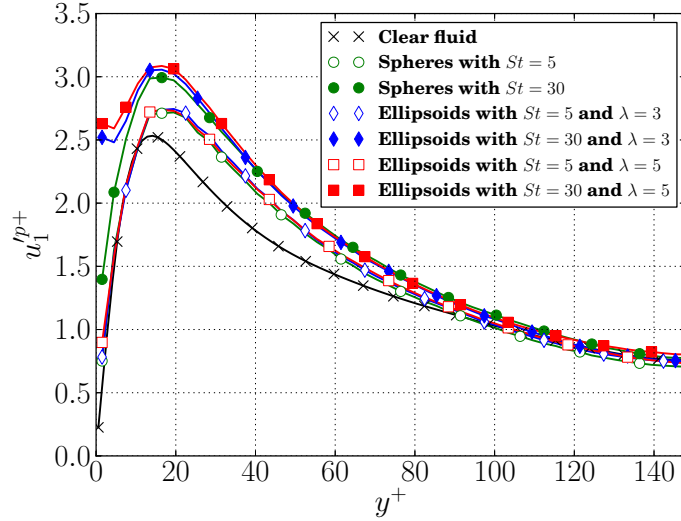


Figure 4.33.: Particle RMS velocity in the stream-wise direction as a function of distance to the wall

($0 < y^+ < 10$), it is clearly observed that the elongated shape of ellipsoids increases the particle velocity fluctuations. This is most likely because the collisions between non-spherical ellipsoids and the walls increase the particle velocity fluctuations in the near

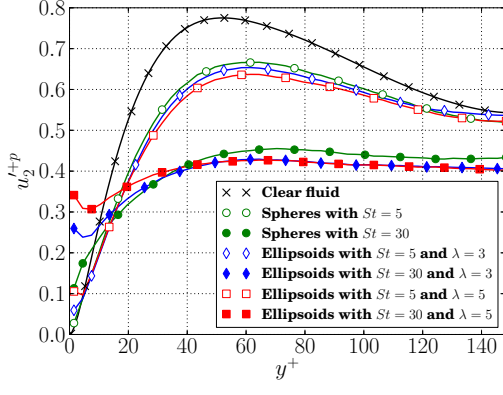


Figure 4.34.: Particle RMS velocity in the wall-normal direction as a function of distance to the wall

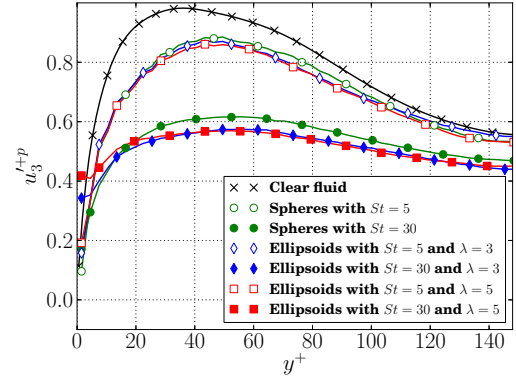


Figure 4.35.: Particle RMS velocity in the span-wise direction as a function of distance to the wall

wall region. Moreover, particles with high inertia (large Stokes number) considerably strengthen this particle-wall collision effect. In the outer region ($10 < y^+ < 150$), the effect of the particle aspect ratio is quite weak, and only a slight increase in $\mathbf{u}_1'^p$ and decrease in $\mathbf{u}_2'^p$ and $\mathbf{u}_3'^p$ are observed in Figs. 4.33 to 4.35. In the stream-wise direction, the large velocity gradient and slip velocity between the two phases significantly strengthen the momentum transfer, thus increasing both fluid and particle stream-wise RMS velocities. Without the effects of non-slip conditions and viscosity on discrete particles, the magnitudes of particle stream-wise velocity fluctuations is significantly larger than those for the fluid phase in the outer region ($10 < y^+ < 150$), comparing Fig. 4.33 to Fig. 4.6. In the wall-normal and span-wise directions, particles with high inertia can strongly resist the effects of fluid turbulence. As a result, the particle velocity fluctuations in these two directions are much smaller than the fluid fluctuations between $10 < y^+ < 150$. As expected, these phenomena are considerably enhanced with increasing particle inertia.

4.5.3. Velocity correlation coefficients between fluid and particle phases

The relationship between the fluid flow velocities and particle velocities plays an important role in determining the interactions between the two phases. Figs. 4.36 and 4.37 show the velocity correlation coefficients for the stream-wise and wall-normal directions, $\hat{\rho}_1^{fp}$ and $\hat{\rho}_2^{fp}$, which are defined as:

$$\hat{\rho}_i^{fp} = \frac{\langle u_i'^f @ p u_i'^p \rangle}{\left[\langle u_i'^f @ p^2 \rangle \langle u_i'^p^2 \rangle \right]^{\frac{1}{2}}} \quad (4.2)$$

There are two major factors affecting the velocity correlations: particle inertia and particle collisions. Particles with high inertia have a low correlation with the flow behaviour. Therefore, the velocity correlations of particles with $St = 30$ are significantly lower than those of particles with $St = 5$, as shown in Figs. 4.36 and 4.37. At the wall, the particle-

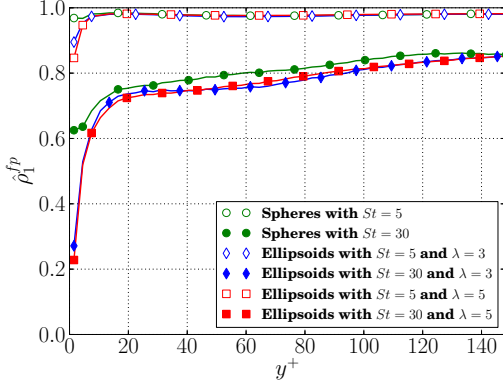


Figure 4.36.: The stream-wise correlation coefficient of particle and fluid velocities as a function of distance to the wall

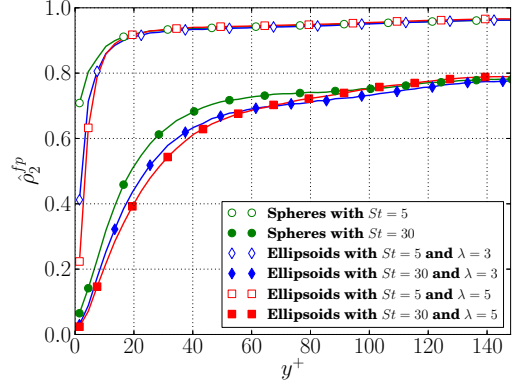


Figure 4.37.: The span-wise correlation coefficient of particle and fluid velocities as a function of distance to the wall

wall collision gives rise to complex dynamics of particles so that $\hat{\rho}^{fp}$ drops quickly in the near wall region. As the high inertia of the particles can enhance the effect of collisions, the velocity correlations resulting from the cases with particles of $St = 30$ are much lower compared to cases with $St = 5$ in the near wall region. Furthermore, the elongated shape of non-spherical ellipsoids tend to have a high particle-wall collision frequency and complex particle dynamics; therefore, the correlations between the particle and fluid velocities near the wall are considerably reduced with increased particle aspect ratio. Fig. 4.36 shows that $\hat{\rho}_1^{fp}$ in the case considering ellipsoids with $St = 30$ and $\lambda = 5$ reaches a minimum around 0.229 next to the wall. As shown in Fig. 4.37, the effects of combining the two factors are even stronger on the span-wise velocity correlation $\hat{\rho}_2^{fp}$, which is close to zero at the wall in the cases considering ellipsoidal particles of $St = 30$. The low values of the velocity correlation coefficients near the wall indicate that velocities of the two phases are statistically independent.

4.5.4. Mean slip velocities between the fluid flow and dispersed particles

Figs. 4.38 to 4.40 show the mean slip velocity between the fluid flow and particles in each of the three directions. Fig. 4.38 shows the slip velocity in the stream-wise direction. Apparently, particles add momentum to the fluid flow in the near wall region ($0 < y^+ < 20$), but obtain momentum from the flow in the outer region ($20 < y^+ < 150$). With increasing Stokes number, the negative stream-wise slip velocity between $0 < y^+ < 20$ decreases, whereas the positive slip velocity rises in the outer region. Near the wall, the magnitude of slip velocity in the stream-wise direction rises as the particle aspect ratio increases. This arises from the complex dynamics of ellipsoids, which are caused by the particle-wall collision. However, the effect of the particle shape does not have much effect in the region between $20 < y^+ < 150$.

As illustrated in Fig. 4.39, the mean slip velocity in wall-normal direction is almost zero in the region of $60 < y^+ < 150$, but it is positive within $0 < y^+ < 60$, peaking at 0.04

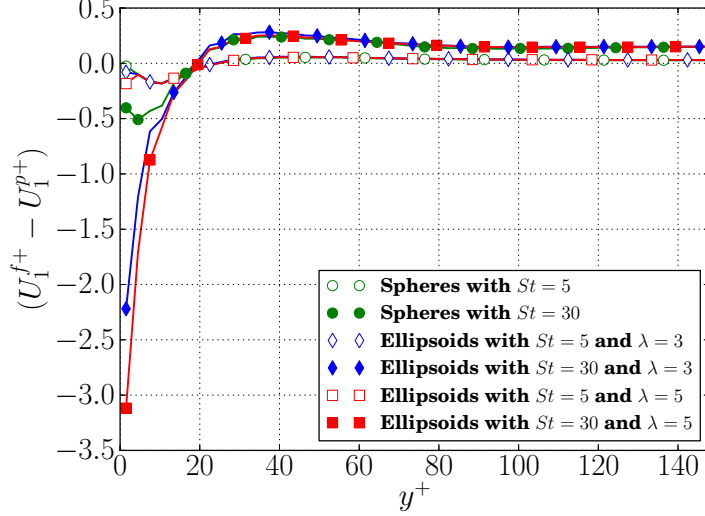


Figure 4.38.: Mean stream-wise slip velocity between dispersed particles and the fluid flow as a function of distance to the wall

around $y^+ = 19$. The positive wall-normal slip velocity indicates that the fluid flow sweeps

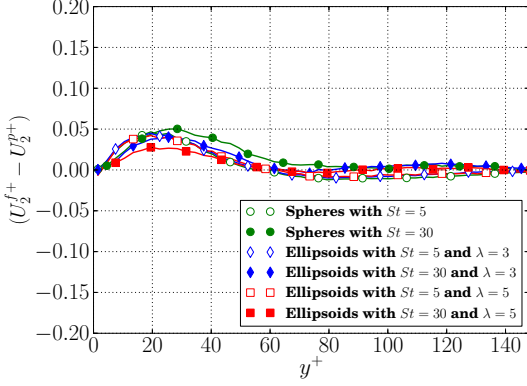


Figure 4.39.: Mean wall-normal slip velocity between dispersed particles and the fluid flow as a function of distance to the wall

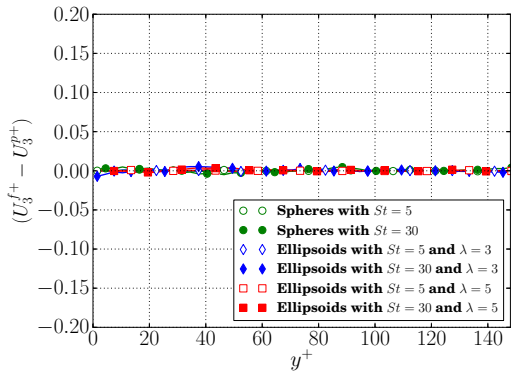


Figure 4.40.: Mean span-wise slip velocity between dispersed particles and the fluid flow as a function of distance to the wall

particles to the wall when particles travel to the wall, but it delays the particle when they reversely move back towards central region. These reflect the main mechanism of particle accumulation in the near wall region. It should be noted that the variance of particle inertia and aspect ratio does not influence the wall-normal slip velocity as well as the span-wise slip velocity. Fig. 4.40 shows that the span-wise slip velocity is close to zero through the whole channel. Therefore, the average momentum transfer in the span-wise direction is negligible.

4.5.5. The angular velocity of particles

The particle angular velocity is determined by the external torques, which are caused by the hydrodynamic interactions and the collisions of particle-particle and particle-wall. As shown in Fig. 4.41, the magnitude of the mean span-wise angular velocity of particles

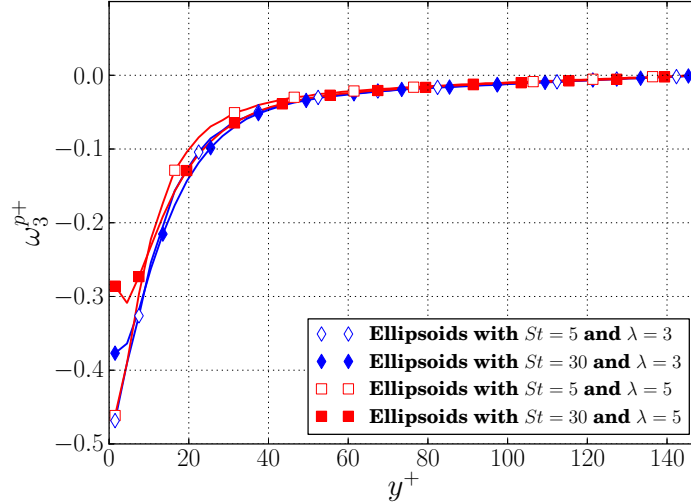


Figure 4.41.: The mean particle angular velocity in the span-wise direction as a function of distance to the wall

peaks at the wall, rapidly decreases to $y^+ \approx 40$ and then gradually decreases to zero at the channel center. In the near wall region ($0 < y^+ < 10$), the lighter particles ($St = 5$) spin quite fast compared to heavier particles ($St = 30$). This phenomena was also observed in [76]. The rotation of particles is determined by the hydrodynamic and collision torques. In the linear sublayer, the fluid velocity gradient has its highest value and almost has the same value for the particle-laden simulations. This gives rise to a large span-wise hydrodynamic torque in all cases. Therefore, the particles with low inertia ($St = 5$) spin faster than the particles with $St = 30$ in the very near wall region ($0 < y^+ < 10$). In the stream-wise and wall-normal directions, however, the particle mean angular velocities are almost zero throughout the channel.

4.5.6. The orientation of ellipsoidal particles

The orientation of non-spherical particles in the channel flow strongly affects particle-fluid interactions. In the previous studies [71, 77, 108], which neglected the effect of collisions and effects of particles on fluid flow, the particle orientation was described by the mean absolute values of direction cosines. However, the non-linear cosine function may underestimate or overestimate the interpolation of the effect of the orientation angles. Therefore, this chapter directly analyses the mean orientation angles (θ_i) of particles between the vector of particle major axis (\mathbf{X}^p) aligning with the x axis of body space and axes of world space, as depicted in Fig. 4.42. As shown from Figs. 4.43 to 4.45, all three orientation angles θ_i vary between 0° and 90° , and they are correlated with each other. Moreover, their

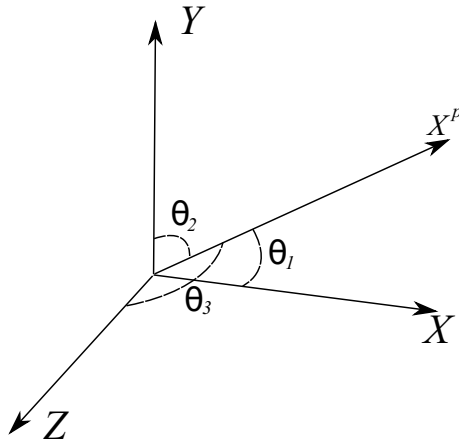


Figure 4.42.: Three orientation angle θ_i between three axes of world space and the vector of the ellipsoid major axis \mathbf{X}^p , which aligns with the x axis of body space, in world space.

sum must always equal to 180° . As a result, a random distribution of particle orientation would lead to mean orientation angles of 60° , not the mid-value of 45° .

Fig. 4.43 shows that the mean angle (θ_3) in the span-wise direction peaks near the wall, between 73° and 85° for the various ellipsoids. The large value of θ_3 in the near wall region

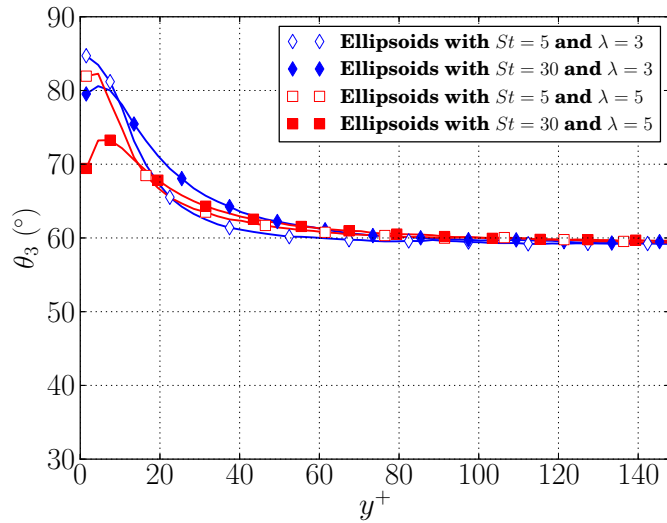


Figure 4.43.: Mean orientation angle θ_3 between particle Major axis vector x^p and z axis of world space as a function of distance to the wall

implies that the ellipsoids tend to on average align in the x - y plane and perpendicular to the span-wise direction. This phenomenon arises from the large fluid velocity gradients in the wall-normal direction in the near wall region. Particles with high inertia are less affected by the fluid flow compared to particles with lower inertia, and thus the peak of θ_3 for ellipsoids with $St = 30$ is lower than for particles with low particle inertia ($St = 5$). Furthermore, increasing the aspect ratio of the ellipsoids reduces the peak of θ_3 , most likely due to the more complex particle dynamics caused by the particle-wall collisions. As shown in Fig. 4.44, the stream-wise mean angle θ_1 of the ellipsoids reaches a minimum

value in the buffer layer. As the Stokes number rises, the minimum value of θ_1 increases. On the other hand, the mean angle θ_2 in the wall-normal direction shown in Fig. 4.45

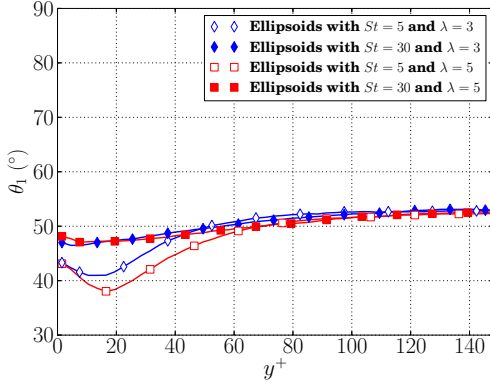


Figure 4.44.: Mean orientation angle θ_1 between particle major axis x^p and x axis of world space as a function of distance to the wall

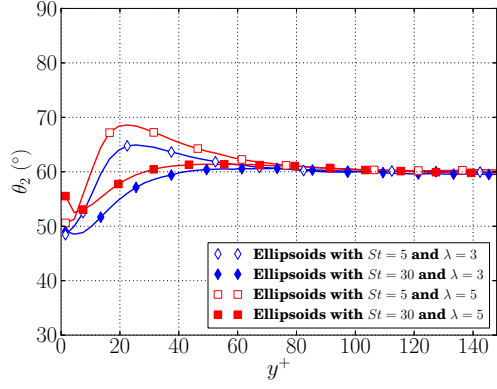


Figure 4.45.: Mean orientation angle θ_2 between particle major axis x^p and y axis of world space as a function of distance to the wall

peaks in the buffer layer, around $y^+ \approx 20$, for ellipsoids with $St = 5$. For the $St = 30$ cases, θ_2 gradually rises from the wall to the central region. It should be noted that both effects of the Stokes number and particle aspect ratio do not influence the mean angles θ_i in the outer region ($60 < y^+ < 150$), as illustrated from Figs. 4.43 to 4.45. θ_i remains around 60° in wall-normal and span-wise directions and 53° in stream-wise direction in the central region of the channel. Although the mean angles at channel center are close to 60° , this does not suffice to conclude that the ellipsoids are randomly distributed. The distribution of these angles need to be further analysed.

The frequency of the orientation angles at different locations provides another way of analysing the orientation of particles by directly showing how orientation angles are distributed at a particular position in the channel. The distributions of the orientation angles

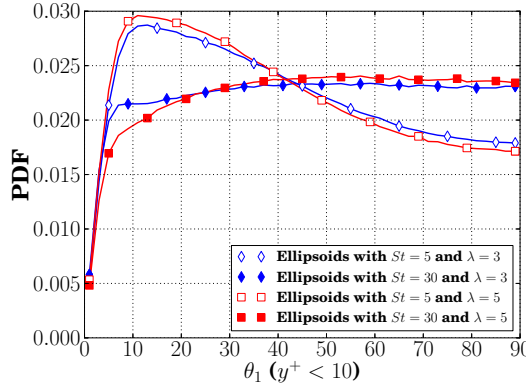


Figure 4.46.: The distribution of θ_1 in the near wall region ($y^+ < 10$).

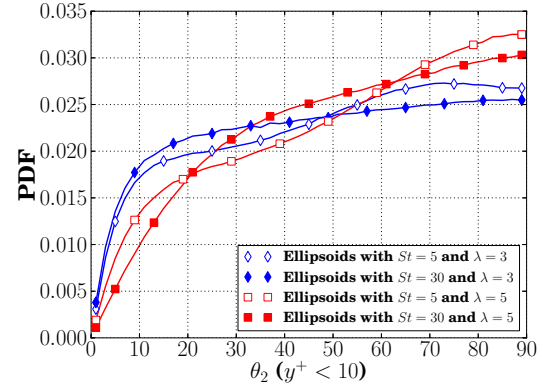


Figure 4.47.: The distribution of θ_2 in the near wall region ($y^+ < 10$).

θ_i in the near wall region ($0 < y^+ < 10$) and at channel center are shown from Figs. 4.46

to 4.51. Fig. 4.48 displays that high possibility of θ_3 in the near wall region ($0 < y^+ < 10$)

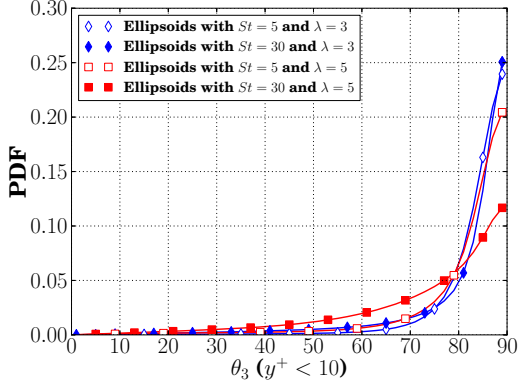


Figure 4.48.: The distribution of θ_3 in the near wall region ($y^+ < 10$).

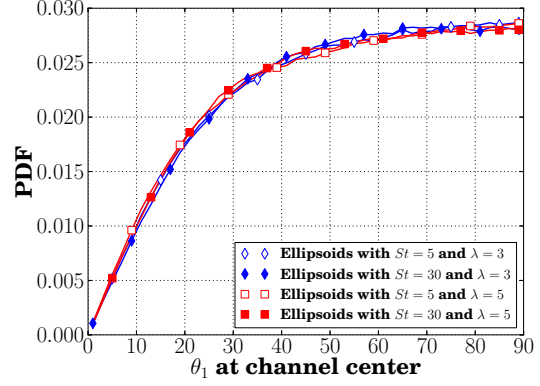


Figure 4.49.: The distribution of θ_1 at channel center.

is found between 80° and 90° , peaking at 90° . This confirms that the ellipsoids align in the x-y plane. Figs. 4.49 to 4.51 show that all three angles have similar distributions in the channel center and that their probability density functions (pdf's) increase from 0° to 90° , not uniformly distributed. However, as orientation angles in all directions are correlated

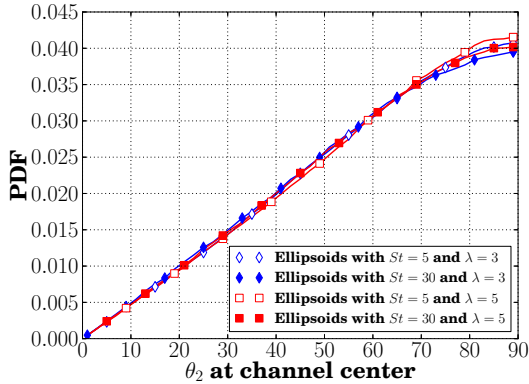


Figure 4.50.: The distribution of θ_2 at channel center.

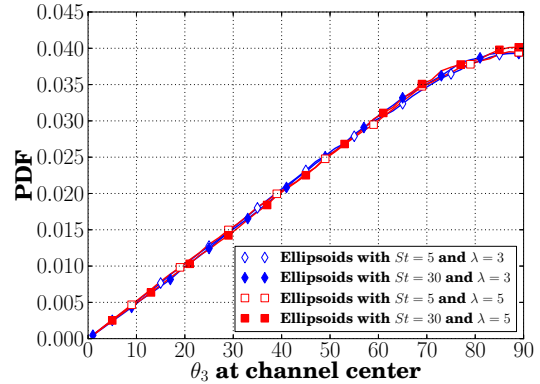


Figure 4.51.: The distribution of θ_3 at channel center

with each other, these results of the angle distribution do not imply that ellipsoids are randomly distributed in the central region of the channel, nor that they have a preferential orientation.

To precisely analyse the orientation of ellipsoidal particles, another method is proposed here. The particle major axis vector \mathbf{x}^p , can be projected on three planes: y-z, x-z and x-y planes, which are the planes perpendicular to the x, y and z axis of world space, respectively. In each plane, the orientation of each 2-D projected vector x_{jk}^p can be represented by an angle, ψ_i , between the projected vector and one axis of world space, as depicted in Fig. 4.52. ψ_i varies between 0° and 180° and can be expressed as

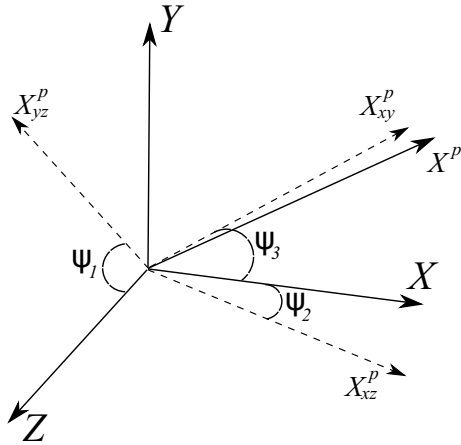


Figure 4.52.: The particle major axis \mathbf{x}^p projects on the y-z, x-z and x-y planes, leading to three 2-D vectors x_{yz}^p , x_{xz}^p and x_{xy}^p . The angles ψ_i represent the angles between the 2-D vectors x_{yz}^p , x_{xz}^p and x_{xy}^p and the z, x and y axes of world space.

$$\begin{aligned}\psi_1 &= \arctan(X_y^p/X_z^p) \\ \psi_2 &= \arctan(X_z^p/X_x^p) \\ \psi_3 &= \arctan(X_y^p/X_x^p)\end{aligned}\tag{4.3}$$

Although ψ_i only represents the orientation of the projected 2-D vector and loses one degree of the particle orientation, the three components ψ_i together contain all information of the complete particle orientation. Unlike the angle θ_i , three ψ_i are not directly correlated; therefore, their distributions represent the orientation of the ellipsoids.

Figs. 4.53 to 4.55 show the pdf's of all three angles ψ_i in the near wall region ($0 < y^+ < 10$). In Fig. 4.53, the highest probability of ψ_1 is found at 90° , *i.e.* the particles typically align with the y direction, while the highest probability of ψ_2 shown in Fig. 4.54 is at 0° and 180° , *i.e.* the particles aligns with the x direction. These results are consistent with the result of the mean span-wise angle, θ_3 , as presented in Fig. 4.43 and confirm that ellipsoids tend to align in the x-y plane in the near wall region. The distribution of ψ_3 in Fig. 4.55 indicates that the orientation of particles seems to be randomly distributed in the x-y plane near the wall.

As shown in Figs. 4.56 to 4.58, the distribution of ψ_1 at the channel center is almost uniform, and the probabilities of ψ_2 and ψ_3 are distributed in very narrow region between 0.02 and 0.03. These results imply that there is no preferential orientation of particles in the central region of the channel and the orientation of particles is almost randomly distributed. It should be also noted that the pdfs of the angle ψ_3 are not symmetric in the near wall region ($0 < y^+ < 10$) as shown in Fig. 4.55. Figs. 4.59 and 4.60 show an ellipsoidal particle next to the wall near with ψ_3 less than 90° and ψ_3 more than 90° , respectively. In these two figures, the particle angular velocities ω_3^p are negative in the near wall region as presented in Fig. 4.43. However, the effects of particle-wall collisions are opposite for the two ellipsoid with two different orientation in Figs. 4.59 and 4.60. As illustrated in Fig. 4.59, the collision torque is also negative and increase the magnitude of

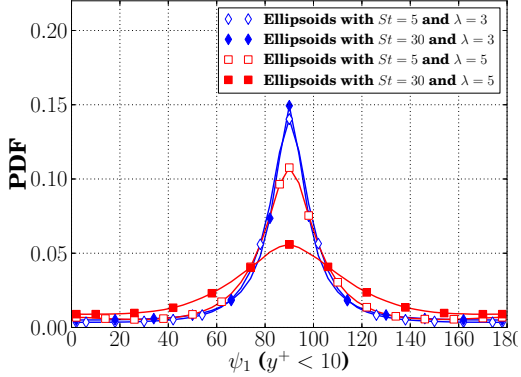


Figure 4.53.: The distribution of ψ_1 in the near wall region ($y^+ < 10$).

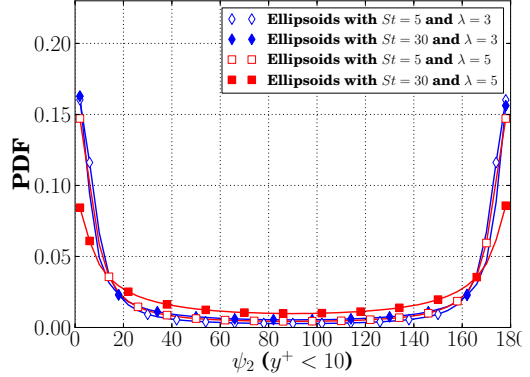


Figure 4.54.: The distribution of ψ_2 in the near wall region ($y^+ < 10$).

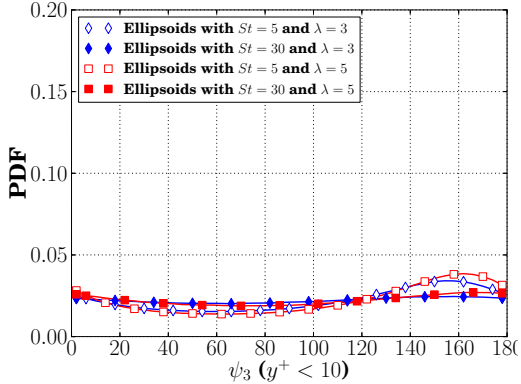


Figure 4.55.: The distribution of ψ_3 in the near wall region ($y^+ < 10$).

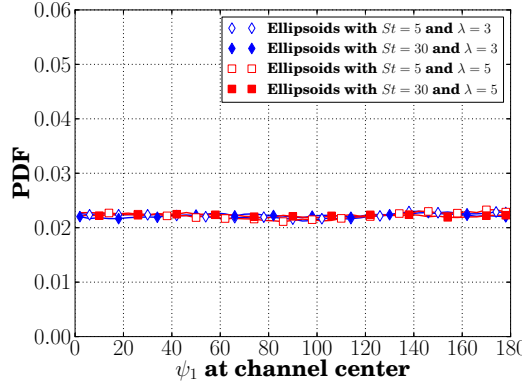


Figure 4.56.: The distribution of ψ_1 at channel center.

the particle angular velocity in the span-wise direction when ψ_3 is less than 90° , whereas the positive torque reduces the magnitude of the particle angular velocity when ψ_3 is more than 90° in Fig. 4.60. The effect of particle-wall collisions causes the asymmetric distribution of ψ_3 for cases with low St number ($St = 5$) in Fig. 4.55, and slightly large distribution of ψ_3 between 90° and 180° in the near wall region can be observed.

4.6. Conclusion

In this chapter, gas-solid turbulent channel flows are calculated using DNS combined with four-way coupling and Lagrangian point-particle approaches. By maintaining a constant pressure difference down the channel the wall shear stress is also maintained constant, so differences in drag show up as an increase in the centerline velocities. The current chapter expands the one-way coupling studies [71, 76, 108] and investigates the effects of particle shape and Stokes number on the both fluid flow and dispersed particles. By applying the soft-sphere collision model, all particle collisions are directly detected and their effects are resolved. Furthermore, a novel Quaternion integration method used in these simulations

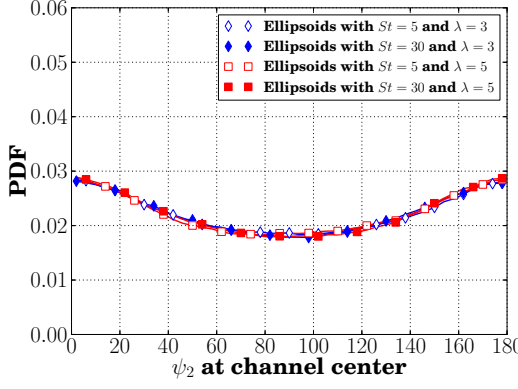


Figure 4.57.: The distribution of ψ_2 at channel center.

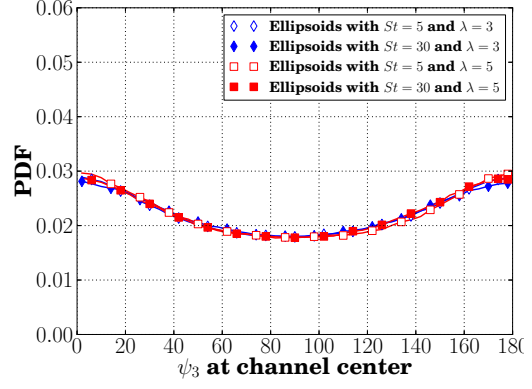


Figure 4.58.: The distribution of ψ_3 at channel center

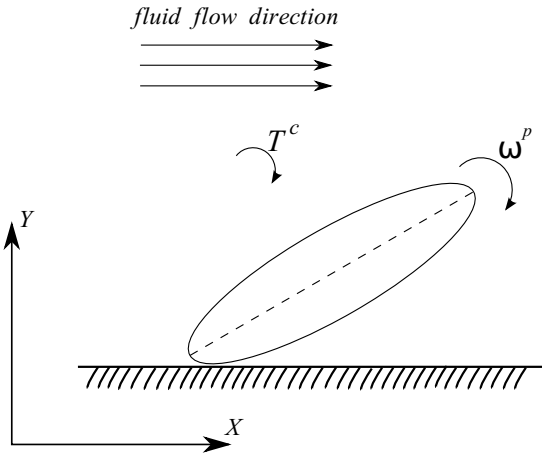


Figure 4.59.: An ellipsoidal particle with ψ_3 less than 90° next to the wall

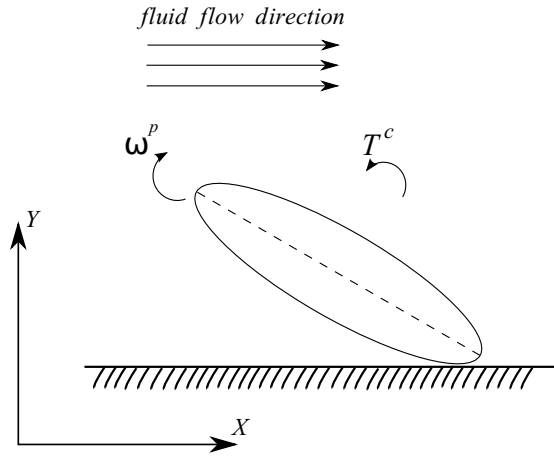


Figure 4.60.: An ellipsoidal particle with ψ_3 more than 90° next to the wall

determines the rotation and orientation of particles and avoids the need of less accurate rotation matrices.

The fluid statistics resulting from the simulations confirm that the presence of ellipsoidal particles with high particle inertia (large Stokes number) and large particle aspect ratio considerably attenuates the flow turbulence intensity. This is because the particles with high inertia cannot respond quickly enough to the behaviour of the fluid flow, thereby delaying the fluid flow and reducing the flow turbulence intensity. In the cases with the same large Stokes number, the elongated shape of ellipsoids further strengthens the effect of particles on the fluid flow, and thus further decreases the flow turbulence. In the near wall region, the magnitudes of the turbulence production (\mathcal{P}) and the fluid flow dissipation rate ($\tilde{\varepsilon}$) decrease significantly with increasing particle inertia and aspect ratio. The effects of particles on the three major components of $\tilde{\varepsilon}$ reflect the details of the changes of the fluid flow dissipation rate and the mean square vorticity. Although the dissipation rate caused by the coupling force from particles ε_p is extremely small in the dilute flows, the presence of particles considerably influences the fluid flow. This is because the ellipsoidal particles with high inertia and large aspect ratio change the velocity profile of the fluid

and indirectly change the fluid flow dissipation rate and the turbulence production. Due to the effect of large velocity gradient in the wall-normal direction, both particle and fluid velocity fluctuations in the stream-wise direction rise with increasing Stokes number. Without the effects of viscosity and the non-slip conditions at the walls on discrete particles, the particle RMS velocity is much higher than the fluid RMS velocity in the stream-wise direction. In the outer region between $10 < y^+ < 150$, the fluid and particle RMS velocities in the wall-normal and span-wise directions decrease with increasing Stokes number. As the response time of particles is noticeably larger than the fluid response time, the particle RMS velocities in these two directions are much lower than the fluid RMS velocities. In the near wall region ($0 < y^+ < 10$), however, particle velocity fluctuations in all three directions rise with increasing Stokes number and particle aspect ratio, due to the complex particle dynamics caused by the collisions between the wall and non-spherical ellipsoids.

It was also found that particles with high inertia preferentially accumulate in the near wall region of the channel. This is because large and slow vortices (usually referred to as “sweeps”) sweep the fluid and particles towards the wall, whereas the particles with relatively high inertia ($St \gg 1$) hardly follow the flow bursts away from the wall. Thus the particles preferentially accumulate in the low speed streaks very near the wall. With increasing Stokes number and particle aspect ratio, however, the peak value of particle volume fraction next to the wall decreases. This is because particles with significantly high inertia and aspect ratio strongly resist the effect of turbulence on them. The results of the large stream-wise slip velocity in the case with large Stokes number imply a strong momentum transfer between the two phases in this direction. However, the mean slip velocities in the other directions are very small through the channel, and thus the momentum transfer is weak in the span-wise and wall-normal directions. Because particles with high inertia cannot respond to the behaviour of the fluid flow, the velocity correlation between particles and the fluid flow are reduced with increasing particle inertia. Very close to the wall, the particle-wall collisions lead to more complex dynamics of ellipsoids than spheres; therefore, the velocities between the ellipsoids and the fluid flow are less correlated in the near wall region than those between spherical particles and the fluid flow.

The results for the orientation angle θ_i show that ellipsoidal particles tend to align in the x-y plane and perpendicular to the span-wise direction in the near wall region. The reason for this is not clear, but is most likely caused by the fluid dynamics of the boundary layer. However, since three θ_i are related to each other, it is not possible to conclude from their mean values and distributions in the central region of the channel that ellipsoids are randomly distributed at channel center, nor that they have a preferential orientation. Therefore, another orientation angle ψ_i is proposed to represent the orientation of ellipsoid. ψ_i represents the orientation of the 2-D projected particle major axis vector on the y-z, x-z, x-y planes, which perpendicular to the x, y and z axes of world space. The uniform distribution of ψ_i in the central region of the channel indicates that the orientation of particles is almost randomly distributed in the central region without any preferential orientation.

In summary, this chapter provides powerful evidence of turbulence reduction if small particles with large inertia and elongated shape are dispersed even in the very dilute concentrations of interest in this work. Important conclusions from this chapter include: the average viscosity of the flow is not affected, the average direct dissipation by the particles is negligible, and the primary mechanism by which the particles affect the flow is by altering the turbulence structure near and around the kinetic energy peak. As a final comment it must be noted that experiments to test the effects seen in this study will only be seen at distances downstream where the particles will have reached equilibrium with the flow. For a pipe or channel we estimate that distance to be in excess of thirty diameters after the flow itself has reached equilibrium (typically about the same distance).

5. Four-way coupled simulations of small particles in turbulent channel flows: the effects of particle volume fraction and a wide range of Stokes number

This chapter is based on the published paper:

F. Zhao, W. K. George and B. G. M. van Wachem, “Four-way coupled simulations of small particles in turbulent channel flows: the effects of particle shape and Stokes number”, submitted to Physics of Fluids (2014).

Abstract

This chapter numerically explores the effects of particle volume fraction and a wide range of Stokes number on the behaviour of gas-solid turbulent channel flows with spherical particles. Four-way coupled simulations are performed by varying the total number of particles and the inertia of the particles. The statistics of the fluid flow show that the fluid turbulence intensity is attenuated when adding particles with high inertia, *i.e.* large Stokes number. In cases with high Stokes number, increasing particle volume fraction (α^p) can significantly strengthen the attenuation of turbulence. In the near wall region, the phenomena of low-speed streaks is much more clearly observed in the cases with high particle inertia and large particle volume fraction. The particles accumulate preferentially in the low-speed streak areas, far away from large vortices. This phenomena is not affected by varying Stokes number in a range of $3 < St < 50$ or particle volume fraction. Moreover, heavy particles in the channel flow preferentially accumulates in the near wall region. For dilute flows laden with particles and relatively low Stokes number ($1 < St \leq 10$), more particles accumulates in the near wall region as Stokes number rises. However, when the Stokes number exceeds 20, the particles with considerably high inertia strongly resist the effect of turbulence on them; thus weakening the phenomena of particle accumulation near the wall.

5.1. Introduction

Chapter 4 studies the effects of the elongated shape and Stokes number on the behaviour of non-spherical particles in a turbulent channel flow, and the particle-laden simulations are performed with only two Stokes numbers (5 and 30). However, the effect of Stokes number on the particle deposition and transport are complex over a wide range of Stokes numbers. Thus the analysis of the Stokes number only based on two Stokes numbers is clearly not enough. In dispersed multiphase flows, the particle volume fraction is also an important parameter, which determines the interaction level between dispersed particles and the fluid flow. Therefore, this chapter focuses on studying the effects of particle volume fraction (α^p) and a wide range of Stokes numbers on the gas-solid channel flow with spherical particles, not considering the effect of particle shape.

In the literature, small solid spherical particles suspended in a wall-bounded turbulent flow have been extensively studied, experimentally *e.g.* [60, 61, 91, 95] and numerically *e.g.* [29, 33, 70, 96, 111]. It is believed that small heavy particles can attenuate the flow turbulence intensity and preferentially accumulate in the near wall region. When the particle volume fraction increases to a higher level ($\alpha^p > 1 \times 10^{-3}$), the particle-particle and particle-wall interactions, *i.e.* particle collisions, become important and considerably change the particle dynamics; therefore, their effects need to be considered in the simulations [92]. Since the local particle volume fraction in the near wall region rises with increasing total particle volume fraction, the effects of inter-particle and particle-wall collisions are much stronger in the near wall region than that in the central region. In this chapter, the simulations are performed, by applying four-way coupled DNS combined with the point-particle approach as the same as the simulations in the last chapter. The applied four-way coupling ensures that the fluid-particle interactions, particle-particle and particle-wall collisions are fully resolved.

Chapter 4 analyses the effect of Stokes number on the fluid flow and dispersed particles in the cases with only two different Stokes numbers ($St = 5$ and $St = 30$), and the fluid turbulence intensity is strongly attenuated in the cases with large Stokes number ($St = 30$). In the channel flow, the deposition and transportation of particles near the wall are quite complex and affected by various parameters: turbulence intensity, sweeps in the large vortices, flow bursting in low-speed streaks and particle inertia (Stokes number). However, only analysing simulations with $St = 5$ and $St = 30$ in Chapter 4 cannot fully discuss the effect of Stokes number on the particle deposition. Therefore, cases with a wider range of Stokes number, from 1 to 50, are performed and analysed in this chapter. Unlike the orientation and rotation of non-spherical ellipsoids in the simulations in Chapter 4 play a key role in determining the fluid-particle interactions and must be properly determined, the dynamics of spheres can be represented by the translational motion and very simplified rotation. Therefore, the orientation and rotation of spherical particles will not be considered in this chapter.

The aim of this chapter is to investigate the effects of particle volume fraction and a wide range of Stokes number on the behaviour of the gas-solid channel flow with spherical particles. The fluid flow is modelled in the DNS framework, and the statistics of the fluid flow,

in particular, the fluid velocity, Reynolds stress, the production of turbulence, the fluid flow dissipation rate, slip velocities and correlations between dispersed particles and the fluid flow, are all analysed among cases considering spheres with various particle volume fraction and Stokes number. To avoid the other parameters affecting the analysis, smooth wall condition are applied at walls, friction Reynolds number for all simulations in this chapter is fixed at 150, and the particle size is also the same in all particle-laden cases. The simulations are performed by only varying the particle volume fraction and Stokes number, and thus the effects of particle inertia and volume fraction can be fully studied. This chapter is outlined as follows. The simulation setting is put forward in Sec. 5.2. Section 5.3 shows the contour plots of the fluid instantaneous velocity and the results of particle distribution in the channel flow. After that, the results of the fluid flow are shown and analysed in Sec. 5.4, while Sec. 5.5 discusses the effects of particle inertia and volume fraction on the particle results and fluid-particle interactions. Finally, some conclusions are drawn in the last section.

5.2. Simulation set-up

The fluid flow is resolved in the framework of DNS, and the governing equations for the fluid phase are the continuity equation 1.32 and Navier-Stokes equation 1.33. The fluid properties are listed in Table 3.1 as the same as those in simulations of Chapter 4. In addition, the numerical setting of the fluid phase and fluid meshes is described in Sec. 3.2.3. The dynamics of spherical particles can be fully described by their translational motion, and thus the rotational motion of particles is not considered in the cases with spheres. The position and linear velocity of a particle are determined by equations 3.6 and 3.7, respectively, applying the second order Verlet scheme. To ensure the accuracy of the soft-sphere collision model for the given particles and flow conditions, the particle time-step Δt^p is chosen to be extremely small, $1 \times 10^{-7}(s)$.

The Stokes number is determined by the particle response time τ_p and the fluid response time τ_f :

$$St = \tau_p / \tau_f \quad (5.1)$$

where the fluid response time τ_f equals 0.001132 in all simulations, *see* Table 3.1, and the sphere response time τ_p for Stokes' drag is expressed as:

$$\tau_p = \frac{\rho^p D^{p2}}{18\mu^f} \quad (5.2)$$

where D^p is the sphere diameter.

The Stokes number is changed by varying the density of spherical particles among different particle-laden simulations, and seven cases covering a wide range of Stokes number from 1 to 50 are performed with the same particle volume fraction, $\alpha^p = 0.0073\%$ (0.2 million particles). There are also two cases with a much higher particle volume fraction,

Table 5.1.: Particle properties in different simulations

St	ρ [kg/m ³]	Diameter (D) [μm]	numbers [-]	Volume fraction [%]
1	45.14	96.0	200,000	0.0073
3	135.42	96.0	200,000	0.0073
5	225.68	96.0	200,000	0.0073
10	450.14	96.0	200,000	0.0073
20	902.80	96.0	200,000	0.0073
30	1354.21	96.0	200,000	0.0073
50	2257.00	96.0	200,000	0.0073
5	225.68	96.0	1,000,000	0.036
30	1354.21	96.0	1,000,000	0.036

$\alpha^p = 0.036\%$ (1 million particles), performed and analysed in this chapter. Table 5.1 lists particle properties in all nine simulations. After the single phase fluid channel flow reaches steady-state, particles are homogeneously positioned in the whole channel with a velocity of the bulk fluid velocity without rotation in each case, and the simulations continue running until the gas-solid channel flow reaching fully developed state again.

5.3. Contour plots of instantaneous fluid velocities and particle distribution

Figs. 5.1 to 5.4 display the instantaneous fluid wall-normal velocity (u_2^f) and distribution of spherical particles in the cross-sectional y-z plane, which lies perpendicular to the stream-wise direction, at channel center $x^+ = 942$ for simulations with $\alpha^p = 0.0073\%$ and various Stokes number ($St = 1$, $St = 5$, $St = 30$ and $St = 50$). The black dots in these figures represent the small particles around this plane. As shown in these contour plots, particles are hardly found in the absolute large velocity zones (dark blue and red zones). This phenomena is also observed from Figs. 5.5 and 5.6, which shows the instantaneous fluid wall-normal velocity (u_2^f) with spheres in the two cases with large particle volume fraction ($\alpha^p = 0.036\%$). Comparing Fig. 5.1 with Fig. 5.6, it is apparent that the turbulence intensity is significantly reduced with the increasing particle volume fraction and Stokes number.

Figs. 5.7 to 5.12 show the instantaneous fluid stream-wise velocity (u_1^f) with spherical particles in the cross-sectional x-z plane, which is perpendicular to the wall-normal direction,

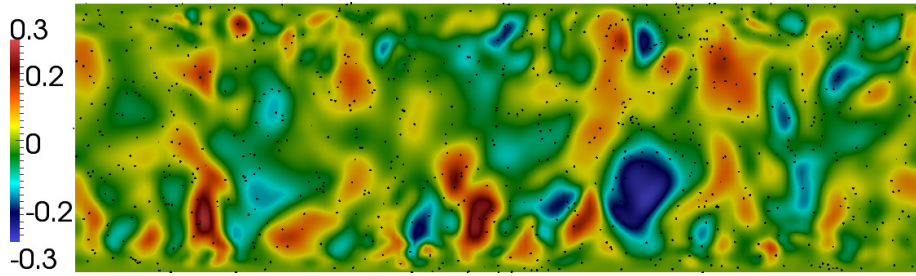


Figure 5.1.: The instantaneous fluid velocity (indicated by colour) in the wall-normal direction and the distribution of spherical particles with $St = 1$ near the cross-sectional y-z plane at $x^+ = 942$ for the case with 0.2 million particles

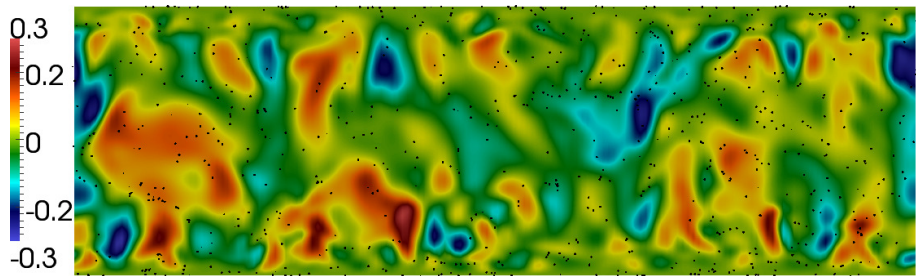


Figure 5.2.: The instantaneous fluid velocity (indicated by colour) in the wall-normal direction and the distribution of spherical particles with $St = 5$ near the cross-sectional y-z plane at $x^+ = 942$ for the case with 0.2 million particles

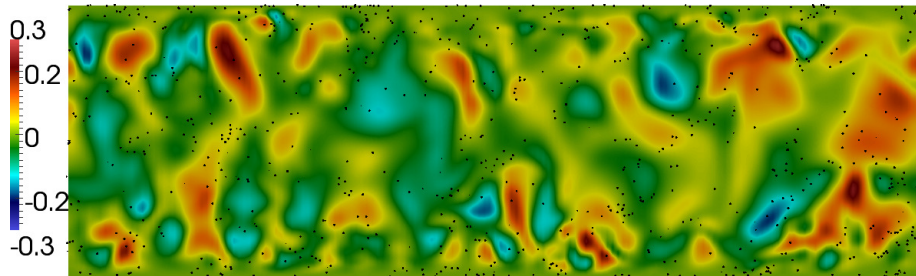


Figure 5.3.: The instantaneous fluid velocity (indicated by colour) in the wall-normal direction and the distribution of spherical particles with $St = 30$ near the cross-sectional y-z plane at $x^+ = 942$ for the case with 0.2 million particles

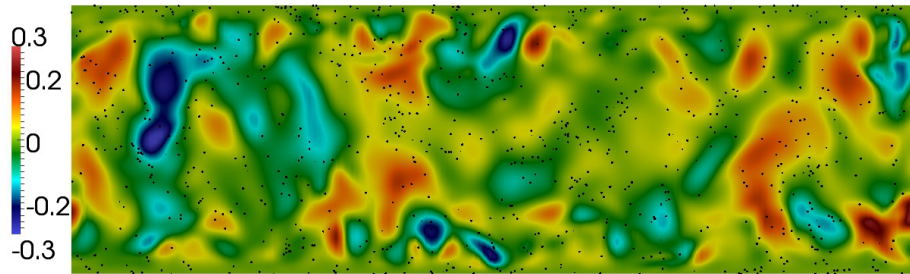


Figure 5.4.: The instantaneous fluid velocity (indicated by colour) in the wall-normal direction and the distribution of spherical particles with $St = 50$ near the cross-sectional y-z plane at $x^+ = 942$ for the case with 0.2 million particles

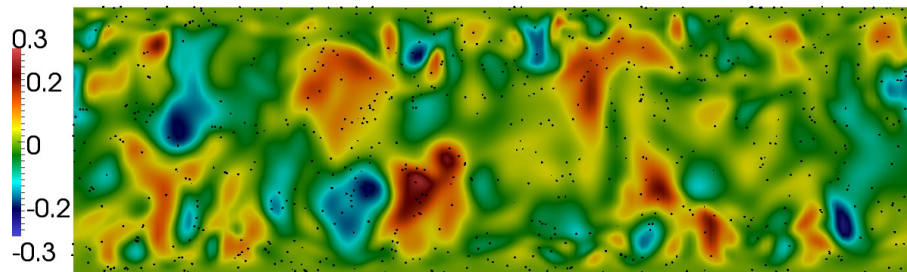


Figure 5.5.: The instantaneous fluid velocity (indicated by colour) in the wall-normal direction and the distribution of spherical particles with $St = 5$ near the cross-sectional y-z plane at $x^+ = 942$ for the cases with 1 million particles

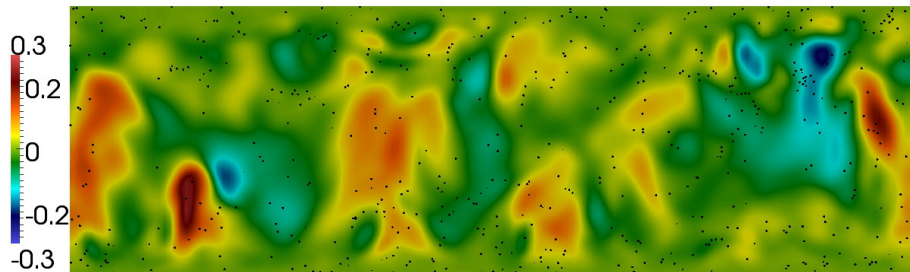


Figure 5.6.: The instantaneous fluid velocity (indicated by colour) in the wall-normal direction and the distribution of spherical particles with $St = 30$ near the cross-sectional y-z plane at $x^+ = 942$ for the cases with 1 million particles

near the wall at $y^+ = 8.0$. From these figures, the phenomena of low-speed streaks (blue areas) in the channel flow are clearly observed, and the low-speed streaks become much wider and are much more clearly seen when adding heavy particles. Between the low-speed streaks, the fluid moves relatively faster (red zones). It is well known that at some point in the low-speed streaks the fluid flow rapidly moves away from the wall, which is known as bursting, and this process is also referred as streak lifting or ejection [57]. In a fully developed turbulent channel flow, the dominant vortical eddies are in the high-speed zones in the near wall region [7]. Slightly away from the wall, these large vortices are long and inclined around 45% to the wall like hairpins [48]. The fluid flow in these large eddy zones (dark red areas) moves towards the wall, called sweeps [21]. To directly illustrate the fluid sweeps and bursting in the channel flow, the fluid velocity in the wall-normal direction across a low-speed streak and across a high speed streak is shown in Figs. 5.13 to 5.16. Fig. 5.13 shows the instantaneous fluid wall-normal velocity (u_2^f) in a cross-sectional x-y plane, which lies perpendicular to the span-wise direction across a low-speed streak, in the case considering spheres with $St = 50$ and $\alpha^p = 0.0073\%$, while Fig. 5.14 shows u_2^f in the x-y plane across a high-speed area in the same simulation. In Fig. 5.13, it is clearly observed that the red and yellow areas close to the wall indicate that the fluid flow moves away from the wall rapidly ($0.05 < u_2^f < 0.2$). In the high speed areas shown in Fig. 5.14, the green and light blue areas near the wall imply that the fluid flow move towards the wall slowly ($0.05 < u^f < 0$). The similar phenomena is also found in the case with $St = 30$ and $\alpha^p = 0.036\%$, shown in Figs. 5.15 and 5.16.

The particles are definitely affected by these fluid bursting and sweeps. As the particle size is too small, the distribution of particles between the high-speed and low-speed streaks cannot be clearly seen from the figures from Figs. 5.7 to 5.12.

Table 5.2 lists the particle distribution in the low-speed streaks around $y^+ = 8.0$, which is corresponding to the figures plotting the instantaneous fluid stream-wise velocity with particles. As listed in Table 5.2, the low-speed area in the x-z plane at $y^+ = 8.0$ is around 51% to 54% in cases with various Stokes number and particle volume fraction. However, around 59% to 69% particles around $y^+ = 8.0$ in the cases with large Stokes number ($3 \leq St \leq 50$) are found in the low-speed streaks. This indicates particles with high inertia spend more time in the low-speed streaks, *i.e.* areas away from the large vortices, than in the high-speed zones (large vortices). This phenomena is also reported in the previous papers [36, 93]. As illustrated in Table 5.2, the particle preferential concentration is not considerably affected by Stokes number between 3 and 50. This is in good agreement with Goto and Vassilicos [43], which reported that the particle accumulation is irrespective of the Stokes number in a certain range. As particles with extremely low inertia follow the behaviour of the fluid flow, they do not concentrate in the low-speed streaks, as illustrated in the case with $St = 1$ in the Table 5.2.

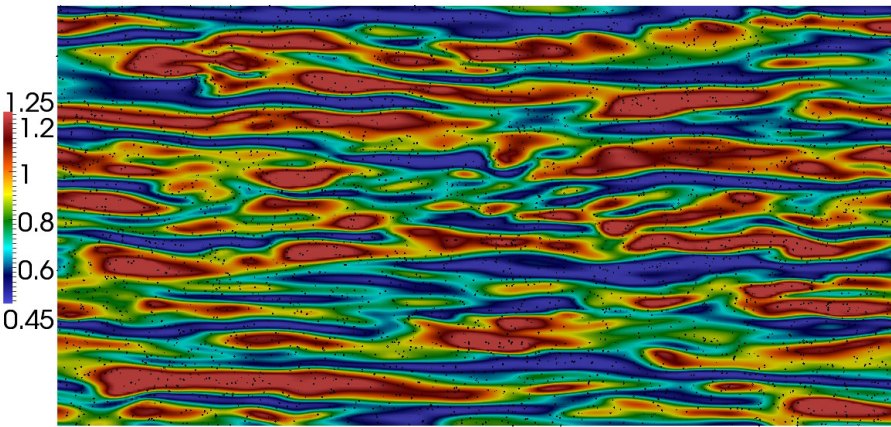


Figure 5.7.: The instantaneous fluid velocity (indicated by colour) in the stream-wise direction and the distribution of spherical particles with $St = 1$ near the cross-sectional x-z plane at $y^+ = 8.0$ for the case with 0.2 million particles

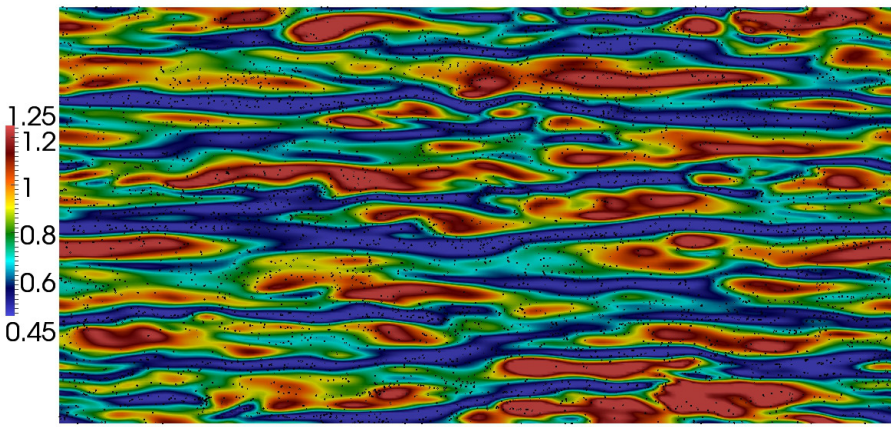


Figure 5.8.: The instantaneous fluid velocity (indicated by colour) in the stream-wise direction and the distribution of spherical particles with $St = 5$ near the cross-sectional x-z plane at $y^+ = 8.0$ for the case with 0.2 million particles

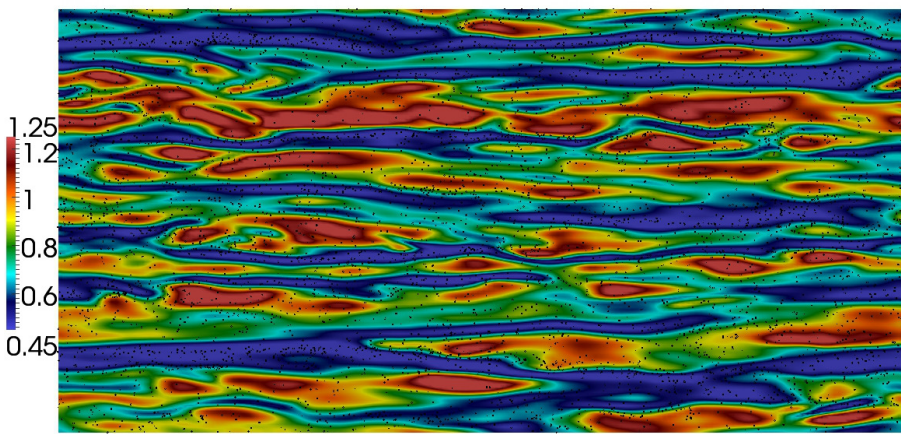


Figure 5.9.: The instantaneous fluid velocity (indicated by colour) in the stream-wise direction and the distribution of spherical particles with $St = 30$ near the cross-sectional x-z plane at $y^+ = 8.0$ for the case with 0.2 million particles

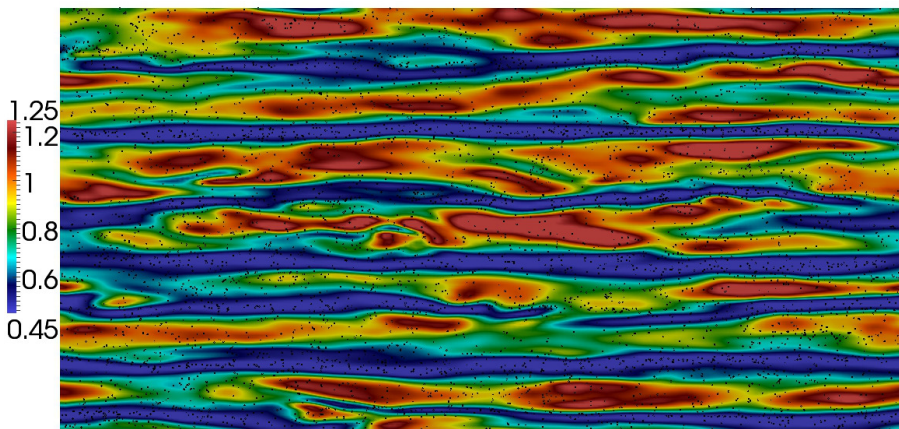


Figure 5.10.: The instantaneous fluid velocity (indicated by colour) in the stream-wise direction and the distribution of spherical particles with $St = 50$ near the cross-sectional x-z plane at $y^+ = 8.0$ for the case with 0.2 million particles

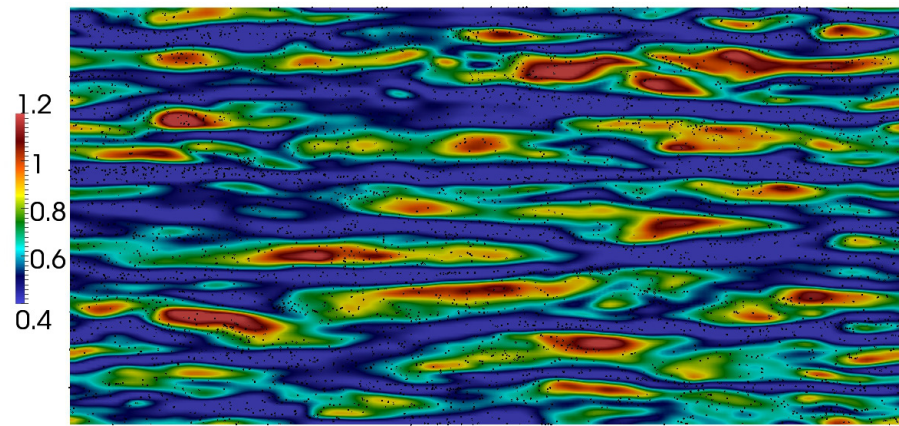


Figure 5.11.: The instantaneous fluid velocity (indicated by colour) in the stream-wise direction and the distribution of spherical particles with $St = 5$ near the cross-sectional x-z plane at $y^+ = 8.0$ for the cases with 1 million particles

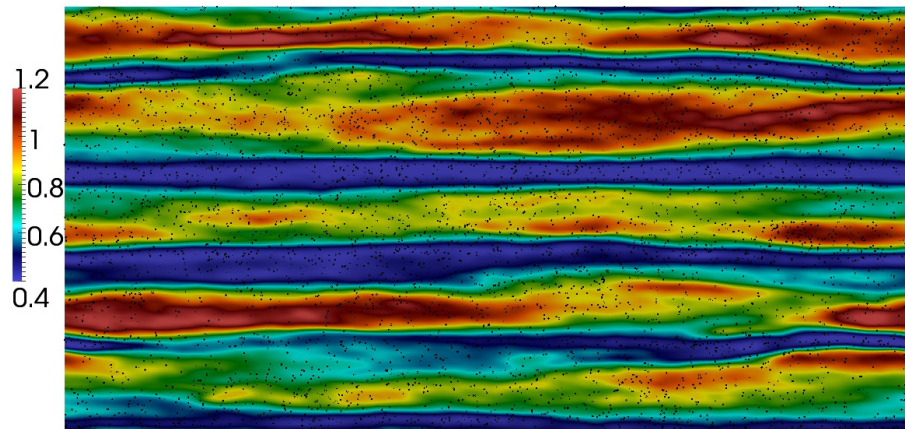


Figure 5.12.: The instantaneous fluid velocity (indicated by colour) in the stream-wise direction and the distribution of spherical particles with $St = 30$ near the cross-sectional x-z plane at $y^+ = 8.0$ for the cases with 1 million particles

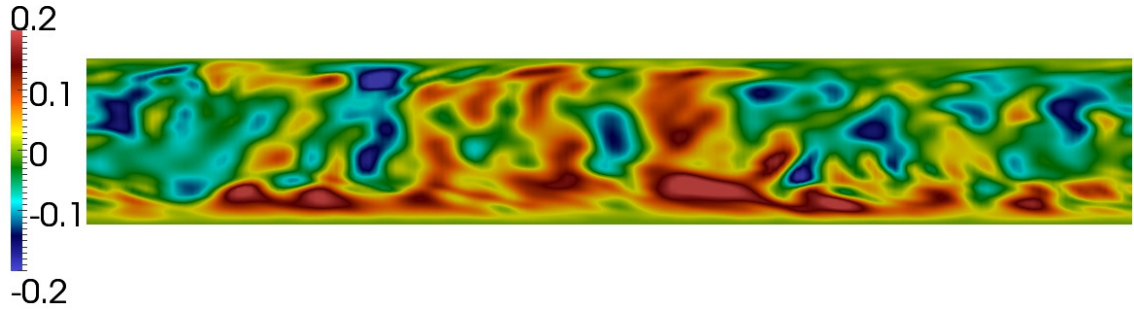


Figure 5.13.: The instantaneous fluid velocity (indicated by colour) in the wall-normal direction and the distribution of spherical particles with $St = 50$ near a x-y plane across a low-speed streak for the case with 0.2 million particles

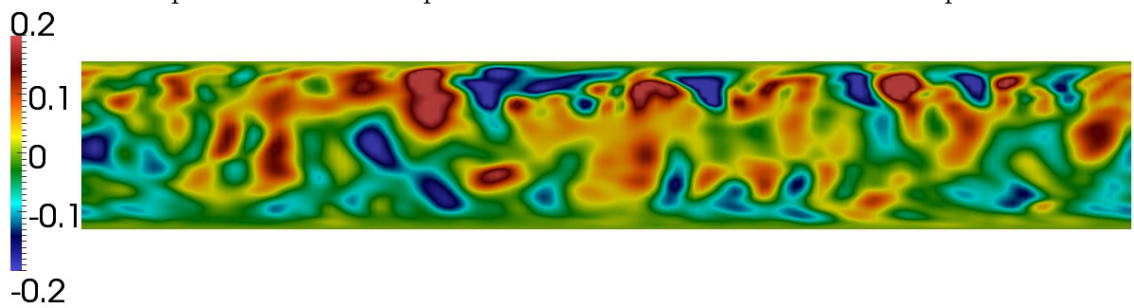


Figure 5.14.: The instantaneous fluid velocity (indicated by colour) in the stream-wise direction and the distribution of spherical particles with $St = 50$ near a x-y plane across a high-speed area for the cases with 0.2 million particles

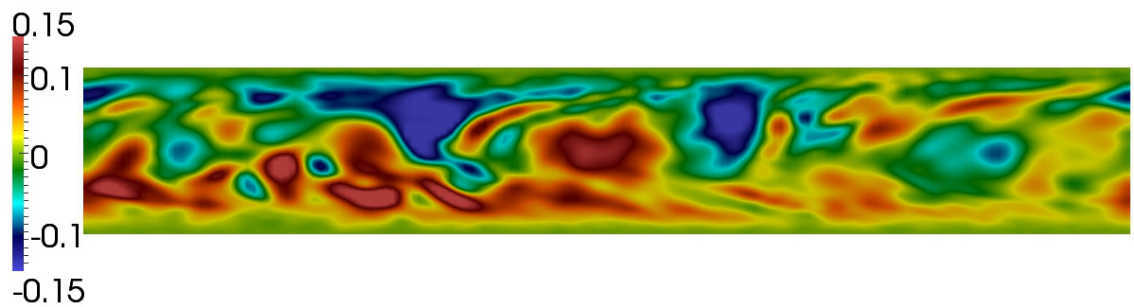


Figure 5.15.: The instantaneous fluid velocity (indicated by colour) in the wall-normal direction and the distribution of spherical particles with $St = 30$ near a x-y plane across a low-speed streak for the case with 1 million particles

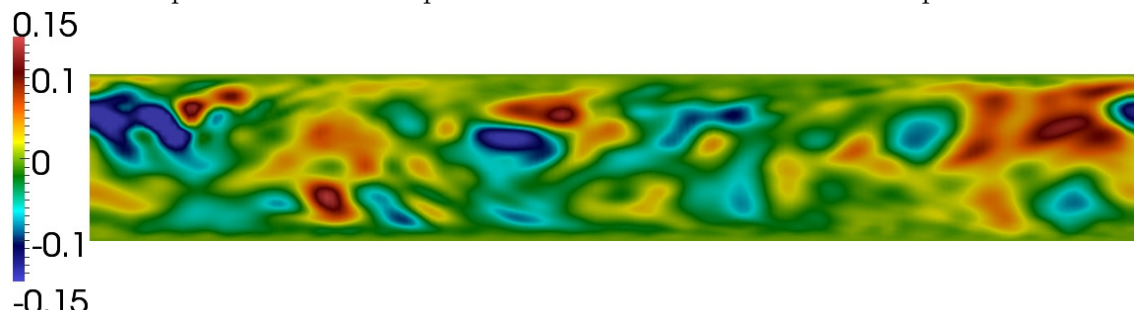


Figure 5.16.: The instantaneous fluid velocity (indicated by colour) in the stream-wise direction and the distribution of spherical particles with $St = 30$ near a x-y plane across a high-speed area for the cases with 1 million particles

Case considering spheres	The area of low-speed fluid flow ($u_1^f - U_1^f < 0$) around $y^+ = 8.0$	Particles in the low speed area around $y^+ = 8.0$
$St = 1$ and $\alpha = 0.0073\%$	52.04%	54.53%
$St = 3$ and $\alpha = 0.0073\%$	53.1%	61.4%
$St = 5$ and $\alpha = 0.0073\%$	53.1%	65.6%
$St = 10$ and $\alpha = 0.0073\%$	54.2%	69.0%
$St = 20$ and $\alpha = 0.0073\%$	53.9%	69.9%
$St = 30$ and $\alpha = 0.0073\%$	53.3%	65.8%
$St = 50$ and $\alpha = 0.0073\%$	51.9%	61.9%
$St = 5$ and $\alpha = 0.036\%$	54.3%	62.9%
$St = 30$ and $\alpha = 0.036\%$	51.5%	58.9%

Table 5.2.: The portion of particles in the low-speed streaks around $y^+ = 8.0$

5.3.1. Particle deposition

In a gas-solid turbulent channel flow, the long hairpin vortices in the high speed areas, sweep fluid flow and particles towards the wall, whereas the particles with relatively high inertia ($St \gg 1$) cannot follow the flow burst which rapidly moves away from the wall in the low-speed streaks near the wall. The combination of these two effects is the main mechanisms by which the particles with high inertia preferentially accumulate in the near wall region. In the gas-solid channel flow, the fluid bursts and sweeps moving the fluid flow towards and away from the wall must be balance (to satisfy mass conservation). The discrete particles have no such conservation law, so can accumulate. This phenomena of particle accumulation near the wall can be clearly observed in Figs. 5.17 and 5.19. Fig. 5.17 compares the local particle volume fraction $\langle \alpha_y^p \rangle$ in the wall normal direction among four cases with two Stokes numbers ($St = 5$ and $St = 30$) and two total particle volume fraction ($\alpha^p = 0.0073\%$ and $\alpha^p = 0.036\%$). In Fig. 5.17, increasing the total particle volume fraction considerably increases the peak value of $\langle \alpha_y^p \rangle$ next to the wall in the cases with $St = 5$. However, in the two cases with $St = 30$, 5 times rise in total particle volume fraction (from 0.2 million to 1 million spheres) only slightly increases the peak value of $\langle \alpha_y^p \rangle$ next to the wall. This is because increasing the total particle volume fraction in the simulation with large Stokes number considerably strengthens the attenuation of the turbulence, and thus weakens both effects of the fluid burst and sweep significantly. Moreover, particles with considerably high inertia strongly resist the effect of flow turbulence on them. Fig. 5.18 shows the ratio of the local particle volume fraction $\langle \alpha_y^p \rangle$ to the average particle volume fraction α^p are close in the region between $40 < y^+ < 150$.

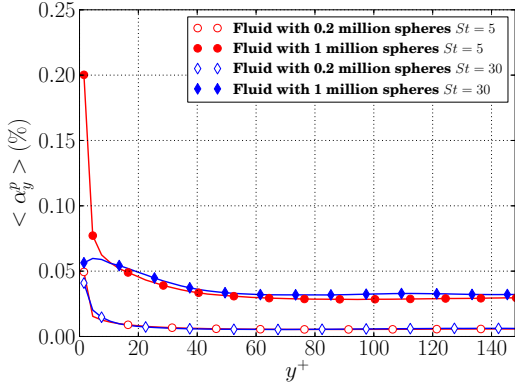


Figure 5.17.: The local particle volume fraction $\langle \alpha_y^p \rangle$ in the wall normal direction as a function of distance to the wall

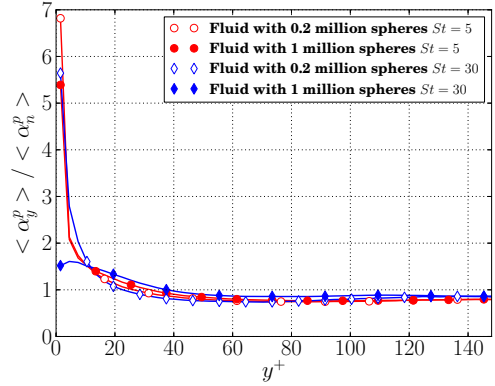


Figure 5.18.: The ratio of the local particle volume fraction $\langle \alpha_y^p \rangle$ and the average particle volume fraction $\langle \alpha_n^p \rangle$

This indicates that the effects of Stokes number and total particle volume fraction on the particle distribution can be negligible in the central region of the channel.

Fig. 5.19 shows the local particle volume fraction $\langle \alpha_y^p \rangle$ in the cases with various Stokes numbers (from 1 to 50) and low total particle volume fraction ($\alpha^p = 0.0073\%$). $\langle \alpha_y^p \rangle$ in all particle-laden cases peaks near the wall. To clearly show and analyse the peak and minimum values of $\langle \alpha_y^p \rangle$ in the cases with a wide range of Stokes number, the peak and minimum values of $\langle \alpha_y^p \rangle$ are shown in Fig. 5.20 as a function of Stokes number. In the case with $St = 1$, particles with extremely low inertia follow the behaviour of the fluid flow, moving away or towards the wall. Therefore, the peak value of $\langle \alpha_y^p \rangle$ is very low next to the wall. With increasing Stokes number from 1 to a relatively high level, particles cannot exactly follow the fluid flow, and the main mechanism of particle accumulation confines more particles to stay in the near wall region. This results in the peak value of $\langle \alpha_y^p \rangle$ rising with increasing Stokes number from 1 to 10 shown in Fig. 5.19. However, continuing to increase Stokes number, particles with extremely high inertia strongly resist the effect of the fluid flow on them; therefore, the peak value of $\langle \alpha_y^p \rangle$ near the wall decreases as Stokes number rises from 10 to 50.

5.4. Fluid flow statistics

In this section, fluid statistics are shown and analysed, including the fluid velocity, the production of turbulence and the fluid flow dissipation rate. All the statistical results are compared among the simulations with various Stokes number and particle volume fraction.

5.4.1. Fluid velocity

Figs. 5.21 to 5.25 show the fluid velocity statistics as a function of distance from the wall ($y^+ = 0$) to the channel center ($y^+ = 150$) for a clear fluid case and cases with the same

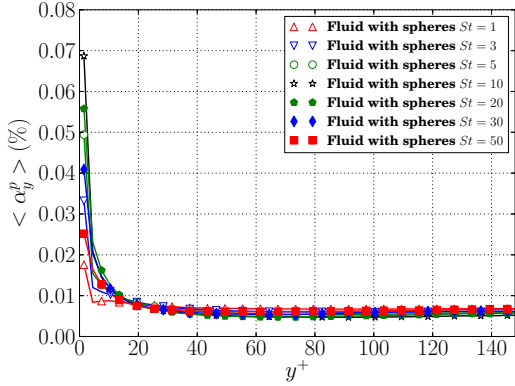


Figure 5.19.: The local particle volume fraction $\langle \alpha_y^p \rangle$ in the wall normal direction as a function of distance to the wall in the cases with low total particle volume fraction ($\alpha^p = 0.0073\%$)

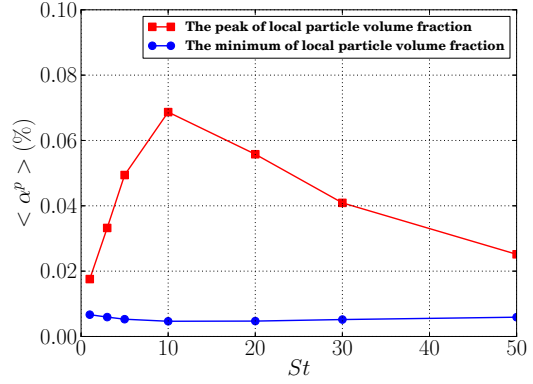


Figure 5.20.: The peak and minimum values of local particle volume fraction $\langle \alpha_y^p \rangle$ in the wall normal direction as a function of Stokes number in the cases with low total particle volume fraction ($\alpha^p = 0.0073\%$)

low particle volume fraction ($\alpha^p = 0.0073\%$) and various Stokes number ($1 < St < 50$). Fig. 5.21 shows the mean fluid velocity U_1^f in the flow direction. In Fig. 5.21, the magni-

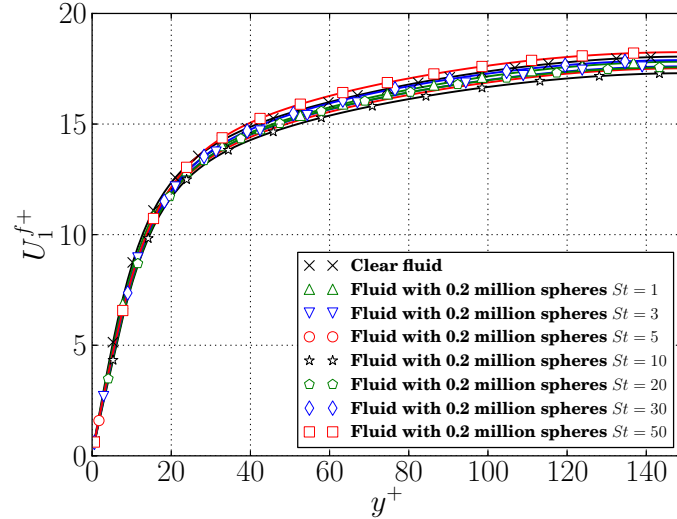


Figure 5.21.: Fluid stream-wise mean velocity as a function of distance to the wall

tude of U_1^f in the case of the largest Stokes number ($St = 50$) is larger than that of the other particle-laden cases in the region of $40 < y^+ < 150$. This is because particles with considerably high inertia reduce the turbulence intensity and cause a drag reduction in the fluid flow. In the inner linear sublayer ($0 < y^+ < 5$), the curves of U_1^f in all cases nearly coincide, and this collapse implies that the viscosity of the fluid flow must be constant in all particle-laden and clear flow simulations. Therefore the drag reduction is not caused by the change of viscosity due to the particles.

Figs. 5.22 to 5.24 show the fluid velocity fluctuations $u_i'^f$ in all three directions. In Fig. 5.22,

$u_1'^f$ between $20 < y^+ < 150$ slightly increases as Stokes number rises. Because the stream-wise fluid velocity has a large velocity gradient with respect to the wall-normal direction, particles with high inertia moving in the wall-normal direction lead to a large momentum transfer between the fluid flow and particles. This large momentum transfer strengthens the velocity fluctuations of both the particles and the fluid flow in the stream-wise direction. Increasing Stokes number strengthens the momentum transfer and thus increase $u_1'^f$. On the other hand, the fluid RMS velocities in the wall-normal and span-wise directions ($u_2'^f$ and $u_3'^f$) decrease with increasing Stokes number as illustrated in Figs. 5.23 and 5.24, respectively. Unlike the stream-wise velocity has large gradient, the mean velocities in

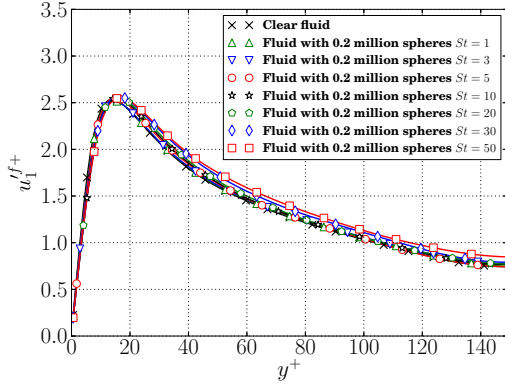


Figure 5.22.: Fluid velocity RMS in the stream-wise direction as a function of distance to the wall

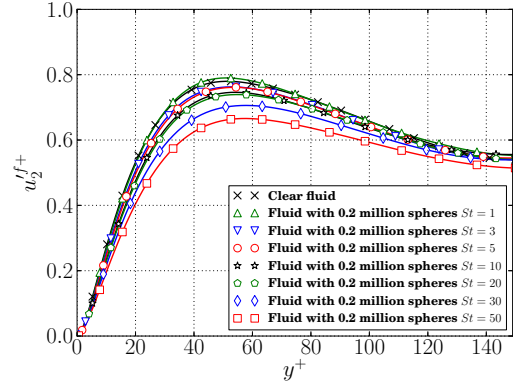


Figure 5.23.: Fluid velocity RMS in the wall-normal direction as a function of distance to the wall

these two directions are zero throughout the channel, and thus the velocity gradients are also exactly zero. The reduction of $u_2'^f$ and $u_3'^f$ is because particles with high inertia cannot respond quickly to changes of the fluid flow and delay it. Fig. 5.25 shows the

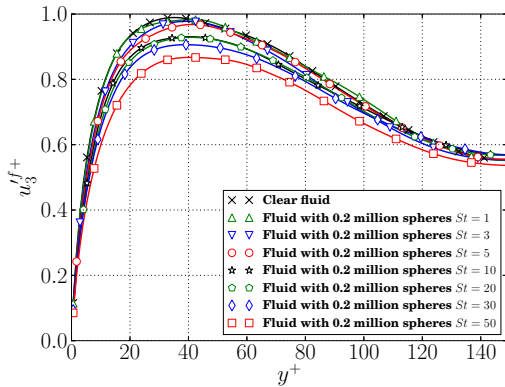


Figure 5.24.: Fluid velocity RMS in the span-wise direction as a function of distance to the wall

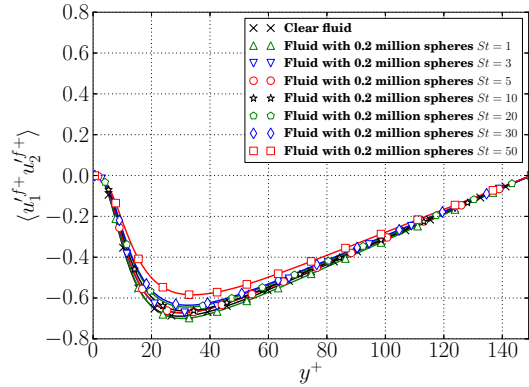


Figure 5.25.: Reynolds stress $\langle u_1'^f u_2'^f \rangle$ as a function of distance to the wall

Reynolds stress, as expected, decreases when adding heavy particles, and the magnitude of the Reynolds stress decreases with increasing Stokes number.

Figs. 5.26 to 5.30 display the results of the fluid velocity in the clear fluid case and cases with two different particle volume fraction (α^p) and two different Stokes numbers (St). In

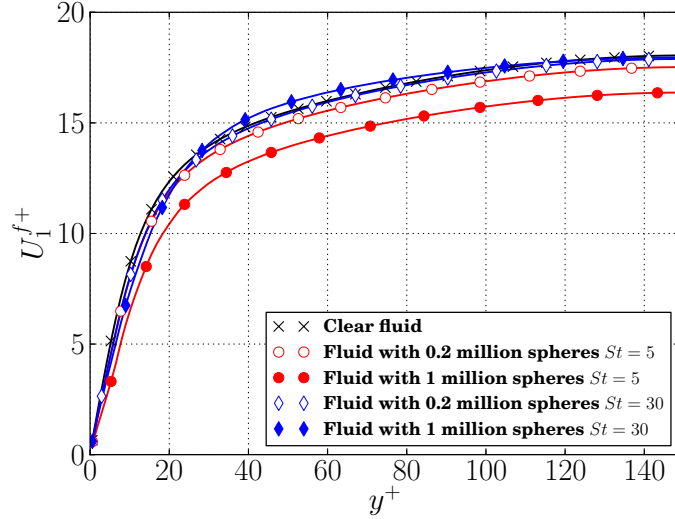


Figure 5.26.: Fluid stream-wise mean velocity as a function of distance to the wall

Fig. 5.26, the mean fluid velocity U_1^f in the cases with large Stokes number ($St = 30$) rises in the region between $40 < y^+ < 100$ with increasing the particle volume fraction α^p from 0.0073% to 0.036%. However, U_1^f in the central region is slightly lower in the cases with low Stokes number ($St = 5$) than that in the clear fluid case. This is because particles with relatively low inertia only slightly reduce turbulence, and much more particles in the near wall region can strongly strengthen momentum transfer from particles to the fluid flow, resulting in reduction of the mean fluid velocity gradient in the bufferlayer. Increasing α^p in particle-laden cases just strengthens the effect of particles on the fluid flow between $10 < y^+ < 150$, as illustrated in Fig. 5.26. In the linear sublayer, U_1^f almost coincides for all cases. This confirms that the particles have nothing to do with viscosity.

Figs. 5.27 to 5.29 show the fluid velocity fluctuations in all three directions. As can be

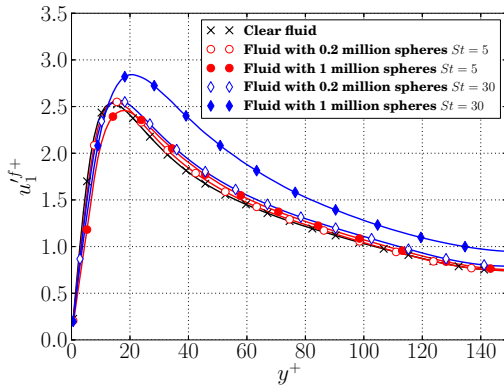


Figure 5.27.: Fluid velocity RMS in the stream-wise direction as a function of distance to the wall

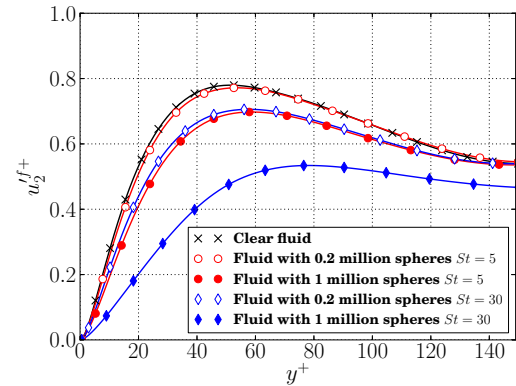


Figure 5.28.: Fluid velocity RMS in the wall-normal direction as a function of distance to the wall

seen from Fig. 5.27, in the region between $20 < y^+ < 150$, the fluid RMS velocity in the stream-wise direction $u_1'^f$ in the cases with $St = 30$ increases significantly as α^p rises. This is because large α^p strongly enhances the momentum transfer between the two phases for the cases considering particles with high inertia, and thus increasing the fluid velocity fluctuations in the stream-wise direction. For the case with $\alpha^p = 0.036$ and $St = 5$, the relatively small peak value of $u_1'^f$ is caused by the lower mean fluid velocity.

In the wall-normal and span-wise directions, as explained earlier, particles with high inertia do not follow the particle behaviour and delay the fluid flow; therefore, the fluid velocity fluctuations in these two directions ($u_2'^f$ and $u_3'^f$) are reduced with increasing particle inertia. As illustrated in Figs. 5.28 and 5.29, it is apparent that the effect of particles on $u_2'^f$ and $u_3'^f$ are considerably strengthened by increasing particle volume fraction in the cases with the same Stokes number.

Fig. 5.30 shows the fluid Reynolds stress decreases with the increasing particle volume fraction and particle inertia. As shown in Figs. 5.25 and 5.30, the reduction of Reynolds

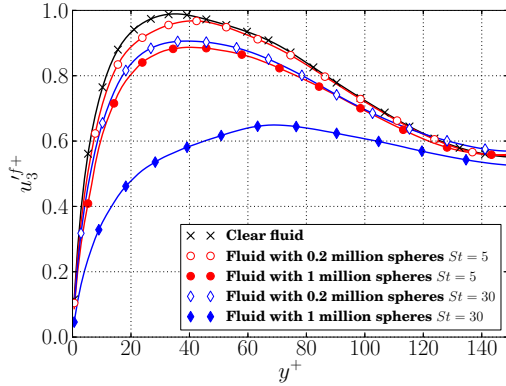


Figure 5.29.: Fluid velocity RMS in the span-wise direction as a function of distance to the wall

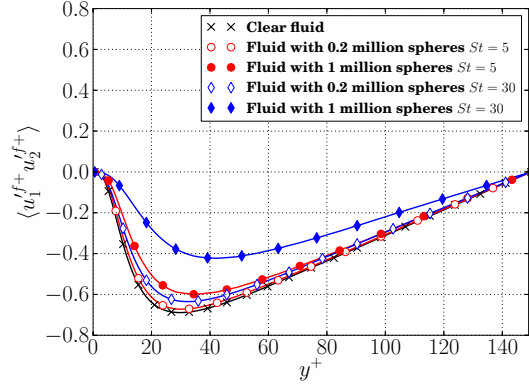


Figure 5.30.: Reynolds stress $\langle u_1'^f u_2'^f \rangle$ as a function of distance to the wall

stresses in the particle-laden cases indicates that the presence of particles with high inertia attenuates the fluid turbulence, and increasing the particle volume fraction and Stokes number strengthen the turbulence reduction. It should be also noted that fluid velocity fluctuations and Reynolds stresses slightly shift towards the center of the channel in the particle-laden cases. Moreover, all profiles of the mean velocity and RMS fluid velocity in the stream-wise direction collapse in the inner linear sublayer ($y^+ < 5$). These results confirm that the particles have at most a very minimal effect on the fluid viscosity. The changes of the profiles away from the wall are caused by the changes of turbulence structure.

5.4.2. The turbulence modulation

5.4.2.1. Turbulence transport terms

On the left hand side of equation 3.2, the three transport terms (turbulence itself, the pressure fluctuations and viscous stresses) only transport TKE from one location to another, but do not generate any energy. Figs. 5.31 to 5.33 display these turbulence transport terms

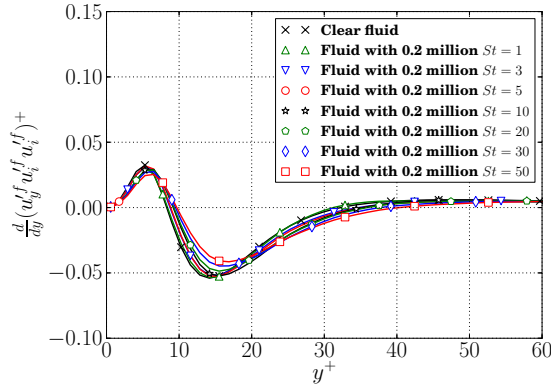


Figure 5.31.: TKE turbulence itself transport term as a function of distance to the wall

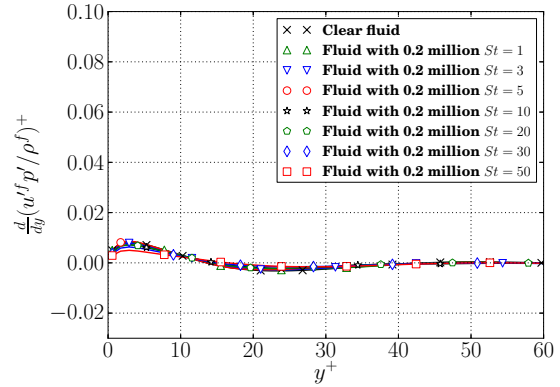


Figure 5.32.: TKE pressure fluctuation transport term as a function of distance to the wall

between $0 < y^+ < 60$ in the cases with $\alpha^p = 0.0073\%$ and various Stokes numbers. From these three figures, the peak and minimum values of these transport terms only slightly decrease with increasing Stokes number, due to the very small particle volume fraction. By contrast, Fig. 5.34 to Fig. 5.36 show that increasing the particle volume fraction con-

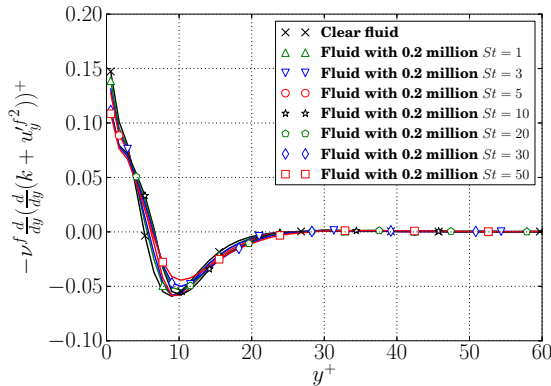


Figure 5.33.: TKE viscous transport term as a function of distance to the wall

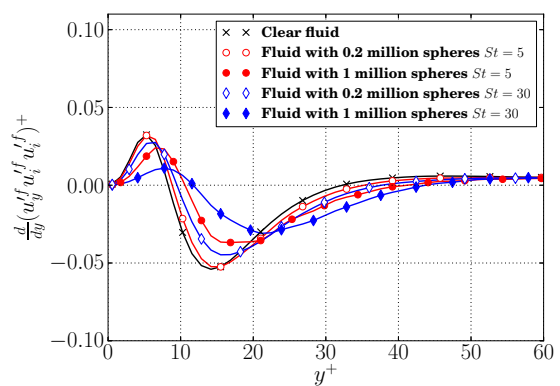


Figure 5.34.: TKE turbulence itself transport term as a function of distance to the wall

siderably decreases the peak and minimum magnitudes of the turbulence transport terms. As can be seen from Figs. 5.33 and 5.36, the viscous transport term peaks next to the wall. This means that the viscous term transports TKE to the wall, where the fluid flow dissipation rate $\tilde{\varepsilon}$ peaks. It should be noted that the magnitudes of all the three transport terms are very small, close to zero, in the central region of the channel in all particle-laden

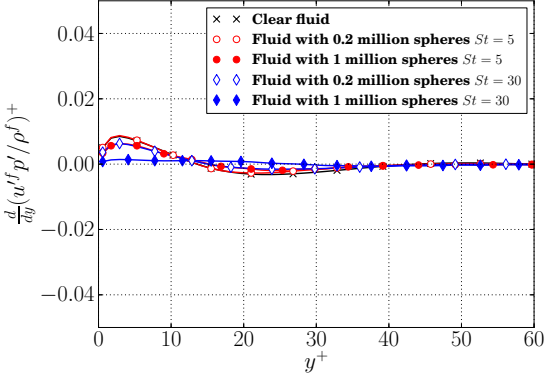


Figure 5.35.: TKE pressure fluctuation transport term as a function of distance to the wall

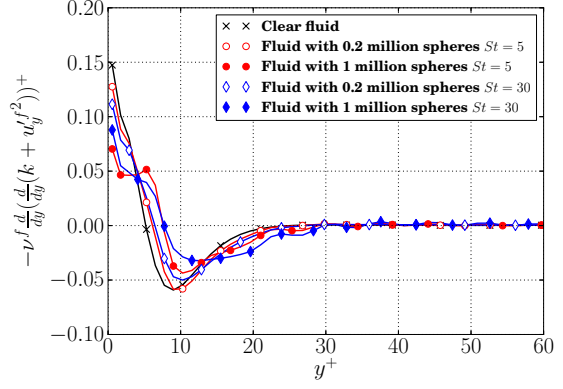


Figure 5.36.: TKE viscous transport term as a function of distance to the wall

cases and the clear fluid case. This indicates that the turbulence transport in the central region is extremely weak and is not affected by adding heavy particles.

5.4.2.2. The production of turbulence

Figs. 5.37 and 5.38 show the production of turbulence (\mathcal{P}) for the cases with various particle volume fraction and various Stokes numbers. In Fig. 5.37, as expected, the peak

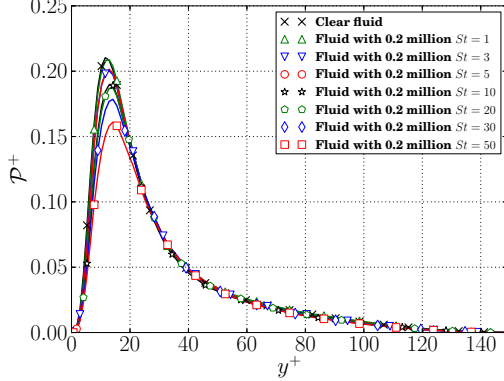


Figure 5.37.: Turbulence kinetic energy production as a function of distance to the wall

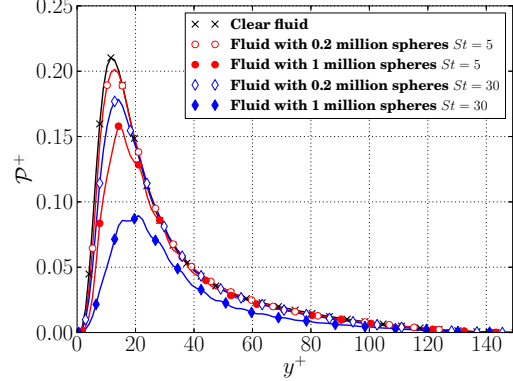


Figure 5.38.: Turbulence kinetic energy production as a function of distance to the wall

magnitude of \mathcal{P} decreases with increasing Stokes number. It is clearly observed from Fig. 5.38 that the production \mathcal{P} is considerably reduced by increasing particle volume fraction. The peak value of \mathcal{P}^+ decreases from 0.208 in the clear flow simulation to 0.091 in the case with $\alpha^p = 0.036\%$ and $St = 30$.

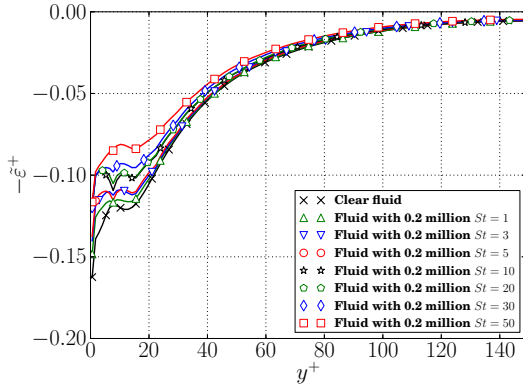


Figure 5.39.: Turbulence kinetic energy dissipation rate as a function of distance to the wall

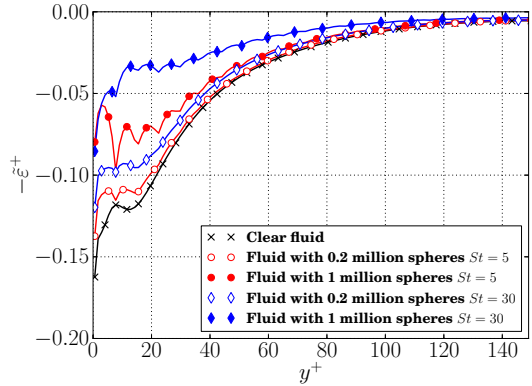


Figure 5.40.: Turbulence kinetic energy dissipation rate as a function of distance to the wall

5.4.2.3. The fluid flow dissipation rate

Figs. 5.39 and 5.40 display the negative fluid flow dissipation rate ($-\tilde{\varepsilon}$). The magnitudes of $\tilde{\varepsilon}$ is reduced significantly by increasing Stokes number and particle volume fraction in the near wall region, where particles accumulate. In the central region, the effect of particles on the flow dissipation rate are not clearly observed and the magnitude of $\tilde{\varepsilon}^+$ in all cases is close to zero as illustrated in Figs. 5.39 and 5.40.

5.4.2.4. Dissipation rate caused by the coupling force of the particles

In equation 3.3, the dissipation rate caused by the coupling force of the particles, ε_p , is the value of the covariance of the particle-fluid interaction force fluctuations and fluid velocity fluctuations and it is affected by the local particle volume fraction α_y^p and Stokes number. Figs. 5.41 and 5.42 show ε_p in the cases with various Stokes numbers and in the cases with different particle volume fraction, respectively. As can be seen from these two figures, the largest magnitude of ε_p is in the near wall region, around $y^+ = 6.5$. In Fig. 5.41, the largest peak magnitudes of ε_p is found in the case with $St = 10$. This is because much more particles with $St = 10$ accumulate in the near wall region, compared to the other cases with high or low Stokes numbers. As $\langle \alpha_y^p \rangle$ next to the wall is much larger in the case with $\alpha^p = 0.036\%$ and $St = 5$ than the other cases in Fig. 5.17, the peak magnitude of ε_p in this case also has the largest magnitude shown in Fig. 5.42. Comparing with the fluid dissipation rate $\tilde{\varepsilon}$ in Figs. 5.39 and 5.40, the magnitudes of ε_p are significantly smaller in all cases and can be negligible. However, the presence of small particles with high inertia still influences the turbulence intensity significantly. This is because the dispersed particles vary the velocity profile of the fluid and indirectly change the fluid flow dissipation rate and the production of turbulence. Therefore, the effect of particles is still important, and the two-way coupling should be taken into account.

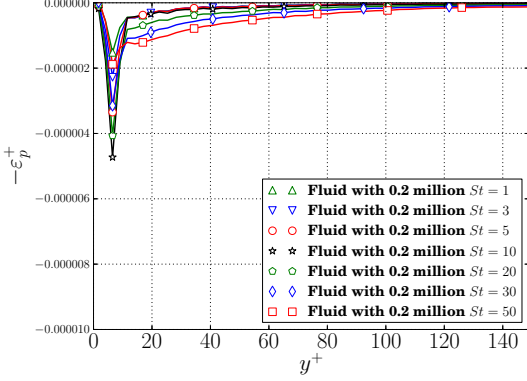


Figure 5.41.: The dissipation rate caused by the coupling force from particles as a function of distance to the wall

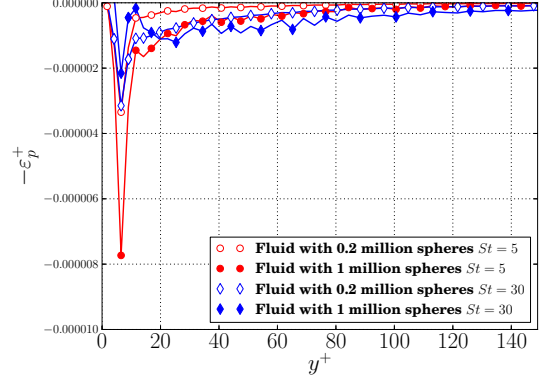


Figure 5.42.: The dissipation rate caused by the coupling force from particles as a function of distance to the wall

5.4.2.5. Components in the fluid dissipation rate

In equation 1.16, the fluid flow dissipation rate $\tilde{\varepsilon}$ is determined by the fluid viscosity ν^f and the fluid mean square derivatives. As explained in Sec. 5.4.1, the viscosity is constant and not changed in all particle-laden simulations, the reduction of $\tilde{\varepsilon}$ as shown in Figs. 5.39 and 5.40 must be caused by the changes of the fluid mean square derivatives. The fluid flow dissipation rate $\tilde{\varepsilon}$ consists of twelve components expressed as equation 1.17. From the twelve components, only the $\langle u_{1,2}^{\prime f} \rangle$, $\langle u_{3,2}^{\prime f} \rangle$ and $\langle u_{1,3}^{\prime f} \rangle$ mainly contribute to $\tilde{\varepsilon}$, and the magnitudes of all the other components can be negligible. These three mean square derivatives are shown in Figs. 5.43 to 5.48.

As can be seen in Fig. 5.43, $\langle u_{1,2}^{\prime f} \rangle$ decreases with increasing Stokes number in the cases with the same low particle volume fraction ($\alpha^p = 0.0073\%$) in the region between $5 < y^+ < 40$. Within $y^+ < 5$, $\langle u_{1,2}^{\prime f} \rangle$ in the cases with $St = 10$ and 20 is smaller than that in the case with $St = 30$. This is because more particles accumulate near the wall in the cases with $St = 10$ and $St = 20$ than in the case with $St = 30$, and this strengthens the effect of particles reducing $\langle u_{1,2}^{\prime f} \rangle$. In Figs. 5.44 and 5.45, $\langle u_{3,2}^{\prime f} \rangle$ and $\langle u_{1,3}^{\prime f} \rangle$ are also reduced as Stokes number rises between $0 < y^+ < 40$. In the region between $100 < y^+ < 150$, the effect of Stokes number on these mean square derivatives can be negligible in the particle-laden cases with low particle volume fraction ($\alpha^p = 0.0073\%$).

Figs. 5.46 to 5.48 show the three main components of the fluid flow dissipation rate $\tilde{\varepsilon}$ in the cases with various particle volume fraction. As can be seen in Fig. 5.46, $\langle u_{1,2}^{\prime f} \rangle$ decreases with increasing Stokes number and particle volume fractions in the near wall region ($5 < y^+ < 20$). However, $\langle u_{1,2}^{\prime f} \rangle$ in the case with $St = 5$ and $\alpha = 0.036\%$ is even lower than that in the case with $St = 30$ and $\alpha = 0.036\%$ next to the wall ($y^+ < 3$). This is because much more particles in the case $St = 5$ and $\alpha = 0.036\%$ accumulate next to the wall ($y^+ < 3$), compared to the case with $St = 30$ and $\alpha = 0.036\%$. This explains the steep increase and decrease of $\tilde{\varepsilon}$ in the case with $St = 5$ and $\alpha = 0.036\%$ near the wall shown in Fig. 5.40. Figs. 5.47 and 5.48 display the magnitudes of $\langle u_{3,2}^{\prime f} \rangle$ and $\langle u_{1,3}^{\prime f} \rangle$ decrease with increasing Stokes number and particle volume fraction through the whole

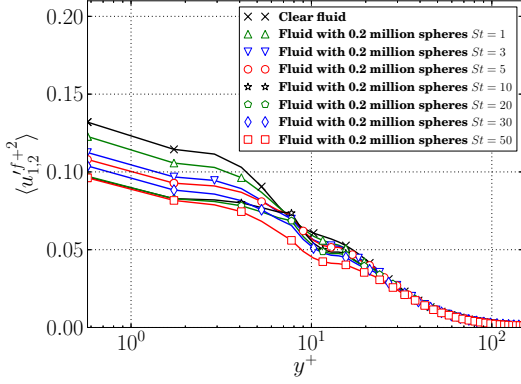


Figure 5.43.: Mean-square derivative $\langle u'^{f+2}_{1,2} \rangle$ as a function of distance to the wall

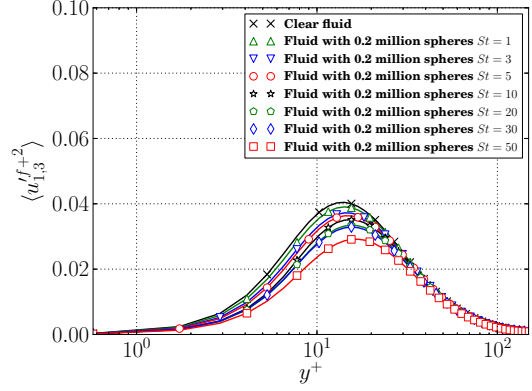


Figure 5.44.: Mean-square derivative $\langle u'^{f+2}_{1,3} \rangle$ as a function of distance to the wall

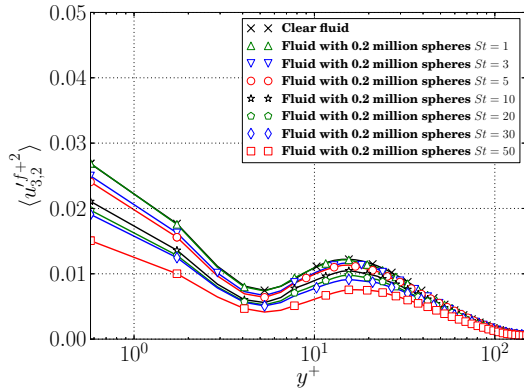


Figure 5.45.: Mean-square derivative $\langle u'^{f+2}_{3,2} \rangle$ as a function of distance to the wall

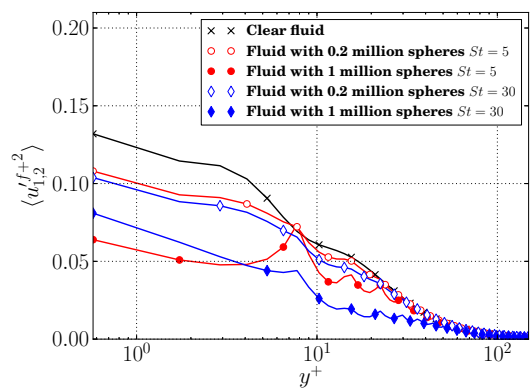


Figure 5.46.: Mean-square derivative $\langle u'^{f+2}_{1,2} \rangle$ as a function of distance to the wall

channel.

As shown in the Figs. 5.39 and 5.40, the magnitude of the fluid flow dissipation rate $\tilde{\varepsilon}$ decreases in the near wall region ($0 < y^+ < 20$). The local peak and minimum of $\tilde{\varepsilon}$ in the near wall region are caused by the reflect of $\langle u'^f_{1,2} \rangle$ between $10 < y^+ < 20$ and local peak and minimum in $\langle u'^f_{3,2} \rangle$ and $\langle u'^f_{1,3} \rangle$. It should be also noted that the influence of the effect of particles on these three mean square derivatives is in the different region. As can be seen from Figs. 5.43 and 5.46, large reduction of $\langle u'^f_{1,2} \rangle$ caused by the presence of particles is found close to the wall ($0 < y^+ < 10$) and considerably influenced by the local particle volume fraction $\langle \alpha_y^p \rangle$ next to the wall and the Stokes number. In Figs. 5.44 and 5.47, the decrease of $\langle u'^f_{3,2} \rangle$ is in the buffer layer between $10 < y^+ < 20$, not at the wall. $\langle u'^f_{1,3} \rangle$ in the cases considering heavy particles decreases in the region between $0 < y^+ < 30$ as shown in Figs. 5.45 and 5.48.

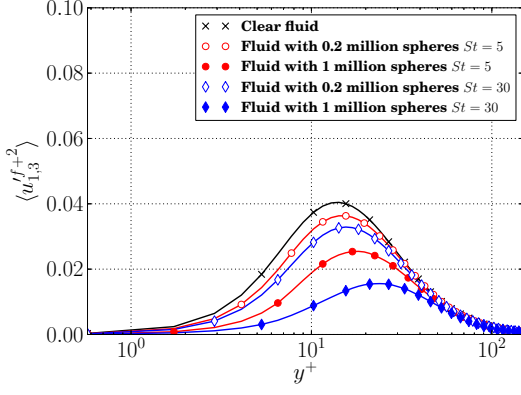


Figure 5.47.: Mean-square derivative $\langle u_{1,3}^{ff^2} \rangle$ as a function of distance to the wall

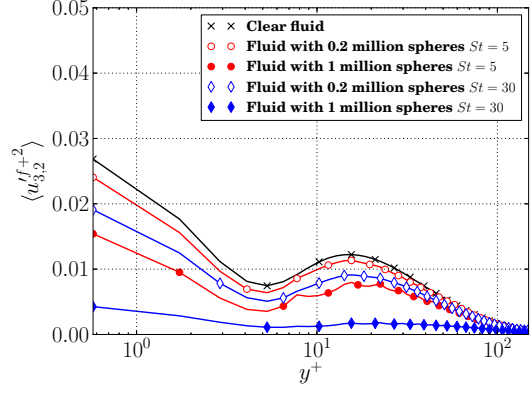


Figure 5.48.: Mean-square derivative $\langle u_{3,2}^{ff^2} \rangle$ as a function of distance to the wall

5.5. Particle statistics

To sample and analyse the statistics of discrete particles, the whole channel is divided into 100 equally spaced bins in the wall-normal direction, and a particle is determined in which bin based on the position of its mass center.

5.5.1. Particle velocity statistics

Figs. 5.49 to 5.52 show the statistics of the particle velocity in the particle-laden cases with various Stokes number and small particle volume fraction ($\alpha^p = 0.0073\%$), while Figs. 5.53 to 5.56 display the results in the cases with various particle volume fraction and Stokes number. As can be seen from these figures, the particle mean velocity and particle velocity fluctuations all increase with increasing St and α^p in the near wall region ($0 < y^+ < 10$).

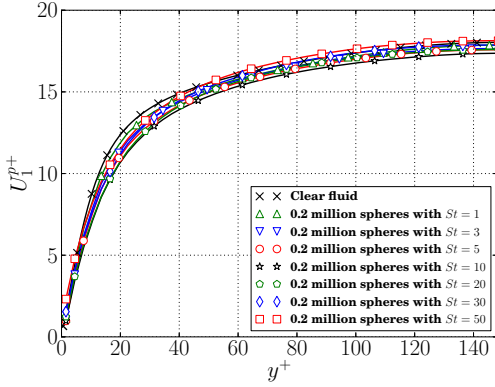


Figure 5.49.: Particle mean velocity in the stream-wise direction as a function of distance to the wall

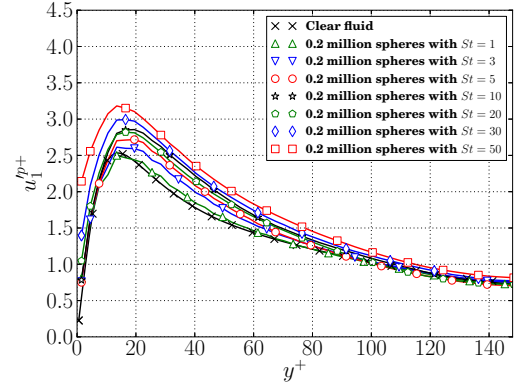


Figure 5.50.: Particle RMS velocity in the stream-wise direction as a function of distance to the wall

This is because particles are not directly affected by the non-slip condition of the wall.

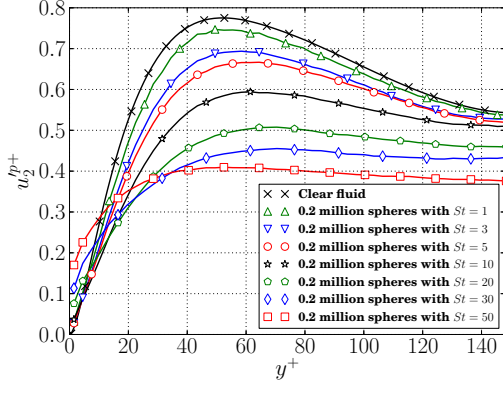


Figure 5.51.: Particle RMS velocity in the wall-normal direction as a function of distance to the wall

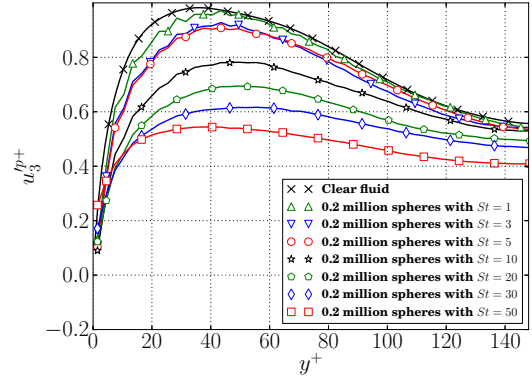


Figure 5.52.: Particle RMS velocity in the span-wise direction as a function of distance to the wall

Particles with high inertia can strongly resist the effects of the fluid flow and fluid velocity gradient caused by the wall effect, while increasing particle volume fraction strengthens the turbulence attenuation and thus further weaken the effect of the fluid flow on the particles. Figs. 5.50 to 5.52 and Figs. 5.54 to 5.56 show the particle RMS velocities in all three directions. In the outer region ($10 < y^+ < 150$), the particle RMS velocities in the stream-wise direction shown in Figs. 5.50 and 5.54 strikingly increases with increasing St and α^p , whereas particle velocity fluctuations in the wall-normal and span-wise directions

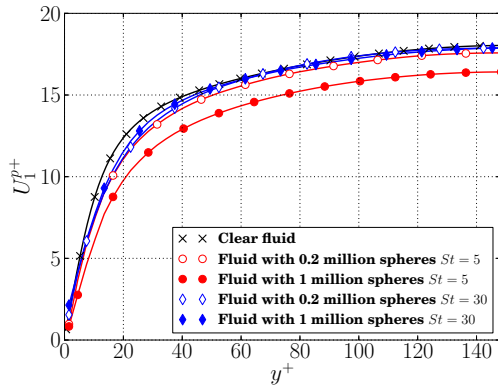


Figure 5.53.: Particle mean velocity in the steam-wise direction as a function of distance to the wall

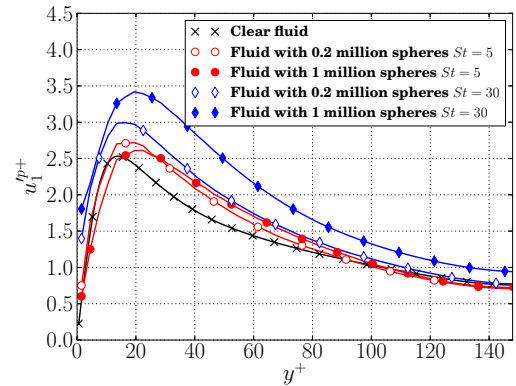


Figure 5.54.: Particle RMS velocity in the stream-wise direction as a function of distance to the wall

considerably decreases as St and α^p rise. These particle velocity fluctuations are consistent with fluid RMS velocities in the outer region.

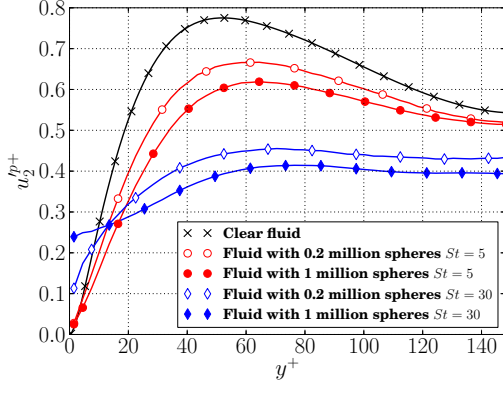


Figure 5.55.: Particle RMS velocity in the wall-normal direction as a function of distance to the wall

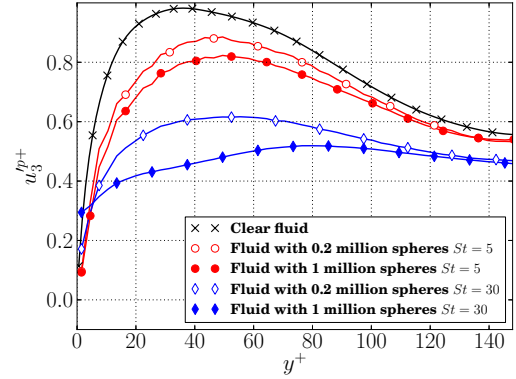


Figure 5.56.: Particle RMS velocity in the span-wise direction as a function of distance to the wall

5.5.2. Particle-fluid interactions

5.5.2.1. Slip velocity between particle and fluid mean velocities

In equation 3.10, the drag force on a spherical particle is determined by the slip velocity between the fluid flow and the sphere. Figs. 5.57 to 5.62 show the mean slip velocity in all three directions in the cases with various Stokes number and in the cases with different particle volume fractions. It is clearly observed from Figs. 5.57 and 5.60 that the slip velocity in the stream-wise direction ($U_1^f - U_1^p$) is negative in the near wall region ($0 < y^+ < 20$) and positive in the outer region ($30 < y^+ < 150$). These indicate that the particles transfer the momentum to the fluid flow in the near wall region but the fluid flow transfer the momentum back to the particles in the central region. As can be seen from Fig. 5.57, the magnitude of the stream-wise slip velocity is enlarged with increasing Stokes number. In Fig. 5.60, $(U_1^f - U_1^p)$ in the central region is not affected by varying the

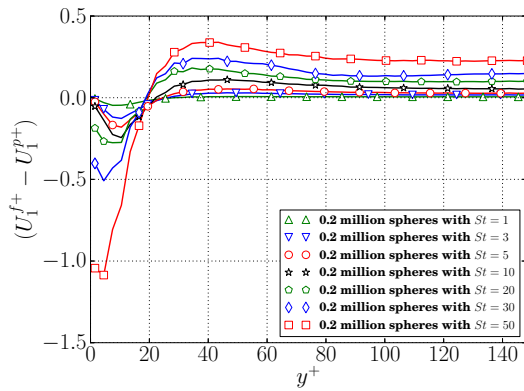


Figure 5.57.: Mean stream-wise slip velocity between particles and the fluid flow as a function of distance to the wall

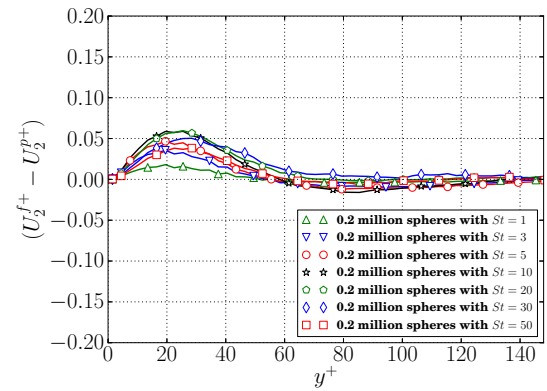


Figure 5.58.: Mean wall-normal slip velocity between particles and the fluid flow as a function of distance to the wall

particle volume fraction. However, the magnitude of $(U_1^f - U_1^p)$ rises with increasing α^p

in the cases considering particles with high inertia ($St = 30$). This is because in the cases with $St = 30$ particle mean velocity in the stream-wise direction in the near wall region considerably increases as α^p increases. The slip velocity in the wall-normal direction is

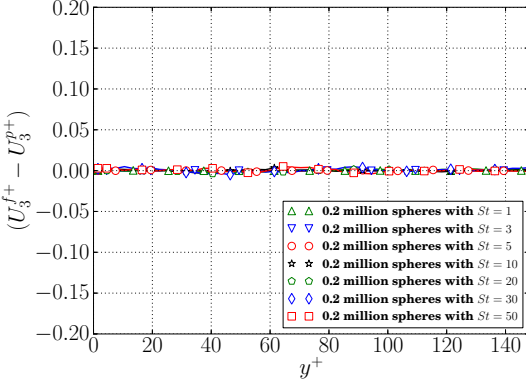


Figure 5.59.: Mean span-wise slip velocity between particles and the fluid flow as a function of distance to the wall

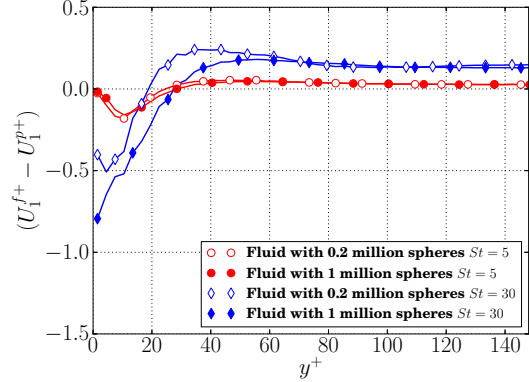


Figure 5.60.: Mean stream-wise slip velocity between particles and the fluid flow as a function of distance to the wall

almost 0 in the outer region ($60 < y^+ < 150$) in all the simulations, but positive within $0 < y^+ < 60$, as shown in Figs. 5.58 and 5.61. The positive wall-normal slip velocity reflects the main mechanism by which particles with high inertia accumulate close to the wall in the gas-solid turbulent channel flow. In Figs. 5.59 and 4.40, the span-wise slip velocity is close to zero through the whole channel in all cases, and both effects of Stokes

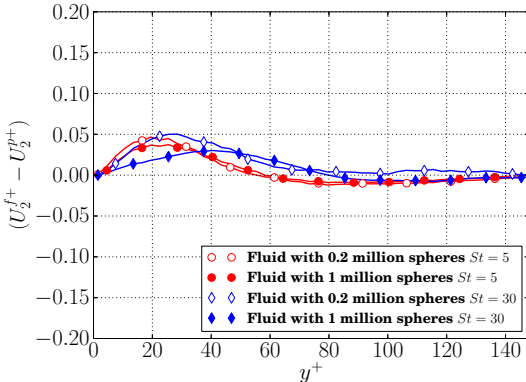


Figure 5.61.: Mean wall-normal slip velocity between particles and the fluid flow as a function of distance to the wall

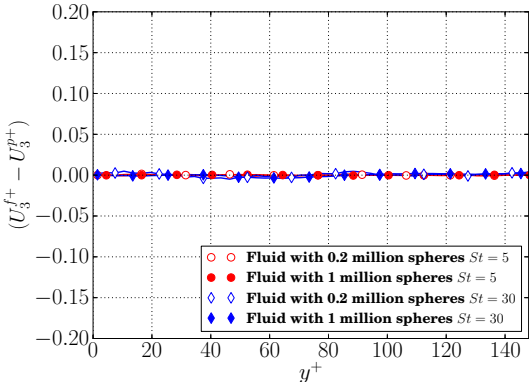


Figure 5.62.: Mean span-wise slip velocity between particles and the fluid flow as a function of distance to the wall

number and particle volume fractions are negligible as well as the momentum transfer in the span-wise direction.

5.5.2.2. The correlation coefficient between fluid and particle velocities

The velocity correlation coefficients $\hat{\rho}_i^{fp}$ in the stream-wise and wall-normal directions between the fluid flow and the particles are displayed in Figs. 5.63 to 5.66. As the effect of particle-wall collisions causes complex dynamics of particles, the velocity correlation coefficient $\hat{\rho}_i^{fp}$ in the near wall region is much lower than in the outer region, and the minimum of $\hat{\rho}_i^{fp}$ are next to the wall. As shown in these figures, the minimum value of $\hat{\rho}_i^{fp}$ reduces with increasing Stokes number and particle volume fraction. Comparing Fig. 5.63

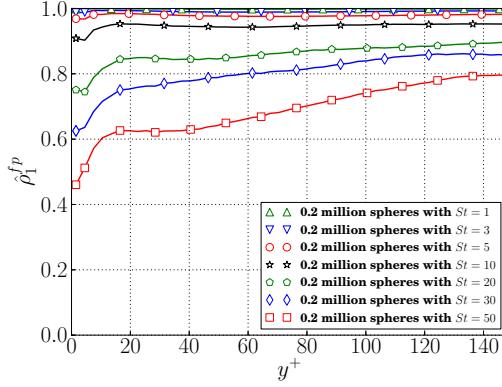


Figure 5.63.: The stream-wise correlation coefficient of particle and fluid velocities as a function of distance to the wall

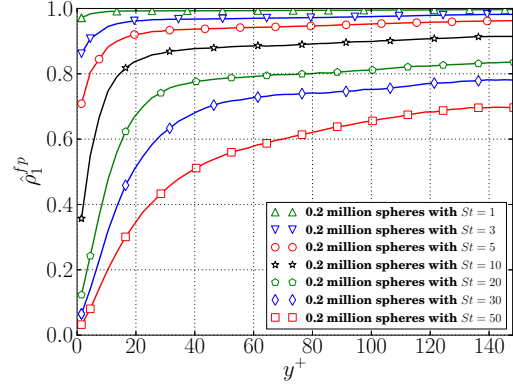


Figure 5.64.: The wall-normal correlation coefficient of particle and fluid velocities as a function of distance to the wall

and Fig. 5.65 with Fig. 5.64 and Fig. 5.66, the effect of the particle-wall collision on $\hat{\rho}_2^{fp}$ is significantly stronger than $\hat{\rho}_1^{fp}$ in the near wall region.

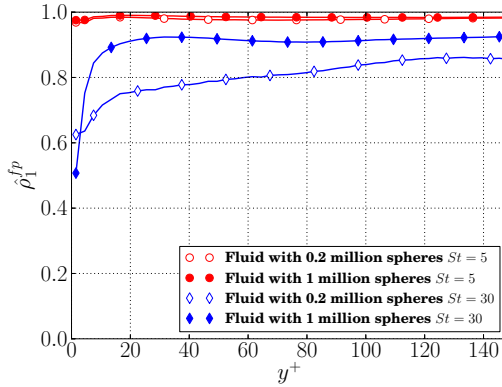


Figure 5.65.: The stream-wise correlation coefficient of particle and fluid velocities as a function of distance to the wall

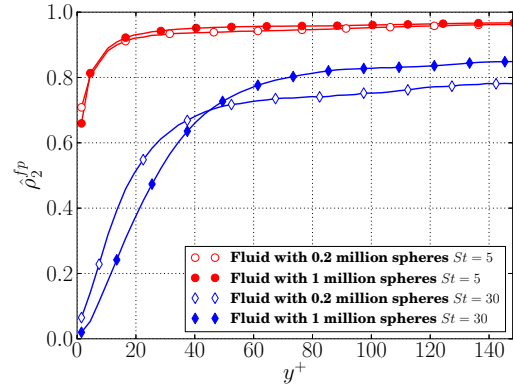


Figure 5.66.: The wall-normal correlation coefficient of particle and fluid velocities as a function of distance to the wall

5.6. Conclusions

In this chapter, the behaviour of spherical particles suspended in a turbulent channel flow is investigated, and the effects of the particle volume fraction and the Stokes number are analysed. Like the simulations in the last chapter, all the simulations in this chapter are performed by applying four-way coupled DNS with the Lagrangian point-particle method. The contour plots of the stream-wise velocity in x-z plane at $y^+ = 8$ near the wall show the low-speed streaks are much wider and more clearly seen in the cases with large Stokes number (St) and high particle volume fraction (α^p), compared to the cases with relatively small St and low α^p . The particles with high inertia spend more time in the low-speed areas than in the high-speed zones (large vortices). This phenomena is not affected by the particle volume fraction and Stokes number within the range between $3 < St < 50$.

The results of the local particle volume fraction $\langle \alpha_y^p \rangle$ indicate that $\langle \alpha_y^p \rangle$ in gas-solid channel flows with spheres peaks next to the wall. This is because the large and long vortices sweep both the fluid and particles towards the wall, whereas the particles with relatively high inertia ($St \gg 1$) hardly follow the fluid flow bursting to rapidly move away from the wall in the low-speed areas near the wall. For the cases with various Stokes number and the same low particle volume fraction, $\langle \alpha_y^p \rangle$ next to the wall peaks in the case with $St = 10$. For the cases with relatively low Stokes number ($St = 5$), the peak value of the local $\langle \alpha_y^p \rangle$ near the wall increase as the total α^p rises. However, when the total α^p increase to a high level, the peak of the local α^p in the cases with large Stokes number ($St = 30$) only slightly increases with the total α^p . This is because increasing the total α^p in the cases with large particle inertia can considerably reduce the turbulence intensity so that the fluid effects confining the particles near the wall are strongly weakened.

The results of the turbulence terms (Reynolds stress, the production of turbulence and the fluid flow dissipation rate) confirm that the turbulence intensity of the fluid flow is considerably attenuated with the increasing Stokes number and particle volume fraction. The three main components of the flow dissipation rate directly show how the dissipation rate varies in the near wall region with Stokes number and particle volume fraction.

In the region between $20 < y^+ < 150$, particle and fluid RMS velocities in the stream-wise direction rise with the increasing Stokes number and particle volume fraction, due to the large fluid velocity gradient. However, as the particles with high inertia slow down the fluid flow, velocity fluctuations of both particle and fluid phases decrease in the wall-normal and span-wise directions. In the near wall region ($0 < y^+ < 10$), particles are not influenced by the non-slip conditions, but the dynamics of the particles strongly affected by the particle-wall collisions. The increase of St and α^p can strengthen the effect of the particle-wall collision but resist the effect of the turbulence on the particles. Therefore, the particle velocity fluctuations increase as St and α^p rise in the near wall region. The results of the slip velocities show that the magnitude of the stream-wise slip velocity increases with the increasing St .

In this chapter, the results of the gas-solid channel flows with spherical particles demonstrate that the turbulence intensity of the fluid flow decreases with the increasing Stokes number and particle volume fractions, and the particle accumulation near the wall is also

strongly influenced by Stokes number and particle volume fraction.

6. Summary and recommendation for future plans

6.1. Summary

This research work applies a four-way coupled framework to predict the behaviour of gas-solid turbulent channel flows with non-spherical and spherical particles, and investigates the effects of particle volume fraction, particle shape and Stokes number on the behaviour of both the fluid flow and the particles. Previous studies, *e.g* [71, 77, 108], have performed one-way coupled simulations of the turbulent channel flow with ellipsoidal particles. These previous studies ignore the effect of particles on the fluid flow and also do not resolve the inter-particle and particle-wall collisions. However, at which level of particle volume fraction or mass loading the effects of the particles on the fluid flow, inter-particle and particle-wall collisions become significant is still uncertain for gas-solid multiphase flows with non-spherical particles; therefore, without considering these effects, the one-way coupled simulations in those previous studies may not be reliable and accurate. Moreover, only the statistics of dispersed particles are discussed in these one-way coupling studies. To perform more accurate simulations, this study applies the four-way coupling combined the point-particle approach to fully describe the gas-solid turbulent channel flows. The effects of the fluid flow and dispersed particles on both phases are all considered in this work, including the effect of the fluid flow on dispersed particles, the effect of the particles on the fluid flow, inter-particle and particle-wall collisions. This arrangement ensures that the results of both the fluid flow and particles can be analysed and the effects of particle inertia, particle volume fraction and particle shape can be investigated in this study.

Spherical particles are predominantly governed by translational motion only. However, for non-spherical particles the rotation and their orientation are important as well. In gas-solid multiphase flows, the orientation of non-spherical particles influences the fluid-particle and particle-particle interactions. In the previous studies, the orientation and rotation of non-spherical ellipsoids are described by Unit Quaternions in the conjunction with rotation matrices, and the integration of unit Quaternions are all based on Taylor expansions in their studies. These methods all vary the length of the unit Quaternions, and the Quaternions need to be re-normalised after each particle time step to keep their unit length. However, the renormalisation changes the relationship between the components in a Quaternion and leads to numerous errors when modelling the rotation of non-spherical particles. To more accurately and efficiently represent the rotation of particles, this thesis proposes a novel Quaternion integration method, called predictor-corrector direct multiplication (PCDM) method, to update the Unit Quaternions. This novel algorithm avoids

the use of subtraction or addition of Quaternions and applies the multiplication of unit Quaternions only. Therefore, the unit length of the Quaternions is preserved without the re-normalisation procedure. Moreover, this algorithm is based on the corrector-predictor method so that the various time-levels are not mixed. In the Quaternion framework, a new Quaternion expression is derived to relate second order tensors between different coordinate frameworks, and thus the corresponding rotation matrices can be removed from this study. The comparison between the novel predictor-corrector direct multiplication method and other three Quaternion integration methods from the literature shows that the PCDM method has a higher order rate of convergence than other methods from the literature and has a significant improvement in the accuracy of describing rotation. This thesis applies unit Quaternions solely with the PCDM method to accurately represent the orientation and rotation of non-spherical particles, so that more accurate results of the particle orientation are obtained in this study than those in the previous studies.

To perform more accurate simulations of gas-solid turbulent channel flows, the four-way coupled DNS combined with the point-particle approach is applied in this study. The four-way coupling and direct numerical simulation (DNS) guarantee the accuracy of the fluid flow and take the effect of particles on the fluid turbulence and the particle collision into account. Unlike the one-way coupled studies [71, 77, 108], these arrangements enable this study to investigate the change of the fluid flow turbulence caused by the dispersed particles.

In Chapter 4, the effects of Stokes number and elongated shape of ellipsoids on both particles and fluid flow are studied by comparing simulations considering ellipsoidal particles with various Stokes number and particle aspect ratio. The fluid results of fluid RMS velocities, Reynolds stress, the production of turbulence and the fluid flow dissipation rate all show that the presence of ellipsoidal particles with high inertia (large Stokes number) and large particle aspect ratio can attenuate the turbulence intensity significantly. This is because particles with high inertia cannot respond quickly to the changes of the fluid behaviour, delaying the fluid flow and attenuating the turbulence intensity. In the cases with the same large Stokes number, the elongated shape of ellipsoids further strengthens the effect of particles on the fluid flow, and thus further decreasing the flow turbulence. Although the dissipation rate caused by the coupling force from particles, ε_p , is extremely small in the dilute flows, the presence of particles can still considerably influence the fluid flow. This is because the dispersed particles affect the velocity profile of the fluid and indirectly change the fluid flow dissipation rate and the production of turbulence. These fluid results indicate that the effect of the fluid flow on particles should be included in the simulations, which requires at least two-way coupling. From the results of the particle distribution, it is apparent that the particles with high inertia preferentially accumulate in the near wall region of the channel. The main mechanisms behind this phenomena of particle accumulation in the channel flow are that large and slow vortices (usually referred to as “sweeps”) sweep the fluid and particles towards the wall, whereas the particles with relatively high inertia ($St \gg 1$) cannot follow the flow bursts away from the wall. Thus the particles preferentially accumulate in the low speed streaks very near the wall. With

increasing Stokes number and particle aspect ratio, however, the peak value of particle volume fraction next to the wall decreases. This is because particles with significantly high inertia and aspect ratio strongly resist the effect of turbulence on them. The results of the large stream-wise slip velocity in the case with large Stokes number imply a strong momentum transfer between the two phases in this direction. However, the mean slip velocities in the other directions are very small through the channel, and thus the momentum transfer is weak in the span-wise and wall-normal directions. Because particles with high inertia cannot respond quickly to the behaviour of the fluid flow, the velocity correlation between particles and the fluid flow are reduced with increasing particle inertia. Very close to the wall, the particle-wall collisions lead to more complex dynamics of ellipsoids than spheres; therefore, the velocities between the ellipsoids and the fluid flow are less correlated in the near wall region than those between spherical particles and the fluid flow.

The previous studies [71, 77, 108] analyse the orientation of ellipsoids by representing the mean absolute cosine values of the orientation angles. However, the non-linear cosine function may underestimate or overestimate the interpolation of the effect of the orientation angles. Therefore, this study directly analyses the mean orientation angles (θ_i) of particles between the vector of particle major axis (\mathbf{X}^p) aligning with the x axis of body space and axes of world space. The results of mean θ_i shows that ellipsoidal particles tend to align in the x-y plane and perpendicular to the span-wise direction in the near wall region. This is most likely caused by the fluid dynamics of the boundary layer. However, due to three θ_i related to each other, their mean values and distribution in the central region of the channel cannot sufficiently conclude that ellipsoids are randomly distributed at channel center, nor that they have a preferential orientation. Therefore, another orientation angle ψ_i is proposed to represent the orientation of ellipsoid. ψ_i represents the orientation of the 2-D projected particle major axis vector on the y-z, x-z, x-y planes, which perpendicular to the x, y and z axes of world space. The uniform distribution of ψ_i in the central region of the channel indicates that the orientation of particles is almost randomly distributed in the central region without any preferential orientation.

The results of ellipsoidal particles described in Chapter 4 confirm that the fluid turbulence is attenuated by adding small and heavy particles, even in the dilute flow. The turbulence intensity decreases with increasing particle inertia and particle aspect ratio. Moreover, the particle statistical results in the very near wall region prove that particle-particle and particle-wall collisions have some effect on ellipsoid behaviours.

Chapter 5 considers only spherical particles, and investigates the effect of Stokes number and particle volume fraction on the flow. The fluid results show that the turbulence intensity of the fluid flow is considerably attenuated with increasing Stokes number and particle volume fraction. The stream-wise velocity contour plots in the near wall region show that the low-speed streaks are much wide and much clearly observed in the case with large Stokes number and large particle volume fraction. The results of particle distribution around $y^+ = 8$ show that particles preferentially accumulate in the low-speed streaks and avoid the areas of large vortices, and this phenomena is not influenced by Stokes number

(between $3 < St < 50$) and particle volume fractions. The results of the local particle volume fraction $\langle \alpha_y^p \rangle$ indicate that $\langle \alpha_y^p \rangle$ of the spherical particles in the channel flows peaks next to the wall.

This study expands the previous one-way coupling studies [70, 71, 77, 108] to investigate the gas-solid channel flows with non-spherical ellipsoids. The results of the four-way coupled simulations show that the fluid turbulence is attenuated by adding small particles with high inertia, even in the very dilute flow of interest in this work. The elongated shape of non-spherical ellipsoids somewhat influence the flow turbulence, and the particle-wall collision for ellipsoidal particles affects the dynamics of particles and the particle statistics significantly in the near wall region. It should be noted that the average viscosity of the flow is not affected, the average direct dissipation by the particles is negligible, and the primary mechanism by which the particles affect the flow is by altering the turbulence structure near and around the kinetic energy peak. As this study applies the more accurate PCDM methods to determine the rotation and orientation of non-spherical particles, more accurate results of the particle orientation are shown and discussed in the thesis.

6.2. Future plans

The research work presented in this thesis investigates the effects of Stokes number, elongated shape of ellipsoids and particle volume fraction on the behaviour of gas-solid channel flows, and the results show that the elongated shape and the particle collision between non-spherical particles influence the gas-solid channel flow. Therefore, future work should apply four-way coupling for modelling gas-solid multiphase flows with non-spherical particles rather than the one-way coupling. However, four-way coupled simulations require substantial computational time and source. Due to the limited computation capacity, the aspect ratio of elongated ellipsoids applied in this study is confined at quite low value (3 and 5), and the particle volume fraction is also limited at a very low level (0.0073% to 0.036%). With increasing computing power, the future work should focus on modelling gas-solid channel flows with much longer ellipsoids and dense flows.

In the literature, the hydrodynamic drag on ellipsoids and spheres are well approximated, but the effects of the fluid flow on solid particles with other complex non-spherical shapes have not been well studied and predicted yet; therefore, the particle shape is limited to the ellipsoidal and spherical particles in this work. As the dispersed multiphase flow with non-spherical particles is of growing interest, the complex interactions between the fluid flow and non-spherical particles will be extensively studied experimentally and numerically in the near future. In all the simulations of this study, the smooth wall condition is applied, and friction Reynolds number is fixed at 150. Therefore, the effects of these two parameters on the gas-solid channel flows are not discussed in this thesis. It is well reported that the rough wall influences significantly on both fluid and particle phases for gas-solid channel flows with spheres. As the collision between the wall and non-spherical particles are more complex than spherical particles, it is worthwhile to investigate the effect of rough wall on the dynamics and orientation of non-spherical particles. This is

also a good research direction in the future.

Bibliography

- [1] Allen, M. P. and Tildesley, D. J. (1989). *The Computer Simulation of Liquids, Vol 42.* Oxford University Press.
- [2] Altmann, S. L. (1986). *Rotations, Quaternions, and Double Groups*, volume 3. Clarendon Press Oxford, England.
- [3] Andersson, H. I., Zhao, L., and Barri, M. (2012). Torque-coupling and particle-turbulence interactions. *Journal of Fluid Mechanics*, **696**, 319–329.
- [4] Antonia, R. A. and Kim, J. (1994). A numerical study of local isotropy of turbulence. *Physics of Fluids*, **6**(2), 834–841.
- [5] Antonia, R. A., Kim, J., and Browne, L. W. B. (1991). Some characteristics of small-scale turbulence in a turbulent duct flow. *Journal of Fluid Mechanics*, **233**(0), 369–388.
- [6] Arribas, M., Elipe, A., and Palacios, M. (2006). Quaternions and the rotation of a rigid body. *Celestial Mech Dyn Astr*, **96**(3-4), 239–251.
- [7] Bakewell, H. P. (1967). Viscous Sublayer and Adjacent Wall Region in Turbulent Pipe Flow. *Physics of Fluids*, **10**(9), 1880.
- [8] Balachandar, S. and Eaton, J. K. (2010). Turbulent Dispersed Multiphase Flow. *Annual Review of Fluid Mechanics*, **42**(1), 111–133.
- [9] Baraff, D. (1997). An Introduction to Physically Based Modeling : Rigid Body Simulation I Unconstrained Rigid Body Dynamics Rigid Body Simulation. *SIGGRAPH Course Notes*.
- [10] Benavides, A. and van Wachem, B. (2009). Eulerian-Eulerian prediction of dilute turbulent gas-particle flow in a backward-facing step. *International Journal of Heat and Fluid Flow*, **30**(3), 452–461.
- [11] Benson, M., Tanaka, T., and Eaton, J. K. (2005). Effects of Wall Roughness on Particle Velocities in a Turbulent Channel Flow. *Journal of Fluids Engineering - Transactions of the ASME*, **127**(2), 250 – 256.
- [12] Betsch, P. and Siebert, R. (2009). Rigid body dynamics in terms of quaternions: Hamiltonian formulation and conserving numerical integration. *International Journal for Numerical Methods in Engineering*, **79**(4), 444–473.
- [13] Betsch, P. and Steinmann, P. (2001). Constrained integration of rigid body dynamics. *Computer Methods in Applied Mechanics and Engineering*, **191**(3-5), 467–488.

- [14] Brenner, H. (1963). The Stokes resistance of an arbitrary particle. *Chemical Engineering Science*, **18**(1), 1–25.
- [15] Brenner, H. (1964a). The Stokes resistance of an arbitrary particle-III: Shear fields. *Chemical Engineering Science*, **19**(9), 631–651.
- [16] Brenner, H. (1964b). The Stokes resistance of an arbitrary particle-IV Arbitrary fields of flow. *Chemical Engineering Science*, **19**(9), 631–651.
- [17] Bruchmüller, J., Gu, S., Luo, K. H., and van Wachem, B. (2010). Discrete Element Method for Multiscale Modeling. *Journal of Multiscale Modelling*, **02**(01n02), 147.
- [18] Celledoni, E. and Säfström, N. (2006). Efficient time-symmetric simulation of torqued rigid bodies using Jacobi elliptic functions. *Journal of Physics A: Mathematical and General*, **39**(19), 5463–5478.
- [19] Celledoni, E., Fassò, F., Säfström, N., and Zanna, A. (2008). The exact computation of the free rigid body motion and its use in splitting methods. *SIAM Journal on Scientific Computing*, **30**, 2084–2112.
- [20] Chou, J. (1992). Quaternion kinematic and dynamic differential equations. *IEEE Transactions on Robotics and Automation*, **8**(1), 53–64.
- [21] Corino, E. and Brodkey, R. S. (1969). A visual investigation of the wall region in turbulent flow. *Journal of Fluid Mechanics*, **37**(01), 1–30.
- [22] Crowe, C. T., Sharma, M. P., and Stock, D. E. (1977). The Particle-Source-In Cell (PSI-CELL) Model for Gas-Droplet Flows. *Journal of Fluids Engineering*, **99**(2), 325–333.
- [23] Crowe, C. T., Sommerfeld, M., and Tsuji, Y. (1998). *Multiphase Flows with Droplets and Particles*. CRC Press.
- [24] Cundall, P. A. and Strack, O. D. L. (1979). A discrete numerical model for granular assemblies. *Géotechnique*, **29**(1), 47–65.
- [25] Dastan, A. and Abouali, O. (2013). Microfiber motion and web formation in a microchannel heat sink: A numerical approach. *Computers & Fluids*, **71**, 28–40.
- [26] Delaney, G. W. and Cleary, P. (2010). The packing properties of superellipsoids. *EPL (Europhysics Letters)*, **89**(3), 34002.
- [27] Denner, F. and van Wachem, B. (2014). Fully-coupled balanced-force VOF framework for arbitrary meshes with least-squares curvature evaluation from volume fractions. *Numerical Heat Transfer, Part B: Fundamentals*, **65**(3), 218–255.
- [28] Diebel, J. (2006). Representing attitude: Euler angles, unit quaternions, and rotation vectors. Technical report, Stanford University, California, USA.

- [29] Eaton, J. K. (2009). Two-way coupled turbulence simulations of gas-particle flows using point-particle tracking. *International Journal of Multiphase Flow*, **35**(9), 792–800.
- [30] Eberly, D. (2002a). Quaternion algebra and calculus. *Magic Software, Inc*, **21**, 1–10.
- [31] Eberly, D. (2002b). Rotation representations and performance issues. *Magic Software*, **6006**, 1–13.
- [32] Elghobashi, S. and Truesdell, G. C. (1993). On the two-way interaction between homogeneous turbulence and dispersed solid particles. I: Turbulence modification. *Physics of Fluids A*, **5**(7), 1790.
- [33] Eskin, D. (2005). Modeling dilute gas-particle flows in horizontal channels with different wall roughness. *Chemical Engineering Science*, **60**(3), 655–663.
- [34] Evans, D. and Murad, S. (1977). Singularity free algorithm for molecular dynamics simulation of rigid polyatomics. *Molecular Physics*, **34**(2), 327–331.
- [35] Fan, F.-G. and Ahmadi, G. (1995). A sublayer model for wall deposition of ellipsoidal particles in turbulent streams. *Journal of Aerosol Science*, **26**(5), 813–840.
- [36] Fessler, J. R., Kulick, J. D., and Eaton, J. K. (1994). Preferential concentration of heavy particles in a turbulent channel flow. *Physics of Fluids*, **6**(11), 3742.
- [37] Gallily, I. and Cohen, A. (1979). On the orderly nature of the motion of nonspherical aerosol particles. II. Inertial collision between a spherical large droplet and an axially symmetrical elongated particle. *Journal of Colloid and Interface Science*, **68**(2), 338–356.
- [38] George, W. (2005). *Lectures in Fluid Mechanics*.
- [39] George, W. and Hussein, H. J. (1991). Locally axisymmetric turbulence. *Journal of Fluid Mechanics*, **233**, 1–23.
- [40] George, W. K. (2010). Lectures in Turbulence for the 21st Century. Technical report.
- [41] Gillissen, J., Boersma, B. J., Mortensen, P., and Andersson, H. (2008). Fibre-induced drag reduction. *Journal of Fluid Mechanics*, **602**, 209–218.
- [42] Gillissen, J. J. J., Boersma, B. J., Mortensen, P. H., and Andersson, H. I. (2007). On the performance of the moment approximation for the numerical computation of fiber stress in turbulent channel flow. *Physics of Fluids*, **19**(3), 035102.
- [43] Goto, S. and Vassilicos, J. C. (2006). Self-similar clustering of inertial particles and zero-acceleration points in fully developed two-dimensional turbulence. *Physics of Fluids*, **18**(11), 115103;1–10.
- [44] Grassia, F. S. (1998). Practical Parameterization of Rotations Using the Exponential Map. *The Journal of Graphics Tools*, **3**, 1–13.

- [45] Gspöner, A. and Hurni, J.-P. (1993). The physical heritage of Sir W.R. Hamilton. In *The Mathematical Heritage of Sir William Rowan Hamilton - commemorating the sesquicentennial of the invention of quaternions*, pages 1–37, Trinity College, Dublin.
- [46] Hairer, E. and Vilmart, G. (2006). Preprocessed discrete MoserVeselov algorithm for the full dynamics of a rigid body. *Journal of Physics A: Mathematical and General*, **39**(42), 13225–13235.
- [47] Hamilton, W. R. (1844). On quaternions; or on a new system of imaginaries in Algebra. *The London, Edinburgh and Dublin Philosophical Magazine and Journal of Science(3rd Series)*, **15 - 36**, 1–306.
- [48] Head, M. and Bandyopadhyay, P. (1981). New aspects of turbulent boundary-layer structure. *Journal of Fluid Mechanics*, **107**(1981), 297–338.
- [49] Hoffmann, G. (1978). Application of Quaternions. Technical Report February 1978, Technische Universität Braunschweig.
- [50] Hoover, W. G. (1986). *Lecture Notes in Physics Molecular Dynamics*. Springer, US.
- [51] Ibanez, L. (2001). Tutorial on Quaternions Part I. Technical Report 8, Insight Segmentation and Registration Toolkit, ITK.
- [52] Jeffery, G. B. (1922). The motion of ellipsoidal particles immersed in a viscous fluid. *Proceedings of the Royal Society of London. Series A, Containing Papers of a Mathematical and Physical Character*, **102**(715), 161–179.
- [53] Karney, C. F. F. (2007). Quaternions in molecular modeling. *Journal of Molecular Graphics and Modelling*, **25**(5), 595–604.
- [54] Kim, J. and Antonia, R. A. (1993). Isotropy of the small scales of turbulence at low Reynolds number. *Journal of Fluid Mechanics*, **251**, 219–238.
- [55] Kim, J., Moin, P., and Moser, R. (1987). Turbulence statistics in fully developed channel flow at low Reynolds number. *Journal of Fluid Mechanics*, **177**(1), 133–166.
- [56] Kleppmann, M. (2007). Simulation of colliding constrained rigid bodies. Technical Report 683, University of Cambridge, UCAM-CL-TR-683, ISSN 1476-2986.
- [57] Kline, S. J., Reynolds, W. C., Schraub, F. A., and Runstadler, P. W. (1967). The structure of turbulent boundary layers. *Journal of Fluid Mechanics*, **30**(04), 741–773.
- [58] Kosenko, I. (1998). Integration of the equations of a rotational motion of a rigid body in quaternion algebra. The Euler case. *Journal of Applied Mathematics and Mechanics*, **62**(2), 193–200.
- [59] Kuipers, J. B. (1999). Quaternions and rotation sequences. *Materials Science and Engineering A*, **271**(d), 322–333.

- [60] Kulick, J. D., Fessler, J. R., and Eaton, J. K. (1994). Particle response and turbulence modification in fully developed channel flow. *Journal of Fluid Mechanics*, **277**(1), 109–134.
- [61] Kussin, J. and Sommerfeld, M. (2002). Experimental studies on particle behaviour and turbulence modification in horizontal channel flow with different wall roughness. *Experiments in Fluids*, **33**(1), 143–159.
- [62] Lain, S., Sommerfeld, M., and Kussin, J. (2002). Experimental studies and modelling of four-way coupling in particle-laden horizontal channel flow. *International Journal of Heat and Fluid Flow*, **23**(5), 647–656.
- [63] Langston, P. A., Al-Awamleh, M. A., Fraige, F. Y., and Asmar, B. N. (2004). Distinct element modelling of non-spherical frictionless particle flow. *Chemical Engineering Science*, **59**(2), 425–435.
- [64] Latham, J. and Munjiza, A. (2004). The modelling of particle systems with real shapes. *Philosophical Transactions of the Royal Society of London. Series A: Mathematical, Physical and Engineering Sciences*, **362**(1822), 1953.
- [65] Lin, J., Zhang, W., and Yu, Z. (2004). Numerical research on the orientation distribution of fibers immersed in laminar and turbulent pipe flows. *Journal of Aerosol Science*, **35**(1), 63–82.
- [66] Mallouppas, G. and van Wachem, B. (2010). Modelling of dense particle-laden pipe flow and a free jet. In *12th Workshop on Two-Phase Flow Predictions, Germany, 22 - 25 March*, number March, pages 1–17.
- [67] Mallouppas, G. and van Wachem, B. (2013). Large Eddy Simulations of Turbulent Particle-Laden Channel Flow. *International Journal of Multiphase Flow*, **54**, 65–75.
- [68] Mallouppas, G., George, W. K., and van Wachem, B. (2013). New forcing scheme to sustain particle-laden homogeneous and isotropic turbulence. *Physics of Fluids*, **25**(083304).
- [69] Marchioli, C. and Soldati, A. (2013). Rotation statistics of fibers in wall shear turbulence. *Acta Mechanica*, **224**(10), 2311–2329.
- [70] Marchioli, C., Soldati, A., Kuerten, J. G. M., Arcen, B., Taniere, A., Goldensoph, G., Squires, K. D., Cargnelutti, M. F., and Portela, L. M. (2008). Statistics of particle dispersion in direct numerical simulations of wall-bounded turbulence: Results of an international collaborative benchmark test. *International Journal of Multiphase Flow*, **34**(9), 879–893.
- [71] Marchioli, C., Fantoni, M., and Soldati, A. (2010). Orientation, distribution, and deposition of elongated, inertial fibers in turbulent channel flow. *Physics of Fluids*, **22**(3), 033301.

- [72] Maxey, M. R. and Riley, J. J. (1983). Equation of motion for a small rigid sphere in a nonuniform flow. *Physics of Fluids*, **26**(4), 883.
- [73] McLachlan, R. I. and Zanna, A. (2003). The discrete Moser-Veselov algorithm for the free rigid body, revisited. Technical report, University of Bergen.
- [74] Mindlin, R. D. and Deresiewicz, H. (1953). Elastic spheres in contact under varying oblique forces. *J. of Appl. Mech.*, **20**, 327–344.
- [75] Mohanarangam, K. and Tu, J. (2007). Two-fluid model for particle-turbulence interaction in a backward-facing step. *AICHE Journal*, **53**(9), 2254–2264.
- [76] Mortensen, P., Andersson, H., Gillissen, J., and Boersma, B. J. (2008a). Dynamics of prolate ellipsoidal particles in a turbulent channel flow. *Physics of Fluids*, **20**(9), 093302.
- [77] Mortensen, P., Andersson, H., Gillissen, J., and Boersma, B. (2008b). On the orientation of ellipsoidal particles in a turbulent shear flow. *International Journal of Multiphase Flow*, **34**(7), 678–683.
- [78] Moser, J. and Veselov, A. P. (1991). Discrete versions of some classical integrable systems and factorization of matrix polynomials. *Communications in Mathematical Physics*, **139**(2), 217–243.
- [79] Oliveira, J., Mark, A., and van Wachem, B. (2007). A Fully Coupled and Implicit Immersed Boundary Method for Multiphase Flows. In *ICMF*, number 2003, pages 1–9.
- [80] Olson, J. and R.J. Kerekes (1998). The motion of fibres in turbulent flow. *Journal of Fluid Mechanics*, **377**, 47–64.
- [81] Paschkewitz, J. S., Dubief, Y., Dimitropoulos, C. D., Shaqfeh, E. S. G., and Moin, P. (2004). Numerical simulation of turbulent drag reduction using rigid fibres. *Journal of Fluid Mechanics*, **518**, 281–317.
- [82] Pope, S. B. (2000). *Turbulent Flows*. Cambridge Univ Press, Cambridge, 6th edition.
- [83] Portela, L. and Oliemans, R. (2003). Eulerian - Lagrangian DNS/LES of particle - turbulence interactions in wall-bounded flows. *International Journal for Numerical Methods in Fluids*, **43**(9), 1045–1065.
- [84] Press, W. H., Teukolsky, S. A., Vetterling, W. T., and Flannery, B. P. (1992). *Numerical Recipes in C*, volume 29. Cambridge University Press.
- [85] Qi, D. (2006). Direct simulations of flexible cylindrical fiber suspensions in finite Reynolds number flows. *The Journal of Chemical Physics*, **125**(11), 114901.
- [86] Rowe, P. N. (1961). Drag forces in a hydraulic model of a fluidized bed, part II. *Trans. Inst. Chem. Engrs.*, **39**, 175–180.

- [87] Sabatini, A. M. (2005). Quaternion-based strap-down integration method for applications of inertial sensing to gait analysis. *Medical & Biological Engineering & Computing*, **43**(1), 94–101.
- [88] Schiller, L. and Naumann, A. (1933). Über die grundlegenden Berechnungen bei der Schwerkraftaufbereitung. *Ver. Deut. Ing.*, **77**, 318–320.
- [89] Shapiro, M. and Goldenberg, M. (1993). Deposition of glass fiber particles from turbulent air flow in a pipe. *Journal of Aerosol Science*, **24**(1), 65–87.
- [90] Sommerfeld, M. and Kussin, J. (2003). Analysis of collision effects for turbulent gas-particle flow in a horizontal channel. Part II. Integral properties and validation. *International Journal of Multiphase Flow*, **29**(4), 701–718.
- [91] Sommerfeld, M. and Kussin, J. (2004). Wall roughness effects on pneumatic conveying of spherical particles in a narrow horizontal channel. *Powder Technology*, **142**(2-3), 180–192.
- [92] Sommerfeld, M., van Wachem, B., and Oliemans, R. (2008). *Best Practice Guidelines for Dispersed Turbulent Multi-Phase Flow Computations*. ERCOFTAC, Brussels.
- [93] Squires, K. D. and Eaton, J. K. (1991). Preferential concentration of particles by turbulence. *Physics of Fluids A: Fluid Dynamics*, **3**(5), 1169.
- [94] Taylor, G. (1935). Statistical theory of turbulence. *Proceedings of the Royal Society of London. Series A*, pages 421–444.
- [95] Tsuji, Y., Morikawa, Y., and Shiomi, H. (1984). LDV measurements of an air-solid two-phase flow in a vertical pipe. *Journal of Fluid Mechanics*, **139**, 417–434.
- [96] Tsuji, Y., Morikawa, Y., and Tanaka, T. (1987). Numerical simulation of gas-solid two-phase flow in a two-dimensional horizontal channel. *International Journal of Multiphase Flow*, **13**(5), 671–684.
- [97] Tsuji, Y., Tanaka, T., and Ishida, T. (1992). Lagrangian numerical simulation of plug flow of cohesionless particles in a horizontal pipe. *Powder Technology*, **71**(3), 239–250.
- [98] van Wachem, B., Schouten, J. C., Krishna, R., and Bleek, C. M. V. D. (1999). Validation of the Eulerian simulated dynamic behaviour of gas-solid fluidised beds. *Chemical Engineering Science*, **54**, 2141–2149.
- [99] van Wachem, B., Van der Schaaf, J., Schouten, J., Krishna, R., and van den Bleek, C. (2001). Experimental validation of Lagrangian-Eulerian simulations of fluidized beds. *Powder Technology*, **116**(2), 155–165.
- [100] van Wachem, B., Zastawny, M., Mallouppas, G., Zhao, F., Denner, F., and Pennefather, J. (2012). <http://www.multiflow.org/>.

- [101] van Wachem, B., Zastawny, M., Mallouppas, G., and Zhao, F. (2013). Modelling of gas-solid turbulent flows with non-spherical particles. In *8th International Conference on Multiphase Flow (ICMF 2013)*, pages 1–6.
- [102] Walton, O. R. (1993). Numerical simulation of inclined chute flows of monodisperse, inelastic, frictional spheres. *Mechanics of Materials*, **16**, 239–247.
- [103] Walton, O. R. and Braun, R. L. (1993). Simulation of rotary-drum and repose tests for frictional spheres and rigid sphere clusters. *DOE/NSF Workshop on Flow of Particulates*.
- [104] Whitmore, S. A., Hughes, L., and Calif (2000). Closed-form Integrator for the Quaternion (Euler Angle) Kinematics Equations, US patent.
- [105] Yeung, P. K. and Pope, S. B. (1988). An algorithm for tracking fluid particles in numerical simulations of homogeneous turbulence. *Journal of Computational Physics*, **79**, 373–416.
- [106] Zastawny, M., Mallouppas, G., Zhao, F., and van Wachem, B. (2012a). Derivation of drag and lift force and torque coefficients for non-spherical particles in flows. *International Journal of Multiphase Flow*, **39**, 227–239.
- [107] Zastawny, M., Pennefather, J., and van Wachem, B. (2012b). Improving Immersed Boundary methods for DNS of gas-solid flows. In *13th Workshop on Two-Phase Flow Predictions, Halle Germany, 17 - 20 September 2012*, number September.
- [108] Zhang, H., Ahmadi, G., Fan, F.-G., and McLaughlin, J. B. (2001). Ellipsoidal particles transport and deposition in turbulent channel flows. *International Journal of Multiphase Flow*, **27**(6), 971–1009.
- [109] Zhao, F. and van Wachem, B. (2013a). A novel Quaternion integration approach for describing the behaviour of non-spherical particles. *Acta Mechanica*, **224**(12), 3091–3109.
- [110] Zhao, F. and van Wachem, B. (2013b). Direct numerical simulation of ellipsoidal particles in turbulent channel flow. *Acta Mechanica*, **224**(10), 2331 – 2358.
- [111] Zhao, L. and Andersson, H. I. (2011). On particle spin in two-way coupled turbulent channel flow simulations. *Physics of Fluids*, **23**(9), 093302.

A. Turbulent Kinetic energy (TKE) equation

The TKE equation is derived from the Navier-Stokes equation through several operations and averaging. It is convenient to analyse the flow properties, using Reynolds decomposition, which decompose the properties into two parts: mean components and fluctuating components. Assuming the flow density, ρ^f , is constant, the Navier-Stokes equation for a single phase fluid flow is defined by,

$$\rho^f \left[\frac{\partial(U_i^f + u_i'^f)}{\partial t} + (U_j^f + u_j'^f) \frac{\partial(U_i^f + u_i'^f)}{\partial x_j} \right] = -\frac{\partial(P + p'^f)}{\partial x_i} + \frac{\partial(\tau_{ij} + \tau_{ij}'^f)}{\partial x_j} \quad (\text{A.1})$$

Averaging equation A.1 yields:

$$\rho^f \left[\frac{\partial U_i^f}{\partial t} + U_j^f \frac{\partial U_i^f}{\partial x_j} \right] = -\frac{\partial P}{\partial x_i} + \frac{\partial \tau_{ij}}{\partial x_j} - \rho^f \langle u_j'^f \frac{\partial u_i'^f}{\partial u_j} \rangle \quad (\text{A.2})$$

where the additional term, $\rho^f \langle u_j'^f \frac{\partial u_i'^f}{\partial u_j} \rangle$, is obtained from the velocity divergence term. Based on the incompressible assumption, the continuity equation is expressed as

$$\frac{\partial(U_i^f + u_i'^f)}{\partial x_i} = 0 \quad (\text{A.3})$$

averaging the above equation yields

$$\frac{\partial U_i^f}{\partial x_i} = 0 \quad (\text{A.4})$$

so,

$$\frac{\partial u_i'^f}{\partial x_i} = 0 \quad (\text{A.5})$$

The last term in equation A.2 can be modified as:

$$\langle u_j'^f \frac{\partial u_i'^f}{\partial u_j} \rangle + \langle u_i'^f \frac{\partial u_j'^f}{\partial x_j} \rangle = \langle u_j'^f \frac{\partial u_i'^f}{\partial u_j} \rangle + 0 = \frac{\partial}{\partial x_j} \langle u_i'^f u_j'^f \rangle \quad (\text{A.6})$$

and equation A.2 now can be expressed as

$$\rho^f \left[\frac{\partial U_i^f}{\partial t} + U_j^f \frac{\partial U_i^f}{\partial x_j} \right] = -\frac{\partial P}{\partial x_i} + \frac{\partial}{\partial x_j} [\tau_{ij}^f - \rho^f \langle u_i'^f u_j'^f \rangle] \quad (\text{A.7})$$

where $-\rho^f \langle u_i'^f u_j'^f \rangle$ is the Reynolds stress. Equation A.1 subtracting equation A.2 yields a new equation

$$\rho^f \left[\frac{\partial u_i'^f}{\partial t} + U_j^f \frac{\partial u_i'^f}{\partial x_j} \right] = - \frac{\partial p'^f}{\partial x_i} + \frac{\partial \tau_{ij}'^f}{\partial x_j} - \rho^f [u_j'^f \frac{\partial U_i^f}{\partial x_j}] - \rho^f \left\{ u_j'^f \frac{\partial u_i'^f}{\partial x_j} - \langle u_j'^f \frac{\partial u_i'^f}{\partial x_j} \rangle \right\} \quad (\text{A.8})$$

Multiplying equation A.8 by $u_k'^f$ and averaging:

$$\begin{aligned} \rho^f \left[\langle u_k'^f \frac{\partial u_i'^f}{\partial t} \rangle + U_j^f \langle u_k'^f \frac{\partial u_i'^f}{\partial x_j} \rangle \right] &= - \langle u_k'^f \frac{\partial p'^f}{\partial x_i} \rangle + \langle u_k'^f \frac{\partial \tau_{ij}'^f}{\partial x_j} \rangle \\ &\quad - \rho^f [\langle u_k'^f u_j'^f \rangle \frac{\partial U_i^f}{\partial x_j}] - \rho^f \left\{ \langle u_k'^f u_j'^f \frac{\partial u_i'^f}{\partial x_j} \rangle \right\} \end{aligned} \quad (\text{A.9})$$

in which the subscript i and k can be interchanged, and a new equation is obtained:

$$\begin{aligned} \rho^f \left[\langle u_i'^f \frac{\partial u_k'^f}{\partial t} \rangle + U_j^f \langle u_i'^f \frac{\partial u_k'^f}{\partial x_j} \rangle \right] &= - \langle u_i'^f \frac{\partial p'^f}{\partial x_k} \rangle + \langle u_i'^f \frac{\partial \tau_{ij}'^f}{\partial x_j} \rangle \\ &\quad - \rho^f [\langle u_i'^f u_j'^f \rangle \frac{\partial U_k^f}{\partial x_j}] - \rho^f \left\{ \langle u_i'^f u_j'^f \frac{\partial u_k'^f}{\partial x_j} \rangle \right\} \end{aligned} \quad (\text{A.10})$$

Adding equation A.9 and equation A.10 together yields an equation:

$$\begin{aligned} \frac{\partial \langle u_i'^f u_k'^f \rangle}{\partial t} + U_j^f \frac{\partial \langle u_i'^f u_k'^f \rangle}{\partial x_j} &= - \frac{1}{\rho^f} \left[\langle u_i'^f \frac{\partial p'^f}{\partial x_k} \rangle + \langle u_k'^f \frac{\partial p'^f}{\partial x_i} \rangle \right] \\ &\quad - \left[\langle u_i'^f u_j'^f \frac{\partial u_k'^f}{\partial x_j} \rangle + \langle u_k'^f u_j'^f \frac{\partial u_i'^f}{\partial x_j} \rangle \right] \\ &\quad + \frac{1}{\rho^f} \left[\langle u_i'^f \frac{\partial \tau_{kj}'^f}{\partial x_j} \rangle + \langle u_k'^f \frac{\partial \tau_{ij}'^f}{\partial x_j} \rangle \right] \\ &\quad - \left[\langle u_i'^f u_j'^f \rangle \frac{\partial U_k^f}{\partial x_j} + \langle u_k'^f u_j'^f \rangle \frac{\partial U_i^f}{\partial x_j} \right] \end{aligned} \quad (\text{A.11})$$

of which each term on the right hand side can be rearranged as follow.

$$\begin{aligned} \frac{1}{\rho^f} \left[\langle u_i'^f \frac{\partial p'^f}{\partial x_k} \rangle + \langle u_k'^f \frac{\partial p'^f}{\partial x_i} \rangle \right] &= \langle p'^f \left[\frac{\partial u_i'^f}{\partial x_k} + \frac{\partial u_k'^f}{\partial x_i} \right] \rangle \\ &\quad + \frac{\partial}{\partial x_j} [\langle p'^f u_i'^f \rangle \delta_{kj} + \langle p'^f u_k'^f \rangle \delta_{ij}] \end{aligned} \quad (\text{A.12})$$

The second term can be rearranged as:

$$\left[\langle u_i'^f u_j'^f \frac{\partial u_k'^f}{\partial x_j} \rangle + \langle u_k'^f u_j'^f \frac{\partial u_i'^f}{\partial x_j} \rangle \right] = \frac{\partial}{\partial x_j} \langle u_i'^f u_k'^f u_j'^f \rangle \quad (\text{A.13})$$

The third term is rewritten as:

$$\frac{1}{\rho^f} \left[\left\langle u_i'^f \frac{\partial \tau_{kj}'^f}{\partial x_j} \right\rangle + \left\langle u_k'^f \frac{\partial \tau_{ij}'^f}{\partial x_j} \right\rangle \right] = \frac{\partial}{\partial x_j} \left[\left\langle u_i'^f \tau_{kj}'^f \right\rangle + \left\langle u_k'^f \tau_{ij}'^f \right\rangle \right] - \left[\left\langle \tau_{ij}'^f \frac{\partial u_k'^f}{\partial x_j} \right\rangle + \left\langle \tau_{kj}'^f \frac{\partial u_i'^f}{\partial x_j} \right\rangle \right] \quad (\text{A.14})$$

For a Newtonian fluid flow, the stress, $\tau_{ij}'^f$, can be replaced by the Newtonian constitutive relation, rearranging the above equation as:

$$\frac{1}{\rho^f} \left[\left\langle u_i'^f \frac{\partial \tau_{kj}'^f}{\partial x_j} \right\rangle + \left\langle u_k'^f \frac{\partial \tau_{ij}'^f}{\partial x_j} \right\rangle \right] = 2\nu \frac{\partial}{\partial x_j} \left[\left\langle u_i'^f s_{kj}'^f \right\rangle + \left\langle u_k'^f s_{ij}'^f \right\rangle \right] - 2\nu \left[\left\langle s_{ij}'^f \frac{\partial u_k'^f}{\partial x_j} \right\rangle + \left\langle s_{kj}'^f \frac{\partial u_i'^f}{\partial x_j} \right\rangle \right] \quad (\text{A.15})$$

Therefore, equation A.11 can be expressed by

$$\begin{aligned} \frac{\partial \left\langle u_i'^f u_k'^f \right\rangle}{\partial t} + U_j^f \frac{\partial \left\langle u_i'^f u_k'^f \right\rangle}{\partial x_j} &= \left\langle p'^f \left[\frac{\partial u_i'^f}{\partial x_k} + \frac{\partial u_k'^f}{\partial x_i} \right] \right\rangle \\ &\quad + \frac{\partial}{\partial x_j} \left\{ \left[\left\langle p'^f u_i'^f \right\rangle \delta_{kj} + \left\langle p'^f u_k'^f \right\rangle \delta_{ij} \right] + \left\langle u_i'^f u_k'^f u_j'^f \right\rangle \right. \\ &\quad \left. + 2\nu \left[\left\langle u_i'^f s_{kj}'^f \right\rangle + \left\langle u_k'^f s_{ij}'^f \right\rangle \right] \right\} \\ &\quad - \left[\left\langle u_i'^f u_j'^f \right\rangle \frac{\partial U_k^f}{\partial x_j} + \left\langle u_k'^f u_j'^f \right\rangle \frac{\partial U_i^f}{\partial x_j} \right] \\ &\quad - 2\nu \left[\left\langle s_{ij}'^f \frac{\partial u_k'^f}{\partial x_j} \right\rangle + \left\langle s_{kj}'^f \frac{\partial u_i'^f}{\partial x_j} \right\rangle \right] \end{aligned} \quad (\text{A.16})$$

This is Reynolds stress equation.

If the subscript $i = k$, Reynolds stress equation is simplified into:

$$\begin{aligned} \left[\frac{\partial}{\partial t} \left\langle u_i'^f u_i'^f \right\rangle + U_j^f \frac{\partial}{\partial x_j} \left\langle u_i'^f u_i'^f \right\rangle \right] &= \frac{\partial}{\partial x_j} \left\{ \left\langle u_i'^f u_i'^f u_j'^f \right\rangle + 2 \frac{\left\langle u_j'^f p'^f \right\rangle}{\rho^f} - 4\nu^f \left\langle s_{ij}'^f u_i'^f \right\rangle \right\} \\ &\quad - 2 \left\langle u_i'^f u_j'^f \right\rangle \frac{\partial U_i^f}{\partial x_j} - 4\nu^f \left\langle s_{ij}'^f \frac{\partial u_i'^f}{\partial x_j} \right\rangle \end{aligned} \quad (\text{A.17})$$

The turbulence kinetic energy, k , is defined by

$$k = \frac{1}{2} \left\langle u_i'^f u_i'^f \right\rangle \quad (\text{A.18})$$

then the term $\left\langle u_i'^f u_i'^f \right\rangle$ in equation A.17 can be replaced by k , and the new equation is the Turbulence kinetic equation (TKE) equation, given as:

$$\frac{\partial k}{\partial t} + U_j^f \frac{\partial k}{\partial x_j} = \frac{\partial}{\partial x_j} \left\{ \frac{1}{2} \langle u_i'^f u_i'^f u_j'^f \rangle + \frac{\langle u_j'^f p'^f \rangle}{\rho^f} - 2\nu^f \langle s_{ij}'^f u_i'^f \rangle \right\} - \langle u_i'^f u_j'^f \rangle \frac{\partial U_i^f}{\partial x_j} - 2\nu^f \langle s_{ij}'^f \frac{\partial u_i'^f}{\partial x_j} \rangle \quad (\text{A.19})$$

where the first three divergence terms in the brace on the right hand side present the three transport terms: turbulence itself transport, the pressure fluctuation transport and viscous stress transport respectively, the fourth term $-\langle u_i'^f u_j'^f \rangle \frac{\partial U_i^f}{\partial x_j}$ is the production of turbulence, and the last term $\nu^f \langle s_{ij}'^f \frac{\partial u_i'^f}{\partial x_j} \rangle$ presents the fluid flow dissipation rate, $\tilde{\varepsilon}$. The above computation follows the lecture notes [40], in which more detail about TKE equation is described.

A.1. TKE equation in fully developed channel flow

A fully developed channel flow is a steady flow, in which the flow statistics is independent of the flow initial conditions and time. Therefore, the first term in the TKE equation A.19 ($\frac{\partial k}{\partial t}$) is equal to zero. In a fully developed channel flow, the stream-wise and span-wise directions are considered as homogeneous directions. In these two directions, all time averaged variables are in essential identical, and time averaged partial differential variables equals zero. Therefore, in the TKE equation the differential term $\frac{\partial}{\partial x_j}$ is reduced to $\frac{\partial}{\partial x_2}$, and so all repeat subscript j is fixed to 2 (the wall-normal direction). The second term $U_j^f \frac{\partial k}{\partial x_j}$ on the left hand of equation A.19 equals:

$$U_j^f \frac{\partial k}{\partial x_j} = U_2^f \frac{\partial k}{\partial x_2} \quad (\text{A.20})$$

where U_2^f is zero, and thus this term is also zero.

The production of turbulence, \mathcal{P} , can be simplified as:

$$\begin{aligned} \mathcal{P} &= -\langle u_i'^f u_j'^f \rangle \frac{\partial U_i^f}{\partial x_j} \\ &= -\langle u_i'^f u_2'^f \rangle \frac{\partial U_i^f}{\partial x_2} \end{aligned} \quad (\text{A.21})$$

The mean velocity gradient $\frac{\partial U_1^f}{\partial x_2}$ and $\frac{\partial U_3^f}{\partial x_2}$ are zero; therefore, \mathcal{P} in the channel flow is given as

$$\mathcal{P} = -\langle u_1'^f u_2'^f \rangle \frac{\partial U_1^f}{\partial x_2} \quad (\text{A.22})$$

The fluid dissipation rate, $\tilde{\varepsilon} = 2\nu^f \langle s_{ij}'^f \frac{\partial u_i'^f}{\partial x_j} \rangle$, can be expressed as:

$$\tilde{\varepsilon} = 2\nu^f \langle s_{ij}'^f s_{ij}'^f \rangle \quad (\text{A.23})$$

The all three transport terms are expressed as:

$$\begin{aligned} \frac{\partial}{\partial x_j} \left\{ \frac{1}{2} \langle u_i' f u_i' f u_j' f \rangle + \frac{\langle u_j' f p' f \rangle}{\rho^f} - 2\nu^f \langle s_{ij}' f u_i' f \rangle \right\} = \\ \frac{\partial}{\partial x_2} \left\{ \frac{1}{2} \langle u_i' f u_i' f u_2' f \rangle + \frac{\langle u_2' f p' f \rangle}{\rho^f} - 2\nu^f \langle s_{i2}' f u_i' f \rangle \right\} \end{aligned} \quad (\text{A.24})$$

where the viscous transport term, $2\nu^f \langle s_{i2}' f u_i' f \rangle$, can be further simplified into:

$$2\nu^f \langle s_{i2}' f u_i' f \rangle = \nu \left[\langle \frac{\partial u_i' f}{\partial x_2} u_i' f \rangle + \langle \frac{\partial u_2' f}{\partial x_i} u_i' f \rangle \right] \quad (\text{A.25})$$

where $\langle \frac{\partial u_i' f}{\partial x_2} u_i' f \rangle$ equals:

$$\langle \frac{\partial u_i' f}{\partial x_2} u_i' f \rangle = \frac{\partial \langle u_i' f u_i' f \rangle}{\partial x_2} - \langle \frac{\partial u_i' f}{\partial x_2} u_i' f \rangle \quad (\text{A.26})$$

so,

$$2 * \frac{\partial k}{\partial x_2} = 2 * \langle \frac{\partial u_i' f}{\partial x_2} u_i' f \rangle \quad (\text{A.27})$$

$$\frac{\partial k}{\partial x_2} = \langle \frac{\partial u_i' f}{\partial x_2} u_i' f \rangle \quad (\text{A.28})$$

A similar treatment can be also used on the second term on the right hand side of equation A.25:

$$\begin{aligned} \langle \frac{\partial u_2' f}{\partial x_i} u_i' f \rangle &= \frac{\partial \langle u_2' f u_i' f \rangle}{\partial x_i} - \langle \frac{\partial u_i' f}{\partial x_i} u_2' f \rangle \\ &= \frac{\partial \langle u_2' f u_2' f \rangle}{\partial x_2} + 0 \\ &= \frac{\partial \langle u_2' f^2 \rangle}{\partial x_2} \end{aligned} \quad (\text{A.29})$$

Therefore the three transport terms are given by:

$$\frac{\partial}{\partial x_2} \left\{ \frac{1}{2} \langle u_i' f u_i' f u_2' f \rangle + \frac{\langle u_2' f p' f \rangle}{\rho^f} - \frac{\partial}{\partial x_2} (k + u_2' f^2) \right\} \quad (\text{A.30})$$

Finally, the TKE equation for a fully developed flow is expressed as

$$\frac{d}{dy} \left(\frac{1}{2} \langle u_2' f u_i' f u_i' f \rangle + \frac{u_2' f p' f}{\rho^f} - \nu^f \frac{d}{dy} (k + u_2' f^2) \right) = - \langle u_1' f u_2' f \rangle \frac{\partial U_1^f}{\partial x_2} - 2\nu^f \langle s_{ij}' f s_{ij}' f \rangle \quad (\text{A.31})$$

For four-way coupled simulations of gas-solid channel flow with the point-particle approach, a source term, Π , from coupled forces of particles is added into the Navier-Stokes equation A.1. Therefore, a new term appear in the TKE equation for gas-solid multiphase flows. The TKE equation for a fully developed gas-solid channel flow is defined by:

$$\frac{d}{dy} \left(\frac{1}{2} \langle u_2'^f u_i'^f u_i'^f \rangle + \frac{u_2'^f p'^f}{\rho^f} - \nu^f \frac{d}{dy} (k + u_2'^f)^2 \right) = - \langle u_1'^f u_2'^f \rangle \frac{\partial U_1^f}{\partial x_2} - 2\nu^f \langle s_{ij}'^f \frac{\partial u_i'^f}{\partial x_j} \rangle - \varepsilon_p \quad (\text{A.32})$$

where the dissipation rate caused by the coupling force from particles, ε_p , is directly derived from Π_i , given as:

$$\varepsilon_p = - \langle \Pi_i'^f u_i'^f \rangle \quad (\text{A.33})$$

A.2. The fluid flow dissipation rate

The fluid dissipation rate $\tilde{\varepsilon}$ can be decomposed and represented by its components.

$$\begin{aligned} \tilde{\varepsilon} &= 2\nu^f \langle s_{ij}'^f \frac{\partial u_i'^f}{\partial x_j} \rangle \\ &= \nu \left[\langle \frac{\partial u_i'^f}{\partial x_j} \frac{\partial u_i'^f}{\partial x_j} \rangle + \langle \frac{\partial u_j'^f}{\partial x_i} \frac{\partial u_i'^f}{\partial x_j} \rangle \right] \end{aligned} \quad (\text{A.34})$$

Using index representation ($\frac{\partial u_j'^f}{\partial x_i} = \langle u_{i,j}'^f \rangle$)

$$\tilde{\varepsilon} = \left[\langle u_{i,j}'^f \rangle + \langle u_{i,j}'^f u_{j,i}'^f \rangle \right] \quad (\text{A.35})$$

where the first term on the right hand side is:

$$\begin{aligned} \langle u_{i,j}'^f \rangle &= \langle u_{1,1}'^f \rangle + \langle u_{2,2}'^f \rangle + \langle u_{3,3}'^f \rangle \\ &\quad + \langle u_{1,2}'^f \rangle + \langle u_{2,1}'^f \rangle + \langle u_{1,3}'^f \rangle + \langle u_{3,1}'^f \rangle + \langle u_{3,2}'^f \rangle + \langle u_{2,3}'^f \rangle \end{aligned} \quad (\text{A.36})$$

and the second term can be expressed by:

$$\begin{aligned} \langle u_{i,j}'^f u_{j,i}'^f \rangle &= \langle u_{1,1}'^f \rangle + \langle u_{2,2}'^f \rangle + \langle u_{3,3}'^f \rangle \\ &\quad + \langle u_{1,2}'^f u_{2,1}'^f \rangle + \langle u_{1,3}'^f u_{3,1}'^f \rangle + \langle u_{2,3}'^f u_{3,2}'^f \rangle \\ &\quad + \langle u_{2,1}'^f u_{1,2}'^f \rangle + \langle u_{3,1}'^f u_{1,3}'^f \rangle + \langle u_{3,2}'^f u_{2,3}'^f \rangle \end{aligned} \quad (\text{A.37})$$

Therefore, the fluid flow turbulence dissipation rate $\tilde{\varepsilon}$ can be expressed by:

$$\begin{aligned} \tilde{\varepsilon} &= -\nu [2(\langle u_{1,1}'^f \rangle + \langle u_{2,2}'^f \rangle + \langle u_{3,3}'^f \rangle) \\ &\quad + (\langle u_{1,2}'^f \rangle + \langle u_{2,1}'^f \rangle + \langle u_{1,3}'^f \rangle + \langle u_{3,1}'^f \rangle + \langle u_{3,2}'^f \rangle + \langle u_{2,3}'^f \rangle) \\ &\quad + 2(\langle u_{1,2}'^f u_{2,1}'^f \rangle + \langle u_{1,3}'^f u_{3,1}'^f \rangle + \langle u_{2,3}'^f u_{3,2}'^f \rangle)] \end{aligned} \quad (\text{A.38})$$

B. Some characteristics of turbulence in gas-solid channel flows

The aim of this Appendix is to expand the study of investigating the effects of particle shape and Stokes number on the fluid turbulence in Sec. 4.3. More turbulence terms are discussed here, such as all twelve components of the fluid flow dissipation rate, the Taylor scales and Kolmogorov scales in the gas-solid channel flows with non-spherical ellipsoids.

B.1. The components of dissipation rate

In chapter 4, Sec. 4.3.2.4 only shows and analyses the effects of particle inertia and shape on the three major components ($\langle u_{1,2}^{\prime f+2} \rangle$, $\langle u_{3,2}^{\prime f+2} \rangle$ and $\langle u_{1,3}^{\prime f+2} \rangle$), not all the components of the fluid flow dissipation rate ($\tilde{\varepsilon}$). The following 12 figures from Figs. B.1 to B.12, display all the twelve components of $\tilde{\varepsilon}$. Comparing these twelve Figures, it is

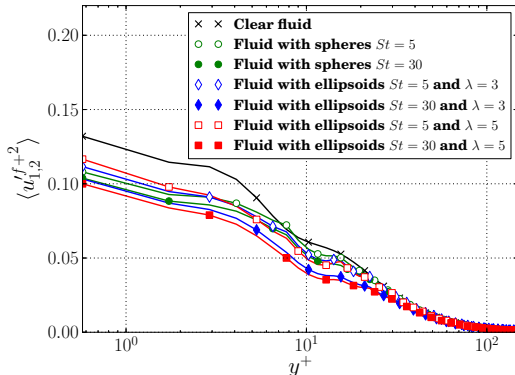


Figure B.1.: Mean-square derivative $\langle u_{1,2}^{\prime f+2} \rangle$ as a function of distance to the wall

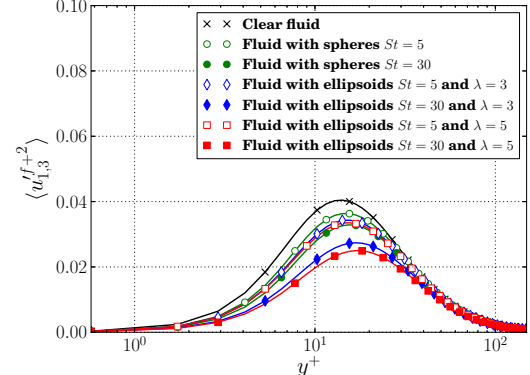


Figure B.2.: Mean-square derivative $\langle u_{1,3}^{\prime f+2} \rangle$ as a function of distance to the wall

apparent that $\langle u_{1,2}^{\prime f+2} \rangle$, $\langle u_{3,2}^{\prime f+2} \rangle$ and $\langle u_{1,3}^{\prime f+2} \rangle$ are significantly larger than the other nine components. This confirms that only these three components mainly contribute to $\tilde{\varepsilon}$. As can be seen in Figs. B.1 and B.3, $\langle u_{1,2}^{\prime f+2} \rangle$ and $\langle u_{3,2}^{\prime f+2} \rangle$ peaks at the wall, due to the wall effect. However, the other seven mean square derivatives are almost zero at the wall and their peak points are found in the region between $20 < y^+ < 60$. Therefore, only $\langle u_{1,2}^{\prime f+2} \rangle$ and $\langle u_{3,2}^{\prime f+2} \rangle$ contributes to the largest absolute value of $\tilde{\varepsilon}$ at the wall, as illustrated in Fig. 4.13. As shown from Figs. B.1 to B.9, nine mean square derivatives are all positive, and their peak values decrease from $\langle u_{1,2}^{\prime f+2} \rangle$ in Fig. B.1 to $\langle u_{2,1}^{\prime f+2} \rangle$

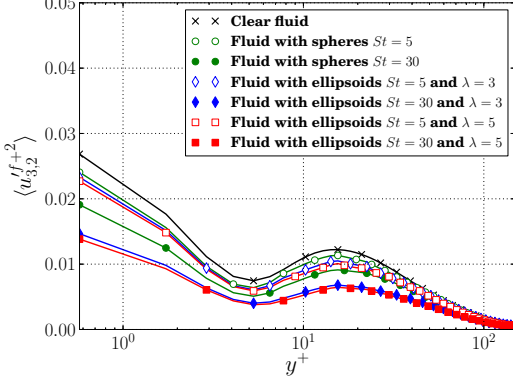


Figure B.3.: Mean-square derivative $\langle u_{3,2}^{f+2} \rangle$ as a function of distance to the wall

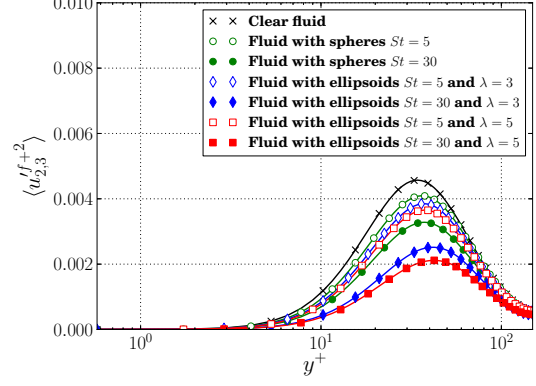


Figure B.4.: Mean-square derivative $\langle u_{2,3}^{f+2} \rangle$ as a function of distance to the wall

in Fig. B.9. As reported in Sec. 4.3.2.4, $\langle u_{1,2}^{f+2} \rangle$, $\langle u_{3,2}^{f+2} \rangle$ and $\langle u_{1,3}^{f+2} \rangle$ decrease as

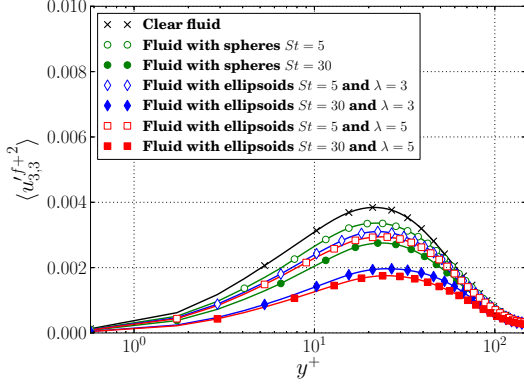


Figure B.5.: Mean-square derivative $\langle u_{3,3}^{f+2} \rangle$ as a function of distance to the wall

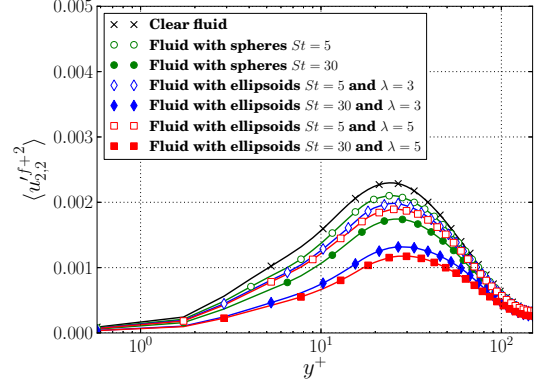


Figure B.6.: Mean-square derivative $\langle u_{2,2}^{f+2} \rangle$ as a function of distance to the wall

the Stokes number and the ellipsoid aspect ratio increase. The results in Figs. B.4 to B.9 show that increasing particle inertia and aspect ratio also reduces the magnitudes of the other 6 mean-square derivatives.

Figs. B.10 to B.12 show the three cross derivatives, of which the negative values make negative contribution to the fluid dissipation rate, $\tilde{\varepsilon}$, and positive contribution to vorticity, $\langle \omega f^2 \rangle$. As expected, the peak magnitudes of these cross terms are considerably reduced with increasing particle inertia and aspect ratio. It is clearly observed from Figs. B.1 to B.12 that all the magnitudes of $\tilde{\varepsilon}$ components are extremely small at the channel center, and the effects of particle shape and Stokes number on the fluid flow dissipation rate are not of importance in the central region of the channel.

To accurately describe the fluid flow dissipation rate, all twelve components should be calculated and taken into account. In the literature, some assumptions were made to simplify the computation of the fluid dissipation rate, due to the limitation of computation capacity. The fluid flow in the central region of the channel may be assumed as homoge-

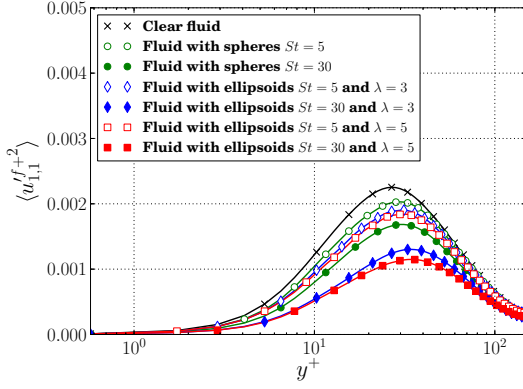


Figure B.7.: Mean-square derivative $\langle u_{1,1}^{\prime f+2} \rangle$ as a function of distance to the wall

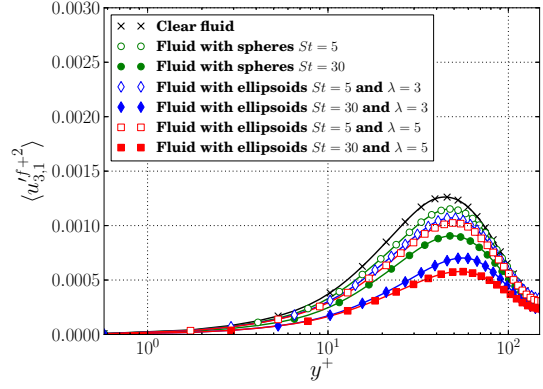


Figure B.8.: Mean-square derivative $\langle u_{3,1}^{\prime f+2} \rangle$ as a function of distance to the wall

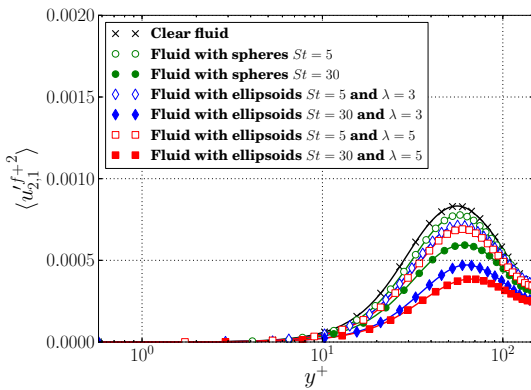


Figure B.9.: Mean-square derivative $\langle u_{2,1}^{\prime f+2} \rangle$ as a function of distance to the wall

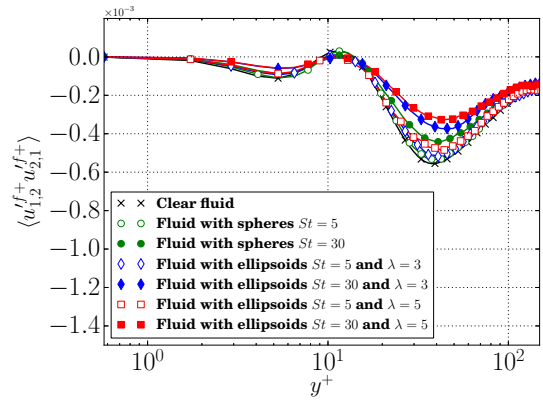


Figure B.10.: Cross derivative $\langle u_{1,2}^{\prime f+} u_{2,1}^{\prime f+} \rangle$ as a function of distance to the wall

neous, isotropic or local axis-symmetric flows. These assumptions are corresponding four different fluid dissipation rates: isotropic dissipation rate ($\tilde{\varepsilon}_{iso}$), homogeneous dissipation rate ($\tilde{\varepsilon}_{hom}$) and two axisymmetric dissipation rates ($\tilde{\varepsilon}_{axis_1}$ and $\tilde{\varepsilon}_{axis_2}$), which are all determined by several or one components of $\tilde{\varepsilon}$ and defined by equations 1.18, 1.20, 1.21 and 1.22 respectively in Sec. 1.3.4. In Sec. 4.3.2.4, Figs. 4.18 to 4.21 display the ratios of $\tilde{\varepsilon}_{hom}$, $\tilde{\varepsilon}_{iso}$, $\tilde{\varepsilon}_{axis_1}$ and $\tilde{\varepsilon}_{axis_2}$ to $\tilde{\varepsilon}$ respectively, among six simulations considering ellipsoidal particles and one clear fluid flow simulation in Chapter 4. The discrete particles in channel flows do not influence the modelled dissipation rate. At channel center, the deviations of these ratios from 1 represents the errors of these modelled dissipation rates. As respected, the homogeneous dissipation rate ($\tilde{\varepsilon}_{hom}$) are most close to the fluid dissipation rate $\tilde{\varepsilon}$. This indicates that the turbulence flow in the central region of the channel close to the local homogeneous flow.

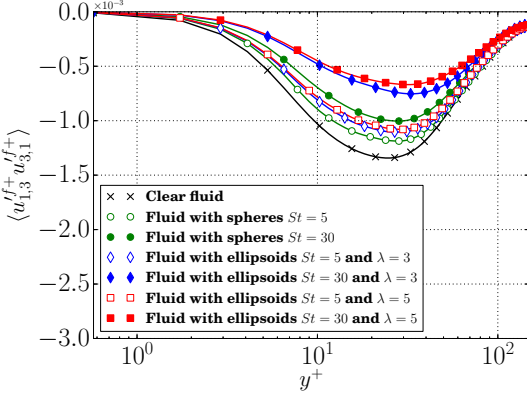


Figure B.11.: Cross derivative $\langle u'_{1,3}^{f+} u'_{3,1}^{f+} \rangle$ as a function of distance to the wall

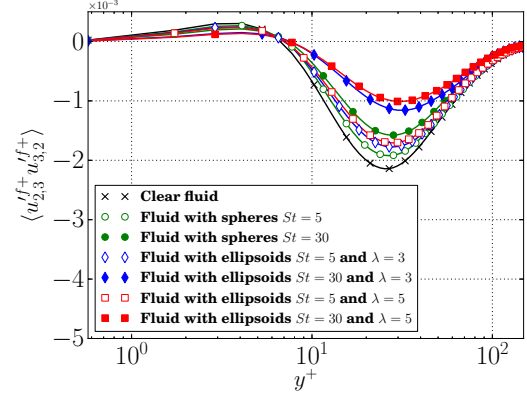


Figure B.12.: Cross derivative $\langle u'_{2,3}^{f+} u'_{3,2}^{f+} \rangle$ as a function of distance to the wall

B.2. Taylor microscales

The Taylor micro-scale is an important length scale for turbulent flows and defined by:

$$\lambda_{ij}^f = \sqrt{2} \frac{\langle u_j'^f \rangle^2}{\langle \frac{\partial u_j'^f}{\partial x_i} \rangle} \quad (\text{B.1})$$

The Taylor micro-scale can be used to characterise the two point velocity correlation in the turbulence flow and the integral length-scales in homogeneous directions. For a fully developed channel flow, the stream-wise and span-wise directions are homogeneous directions, in which there is a longitudinal and two transverse Taylor scales.

Figs. B.13 to B.15 display the longitudinal (λ_{11}^f) and two transverse scales (λ_{21}^f and λ_{31}^f) respectively in the stream-wise direction, while the longitudinal (λ_{33}^f) and two transverse

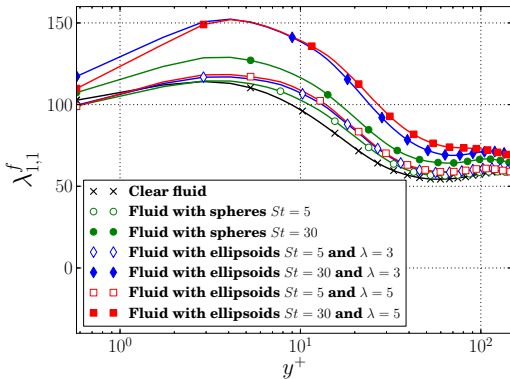


Figure B.13.: The longitudinal Taylor scale in the stream-wise direction

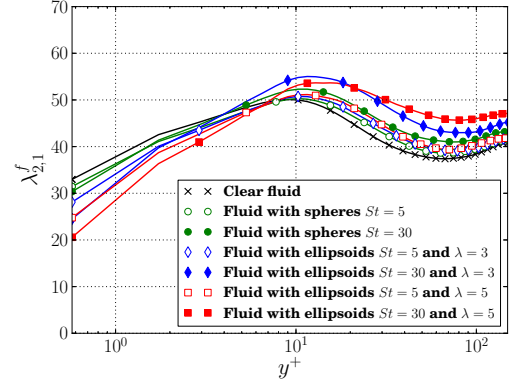


Figure B.14.: The wall-normal transverse Taylor scale in the stream-wise direction

scales (λ_{13}^f and λ_{23}^f) in the span-wise direction are shown in Figs. B.16 to B.18. As shown in these figures, the Taylor micro-scales rises with the increasing particle aspect ratio and

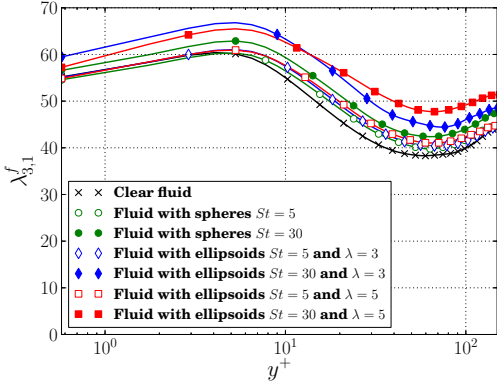


Figure B.15.: The span-wise transverse Taylor scale in the streamwise direction

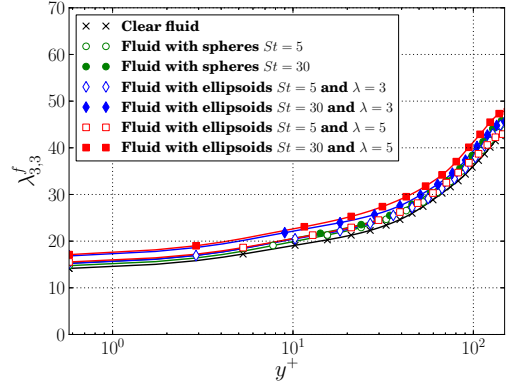


Figure B.16.: The longitudinal Taylor scale in the span-wise direction

St numbers, and both effects are much stronger on the Taylor micro-scales in the streamwise direction than those in the span-wise direction. The increase of Taylor micro-scales

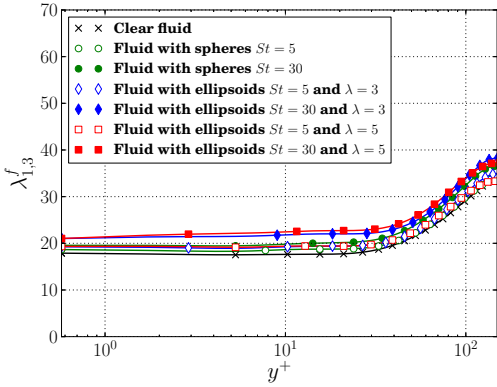


Figure B.17.: The stream-wise transverse Taylor scale in the span-wise direction

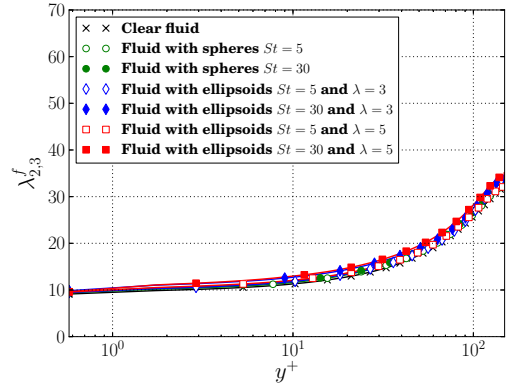


Figure B.18.: The wall-normal transverse Taylor scale in the span-wise direction

implies that the flow turbulence is attenuated by adding heavy particles.

B.3. Kolmogorov scales

Fig. B.19 shows the Kolmogorov length scales among ellipsoid-laden simulations with various particle inertia and particle aspect ratio. Increasing particle inertia and aspect ratio can increase the Kolmogorov length scale (η) through the channel. As the fluid viscosity, ν^f , is a constant and the same in all cases, the rise in η indicates that the fluid flow dissipation rate is reduced.

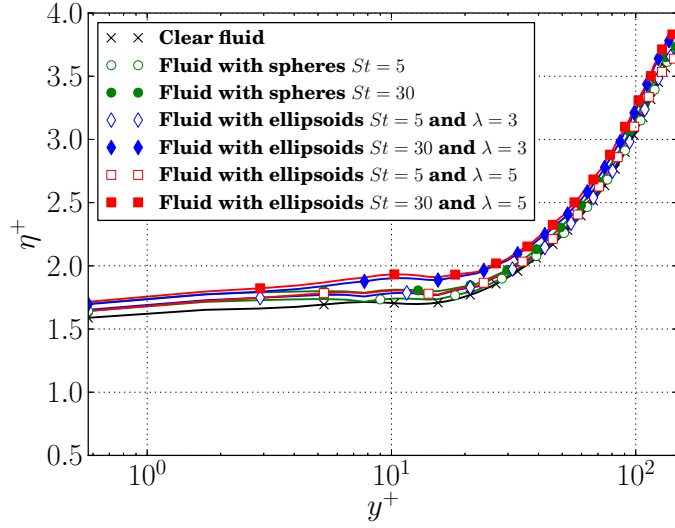


Figure B.19.: The Kolmogorov length scale (η) as a function of distance to the wall

B.4. Summary

In Appendix B, some turbulence terms in gas-solid channel flows are plotted and discussed to expand and support the analysis of the effects of Stokes number and elongated ellipsoid shape on the flow turbulence.

The results of all twelve components of the fluid flow dissipation rate ($\tilde{\varepsilon}$) directly show the peak magnitudes of all the components are reduced with increasing particle inertia and particle aspect ratio, and the effect of particles on $\tilde{\varepsilon}$ are weak in the channel center. The results of Taylor micro-scales and the Kolmogorov length scale also confirm that ellipsoidal particles with high inertia and large aspect ratio of ellipsoidal particles attenuate the turbulence intensity.

C. The distribution of particle angular velocity

Sec. 4.5.5 shows and analyses the mean angular velocity, ω_i^p , of ellipsoidal particles in all three directions. ω_1^p and ω_2^p are close to zero through the whole channel, whereas the magnitude of ω_3^p peaks next to the wall and decreases to the minimum magnitude, zero, at the channel center. It is apparent that the mean particle angular velocity is not significantly affected by varying particle inertia and aspect ratio. In order to investigate the effects of Stokes number and elongated particle shape on the particle angular velocity, the distribution of the particle angular velocity in the near wall and central regions of the channel are plotted from Figs. C.1 to C.6. The pdfs of the particle angular velocity are expressed as:

$$\omega_{i,PDFs}^p = \frac{(\omega_i^p - \omega_{i,mean}^p)}{\omega_i'^p} \quad (C.1)$$

in the near wall region and channel center, the highest probability of $\omega_{i,PDFs}^p$ are found at zero, *i.e.* the mean particle angular velocity.

Figs. C.1 to C.3 display the pdfs of particle angular velocity in the near wall region between $0 < y^+ < 10$. With increasing Stokes number, the highest probability of ω_i^p at the mean

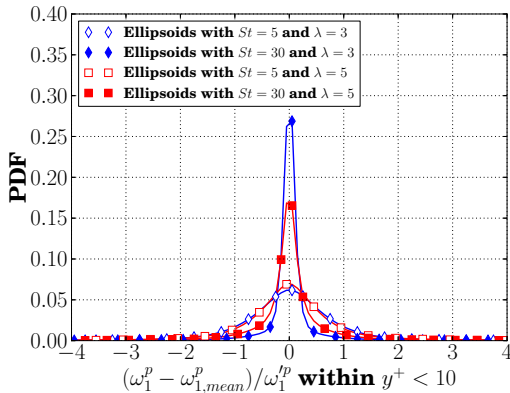


Figure C.1.: The frequency of stream-wise angular velocity in the near wall region of $0 < y^+ < 10$

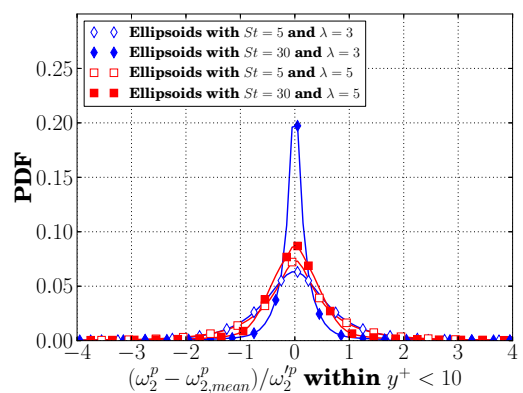


Figure C.2.: The frequency of wall-normal angular velocity in the near wall region of $0 < y^+ < 10$

value rises significantly. This is because particles with high inertia can strongly maintain their motion and resist the fluid effect. In the cases with the same high Stokes number ($St = 30$), ellipsoids with shorter aspect ratio ($\lambda = 3$) encounter a slightly smaller torque and thus the peak value of $\omega_{i,PDFs}^p$ at zero is higher in the near wall region, compared to the ellipsoids with $\lambda = 5$. In contrast, the effect of particle aspect ratio on $\omega_{i,PDFs}^p$ is almost

negligible in the cases with relatively low St ($St = 5$). As can be seen from Figs. C.1 to C.3, the distribution of $\omega_{i,PDFs}^p$ are symmetrical and peak at the mean angular velocities, i.e. $\omega_i^p - \omega_{i,mean}^p = 0$, except $\omega_{3,PDFs}^p$ in the cases with low Stokes number ($St = 5$). As $\omega_{3,mean}^p$ increases significantly in the near wall region and has a large velocity gradient, a slightly large probability are found in the region ($\omega_{3,PDFs}^p > 0$).

Figs. C.4 to C.6 show the pdfs of the particle angular velocity in the central region of the channel in all three directions are symmetric and quite similar to each other. The peak

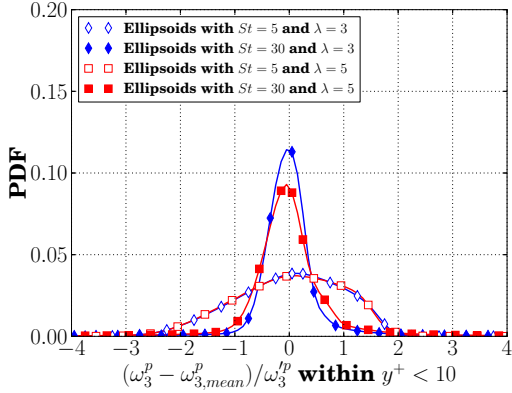


Figure C.3.: The frequency of span-wise angular velocity in the near wall region of $0 < y^+ < 10$

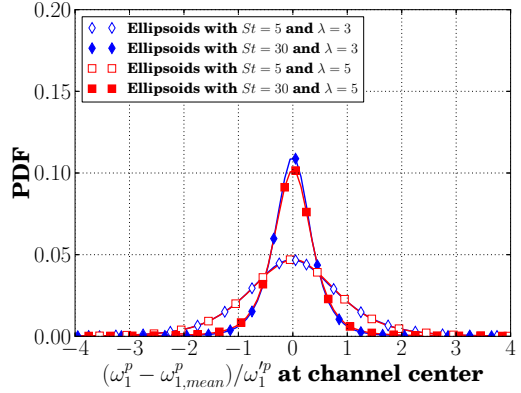


Figure C.4.: The frequency of stream-wise angular velocity in the central region of the channel

value of $\omega_{i,PDFs}^p$ rises with increasing Stokes number, whereas the effect of particle aspect ratio on $\omega_{i,PDFs}^p$ is negligible for all cases at the channel center.

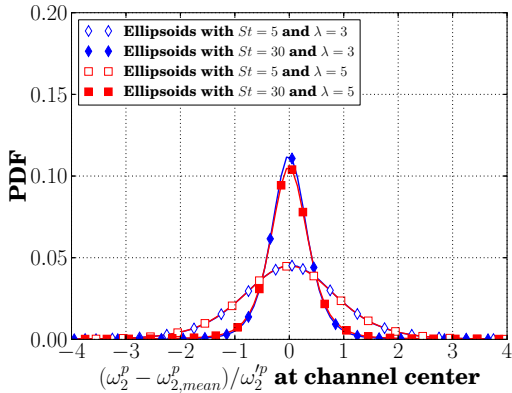


Figure C.5.: The frequency of wall-normal angular velocity in the central region of the channel

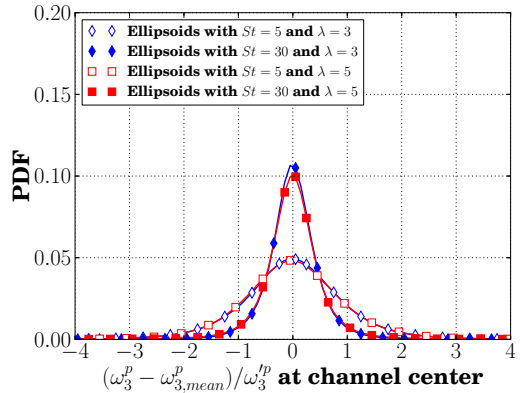


Figure C.6.: The frequency of span-wise angular velocity in the central region of the channel

D. The orientation of ellipsoidal particles

D.1. The comparison of the mean absolute cosine values $|cos(\theta_i)|$ and the mean orientation angles θ_i

Chapter 4 mentions that the previous works [71, 76, 108] analyse the orientation of ellipsoidal particles by representing the mean absolute cosine values ($|cos(\theta_i)|$), not direction discuss the orientation angles θ_i , which is the angles between major axis of an ellipsoidal particle and the axes of world space. θ_i varies linearly between 0° to 90° , but their corresponding cosine values non-linearly change between 1 to 0. The non-linear cosine function may not accurately represent the orientation of ellipsoidal particles. Figs. D.1 to D.3 shows the difference between the mean angles and the angle computed from the mean cosine values in the two cases ($St = 5, \lambda = 3$ and $St = 30, \lambda = 5$). It is clearly observed

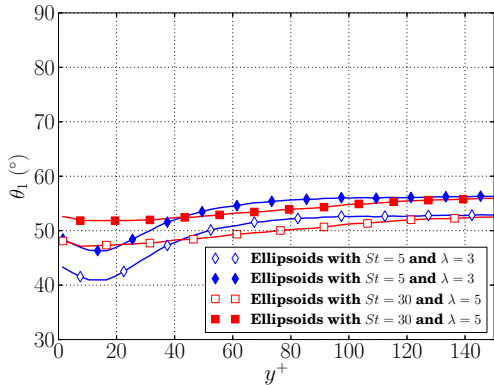


Figure D.1.: The mean orientation angles in the stream-wise direction: \diamond and \square indicate the results of mean angles, while \blacklozenge and \blacksquare represent the angle computed from the results of mean cosine

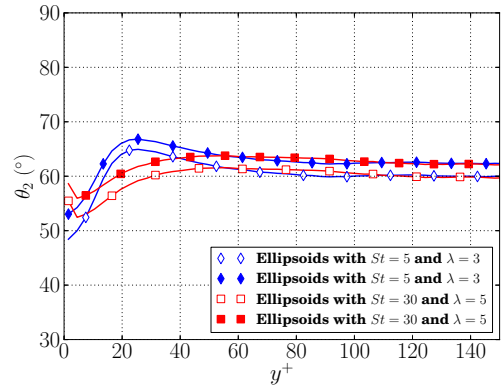


Figure D.2.: The mean orientation angles in the wall-normal direction: \diamond and \square indicate the results of mean angles, while \blacklozenge and \blacksquare represent the angle computed from the results of mean cosine

from Figs. D.1 and D.3 that the angles computed from the mean cosine are larger than the mean orientation angles (θ_i). The results of $|cos(\theta_i)|$ over-estimates the orientation angles.

D.2. The distribution of orientation angle (ψ_i)

As explained in Sec. 4.5.6, the orientation angles, θ_i , are correlated to each other, and their sum must be always equals 180° ; therefore, it cannot conclude from the results of mean θ_i

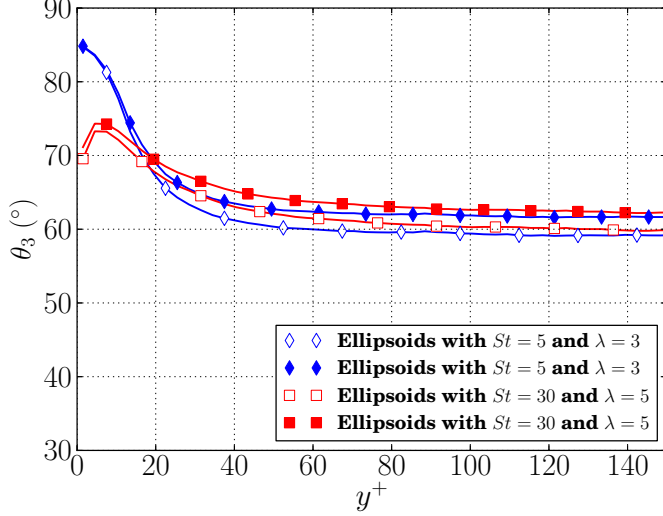


Figure D.3.: The mean orientation angles in the span-wise direction: \diamond and \square indicate the results of mean angles, while \blacklozenge and \blacksquare represent the angle computed from the results of mean cosine

and distribution of θ_i in the channel center that the orientation of ellipsoids in the channel center is randomly distributed or has a preferential orientation. To analyse the orientation of the ellipsoidal particles in the channel center, this study proposes the orientation angles (ψ_i), which represent the angles between the 2-D vectors x_{yz}^p , x_{xz}^p and x_{xy}^p and the z , x and x axes of world space, as shown in Fig. 4.52. As shown from Figs. 4.56 to 4.58, the distribution of ψ_i at channel center indicates that the orientation of the ellipsoids is almost randomly distributed in the central region of the channel. The distribution of ψ_i in the near wall region ($0 < y^+ < 10$) also confirms the ellipsoids align in the X-Y plane which lies perpendicular to the span-wise direction.

Figs. D.4 to D.6 show the distribution of angles ψ_i slightly away from the wall in the buffer-layer ($15 < y^+ < 20$). For the cases with large Stokes number ($St = 30$), the

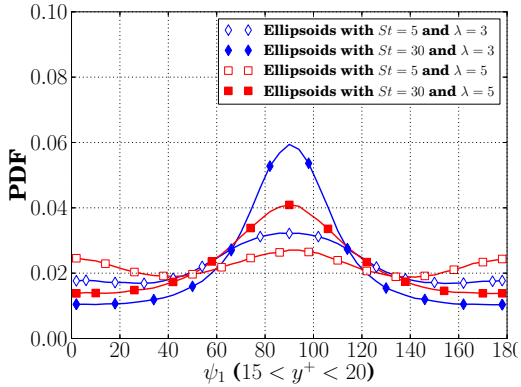


Figure D.4.: The frequency of ψ_1 in the buffer-layer region ($15 < y^+ < 20$).

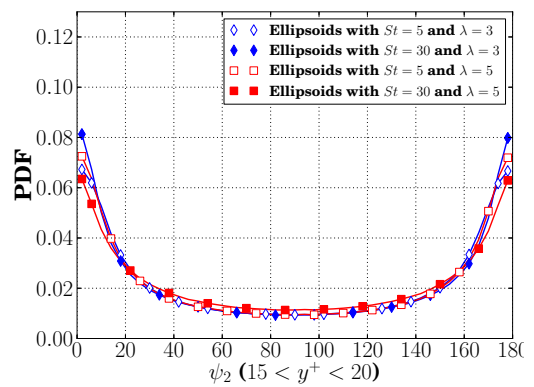


Figure D.5.: The frequency of ψ_2 in the buffer-layer region ($15 < y^+ < 20$).

results of ψ_i are consistent with the results in the near wall region; therefore, ellipsoids

with high inertia ($St = 30$) also tend to align with X-Y plane in the buffer-layer. However, the distribution of ψ_i for ellipsoids with low Stokes number ($St = 5$) in the bufferlayer as illustrated in Figs. D.4 to D.6 are quite different from those in the near wall region. For the ellipsoids with low inertia ($St = 5$), ψ_1 is uniformly distributed, whereas the probability of ψ_2 and ψ_3 peaks around 0° and 180° , *i.e.* the ellipsoids aligns with x axis of world space. These indicate that the orientation of ellipsoids with low inertia ($St = 5$) follows the stream-wise direction in the region between $15 < y^+ < 20$. It can be concluded that ellipsoids with high inertia ($St = 30$) tend to align in X-Y plane in the near wall region between $0 < y^+ < 20$, while ellipsoids with relatively low inertia ($St = 5$) preferentially align in X-Y plane near the wall but follows the stream-wise direction in the bufferlayer of $15 < y^+ < 20$.

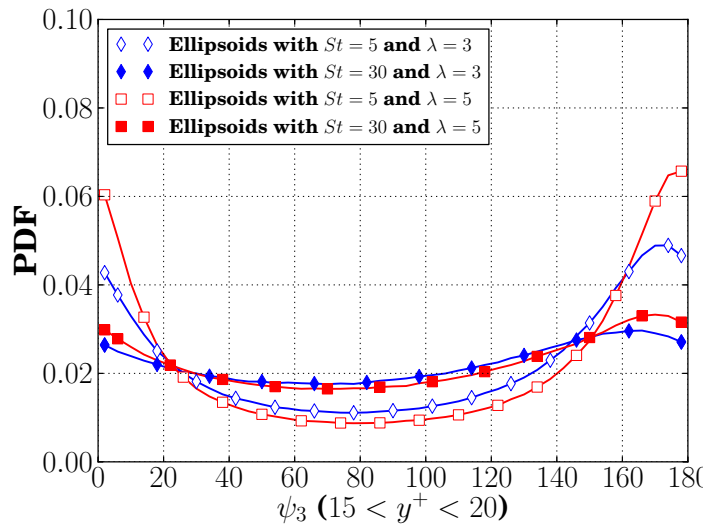


Figure D.6.: The frequency of ψ_3 in the buffer-layer region ($15 < y^+ < 20$).